Optically-selective window coatings of precious metal nanoparticles

by

Nicholas Stokes

A thesis submitted for the

degree of Doctor of Philosophy (Science)

University of Technology, Sydney

2010

Certificate of Originality

I certify that the work in this thesis has not previously been submitted for a degree nor has it been submitted as part of requirements for a degree except as fully acknowledged within the text.

I also certify that the thesis has been written by me. Any help that I have received in my research work and the preparation of the thesis itself has been acknowledged. In addition, I certify that all information sources and literature used are indicated in the thesis.

Signature of Candidate

_____

Acknowledgements

First and foremost, I would like to thank my supervisors Dr. Andrew McDonagh and Prof. Michael Cortie. Their guidance and enthusiasm was essential to this work and my development as a researcher. You both provided a wide branch of knowledge and experience to draw on as well as providing time, patience and guidance for my many queries and questions.

I am grateful for the all the support provided by both AngloGold Ashanti Australia and the Institute for Nanoscale Technology at the University of Technology Sydney. Computational resources were made available by the Australian Centre for Advanced Computing and Communications (AC3) and the Australian Partnership for Advanced Computing (APAC).

I must also thank the people that I have collaborated with over the course of this work. Thanks to Jonathon Edgar for providing the gold nanorods in sufficient quantity and over a range of aspect ratios required for Chapters 5 and 6. Thanks also to Ric Wuhrer for frequent repairs of the EBL system and in particular for many constructive discussions regarding the EBL process. I would also like to thank Keith Moulding for responding quickly and with useful suggestions for fixing the lithography instrument. I would also like to thank Geoff McCredie for help with the vacuum deposition systems. Thanks to Martin Blaber and Nadine Harris for teaching me the DDSCAT software. I also thank Angus Gentle and Matthew Arnold for their help.

Special thanks to my fellow office mates who have made the times very enjoyable, Vijay Bhatia, Martin Blaber, Burak Cankurtaran, Michael Coutts, Jonathon Edgar, Nadine Harris, Rainer Hoft, Tim Lucey, Dakrong Pissuan, Dylan Riessen and Xiaoda Xu.

Last but not least I would like to thank my friends and family for their interest and support.

Table of contents

List of figures

List of tables

Abbreviations

AFM = Atomic Force Microscopy

APTS = aminopropyltrimethoxysilane

AR = aspect ratio

ATO = antimony tin oxide

BSE = Back Scattered Electrons

CTAB = hexadecyltrimethylammonium bromide

DDA = Discrete Dipole Approximation

DDSCAT = Discrete Dipole Approximation for Scattering and Absorption of Light by Irregular Particles

DPN = Dip Pen Nanolithography

e-beam = electron beam

EBL = Electron Beam Lithography

EBPVD = Electron Beam Physical Vapour Deposition

ENFOL = Evanescent Near Field Optical Lithography

EUV-IL = Extreme Ultraviolet – Interference Lithography

FIB = Focused Ion Beam

FSS = Frequency Selective Surface

FTO = fluorine tin oxide

HD = high density

HV = high vacuum

IBL = Ion Beam Lithography

IgG = anti-mouse immunoglobulin G

IPA = isopropyl alcohol

IPL = Ion Projection Lithography

ISO = International Organisation for Standardisation

ITO = indium tin oxide

p-beam = proton beam

PDMS = poly(dimethylsiloxane)

PLL = Planar Lens Lithography

PMMA = poly(methyl methacrylate)

PSS = poly(sodium styrenesulfate)

LBL = Layer by layer

LD = low density

MHA = mercaptohexadeconoic acid

MIBK = methyl isobutyl ketone

MicroSpec = SEE 2100 Microspectrophotometer

MPA = 3-mercaptoproponic acid

MPTS = 3-mercaptopropyltrimethoxysilane

MUA = 11-mercaptoundecanoic acid

NIL = Nanoimprint Lithography

NIR = near infrared

Nu_L = Nusselt Number

PE = Perkin Elmer Lambda 950 UV/Vis/NIR spectrophotometer

Pr = Prandtl Number

PVA = poly vinyl alcohol

PVD = Physical Vapour Deposition

Re_L = Reynolds Number

RIE = Reactive Ion Etching

SAM = self-assembled monolayer

SC = Shading Coefficient

SE = Secondary Electrons

SEIRAS = Surface Enhanced Infrared Reflection Absorption Spectroscopy

SEM = Scanning Electron Microscopy

SERS = Surface Enhanced Raman Scattering

SFIL = Step and Flash Imprint Lithography

SHGC, F_{sol} = Solar Heat Gain Coefficient

SLG = soda lime glass

SPL = Scanned Probe Lithography

STM = Scanning Tunnelling Microscopy

T_{sol} = solar transmittance

T_{vis}, T_{lum} = visible transmittance

TCAB = tetradodecylammonium bromide

TCO = transparent conducting oxide

TMS = bis(ω-trimethylsiloxyundecyl)disulfide

T-NIL = Thermoplastic Nanoimprint Lithography

VP = Variable Pressure

VPSED = Variable Pressure Secondary Electron Detector

ZPAL = Zone Plate Array Lithography

Publications arising from this work

Journal Articles

N. Stokes, A. McDonagh, M. Cortie, 2007, 'Preparation of gold nanostructures by nanolithography', *Gold Bulletin*, **40**, 310.

M. Cortie, N. Stokes, A. McDonagh, 2009, 'Plasmon resonance and electric field amplification of crossed gold nanorods' *Photonics and Nanostructures – Fundamentals and Applications*, **7**, 143.

N. Stokes, J. Edgar, A. McDonagh, M. Cortie, 'Spectrally-selective coatings of gold nanorods on architectural glass' accepted 23rd January 2010, *Journal of Nanoparticle Research,* in press.

Conference Presentations

N. Stokes, A. McDonagh, M. Cortie 'Using electron beam lithography to construct new materials' Australian Research Network for Advanced Materials (ARNAM 07), Kioloa, 8th to 11th July 2007.

N. Stokes, R. Wuhrer, A. McDonagh, M. Cortie 'Electron beam lithography with polymethylmethacrylate films on indium tin oxide coated glass' Australian Conference on Microscopy and Microanalysis (ACMM-20), Perth, 10th to 15th February 2008.

N. Stokes, R. Wuhrer, A. McDonagh, M. Cortie 'Electron beam lithography and the construction of new materials' Australian Institute of Physics (AIP08), Adelaide, 30th November to 5th December 2008.

N. Stokes, A. McDonagh, M. Cortie 'Optical properties of crossed gold nanorods' Nanophotonics Down Under 2009 Devices and Applications (SMONP2009), Melbourne, 21st to 24th June 2009.

N. Stokes, J. Edgar, A. McDonagh, M. Cortie 'Novel nanoparticle-based gold coatings for solar glazing' International Conference of Nanoscience and Nanotechnology (ICONN2010) Sydney, 22nd to 26th February 2010.

Abstract

Energy-efficient window coatings limit the transfer of energy from one side of a window to the other. Their use has the potential to significantly reduce the electrical energy consumed by air conditioning, heating and lighting the interior space of a building. In particular, the use of spectrally selective coatings allows for more control over both the internal climate, the colour of the transmitted light, and the overall energy efficiency of the window coating. Gold nanoparticles, especially the optically anisotropic gold nanorods, offer a uniquely stable and long lasting solution to obtaining tuneable absorption of electromagnetic radiation for a wide range of potential applications. In this thesis the potential of gold nanorods as a spectrally selective coating for window glass is examined, the possible means of securing the nanorods to the glass are explored and their effectiveness as an optical coating compared to current commercially available coatings of similar design. The optical properties of these nanorods and some other shapes with potentially interesting properties are computationally modelled and are compared to the properties of samples fabricated using electron beam lithography and to samples made by wet chemistry. The work shows that gold nanostructures could serve as the basis for a new generation of spectrally-selective coatings for architectural glass.

Chapter 1 of this thesis reviews the fabrication, optical properties and potential applications of gold nanostructures. The fabrication methods reviewed include reported lithographic procedures as well as wet chemical techniques for the formation of gold nanostructures. The optical properties of the gold nanostructures are examined, and the phenomenon of surface plasmon resonance is analysed. Some potential applications for the optical properties of gold nanostructures are explored, and an appraisal is made of window glazing technologies including their operating mechanism. Also, the advantages of the various technologies are reviewed.

In Chapter 2, computational modelling of the optical properties of gold nanoparticles of rod, X and V shapes is carried out. The study shows the surface plasmon resonances of the gold nanoparticles are influenced by the dimensions, spacings and angles of the structures. The polarisation of the incoming light also affects the optical extinction

properties of the investigated nanoparticles. When the structures are aligned in a 1D array, the main surface plasmon resonance peaks are red-shifted compared to the isolated structure. An analysis of the electric field intensity as a function of distance from the structure is conducted to determine the potential use of these structures as an amplifier for two-photon fluorescence.

Chapter 3 explores the electron beam lithography fabrication process, including an examination of the effects of different substrates, chamber pressure, deposition parameters, dose characteristics and post-exposure processes. Due to the reduction in exposure time for conducting glass over insulating glass, further experimentation is conducted with a transparent conducting glass substrate. The formation of large arrays of high quality gold nanostructures is achieved through the comprehensive investigation of deposition conditions and in particular the addition of a short burst of plasma cleaning after the development step. Sufficient areas for rod and X arrays are fabricated to enable the measurement of the optical properties.

The optical properties of the electron beam lithographically fabricated structures are addressed in Chapter 4. A comparison is undertaken between the measured optical properties from structures produced in Chapter 3 to the modelled structures investigated in Chapter 2. Surface plasmon resonance peaks are found on each gold nanostructured sample investigated. However, the optical properties of a single layer of gold nanostructures are insufficient to produce an effective window coating.

Chapter 5 investigates the attachment of gold nanorods onto glass through an application of a molecular binding layer and immersion of the nanorods into a polymer. The use of 3-mercaptopropyltrimethoxysilane to bind gold to glass is found to increase the amount of gold nanorods attaching to glass compared to samples without the binding molecule. However, the immersion of gold nanorods into a polymer layer is found to have the most potential for use as a window coating, as careful control over the gold nanorod concentration could be used to adjust the required optical properties. Mixtures of different aspect ratio gold nanorods combine the different longitudinal plasmon resonances to absorb light over a larger spectral range. Control over the aspect ratio of the nanorods included in the film, ensured control over optical properties. The

optical transmission properties of the large area films of gold nanorod mixtures provided superior window transmission properties in the spectral range 700 – 900 nm compared to a currently commercially available solar laminate window coating.

In Chapter 6 the effect of an electric field on gold nanorods in solution is investigated. Prior reports suggested that the gold nanorods could be aligned under the influence of an AC electric field. No alignment was observed here for wet-chemically produced gold nanorods, with a CTAB stabiliser, when under the influence of an AC or DC electric field. A DC electric field of sufficient strength is found to strip the gold nanorods of the CTAB stabilising agent, which results in gold depositing on the positive electrode.

The final chapter of this thesis, Chapter 7, summarises the work presented and highlights the significant conclusions. It also outlines some directions for possible further research built on and extending from the work presented here.

Chapter 1:

Gold Nanostructures: Fabrication, Optical Properties and Applications

Chapter 1: Gold Nanostructures: Fabrication, Optical Properties and Applications*

1.1. Introduction

Nanotechnology is a relatively new field of applied science and technology that investigates nanoscale matter (with at least one dimension between 1 and 100 nm). Nanomaterials research is currently attracting intense scrutiny where novel and interesting properties of nanoscale structures are investigated. Nanomaterials have significantly different properties compared to macroscale materials due to their drastically increased ratio of surface atoms to internal atoms. There are several physical effects that become more noticeable as the system size decreases including catalytic, electronic, optical and magnetic properties as well as reactivity. For example, metals such as gold, silver, platinum and copper are optically transparent as nanofilms, but are opaque as thicker films.[1,2] Aluminium is combustible in nanoparticulate form yet it is a very stable material in bulk form.[3,4]

Most metal surfaces can oxidise under ambient conditions, and the thickness of the oxide layer may be sufficient to partly or completely negate the functionality of any nanoscale structures constructed on the surface. This is one of the main reasons that gold, which does not form an oxide under ambient conditions,[5] is a very useful material. Gold is readily and conveniently deposited by techniques such as electroplating, electroless deposition and thermal evaporation. Gold also has useful optical characteristics[6,7] that commend its use in many applications operating in the visible and infrared region of the spectrum. Layers of organic molecules may also be assembled on gold surfaces. It is for these various reasons that gold is so attractive for use in diverse nanotechnological investigations.[5]

In recent years, problems associated with climate change have demonstrated the importance of modern materials to reduce the emission of greenhouse gases. A major

* Sections of this chapter have been published. (N. Stokes, A. McDonagh, M. Cortie, 2007, 'Preparation of gold nanostructures by nanolithography', *Gold Bulletin*, **40**, 310.)

producer of greenhouse gases is the power industry. Air-conditioning, heating and lighting are generally required in all large buildings and use significant quantities of electricity. Windows account for a significant portion of light and heat that impact a building. Using energy efficient window coatings allows for the reduction or increase of the internal or external heat transmittance and the visible transmittance. The Kyoto Greenhouse Protocol, which entered into force in Feburary 2005 and included legislation on energy-saving glass to reduce air conditioning or heating costs depending on the climate. The glass industry sold nearly 5 billion m^2 of glass worldwide in 2005 and the market is growing at 4% per annum.[8] A significant portion of this glass is used in windows, resulting in a huge market for window coatings.

Coatings can provide heat protective functions using either reflective or absorptive processes. These two different types of coatings work by blocking certain unwanted wavelengths, but allowing desired wavelengths to pass into or out of the building, a process called spectral selectivity. There are numerous advantages to having spectrally selective window coatings including increasing the visible light transmittance and, in warm climates for example, minimum heat transmittance reduces the need for extra internal illumination and cooling. Coatings can be made to block more unwanted light than clear glass, for example blocking infra-red light to reduce air conditioning or heating costs.

The goal of this project is to investigate gold nanostructures and their optical properties, in spectrally selective window coatings. Experiments were undertaken to investigate optical properties of gold nanostructures using computational modelling and lithography. The computational modelling focused on individual shapes and their optical spectra. This work is presented in the chapter on Computational Modelling of the Optical Properties of Gold Nanostructures. The lithography component, Preparation of Gold Nanostructures on Glass uses an electron beam lithography system to make the modelled structures over a large area and includes measured optical spectra. Experiments to investigate attachment methods of nanorods to glass and the solar properties of the new windows are presented in Chapter 5. Another area of work investigated the influence of an electric field across wet-chemically produced gold nanorods. This is discussed in Chapter 6. Conclusions drawn from this body of work are discussed in Chapter 7.

1.2. Window Technologies

The amount of energy used by humans has increased enormously over the last few decades.[9] One of the highest uses of energy is in building air conditioning. Windows have come under intense scrutiny as the area where the greatest transfer of energy enters or exits a building. It is due to this that much research has been undertaken to limit the transfer of energy via different types of coatings. A single pane of clear float glass is now rarely used in commercial buildings, a large change from 30 years ago, due to the need to reduce building energy consumption without sacrificing the natural lighting benefits of windows.[10] The foremost benefits of a good glazing selection is a reduction in energy demands by buildings, involving heating, cooling and lighting energy.[11] Reductions of up to 50% in energy required for heating and cooling in residential houses, and up to 30% in commercial buildings are possible.[11] Assuming 20% of potential residential house energy reductions are realised, it leads to CO_2 emission reductions of 6.5 million tonnes per annum in Australia.[11] In the US windows are responsible for over 4 quads (4.055×10^{18}J) of annual energy use and cost building owners approximately $40B per year.[12]

The Earth receives approximately 1370 Wm^{-2} of energy irradiated from the sun.[13] The presence of ozone in the atmosphere protects the earth from harmful UV radiation by absorbing light with wavelength shorter than 290 nm.[13] Solar radiation reaching the earth's surface varies according to location, atmospheric conditions, aerosol content, ozone layer condition, time of day, earth-sun distance, solar rotation and activity. Because the solar spectra depend on so many variables, standard spectra have been developed to provide a basis for theoretical evaluation of the effects of solar radiation and as a basis for simulations. The standard solar spectrum, ASTM G173-03, is shown in Figure 1.1. The maximum energy is situated at a wavelength that corresponds to the green portion of the visible spectrum. Although the peak is situated in the visible region, the most energy, ~52%, impacts in the near infra red (NIR) region.

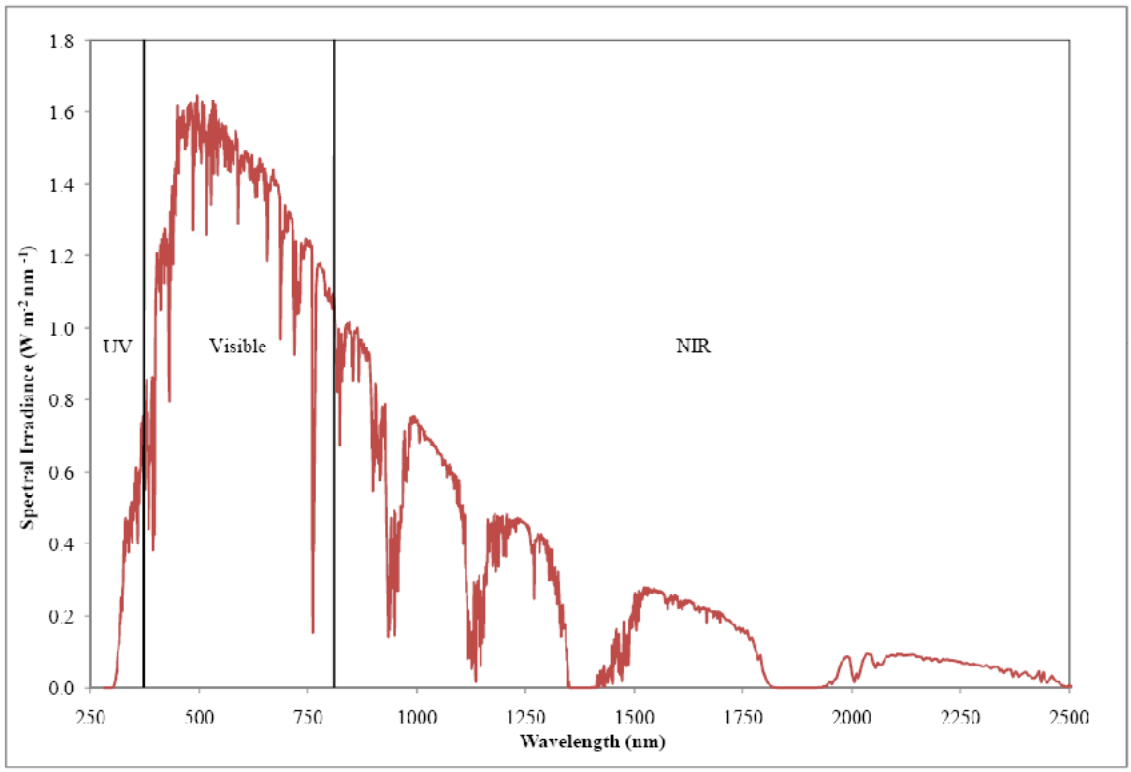

Figure 1.1: Standard solar spectra at sea level. Data from American Society for Materials and Testing (ASTM G173-03).

The solar spectrum differs according to altitude and season. For example, Australia generally has very hot summers, and therefore more energy goes into cooling buildings in summer than heating buildings in winter. As such, window glazing designs are focused on preventing external heat being transferred into buildings. Alternatively, in Europe where average annual temperature is lower, window glazings are designed to keep heat inside the building, reducing heating costs. Glazing selection also depends on window orientation. East and west facing windows require more efficient glazing systems as there is generally a greater heat load imparted on these windows.

Figure 1.2 illustrates energy dispersion of solar radiation incident upon a single pane of G. James Australia's 3 mm clear glass. Transmitted light accounts for approximately 83% of the incident light. About 9% of the energy is absorbed by the window, which is then emitted into and out of the building, with more energy emitted from the front window face.[14] Reflection accounts for about 8% across the whole solar spectrum for uncoated glass.[14,15] Different glazing types allow a coating to either reflect or absorb significant portions or selective portions of the solar spectrum.

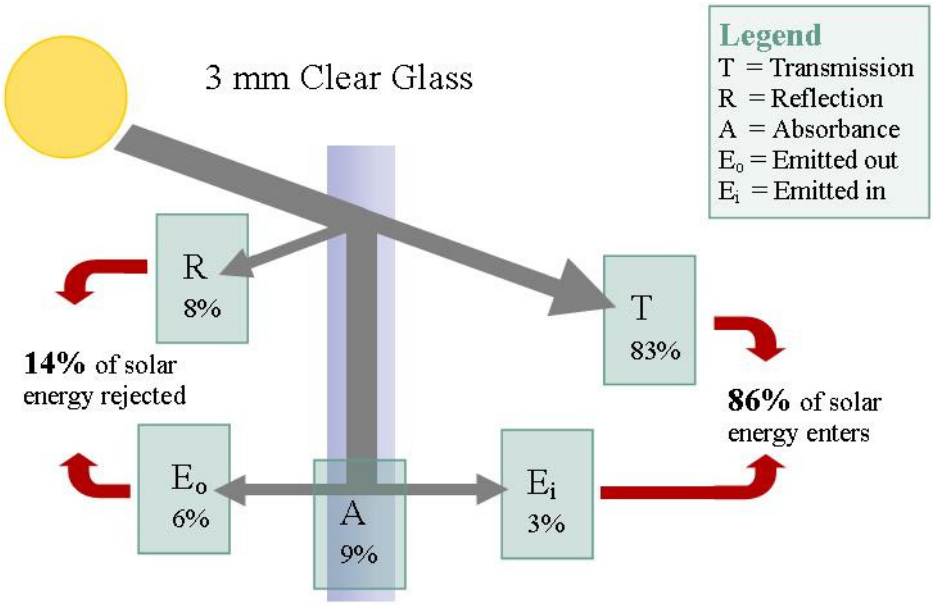

Figure 1.2: Energy distribution through a 3 mm clear glass window. Absorbance is split into emitted in and out.[14]

Energy efficient glazing systems work mainly by either reflection or absorption of incident light. Reflective coatings are one of the most efficient types of energy saving coatings, however good quality coatings usually require thin film vacuum deposition techniques which are expensive. Some countries or cities have proposed legislation that limits the amount of glare allowed to be reflected onto neighbours.[16] Absorption-based coatings are inherently less efficient than reflective coatings as a portion of the absorbed energy is conducted through to the other side of the glass. However, absorption based coatings are much cheaper to produce.

There are many types of glazings that use either method or combinations of these including absorptive glazings, reflective glazings, spectrally selective glazings, angular selective glazings and switchable glazings.

Reflective glazings are designed to reflect the majority of radiation back to its original environment (either interior or exterior). Reflective glazings are naturally more efficient than absorptive coatings because reflecting regions of light removes that energy from the window system. On the other hand, absorptive coatings absorb energy which is dispersed to both the exterior and interior environments, keeping the energy within the window system. Unselective reflective glazings can reflect light in the visible region, and therefore visible transmittance of reflective glazings is often low. The reduced cooling loads due to reflective glazings are partially offset by an increased

lighting load, and the subsequent cooling load required by the increased lighting. Reflective glazings are typically produced using vacuum deposition systems and consist of metal or metal oxide layers on glass and are usually placed on the external window face.

Absorptive coatings are based on a design where energy is absorbed rather than reflected. It is inherently less efficient than reflective based coatings as a significant portion of the absorbed energy is convected and radiated from the inside surface of the window. An example of a G. James Australia absorptive coating and its effect on the increase of absorption as well as the corresponding increase in the emitted energy can be seen in Figure 1.3. Absorptive coatings are often much cheaper to produce and can be retro-fitted to existing windows. Absorptive coated glass is sometimes called 'tinted glass' and is very popular in the automotive industry.

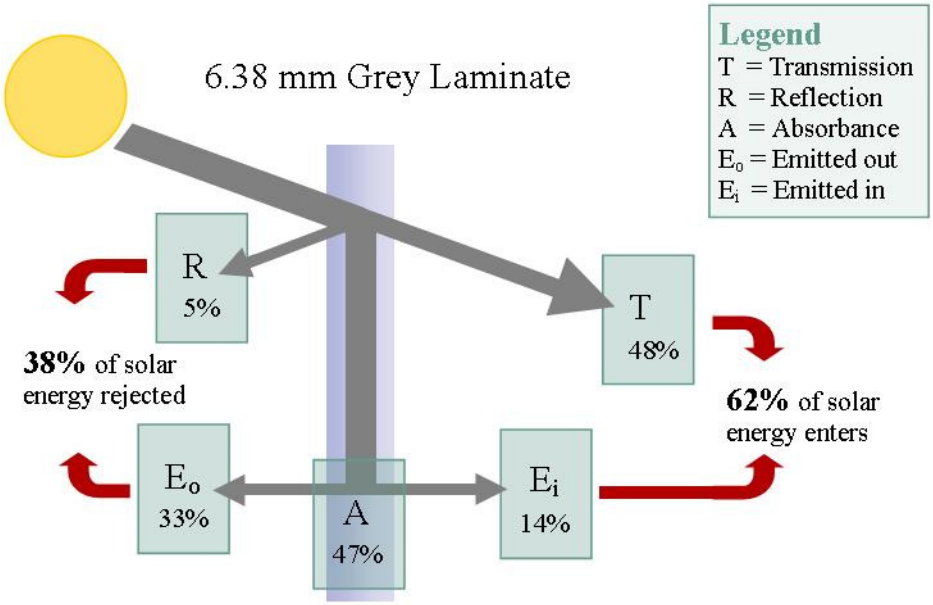

Figure 1.3: Energy distribution of a G. James Australia commercial absorptive window coating.[14]

1.2.1 Spectrally selective coatings

Spectrally selective coatings are specifically designed to be highly transmissive in the visible spectrum whilst blocking infrared radiation. This can result in an excellent shading coefficient and good visible light transmittance.[17] High infrared reflectance can be achieved with a material with high electrical conductivity. Typical spectrally selective coatings consist of more than one layer. Silver coatings consistently have an

antireflection coating attached, which reduces the amount of reflection of visible light, thus increasing its transmission.

The coinage metals (copper, silver and gold) are all potential spectrally selective coating materials. Silver is primarily used in commercial applications, as both copper and gold have absorption bands in the visible region that give rise to a yellow/gold colour.[10] Other metals including iron, chromium and nickel have strong interband transitions that reduce or eliminate the transparency of the material making it unsuitable for window coatings.

The principal mechanism of heat transfer across multilayer glazing is thermal radiation from warm surfaces to cooler surfaces. Glass coated with a low-e (low-emittance) material reflects a significant amount of the radiant heat, lowering the total heat flow through the window. Low-e coatings can be designed to be spectrally selective so that they have low emittance over a selected portion of the spectrum. For example, originally low-e coatings were added to windows in cold climates to reduce the energy flow to outside by reflecting the longer wavelength heat back inside.[18] A high solar gain, low-e coating can cut the loss of heat during the winter and a low solar gain, low-e coating cuts the solar radiant heat during the summer by reflecting this heat back to its source.[19] Solar gain specifically refers to the increase in temperature of a structure or object stemming from solar radiation. Low-e coatings consist of a metal or metal oxide thin film, like FTO ($F:SnO_2$), that are good reflectors in the infrared and transparent to the visible. Generally, higher electrical conductance of the coatings results in a lower emissivity for the product.[20] Low-e coatings have become very popular over recent years. Nearly all glass manufacturers produce their own version of a low-e coating.

1.2.2. Angular reflective coatings

Another type of glazing that has good potential for reducing heat transfer into the interior environment is angular reflective glazing. This is useful in situations where the light at low angles (early morning and late afternoon and more in winter than summer) passes through the window but light at higher incident angles is reflected. This type of design allows people on the inside to see out horizontally and below the horizontal, as shown in Figure 1.4.

The columns attached to the window can be seen in Figure 1.4 and are the result of the microstructure of the films, which is controlled by the conditions used during deposition and are typically made from chromium. Maximum transmittance occurs when incident light is parallel to the columns, allowing clear viewing below the horizontal. Typical overall transmittance is ~68% for a 90 nm thick coating. One complication with this coating is that the incident polarisation is important since only the p-polarised component is affected by the coating.[10]

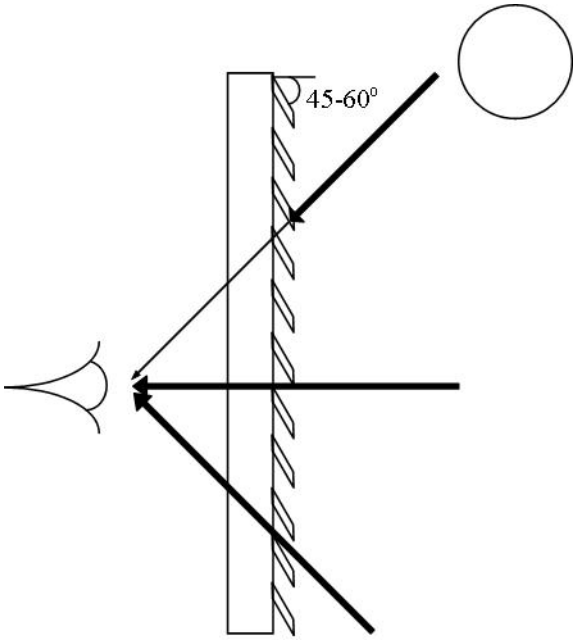

Figure 1.4: Schematic of angular selective films showing the venetian blind-like microcolumns, typically 45-60° from perpendicular and significantly reducing the light from higher angles. Reproduced from reference.[10]

1.2.4. Switchable glazing

The function of a switchable glazing system (the so-called 'smart window') is to control the flow of light and heat into and out of a window. Switchable glazing systems are able to regulate lighting and heating levels for energy management and can save up to 30% on energy over conventional glazing systems. There are many different types of switchable window glazings, based on various physical processes to control and modify light. The types of switchable glazings include electrochromic, dispersed particle, liquid crystal glazing, thermotropic, thermochromic and photochromic. The systems with the greatest solar glazing potential will be discussed in this section. As liquid crystal

glazing currently only allows visual transmission when a voltage is applied, it makes no power savings as the power must stay on when transmittance is wanted. It is therefore only suitable for internal glass walls mainly for privacy reasons and will not be covered within this section. The two challenges facing wide spread use of smart window coatings are (a) the cost of the systems (100 – 1000 US$/$m^2$ for electrochromic windows[21]) and (b) the construction of larger areas of high optical quality.

The essential properties of an electrically activated chromogenic material is that it exhibits a large change in its optical properties upon either a change in applied electric field or an injected or ejected charge. This change in optical properties is exhibited in the form of absorbance, reflectance or scattering.[21] The change depends on the type of material and can form a highly transmissive state or partly reflecting or absorbing state, the change can also occur over part or all of the solar spectrum.[21]

1.2.4.1. Electrochromic glazing

An electrochromic material is a material that changes its optical properties, usually through the development of an absorption band or through an increase in the effective free electron density in the material, also called 'absorptance modulation' and 'reflectance modulation' respectively.[10] The most common electrochromic material currently in use is tungsten oxide (WO_3), and it is particularly noteworthy that WO_3 can be both absorption modulating with amorphous WO_3 films, and reflectance modulating with crystalline WO_3.[10]

Electrochromic windows are the most popular switchable glazings. Electrochromic materials change their transmittance when ions and/or electrons are injected into the material. This method requires an application of power only when changing the optical properties or the tint of the window, and does not require power to keep a particular tint. Using this system allows for precise control over the level of tinting. Electrochromic windows require several layers, which are shown in Figure 1.5. The TCO (transparent conducting oxide), typically either ITO or FTO, produces the required electric field when a potential difference is applied between the two transparent conductors. An electrochromic device requires an ion-containing material (the electrolyte) in close proximity to the electrochromic layer allowing the device to shuttle ions into and out of the electrochromic layer with an applied potential.[10,21] There are several advantages of electrochromic materials over other switchable devices, including: power required only

during switching, only moderate voltages are required to switch (1-5 V), they are specular under all conditions, they have continuous dimming and several designs have long term memory (12-48 h).[21] Some disadvantages with electrochromics are that presently they are very expensive, they respond slowly, have a limited cycle lifetime and larger panels can exhibit an 'iris' effect where the tint changes from the edges inwards.[21-23]

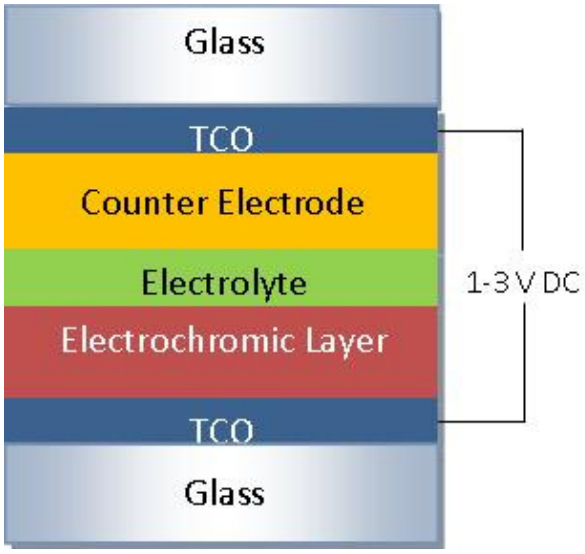

Figure 1.5: Schematic of an electrochromic glazing, where TCO is a transparent conducting oxide. Reproduced from ref.[21]

1.2.4.2. Dispersed particles

Dispersed particles have been used in windows where long thin particles are suspended in an organic fluid or gel. The position and orientation of these particles are initially random and can absorb signifant quantites of light. Under the influence of an electric field, the particles align along the field lines increasing the light transmission. This change in transmission between electrically aligned (ON) and randomly orientated (OFF) is illustrated in Figure 1.6.

Dispersed particle glazing generally consists of 5 layers, the first and last layers are generally a transparent conductor like ITO or FTO-coated glass followed by a dielectric as the second and fourth layers to prevent current flow, and the middle layer is the dispersed particles in a gel or fluid. This format was investigated in the current work, see chapter on Electric Field Interactions with Gold Nanorods

Some problems associated with suspended particle glazing include long term stability, cyclic durability, particle settling and agglomeration, and gap spacing control.[21] However, this has not prevented several companies producing commercial products in architectural glass, automotive mirrors and flat panel displays.[21]

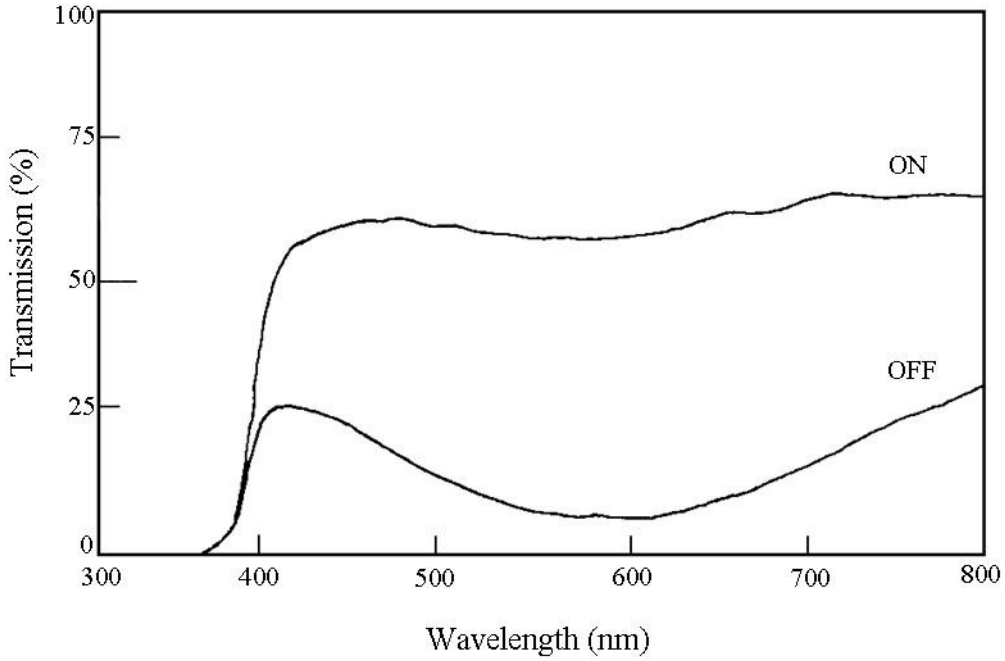

Figure 1.6: Spectral transmittance of a dispersed particle glazing.[21]

1.2.4.3. Thermotropic and thermochromic glazing

Thermotropic and thermochromic glazing, as their names suggest, change phase or colour and therefore the optical properties when there is a change in temperature. For a successful thermotropic glazing the temperature transitions should change from high transmission (>85%), to low transmission (<15%). The temperature at which this phase change occurs must depend upon the local climate and window orientation, typically the temperature transitions should occur between 30 and 80°C for a warmer climate.[24] Predominantly, the change in transmission is caused by a change in scattering, and the total scattering is primarily back scattering, causing the materials to have a high solar reflectance.[10] A significant advantage of thermotropic and thermochromic glazings is that transmission is regulated passively by temperature, so no external field or wiring is required. This also leads to a disadvantage where occasionally an occupant may desire visibility over solar control, which is not possible to achieve with this window system.

Figure 1.7 shows a commercial thermochromic material "Cloud-Gel", which consists of a thermochromic layer sandwiched between two plastic films. The thermochromic layer consists of hydrocarbon copolymers dissolved in water, where at temperatures below a switching point the polymers are elongated and above a switching point the polymer coagulates, forming structures larger than the wavelength of light, causing a massive increase in the amount of scattering. Altering the component concentrations allows for the switching point to be controlled between 10 and 70°C.[25]

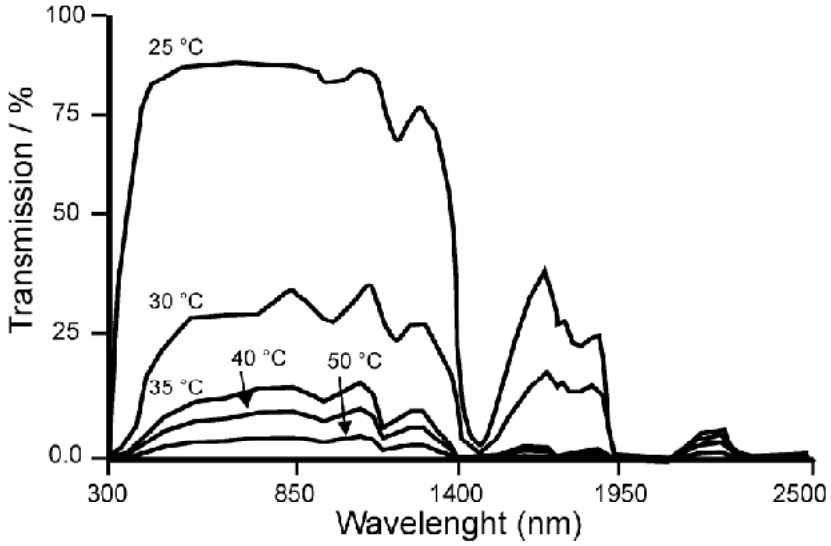

Figure 1.7: Spectral transmittance of a commercial thermochromic window glazing at different temperatures.[24,25]

1.2.5. Glazing efficiencies comparison methods

There are many different methods of comparing windows and their solar shielding properties, unfortunately there is not a single calculation that can convey the total effectiveness of a glazing. As such, comparisons are usually made between the solar heat gain coefficient (SHGC), the shading coefficient, the U value and the visible transmittance. Indeed, commercial glazings are typically measured according to standards ASTM 903-96 (measuring spectral absorptance, reflectance, and transmittance) and ASTM E1585-93 (measuring emittance of architectural flat glass), although these standards have recently been withdrawn and have yet to be replaced.[26] The International Organisation for Standardisation (ISO) also has a standard for a method and reference data for the thermal transmittance of window coatings (ISO

10077 and ISO 15099).[27] Within this section a thorough description of each method is given, followed by current commercial glazing values shown in Section 1.2.6. Current window glazing properties.

A typical Australian window energy saving label can be found in Figure 1.8, the most important optical factors are the U value, the SHGC and the visible transmittance. The fading transmittance and the air infiltration can also be found on some types of window energy rating labels, but as they are not optical performance characteristics they will not discussed further.

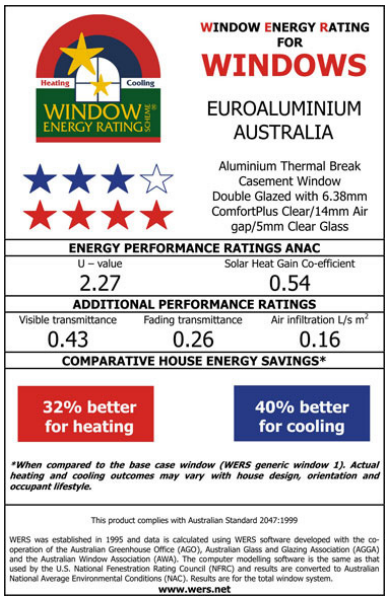

Figure 1.8: An image of a typical Australian window energy saving label.

1.2.5.1. Solar heat gain coefficient (SHGC)

The solar heat gain refers to the increase in temperature of an object from solar radiation. The amount of solar gain increases with sun intensity or the ability of a material to transmit or absorb radiation. The solar heat gain coefficient is the amount of solar heat gain through a window divided by the solar radiation incident on a window. The solar heat gain consists of both the transmitted solar radiation and the portion of absorbed radiation that flows to the interior.[28] The values of SHGC range between 0 and 1, with 1 being an opening with no solar blockage and 0 is an area where no radiation can pass.

1.2.5.2. Shading coefficient

The shading coefficient is a reasonably old term which is still in use although SHGC is used much more frequently. The transmission of solar radiation through an object or area can also be characterised by comparing it to a well known reference glazing material. In this case 3mm clear glass is used, whose SHGC is 0.87. The shading coefficient (SC) is therefore defined as the solar heat gain of product over the solar heat gain of reference material. This is simplified in Equation (1-1). Therefore for a 3mm clear glass window the SC is unity.[28]

$$SC = \frac{SHGC}{SHGC_{ref}} = \frac{SHGC}{0.87} \qquad \textbf{(1-1)}$$

1.2.5.3. U factor

When there is a temperature difference between inside and outside, heat is lost or gained through the window frame and glazing by the combined effects of conduction, convection, and radiation. The U factor of a window assembly represents its insulating value. The U factor is also known as the thermal transmittance or the overall heat transfer coefficient and is the rate of heat transfer through one square metre of a structure divided by the difference in temperature across a structure. The reciprocal of the U factor is the R value and is a measure of the thermal resistance of a structure. The U factor is a measure of the rate of non-solar heat loss or gain through a window assembly. The lower the U factor, the greater a window's resistance to heat flow and the better its insulation.[18,28]

1.2.5.4. Visible transmittance

The visible transmittance is a measure of the amount of visible light transmitted. As the SHGC and the U factor cannot directly show the visible transmittance, window energy rating labels include the visible transmittance. Whilst the visible transmission theoretically has a range between 0 and 1, most values are between 0.3 and 0.8. A high visible transmission is desirable to maximize daylight and user comfort, and reduce internal lighting requirements. For a moderately well shaded window, the visible transmittance value should not be below 0.45 to 0.55, however for a window in direct sunlight lower transmission values can be sought.[18]

1.2.6. Current window glazing properties

Window manufacturers may have many different types and combinations of window glazings available. This section provides a comparison of some of the current commercial glazing properties for different solar glazings. Because window orientation and climate heavily influence the glazing choice, window coatings require different efficiencies, spectral selectivity, and glazing types and there is a wide range of glazing systems that are commercially available. However, using the properties described in Section 1.2.5. Glazing efficiencies comparison methods, it is possible to compare some of the more important characteristics of window coatings. Table 1-1 identifies the visible transmittance, the solar heat gain, the U factor and the shading coefficient of the available clear glass and solar coatings from two large glass manufacturers, Pilkington and G. James Australia.

The application of a tint to a window changes the glazing efficiency, particularly the T_{vis}. For comparison purposes Table 1-1 consists of a clear tint, allowing maximum T_{vis} and a grey tint with the minimum T_{vis} available for a specific glazing type. Laminate coating systems are often greater than 5 mm thick. It is interesting to note that G. James Australia's solar glazing products Solect, Optilight and Solarplus low-e all have a much lower U value than both the clear glass, and Pilkington's solar glazing range. This indicates that G. James emphasises the insulating abilities of solar glazing products. Both manufacturers have a minimum T_{vis} for the reported glazing products in the mid 20's, and also have strong warnings that it is only suitable for specific applications. The SHGC is also typically lower for G. James solar products than Pilkington's. However, the difference between the SHGC values is much smaller than the U values.

Window glazing allowing for a reduced solar heat gain are suitable for warm climates, especially when including a low-e coating to reduce heat loss during the cooler seasons. These types of window coatings are manufactured by G. James Australia, primarily due to the hot summer and the mild winter temperatures in Australia. Pilkington, alternatively, manufactures window coatings using a different method which allows as much heat as possible to enter a building and as little heat as possible to leave. This is where the much higher U values come into account; Pilkington has designed solar coatings (Pilkington Energy Advantage Low-E) to have high thermal transmittance, so that during winter especially solar energy is transferred into the house, and a low-e coating reduces the transfer of heat outside the house. Pilkington's warmer

climate window designs (Solar-E and Eclipse Advantage) are designed to have a smaller solar heat gain, whilst still having a large U value to remove unwanted heat to the external environment.

There is a large range of commercial thermal glazing systems available. The conditions at which solar glazing systems becomes viable are not straightforward due to the effects of different climates, shading and orientations on a window system. However, it is clear that T_{vis} must always be at a reasonable number (greater than 40%) for significant quantities of systems to be sold. The other factors depend on the design of the window system, and if these conditions can be matched, then a commercially viable glazing system can be made.

Table 1-1: Single layer clear and solar glazing parameters from Pilkington and G. James Australia.

Product Name	Manufacturer	Thickness (mm)	U Value ($Wm^{-2}K^{-1}$)	Shading Coefficient	SHGC	T_{vis} (%)	Description
Optifloat Clear[1]	Pilkington	2.997	5.332	0.992	0.861	0.899	Clear Glass
Optifloat Grey Tint[1]	Pilkington	3.2	5.326	0.797	0.689	0.608	Grey Tinted Glass
Energy Advantage Low-E[1]	Pilkington	3.023	4.954	0.87	0.754	0.824	Low-E Clear Glass
SuperGrey[1]	Pilkington	3.2	5.326	0.524	0.448	0.25	High Performance Grey Tint
ArticBlue[1]	Pilkington	3.937	5.304	0.696	0.599	0.65	High Performance Blue Tint
Eclipse Advantage Clear[1]	Pilkington	5.918	4.913	0.744	0.644	0.665	High T_{vis}, Reflective Coating, with glare control
Eclipse Advantage ArticBlue[1]	Pilkington	5.918	4.913	0.497	0.426	0.387	Absorbing & Reflective Coating, with glare control
Solar-E 3mm[1]	Pilkington	3.2	4.956	0.703	0.606	0.601	Absorbs & Rejects most NIR; due to low-e coating, Reflects IR
Solar-E 4mm[1]	Pilkington	3.912	4.938	0.697	0.601	0.599	As above
Solar-E 6mm[1]	Pilkington	5.918	4.886	0.689	0.594	0.599	As above
Clear[2]	G.James Australia	3	5.9	1	0.87	0.9	Clear Glass
Grey Tint[2]	G.James Australia	4	5.9	0.76	0.65	0.54	Grey Tint
Laminated Grey[2]	G.James Australia	6.38	5.8	0.72	0.62	0.44	Laminated Grey
Solect Clear[1]	G.James Australia	6.363	2.786	0.784	0.677	0.812	High performance, Low E laminated glass designed for residential
Solect Grey[1]	G.James Australia	6.437	2.785	0.507	0.434	0.473	As above with grey tint
Optilight Clear[2]	G.James Australia	6.38	3.6	0.78	0.68	0.81	High performance, Low E laminated glass
Optilight Grey[1]	G.James Australia	6.356	2.786	0.572	0.491	0.392	As above with grey tint
SolarPlus Low E Clear LE80i[1]	G.James Australia	5.973	2.563	0.676	0.584	0.812	Optimum thermal insulation product from manufacturer
SolarPlus Low E Clear LE54i[1]	G.James Australia	5.969	2.558	0.493	0.423	0.537	As above with different strength
SolarPlus Low E Grey LE80i[1]	G.James Australia	5.858	2.564	0.45	0.384	0.382	Grey Tint to LE80i clear SolarPlus product
SolarPlus Low E Grey LE54i[1]	G.James Australia	5.828	2.56	0.363	0.308	0.258	Grey Tint to LE54i clear SolarPlus product

[1] Data from Windows 5.2a LBNL windows glazing program — All Environmental Data From National Fenestration Rating Council 100-2001 Summer

[2] Data from G.James Australia Performance Guide

1.3. Surface Plasmon Resonance

Designing optically selective window coatings using nanostructured materials requires investigation of the optical properties and an understanding of the underlying principles, in particular of surface plasmon resonance. This section of the thesis deals especially with the optical properties of gold nanostructures.

A plasma is a medium with equal concentrations of positive and negative charges, of which at least one charge type is mobile. In a solid, the negative charges of the conduction electrons are balanced by an equal concentration of positive charge of the ion cores. A plasmon is the collective oscillation of the conduction electrons of a metal nanoparticle.[29] This is illustrated in Figure 1.9 where the mobile conduction electrons are the plasma that oscillates under the influence of an electric field.

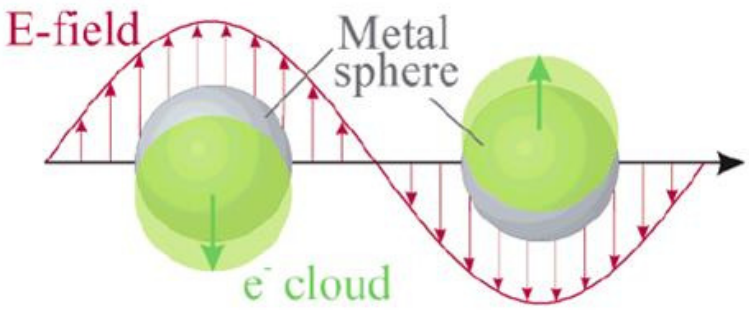

Figure 1.9: Plasmon oscillation for a sphere, with the mobile negatively charged conduction electron cloud, and the stationary positively charged nuclei.[30]

The term "surface" in surface plasmon resonance stems from the fact that, although all electrons are oscillating with respect to the positive-ion background, the main effect producing the restoring force is the surface polarization.[31] Surface plasmons are confined to surfaces and interact strongly with light, resulting in polaritons, which are surface electromagnetic waves that propagate in a direction parallel to the metal/dielectric interface.

Plasmons play a large role in the optical properties of metals. For metal nanospheres the plasma frequency is often situated in the UV part of the spectrum. Such metals include lead, indium, mercury, tin and cadmium but these also readily oxidise making stable nanoparticles much harder to produce and investigate.[32] Gold and to a lesser extent silver form air stable colloids and there uses are investigated more frequently.

Additionally, due to d-d band transitions, the plasma frequency is located in the visible part of the spectrum.[32]

1.3.1. Physics of surface plasmon resonance

The physical origin of light absorption by metallic nanoparticles is the coherent oscillation of the conduction electrons induced by the interacting electromagnetic field. When the conduction electrons oscillate coherently, they displace an electron cloud from the nuclei giving rise to a surface charge distribution. The coulomb attraction between positive and negative charges results in a restoring force, characterised by oscillation frequencies of the electron cloud with respect to the positive background, which are different from those of the incident electromagnetic wave.[30-34] Each collective oscillation with different surface charge distribution is known as surface plasmon resonance. This process is shown for a metal sphere in Figure 1.9 and a metal nanorod in Figure 1.10. The metal nanorod has two main oscillation modes corresponding to the two aspects of the rod, (a) length and (b) width. The number of modes and their frequency is determined by the electron density, effective mass, particle shape, size, dielectric function and its environment.[30,32,33] These factors are discussed in Section 1.3.2. Factors affecting surface plasmon resonance. Higher modes of plasmon excitation can occur, such as the quadrupole mode where half of the electron cloud moves parallel to the electric field and half moves antiparallel.[30,32]

When the dimensions of the conductor are reduced, boundary and surface effects become very important, and for this reason, the optical properties of many metal nanoparticles are dominated by the surface plasmon.[31,32]

Bound electrons do not participate in the collective motion of the electron cloud, thus, surface plasmon resonances are independent of the interband contributions to the dielectric function, except they can act as a positive background changing in some way the environment of the free electrons.[33]

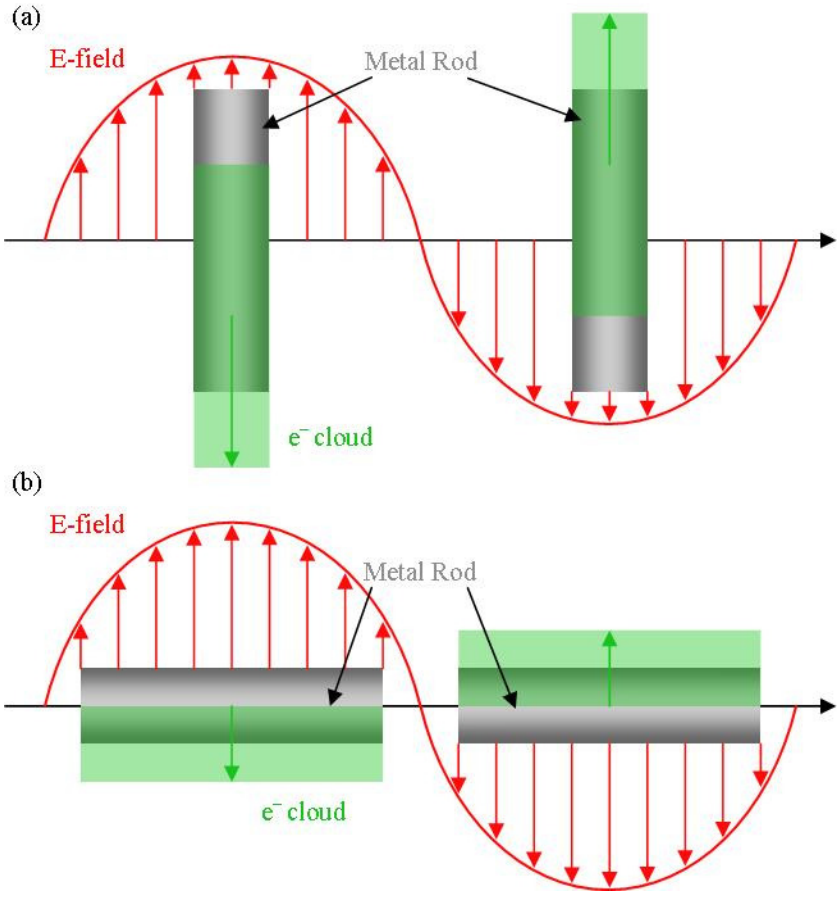

Figure 1.10: Schematic of the interaction of the electric field of the incoming light with the (a) long nanorod aspect causing longitudinal oscillations and (b) short nanorod aspect causing transverse plasmon oscillations. Reproduced from ref.[32]

Strong light absorption and scattering and significant local field enhancements occur at the resonant frequency of the surface plasmon as a consequence of the large optical polarisation associated with the collective electron oscillation.[31,34] These resonances are a small particle effect and are absent in individual atoms as well as bulk material. Thus, the conduction electrons in a nanoparticle act like an oscillator system, whereas in bulk material they act like a relaxator system.[31]

1.3.2. Factors affecting surface plasmon resonance

Factors that affect the surface plasmon resonance of metallic nanoparticles include the density of electrons, the effective electron mass, and the shape and size of the charge distribution.[30,33] This means that different variables can be changed to alter the surface

plasmon resonance of metallic nanoparticles. Some of the more significant effects are discussed below.

Although much interest has been focused on size effects, there are many other factors that affect the resonant frequency and their effect is significantly greater than those of size effects.[32] When the size of a particle increases, the radiation effect becomes increasingly important as the displacement of the electron cloud is no longer homogenous, even for spherical particles, and higher multipolar charge distributions are introduced.[33] The accelerated electrons produce an additional polarisation field that depends on the ratio between the size of the particle and the wavelength of the incident light. Due to this secondary radiation, the electrons experience a damping effect which increases the width of the resonance peak.[33] While the peak position of the surface plasmon absorption is dependent on size there is a much greater effect due to the composition of the nanoparticle.[35]

There is an even more drastic effect on the surface plasmon absorbance when the shape of the nanoparticle is changed rather than its size. This can be seen with gold nanorods, which because of their anisotropic structure, possess some significantly different optical properties compared to spherical particles.[36] Their resonance wavelength depends on the orientation of the incident electric field relative to the particle, which means that resonant oscillations occur along the rod (longitudinal) at lower energies and higher wavelengths and across the rod (transverse) at higher energies and lower wavelengths. Nanorods also have a much higher absorption coefficient at the longitudinal plasmon resonance.[32] When the nanorods are dispersed in a solution, random orientation of the rods occurs due to Brownian motion, which allows for absorption involving both transverse and longitudinal surface plasmon resonance.[32]

Aggregation of nanoparticles, particularly gold, leads to an additional plasmon peak at longer wavelengths due to nanoparticle coupling. Coupling occurs when the electric field, formed from oscillating electrons in one particle, leads to the oscillation of electrons in another particle and can lead to collective plasmon oscillation of the whole aggregate. The frequency and intensity of the collective plasmon oscillation is influenced by the degree of aggregation and the orientation of the particles within the aggregate.[35] Coupling between particles have a much stronger optical effect than coupling with the surrounding medium. This effect can be seen in Figure 1.11 (c) and (f), which shows effect of particles coupling with nearby particles.

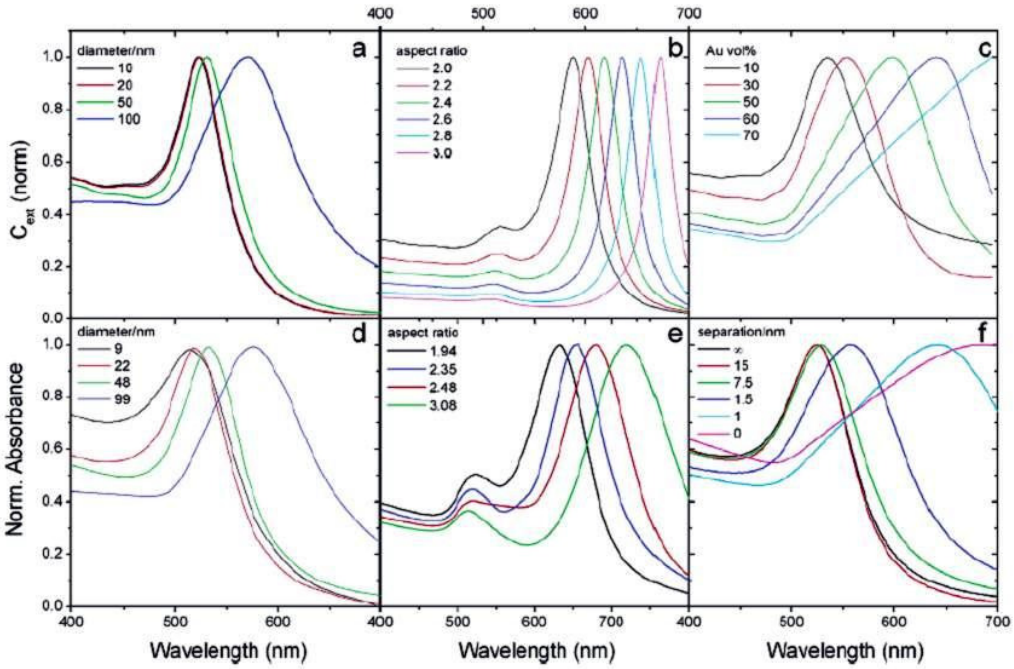

Figure 1.11: Top: Calculated UV-Vis spectra for (a) gold spheres with varying size, (b) gold ellipsoids with varying aspect ratios and (c) thin glass films with varying concentrations of gold. Bottom: Experimental UV-Vis spectra for (d) gold spheres, (e) gold nanorods and (f) multilayer films of glass coated gold spheres with varying interparticle distance.[32]

Figure 1.11 illustrates the effects of size, aspect ratio and gold concentration on the plasmon resonance. These results were obtained from computational modelling as well as experimental results. As the size of the particle increases there is a red-shift of the plasmon absorption band. This also occurs for an increase of the aspect ratio of nanorods.

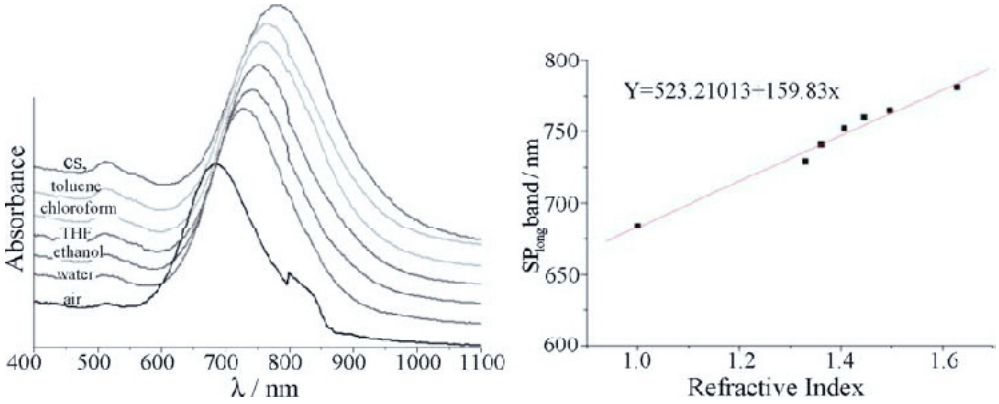

Figure 1.12: Experimental spectra of gold nanorods in different solvents (left) and longitudinal plasmon peak wavelength with respect to the solvent refractive index.[7]

Gold nanorods are solvatochromic (change colour upon changing the solvent). The colour change is dependent on the refractive index of the medium surrounding the nanoparticles. The plasmon resonance wavelength increases with increasing refractive index.[30] Figure 1.12 shows experimental results for different solvents in which gold nanorods are suspended. Also shown is the linear relationship between the refractive index and the longitudinal peak wavelength.[7]

Apart from the multitudes of different methods to alter the size or shape of the nanoparticles, the orientation of nanorods can also alter the surface plasmon resonance. As mentioned above, gold nanorods have two different plasmon resonances corresponding to the longitudinal and transverse aspect of the rod. These resonances can be selectively excited using light polarised parallel or perpendicular to the long axis of the nanorod, respectively.[7] This effect can be seen in Figure 1.13, which shows that when the incident light is polarised parallel to the nanorod (0°) then only the longitudinal resonance is excited. However, when the incident light is polarised perpendicular to the nanorod (90°) then only the transverse resonance is excited. When the light is polarised at other angles both resonances are excited to different extents.

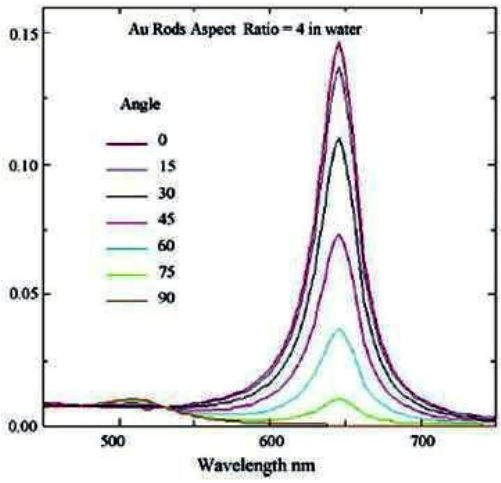

Figure 1.13: Calculated spectra of a vertically orientated gold nanorod in water with an aspect ratio 4. The spectra is calculated for a range of polarisation angles.[7]

1.3.3. Applications of surface plasmon resonance

There have been several applications that have exploited the surface plasmon resonance of small metallic structures. These include the use of nanoparticles in optical devices, sensors and labelling. There are several good reviews of this area.[37,38] Excitation of small metallic nanostructures, at a wavelength where resonance occurs, results in factors including strong light absorption, scattering and an enhancement of the local electromagnetic fields. The nanostructures, as mentioned in Section 1.3.2. Factors affecting surface plasmon resonance, are highly sensitive to base material, size, shape, and environment.[30,33,39,40]

Surface plasmon resonance has been investigated for use in optical and photonic devices and some examples are listed in Section 1.4.3. Optical applications of nanoscale gold structures. Other examples include optical data storage using spectral coding of nanorods, and other optical circuit components.[37]

Surface plasmons can be exploited for microscopy purposes in near-field microscopes. Scanning plasmon near-field microscopy uses incident light coupled to surface plasmon modes of a metallic film (generally gold or silver) deposited on a prism. This allows total internal reflection and the reflected light is detected by a photodiode. As the tip scans the substrate, there is a variation in the reflected light

intensity producing topography dependant signals. This technique allows up to 3 nm resolution.[37,41,42]

Surface plasmon resonance has been applied to sensing applications. One way to shift surface plasmon resonance bands is by altering the surrounding medium (environment). This offers a simple method to detect changes in the environment or to detect attached molecules. Another method is based on the reversible aggregation of metallic nanoparticles through specific linkers, which allows for colorimetric assays. Alternatively, the high scattering from each plasmon resonant particle can be utilised and when a particle is attached to specific molecules it can act as a molecular label. Surface plasmon resonance particles are well known to amplify the signals obtained using techniques such as Surface-Enhanced Raman Scattering (SERS), Surface-Enhanced Infrared Reflection Absorption Spectroscopy (SEIRAS) and many other similar surface enhanced techniques. This area has been well documented and there are several good reviews.[43,44] Briefly, Raman scattering is the inelastic scattering of photons from a molecule where the scattered photons have a different frequency to the incident photons. It is a non-destructive tool for analysis of organic and inorganic compounds. There is only a small quantity of scattered light that is Raman scattered, resulting in research into methods to enhance the effect. These enhancement techniques operate according to two possible mechanisms, electromagnetic (EM) or chemical enhancement. Firstly, EM enhancement, where small metallic nanoparticles attached to a metal surface enhance the surface plasmon resonance, correspondingly enhancing the EM field thereby increasing the Raman scattering by several orders of magnitude, with the possibility of detecting single molecules.[44] Secondly, the chemical enhancement mechanism involves charge transfer between the molecule and the metal surface and involves a change in the electron distribution of the molecule and may cause different enhancements for different vibrational modes. It is also possible that SERS occurs due to combinations from both these EM and chemical enhancement.[44,45]

Because the colour of metallic nanoparticles depends on the refractive index of the surrounding medium, a simple colour change may be used to detect changes in environmental conditions.[37,38,46-51] The following examples use plasmonic materials as sensors to detect changes in the local environment. Watanabe *et al.* used gold nanospheres with surface modification by amide ligands that allows for enhanced optical sensing of anions. The surface plasmon peak shifts as anions bind to the

ligands.[46] Raschke *et al.* uses a similar process, whereby gold nanospheres are functionalised with biotin, followed by streptavidin and a specific binder, which allows for the binding of a complementary molecule. The process of binding the complementary molecule produces a shift in the plasmon peak. With high uniformity of gold spheres, small changes in the peak position may be detected.[48] Briglin *et al.* used alkylamine coated gold nanoparticles as chemically sensitive resistors for the detection of volatile thiol vapours. Thin films of these gold coated particles have a resistance of between 10 kΩ and 10 MΩ when deposited between interdigitated Au/Cr electrodes. The resistance changes when chemiresitive vapours attach themselves to the gold particles, allowing for sensing of the presences of vapours.[49] Meriaudeau *et al.* deposited gold islands on the end of optical fibres, and recorded the optical absorption changes according to the surrounding media. The resonance shifts were determined by transmission spectroscopy through the optical fibre.[50,51] Sun *et al.* have used gold nanoshells to detect changes in the environment through the position of the plasmon resonance peak. The plasmon resonance of gold nanoshells red-shifts when immersed in solvents with higher refractive indices, or when the gold shells were functionalised by alkanethiolate molecules of increasing chain length.[47] These examples show significant investigation of, in particular, gold nanoparticles for use as a sensor detecting changes in local environment, either through detection by molecular binding or change of refractive index of the surrounding medium.

Sensors based on the aggregation of nanoparticles where the plasmon resonance significantly changes compared to single nanoparticles have also been investigated. This idea is based on the ability of molecular recognition, whereby a binding site is functionalised onto a plasmonic substrate and when the complementary molecule binds to the substrate, it causes aggregation of the many plasmonic particles. In this respect, Mirkin's group has functionalised gold nanoparticles by a thiolated oligonucleotide which aggregates in the presence of a complementary oligonucleotide.[52-54] Using this type of method allows for the reversible aggregation of gold particles by heating, that is the DNA strands dehybridized and the particles separate, allowing for detection in the femtomolar range.[52]

A similar process has been investigated using metallic nanoparticles as a labelling agent, which have replaced or complemented existing techniques for radioactive, fluorescent, luminescent and other labels. Metallic nanoparticles can be designed with a

scattering peak at a specific wavelength in the visible spectrum, enabling the detection of single molecules and multiple targets.[37] Examples of using this technique include the use of, in particular, gold and silver nanoparticles, which are coated with a molecule with a specific binding site designed for a specific molecule, so that when bound to the desired molecule the metal nanoparticles can be clearly seen under an optical microscope.[55-58] Oldenburg *et al.* have used silver nanoparticles as labels in a DNA hybridization assay, to screen for a breast cancer gene (molecular recognition) and then under a dark field microscope count the number of nanoparticles bound. This method provides 60 times greater detection over standard fluorescent labels.[56] Mirkin *et al.* used gold nanoparticles to create homogenous colorimetric detection of oligonucleotides, allowing for immediate results determined with no requirement for specialised sensing equipment.[52,53,57]

This thesis investigates the exploitation of surface plasmon resonance of gold nanoparticles for use as a spectrally selective window coating. Surface plasmon resonance and spectral selectivity have already been discussed. In the following section potential fabrication methods for producing gold nanostructures are reviewed.

1.4. Gold Nanostructures

Gold is an excellent material for the realisation of a large number of interesting nanoscale devices and structures due to its unique chemical and optical properties. Gold films thicker than 100 nm are opaque while thinner films may be transparent to visible light and yet remain electrically conductive. This is one example of the significant effects of reducing one dimension into the nanoscale. Gold nanostructures with different dimensions can have quite different optical properties.[59-71]

Nanostructures can be prepared using "top-down" techniques or "bottom-up" techniques. Top-down techniques rely on some type of lithography to either selectively protect or deposit specific areas of gold. Included in this dissertation is a review of nanolithographically produced gold nanostructures and their optical effects.[72] The bottom-up techniques involve mostly wet-chemistry techniques, which allow gold nanostructures to be produced at a fraction of the cost compared to top-down lithographic techniques, and there is not nearly as much wastage of materials. However, direct positioning and designing of the gold nanostructures by this technique requires much more precise control than standard lithographic techniques.

This section reviews the types of gold nanostructures that can be made using nanolithography and by wet chemistry, and where possible will also look at the optical properties of these gold nanostructures.

1.4.1. Nanolithographic methods

Lithography is a method for printing onto surfaces and has been used for centuries. Nanolithography refers to the fabrication of structures where at least one lateral dimension lies in the range of 1 to 100 nm. There have been several good reviews focusing on some of the standard nanolithographic techniques.[73-76] The information presented here describes the application of each technique to fabricating precious metal nanostructures and in particular nanoscale gold structures.

Optical lithography underpins the extraordinary development of information technology. In conventional optical lithography, light is directed through a finely detailed mask onto a layer of photoresist that lies on the surface of a silicon wafer. The

resulting patterns of illumination are used to selectively alter specific regions on the photoresist, which after several iterations of chemical treatment become the transistors, tracks and other features of modern integrated circuits. Optical lithography has limited feature size and is controlled by the diffraction limit of light and the numerical aperture. There has been much interest in using techniques that reduce the wavelength of light, for example using extreme UV lithography, allowing features as small as 45 nm in the 2008 Intel microchips.[77]

Conventional photolithographic processes cannot be used to manufacture smaller nanoscale structures in gold (or any other material) due to limitations imposed by the diffraction of light. New methods of lithography have been developed to overcome this limitation. Naturally, the issue of how to fabricate gold structures at resolutions significantly finer than those routinely used in optical lithography arises. It is shown here that this topic has attracted extensive interest and investigation, and a succinct and up-to-date review of the field is provided. Techniques by which nanoscale gold shapes such as spheres, circles, rods, lines, rings, cylinders, crosses, and squares can be fabricated are discussed.[60-63,65-71,78,79]

1.4.1.1. Electron beam lithography

Electron beam lithography (EBL) uses an electron beam focused onto a substrate coated with a beam-sensitive material and the beam is directed to produce a specific pattern. Because the diffraction limit of electrons is much smaller than that of visible, UV or even X-ray photons, the spatial resolution of EBL is greater than techniques using light. EBL can be used to create nanostructures directly or to construct masks for use with other lithographic techniques.

Gotschy *et al.* used EBL to create metal dot arrays on transparent glass substrates.[80] Insulating substrates complicate the EBL process due to charging effects, which occurs when electrons cannot dissipate from the surface quickly enough, such that regions of the sample where the beam strikes become negatively charged and begin to repel incoming beam electrons. Often this results in images drifting and a skewing of patterns. To prevent charging, the nonconductive substrate requires a conductive layer to disperse excess electrons. Antimony-doped tin oxide,[71] indium-doped tin oxide (ITO)[79-83] and fluorine tin oxide (FTO) all form reasonably transparent conducting layers that will allow EBL to be performed on glass substrates. Gotschy *et al.* used a

thin layer of ITO applied by sputtering. A 60 nm poly(methyl methacrylate) (PMMA) e-beam resist was spin-coated onto ITO-coated glass and an electron beam used to expose a dot array pattern. The exposed resist was removed with solvent and a 10 - 50 nm silver metal layer was then deposited by thermal evaporation. The remaining PMMA layer, together with the excess silver deposited on it, was removed by acetone leaving the silver dot array on the ITO glass.[80]

Lamprecht *et al.* utilized the same procedure except that circular gold nanostructures in two-dimensional arrays were fabricated.[81] EBL allowed the particle shape and interparticle distance in the arrays to be varied independently. The optical effects of plasmon excitation were investigated (see Section 1.4.3.2. Diffraction gratings and photonic crystals.).

Ueno *et al.* also used a similar process to create arrays of gold rods.[60] A 2 nm chromium / 60 nm gold bilayer was deposited onto a mask prepared by EBL; the chromium reportedly improves binding of the gold to the substrate. Arrays of gold rods with aspect ratios (aspect ratio is the ratio of length to width) varying between 1 and 9 were prepared. Figure 1.14 shows an array of rods with aspect ratio of 9.

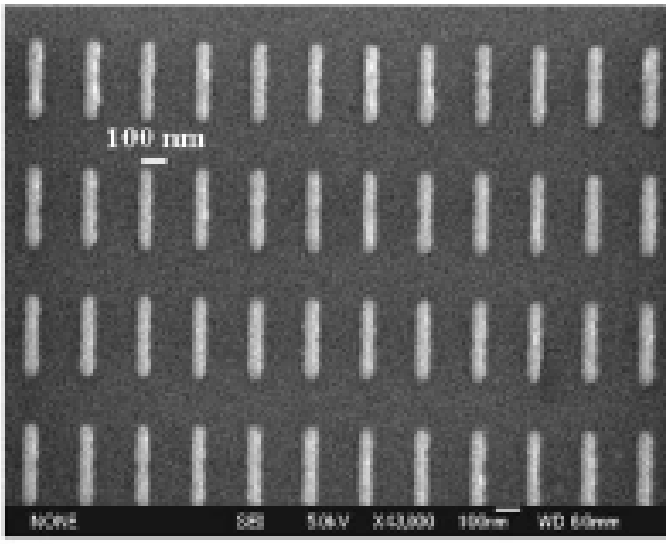

Figure 1.14: Array of gold nanorods with aspect ratio of 9. Each rod has dimensions of 40 nm (w) x 360 nm (l) x 60 nm (h) and are spaced 200 nm apart.[60]

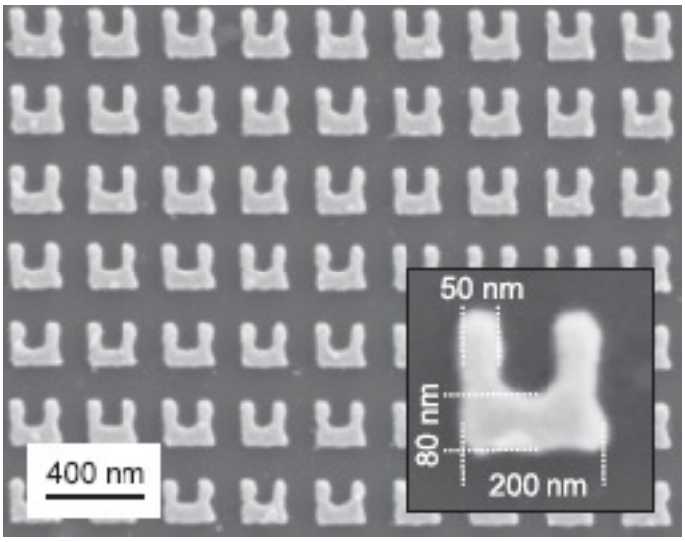

Figure 1.15: SEM image of a 100 μm^2 array of SPRs. The insert shows the dimensions of an individual split ring.[83]

Metamaterials are materials that primarily gain their electromagnetic properties from structure rather than from material they are made of. Metamaterials composed of split ring resonators (SRRs) have been fabricated using EBL by several groups.[82-84] The split rings consist of gold 20 - 30 nm thick and with variable lateral dimensions. The resonators were fabricated in a 100 μm^2 periodic array using PMMA resist on an ITO glass substrate. The pattern and dimensions are shown in Figure 1.15. Optical properties of SRRs have been investigated, and allow the possibilities of negative permittivity and negative permeability at specific wavelengths depending on the resonant frequency of the circuits' structures. Both negative permittivity and permeability give rise to negative refractive index materials. This implies that electrons within the sample move in the opposite direction of the applied electric and magnetic fields.[85,86] Other metamaterials have been fabricated from different shaped structures. Grigorenko *et al.* used EBL to fabricate gold pillars (flat topped cones) 80-90 nm high and ~ 100 nm diameter on a glass substrate and grouped in tightly spaced pairs.[87] Garwe *et al.* have also used EBL and ion beam lithography to create a potential metamaterial.[88] Gold wires 200 x 500 nm with thickness 75 nm were fabricated on glass as a single layer, a double layer with 180 nm PMMA spacer and a double layer with 600 nm layer spacer.

Jefimovs *et al.* created nanostructures to filter infrared radiation.[66] On a conducting gold substrate, a thick (300 - 800 nm) layer of polyimide was applied by spin coating, followed by vapour deposition of a ~50 nm layer of SiO_2, spin coating of a ~100 nm layer of PMMA resist and, finally, sputtering of a ~20 nm conductive Al film to prevent

charging during EBL.[66] A grid pattern was exposed using EBL through the Al layer into the PMMA resist. The thin PMMA layer has a very small interaction volume with the e-beam and enables small, well-defined structures to be formed. The PMMA was then developed with solvent to form a mask for a subsequent reactive-ion etching (RIE) step. The grid pattern was etched into the sublayers using RIE and gold was deposited by electroplating into the voids. Figure 1.16 shows the gold grid structure prepared.

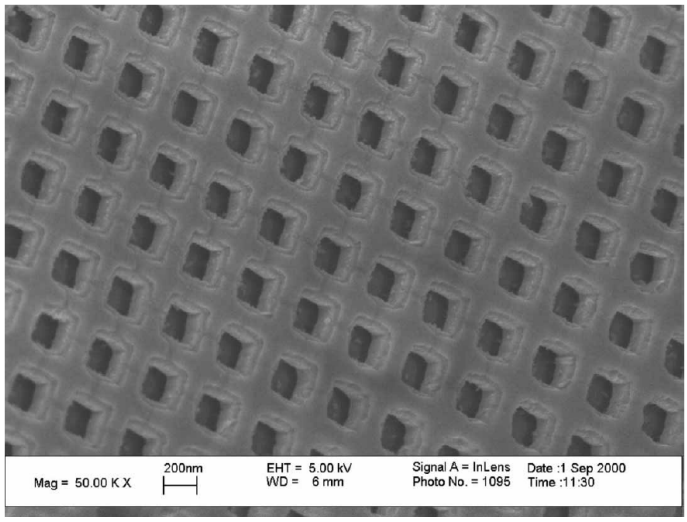

Figure 1.16: SEM image of a gold grid to filter infrared radiation.[66]

Arrays of annular apertures in gold layers have been fabricated on antimony-doped tin oxide coated glass substrates (Figure 1.17).[71] In this procedure, a negative tone resist is used whereby sections not exposed to the e-beam are initially removed. A gold film was then deposited over the entire surface and when the remaining resist was removed, voids in the gold film, in the form of 100 nm rings, were revealed.

Griffith *et al.* developed an additive-layer technique for multiple-material functionality.[89] The procedure involves spin-coating a resist consisting of thiol-capped gold or silver nanoparticles onto a silicon wafer, glass slide or polyimide film substrate. Exposure of the resist to an e-beam removes the stabilising thiol molecules, which results in aggregation of the metal nanoparticles. The unexposed resist was removed using solvent and the remaining sample was annealed to strongly bind the metal nanoparticles to the substrate. Successive layers can be spin-coated directly over previous structures.[89] Figure 1.18 shows a four layered structure with conformal layering, but includes some misalignment.

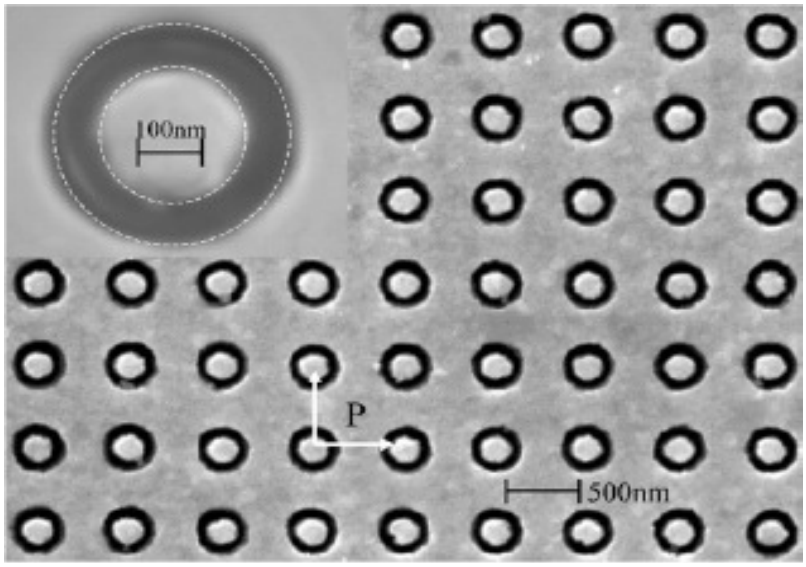

Figure 1.17: SEM image of the annular aperture array pattern after lift-off. Ring diameter 225/360nm (inner diameter/outer diameter).[71]

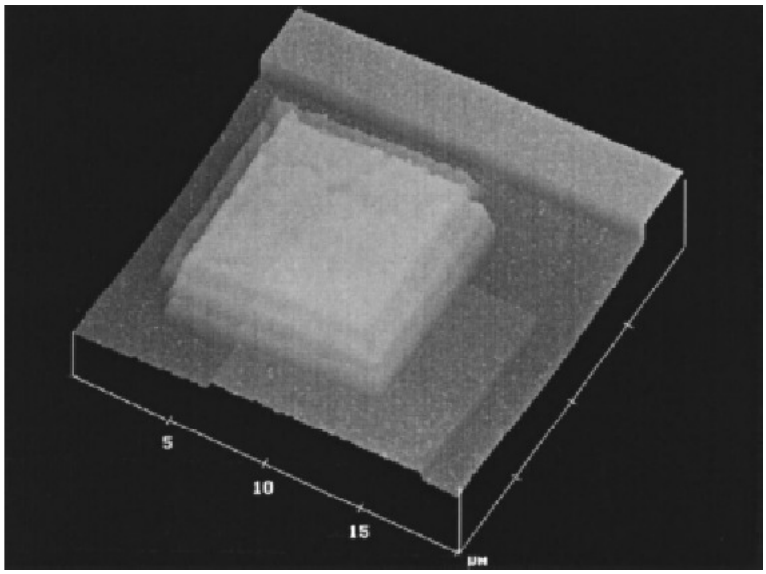

Figure 1.18: AFM image of a four-layered test structure.[89]

Fukushima *et al.* fabricated periodic gold nanostructures consisting of arrays of lines and dots using a somewhat different approach.[70] A sol-gel process was used to prepare SiO_2/TiO_2 containing chloroauric acid ($HAuCl_4$) and laser dyes, and the mixture was spin-coated onto a glass substrate. Gold nanoparticles were generated by reduction of the Au(III) ions using electron beam irradiation directed to form the desired shapes.

1.4.1.2. Nanolithography using beams of ions or atoms

A rather different type of nanolithography is possible if the beam is comprised of ions or atoms instead of electrons. There are three main ion-beam lithography (IBL) techniques, focused ion beam (FIB), proton beam writing (p-beam writing) and ion projection lithography (IPL).[90]

Focused ion beam (FIB) involves a focused heavy-ion beam rastered over a surface creating a pattern through modification of the surface structure (either physically or chemically), deposition of atoms, or removal of atoms from the surface through sputtering.[90,91] Ga or Ar ions are generally used. The processes involved in FIB are shown in Figure 1.19. The small penetration depth of heavy ions into the substrate allows complex 3-dimensional structures to be fabricated with high resolution.[90,92-94] Patterns can be written into virtually any material, however the process is relatively slow.[90,91,95,96] Etching rates may be increased by using reactive gasses,[90-96] or writing into materials like PMMA.[90,97]

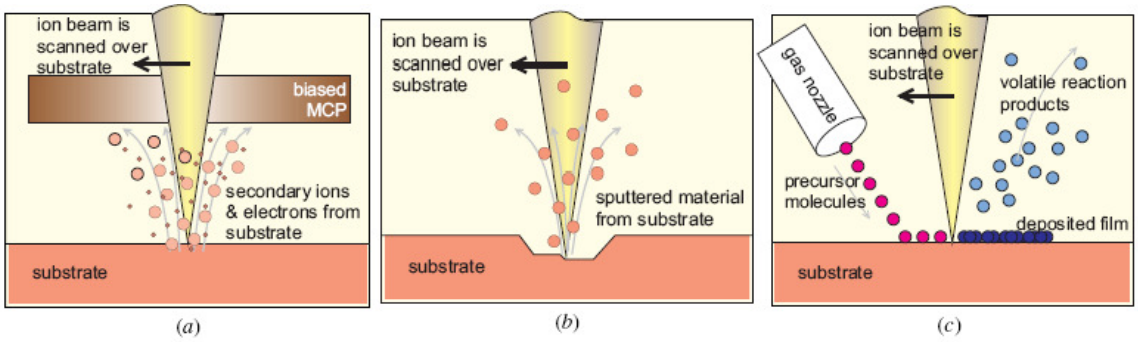

Figure 1.19: Principles of Focused Ion Beam, (a) imaging, (b) milling and (c) deposition. [91]

Hanarp *et al.* used focused ion-beam lithography to create arrays of gold disks.[69] A 20 nm thick gold film was deposited on a glass substrate and polystyrene nanoparticles were self-assembled onto the gold layer from a colloidal solution. The polystyrene particles act as a mask and an argon ion beam was used to etch the gold not covered by particles. The particles were then removed to leave gold disks. The size of the gold disks is controlled by the size of the masking polystyrene particles. Interestingly, the size of the polystyrene particles is temperature dependent, so changing the temperature alters the size of gold disks. This nanolithographic method is capable of producing optical coatings over large areas with controllable size, shape and interparticle spacing.[69]

Proton beam writing and ion projection lithography are related IBL techniques although no reports of their use to make precious metal structures have been forthcoming to date. Proton beam (*p*-beam) writing uses fast (MeV) protons to write deep, precise 3-dimensional patterns into resist layers.[90] The protons penetrate deep into the resist material with minimal surface disruption and little to no beam deviation aside from some end-of-range broadening. This aspect of *p*-beam writing is a significant advantage over EBL techniques in which the lighter electrons scatter far more readily, increasing the difficulty in maintaining very small line widths. Also, secondary electrons produced by the primary proton beam have low energy and therefore limited range, resulting in minimal proximity effects.[90,98] *p*-Beam writing is effective in fabricating high aspect ratio and multi-layer structures within PMMA resist of gratings, columns and other 3D structures.[98]

Ion projection lithography (IPL) uses medium energy ions (~100 keV) projected through a patterned mask for fabrication. A beam of ions uniformly illuminates a large area patterned mask and the transmitted beam is projected onto the surface using electrostatic lenses. IPL has been used to pattern at 50 - 75 nm resolution using a single exposure.[90] With IPL there are no diffraction effects, and the depth of ion penetration is adjustable. The ability to pattern a large area in a single exposure without wet-chemical processing is also quite attractive.[90]

Atom lithography uses atomic beams to create structures on surfaces. There are two variants of the atom lithography process. One method uses a beam of reactive atoms to chemically modify a suitable resist, similar to the etching processes used in EBL and FIB. In the second method, the nanostructure is formed from atoms deposited directly by the beam in selected patterns. Mützel *et al.* utilized atom lithography with an optical light mask.[65] Optical dipole forces concentrated atoms near the nodes of a standing light-wave field. A holographic mirror was used to control a caesium atom beam to deposit a pattern onto a substrate consisting of silicon wafer covered with a 30 nm gold film and self-assembled monolayer of 1-nonanethiol. The 1-nonanethiol layer protects the gold during a wet chemical etching process. The deposited caesium structure attaches to the 1-nonanthiol layer, removing the protective action of the 1-nonanethiol to the etching process. Therefore the pattern defined by the caesium atoms is transferred into the gold layer.[65,99]

1.4.1.3. Nanolithography using visible or ultra-violet light

Optical lithography is capable of producing sub-100 nm patterns with the use of very short wavelengths. Fabrication of sub-50 nm patterns requires the use of a liquid immersion technique and photomask enhancement technologies such as phase-shift masks and optical proximity correction. There have been several published reviews describing this area.[100-104]

Guo *et al.* used interference lithography to create gold gratings that can be used for optical applications.[105] A laser exposed a pattern in a sample consisting of 100 nm thick photoresist deposited onto a 40 nm thick gold film. The exposed resist was removed and the sample was etched using an ion beam to form the pattern in the gold layer. The remaining resist was removed to give the gold structures. Gold nanowire structures with line widths ranging between 115 nm to 200 nm were prepared. The process provides an inexpensive, fast, and versatile means for the fabrication of large area metallic nanostructures.[105]

Nakata *et al.* used lithographical laser ablation to fabricate gratings of lines and circular holes.[106] Light from a femtosecond pulsed laser was passed through a mask and the pattern was imaged onto a gold film on a silica-glass substrate by a coherent optical system. Periodic structures such as nano-sized hole matrices and nano-meshes were generated in a single shot of laser ablation.[106] This process created large area patterns rapidly but the resolution was lower than that using many other lithographic techniques.

Ultraviolet lithography is similar to optical lithography but uses shorter wavelength light resulting in a lower diffraction limit. Using appropriate mirrors and photomasks, the highest resolution reached to date has been slightly better than 30 nm through the use of interference lithography in the extreme ultra-violet region.[107,108] This linewidth was achieved through Extreme Ultra-Violet Interference Lithography (EUV-IL) whereby extreme UV light is passed through two diffraction gratings simultaneously and the corresponding beams periodic interference pattern is exposed into a EUV resist.

Johannsmann *et al.* used UV lithography to create infra-red filters using a cross-shaped pattern in a gold layer (see Figure 1.20).[68] The structure was fabricated using a mask formed by EBL and then applying UV light through the mask onto a resist layer. The imaging accuracy is limited by the wavelength of the UV radiation and by the diffusion processes during the development of the photomaterial.

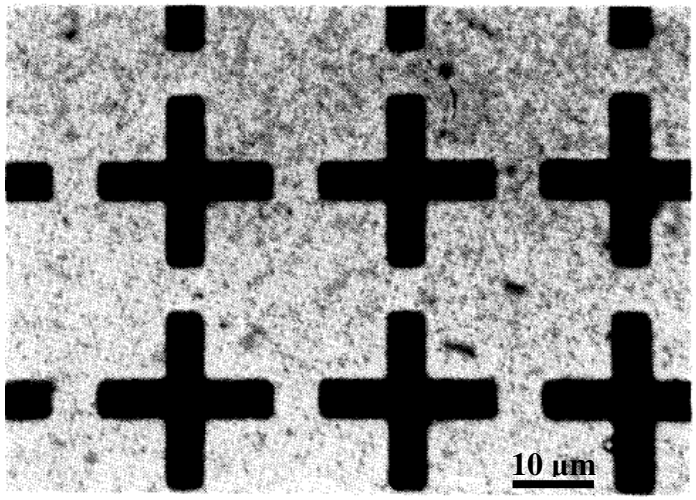

Figure 1.20: Micrograph of a gold resonant mesh on a 3 micron polyimide foil.[68]

Sun *et al.* reported a procedure[109] similar to the EBL technique reported by Griffith *et al.*[89] Exposure of a film of thiol-stabilised gold nanoparticles on silicon by UV radiation oxidised the thiol molecules. The gold nanoparticles aggregated and formed structures that solvent did not remove. Using UV light to oxidise the thiol molecules allowed a mask to be used, giving micrometre-scale structures. The minimum line width produced was 60 nm for Langmuir-Schaeffer films using a UV laser attached to a near-field scanning optical microscope in place of a lamp and mask setup. The lamp and mask setup produced structures that were porous, whereas the UV laser produced dense, continuous structures.

Another recently developed optical lithography technique is zone-plate-array lithography (ZPAL).[110-112] ZPAL is a maskless optical technology that employs an array of optical lenses that focus incident light onto the substrate. A UV laser is reflected off a spatial-light modulator that directs light with adjustable intensity to individual zone plates, where the incident light is focussed onto a resist. The zone-plate-array is fabricated using EBL. The substrate is scanned beneath the array and various patterns can be built up in a dot-matrix fashion.[110,112] Minimum linewidths reported to date are ~ 115 nm.[110]

Evanescent Near-Field Optical Lithography (ENFOL) overcomes the diffraction limit of $\lambda/2$ by utilising the near-field's high-spatial frequency information and has been used to achieve $\lambda/7$ resolution.[113] ENFOL consists of a glass support with an attached tungsten mask produced by EBL which is brought into vacuum contact with a silicon substrate with a layer of bottom anti-reflection coating and a photoresist.[113-115] A UV

light is shone through the mask and the pattern is transferred to the resist. This system requires contact between mask and resist which limits applications. Planar Lens Lithography (PLL) is a subset of ENFOL in which a planar silver lens is added into the system and illuminated near its UV electromagnetic-resonance which projects the near-field (super-lensing), removing the requirement for direct contact.[113-115] The highest resolution achieved has been 145 nm through the use of PLL. Improvement of the silver layer could make PLL a viable next generation lithography technique.

1.4.1.4. X-ray nanolithography

The short wavelengths of X-rays give improved diffraction limits compared to optical lithography. Broadband X-rays, typically from a compact synchrotron radiation source, are used to illuminate masks placed in proximity to a resist-coated wafer. The mask (often prepared by EBL) consists of an X-ray absorber, typically gold, on a membrane that is transparent to X-rays, generally silicon carbide or diamond. There are several good reviews focusing specifically on X-ray lithography.[116-118]

X-rays may generate secondary electrons and while the fine pattern definition is due principally to Auger electrons with very short path lengths, the secondary electrons may sensitize the resist over a larger region than the X-ray exposure. Although this does not affect the pattern pitch resolution, the image exposure contrast may be reduced by factors up to one half. Structures with resolution of ~ 20 nm and less have been published. Deep X-ray lithography uses very short wavelengths of ~ 0.1 nm with modified procedures, to fabricate deeper structures, sometimes three dimensional, with reduced resolution.

Romanato *et al.* produced a 3-dimensional photonic crystal using X-ray lithography.[62] Two gold masks were used; one that created a square array of square holes and another patterned with two triangular arrays of circular holes. The X-rays were directed onto the resist at different angles to generate different patterns. Finally, a 5 nm gold layer is deposited onto the resist to create the 3D photonic crystal.

Metallic 3-dimensional lattices with cubic and Yablonovite structure have been fabricated by X-ray lithography. Yablonovite, also called the 'three cylinder structure', is a distorted rod-connected diamond structure that can be produced by drilling only three holes. The X-ray lithography method is well adapted to fabricate these 3D lattices. The resolution can be controlled to yield lattice parameters of 200 nm.[62]

1.4.1.5. Nanoimprint lithography

Nanoimprint lithography (NIL) is a method of fabricating nanometer scale patterns by mechanical deformation of imprint resist followed by subsequent processes. Because NIL is a pattern transfer process; it is not limited by diffraction, scattering effects, or secondary electrons but it relies on other lithography techniques to generate templates. However, it is possible that self-assembled structures could provide templates of periodic patterns at scales of 10 nm and less. Two processes are used for NIL; thermoplastic nanoimprint lithography and step-and-flash nanoimprint lithography.

Thermoplastic nanoimprint lithography (T-NIL) is the more mature nanoimprint lithography. In a standard T-NIL process, a thin polymer layer of imprint resist is spin coated onto a substrate and a mold is brought into contact with the sample and pressed under pressure. When heated above the glass transition temperature of the polymer, the pattern on the mold is pressed into the polymer film. After cooling, the mold is separated from the sample and the pattern remains imprinted on the substrate.

Step and flash imprint lithography (SFIL) uses a UV curable liquid resist and the mold is normally a transparent material like fused silica. After the mold and the substrate are pressed together, the resist is cured with UV light. After mold separation, a pattern transfer process can be used to transfer the pattern onto the material below.

Li *et al.* used microcontact printing as a soft lithographic process to produce a structure on a bis(ω-trimethylsiloxyundecyl)disulfide (TMS) self-assembled monolayer SAM.[119] A stamp made of poly(dimethylsiloxane) (PDMS) was "inked" with a gold nanoparticle solution and brought into contact with the TMS SAM on a gold substrate. Following the removal of the stamp from the substrate, the substrate was rinsed revealing the pattern. Microcontact printing by Li *et al*. employed ink transfer from an elastomeric stamp to a solid substrate. The ink contained ~ 4 nm diameter gold spheres. The advantage of this lithographic process is that no diffusion occurs upon transfer, allowing more accurate pattern transfer than normal microcontact printing, which relies on absorbate diffusion from the stamp interior to the surface.

Li *et al.* fabricated optically-functional structures using NIL.[63] A PMMA resist was spin-coated onto a substrate, and a mold was then imprinted into the resist. The compressed PMMA was then removed by anisotropic oxygen etching and a gold layer was evaporated onto the sample before the remaining PMMA was lifted off. The mask

produced circular concentric gratings with line widths of about 20 nm. Optical elements can be made with low cost and high throughput.

Similarly, Yu *et al.* used NIL with PMMA resists to create double layer sub-wavelength metal gratings.[120] This was achieved by bypassing the 'lift-off' step listed above. The gold metal gratings are separated by the height of the PMMA layer, allowing different optical properties depending on the amount of the PMMA deposited. NIL has the capability to mold several square centimetres simultaneously but the resolution is lower compared to many other lithographic techniques.

1.4.1.6. Scanned probe lithography

There are several different Scanned Probe Lithographic (SPL) techniques, including AFM and STM atom manipulation, and Dip Pen Nanolithography (DPN). Several good reviews of these specific SPL techniques have been published.[121-125]

AFM and STM use a cantilever tip to push atoms around on surfaces to create patterns. DPN is a SPL technique in which a microscopic "pen" is coated with a chemical compound and brought into contact with a substrate to "write" on the substrate with the compound.

AFM has been used to manipulate gold nanorods, fabricated electrochemically, across a silicon substrate.[126] The nanorods were manipulated using the AFM cantilever, which moved the rods along their transverse and longitudinal axis and could also adjust their rotational orientation. This process provides precise control over position and orientation, and is therefore useful as a basis for building more complex nanostructures.

Direct AFM manipulation has been used to create a straight line of 30 nm gold particles. Colloids of 30 nm diameter gold nanoparticles were deposited onto a substrate and the particles were assembled into a straight line using an AFM in contact mode.[79]

Dip-Pen Nanolithography (DPN) was used to fabricate and functionalise gold nanostructures on a semiconductor substrate.[78] An AFM tip was used to deliver molecules to a surface via a solvent meniscus. This direct-write technique offers high-resolution patterning capabilities for a number of molecular and biomolecular "inks" on a variety of substrates including metals, semiconductors, and monolayer functionalized surfaces. DPN allows control to precisely pattern structures with very accurate positioning. The AFM tip may be used to read, as well as write, nanoscopic features on a surface. Creating nanostructures using DPN is a single step process that does not

require the use of resists. Using a conventional AFM, it is possible to achieve ultra-high resolution features with line widths as small as 10-15 nm and with ~ 5 nm spatial resolution.

Mirkin et al. fabricated gold-containing nanostructures on a silicon substrate coated with successive layers of silicon oxide (500 nm), titanium (1 nm) and a top layer of gold (8-10 nm).[64,78,127,128] Using an AFM tip coated with octadecanethiol[128] or 16-mercaptohexadecanoic acid (MHA),[64,78,127] the thiol was 'written' onto the gold surface. The bound thiol acts as a positive resist and the surrounding areas of the gold/titanium layers were etched using ferricyanide and hydrofluoric acid solutions. The thiol was then photooxidised by irradiation with UV light whereupon it detaches from the surface. The thiol was replaced with a α,ω-dithiol ($HS\text{-}C_6H_{12}\text{-}SH$) or an aminothiol ($HS\text{-}C_2H_4\text{-}NH_2$) compound and the sample immersed in a gold colloid solution whereupon gold nanoparticles adsorbed to the SAM producing the gold/SAM/gold nanoparticle structures. Sub-50 nm arrays of lines and dots were produced using this technique. As well as functionalising the nanostructures with gold nanoparticles, biofunctionalisation was also demonstrated. After the ferricyanide / HF etching steps, any exposed silicon oxide surface was passivated with octadecyltrimethoxysilane and rabbit IgG proteins were then bound to the carboxylic acid groups of the mercaptohexadecanoic acid layer. This procedure therefore generates nanoscale features functionalised with proteins, which may be useful in biosensing applications.

1.4.1.7. Island lithography

Green *et al.* used water vapour to induce the reorganisation of caesium chloride (CsCl) thin films into disordered arrays of hemispherical islands.[67] A thin metal layer (gold or silver) was then deposited onto the structured CsCl film. The CsCl islands, and the thin metal layer attached to them, were removed by immersion in an ultrasonic bath to leave a perforated metallic film. The growth rate of the islands was found to be dominated by the kinetics of dissolution and deposition at the solid/solution boundary.[129] The structured caesium chloride film has also been used as a mask for reactive ion etching.[67] Although this technique does not allow direct writing of specific structures, it is useful for creating patterns that are uniform over a large area.

Bukasov *et al.* used a similar method with polystyrene spheres acting as the template. Different sized spheres designed to cover a tenth of the surface were randomly

deposited on a substrate. A gold layer was deposited on top of the polystyrene spheres at specific angles and then any gold not protected by the spheres was removed by argon ion milling. Following this, the polystyrene spheres were lifted off by transparent tape.[130] The different size spheres allowed for gold nanocrescents of different shapes and the various gold deposition angles allowed for different aspect ratios. With small enough sphere size and deposition angle Bukasov *et al.* managed to also deposit gold nanorings. A similar experiment conducted by Rindzevicius *et al.*[131] constructed nanosized holes in a thin gold film by applying polystyrene spheres to a substrate and depositing a layer of gold before removing the spheres leaving the round holes in the gold. This is an expensive technique and is not suitable for precision placing of nanostructures, or production of complex nanostructures, however it is good for overall uniform shapes across large areas.

Zhang *et al.* have also used a similar process, using dip-coating to deposit polystyrene spheres before deposition of a gold layer. The exact process they used formed ordered arrays of gold nanostructured shuttlecocks, hexagons and dots.[132]

1.4.2. Wet-chemically produced structures

This section looks at gold nanostructures produced by bottom-up techniques, in particular wet chemistry techniques, and compares some other techniques that are used to produce similar structures.

Wet chemical methods to produce nanostructures have significant commercial potential because they have the possibility to be cheaper than most nanolithographic and vacuum deposition techniques. The process to create gold nanoparticles of various shapes will be described here.[133,134]

There are several gold nanostructures that can be made using wet-chemical techniques. These include spheres, rods and wires, triangles, cages and squares, shells, hexagons and other polygons.[133,134] Most structures are made in solution and as such require some type of stabilising agent to prevent nanoparticle aggregation to their more stable form. This includes smaller gold spheres which are initially made in a colloid but without a stabiliser they aggregate and precipitate out of solution. To make different gold nanostructures also requires a shape-inducing agent, normally a surfactant of some kind.

1.4.2.1. Synthesis of gold nanorods

There are three main methods of producing gold nanorods, (i) the template method, (ii) the electrochemical method and (iii) the seeded growth method.

The template method for synthesis consists of electrochemical deposition of gold within the pores of a template membrane, usually made from aluminium oxide or polycarbonate. After the gold is deposited in the pores of the template, the template is dissolved in the presence of a stabilizer. The rods are then dispersed into a solvent by sonication. This process is shown in Figure 1.21 (a). The dimensions of the gold nanorods are directly determined by the size of the pores in the alumina template. Precise control over the pore size allows precise control of rod aspect ratio and there is no limitation on production of mid-range aspect ratio rods unlike current conditions for seeded growth rods. Limitations of using this method include low yield, as only a monolayer of the rods can be made using the template, and the template needs to be remade between each use.[7]

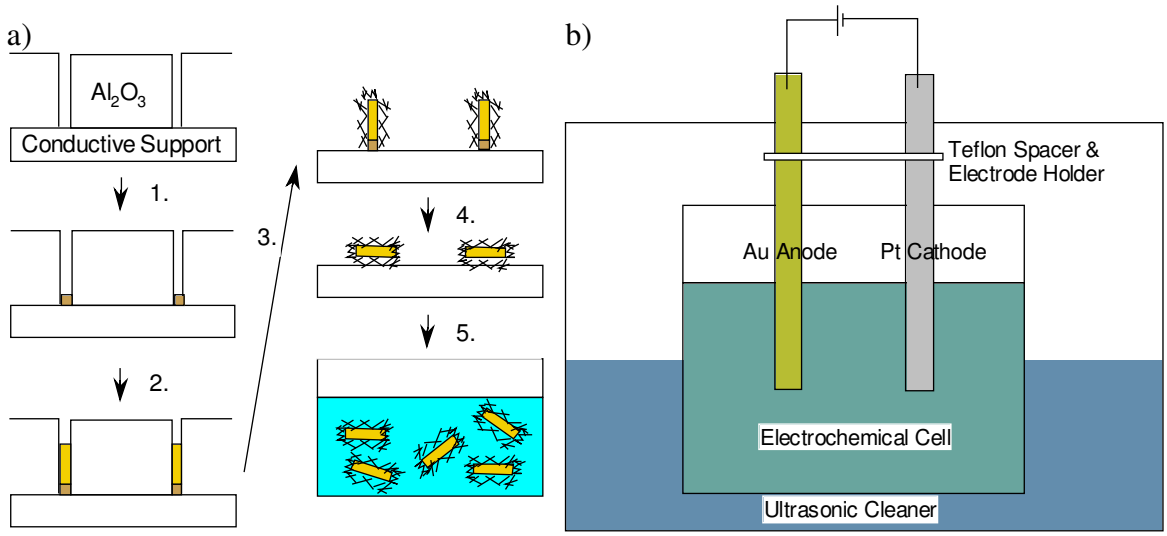

Figure 1.21: (a) Schematic representation of the stages to obtain aqueous dispersions of gold rods using an alumina template. (1) Electrodeposition of copper followed by (2) electrodeposition of gold. (3) The template and (4) the copper are selectively dissolved to release the rods. (5) The rods are then dispersed in water by sonication.[7,135] (b) Diagram of the experimental set-up for the preparation of gold nanorods via the electrochemical method.[7,136]

The electrochemical method is used to prepare high yields of gold nanorods. The synthesis is conducted within a two-electrode electrochemical cell, shown in Figure 1.21 (b). A gold plate is used as a sacrificial anode with a platinum plate as the cathode.

The electrodes are immersed in an electrolytic solution containing a cationic surfactant, hexadecyltrimethylammonium bromide (C_{16}TAB) and a hydrophobic cationic rod-inducing cosurfactant, tetradodecylammonium bromide (TC_{12}AB). The C_{16}TAB acts as both the electrolyte and a stabiliser to prevent aggregation of the nanorods. The electrolytic cell is then placed in an ultrasonic bath at 36 °C to ensure the rods being made are sheared away or broken off the cathode surface. Before electrolysis, acetone and cyclohexane are added to the cell. A steady current of about 3 mA over a period of 30 minutes is suitable for the production of rods.[7,136-138]

There are several different methods to produce gold nanorods using the seeded growth method. The basis of these methods is that small gold nanospheres are produced and these 'seeds' are then grown using gold ions in solution to form larger gold nanostructures. The method to produce the 'seed' is to use a reductant, typically sodium borohydride ($NaBH_4$), to reduce metal salts in water, normally tetrachloroauric acid ($HAuCl_4$). Gold seed particles prepared without the use of a stabilising capping agent produce gold nanospheres of approximately 3.5 nm.[139] A capping agent can affect the size of the seed particles, according to the type and concentration of the capping agent. Larger seed particles produce lower aspect ratio rods.[139]

The second stage of producing gold nanorods using the seeded growth method is the application of a growth solution to the seed solution allowing the seeds to grow into rods. The growth steps are carried out using an aqueous surfactant media, typically CTAB in water and with a gold salt ($HAuCl_4$). Additional nucleation is inhibited by controlling the growth conditions and the addition of ascorbic acid, a weak reducing agent, which prevents reduction of the gold salt without the seed present. The addition of silver nitrate during the growth process increases the yield of the desired aspect ratio.[7] Figure 1.22 shows the rod production process.

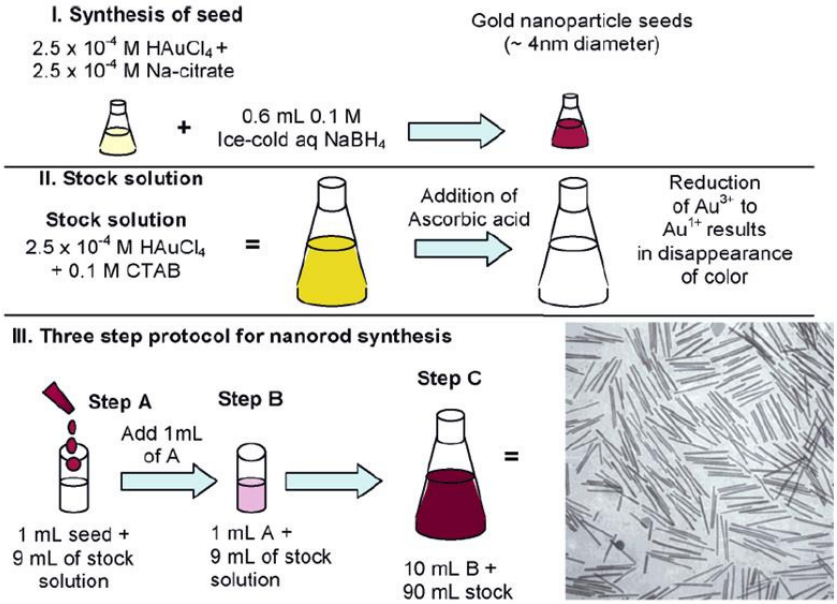

Figure 1.22: Seed-mediated growth approach to making gold nanorods of controlled aspect ratio. Aspect ratio is controlled via the concentration and volume of the different solutions. Different stabilising agents can also be used.[140]

A plausible mechanism for the growth process involves CTA^+ (of the CTAB stabiliser) binding preferentially on the {110} and {100} facets of the nanorod, protecting this portion of the nanorod from binding much gold. As a result more gold is bound along the {111} facets on the ends, which consequently forms the nanorod.[141] The CTAB forms a protective coating, thought to be bilayer in nature, surrounding the gold nanorods that prevent aggregation of the rods. It has been shown that the surfactant molecules provide stabilisation of the highly unstable (110) surface of the gold nanorods.[142,143]

1.4.2.2. Surface chemistry and reactivity of gold nanorods

Gold is an excellent material for nanoscale applications due to its relative stability and resistance to oxidation. Both macro- and nano-sized gold particles have a strong thiophilic (an affinity for binding sulphur) binding affinity and can also bind nitrogen groups and alkynes which can be useful.[5,7,72,144] The presence of surfactant molecules on gold nanorods also influences their reactivity and stability. This section provides a summary of different types of gold nanorod functionalisation and reactivity as reported in the literature.

There have been a number of methods for aligning or assembling gold nanorods or structures reported in the literature. Several of these involve functionalising the nanorods, whilst others involve electrostatic bonding. For example, gold nanorods have been modified with DNA to form 3D aggregates using complementary DNA strands[145] or assembled onto 2D surfaces.[146]

Molecules with thiol groups bind strongly to gold surfaces. Due to the method of creating the majority of rods using a wet-chemical seeded method, the sides of the rods are encased in C_{16}TAB. As such, molecules that have two thiol groups can be used to connect the rods end-end. This directional assembly of the connected gold nanorods is attributed to the protective bilayer of the CTAB, such that the thiol molecules binds preferentially to the {111} face at the ends of the rods where less CTAB is bound.[147-150] Murphy *et al.* used a biotin disulfide added to the rods and the addition of streptavidin causes noncovalent end-end assembly.[140,149] The mechanism behind the end-end assembly seems to require two factors to hold. Firstly, the disulfide must be unsuccessful at displacing the CTAB, which binds preferentially to the sides of the rod, and therefore the disulfide binds more readily to the ends of the rods allowing end-end formation. Secondly, while the biotin binds all over the rods, the streptavidin is sterically constrained to bind to the ends of the rods due to the full biotin coverage blocking the binding sites along the edges of the rods.[149,151]

Thomas *et al.* have also instigated linear assembly of gold nanorods to form chains for the purpose of plasmon coupling (see 1.3. Surface Plasmon Resonance). In this case 3-mercaptopropionic acid (MPA) and 11-mercaptoundecanoic acid (MUA) were used for assembling gold nanorods. These acids have a thiol group that readily binds to the surface of the gold nanorods, at the end for CTAB stabilised rods, and the carboxyl groups assist in the self assembly through intermolecular hydrogen bonding.[147]

Murphy *et al.* reported molecules bound to the entire gold nanorod surface by utilising the electrostatic interaction of the positively charged CTAB bilayer surrounding the nanorods. This charge allows the adsorption of a carboxylic acid-containing polymer to coat the nanorod through a layer-by-layer (LBL) method. Other molecules can then be bound to the carboxylic acid containing polymer. They also used a biotin molecule which differs from those reported above in that these molecules are coating the entire nanorod and not focused on the {111} face. The next step involved the addition of streptavidin molecules, which allow binding of biotin molecules bound

to the gold nanorods and cause aggregation of the nanorods with preferential side-side assembly.[150] The LBL method has also been used to create multilayered films of gold nanorods. Hu *et al.* used linear polyethylenimine as a polymeric adhesive layer with a positive charge, which was attached to an indium tin oxide (ITO) coated glass substrate.[152] On top of this layer was placed a negatively charged layer of poly(sodium styrenesulfonate) (PSS), which allowed the electrostatic binding of the positively charged CTAB capped gold nanorods. To create multiple layers of gold nanorods Hu *et al.* applied another layer of negatively charged PSS, followed by another layer of gold nanorods. This process was repeated several times. The process mentioned above allows for the functionalisation of the gold nanorod by making use of the surfactant layer rather than trying working around it.

Electrostatic interaction has also been used by Berry *et al.* in which they have attached the positively charged CTAB capped gold nanorods onto negatively charged bacteria. It was shown that the nanorods bind to the bacteria, and even conform to the underlying shape. That is, the nanorods bend to interact with as much of the negatively charged bacteria as possible. Berry *et al.* determined that the strength of the electrostatic interaction was on the order of 15 nN.[153]

Biorecognition is a promising approach towards nano self-assembly. Biorecognition involves two or more molecules that selectively recognise and bind on a molecular level, some examples of this include antibody-antigen, avidin-biotin and aptamer-protein. These receptor-ligand mechanisms, when combined with nanoparticles, can be an effective template for creating larger area nanostructures.[148] Chang *et al.* have modified gold nanorods by attaching anti-mouse immunoglobulin G (IgG) to the ends of the nanorods. The addition of mouse IgG, which has two binding sites allows for the end-end binding of gold nanorods. The distance between these rods can be altered by changing the chain length of the molecule binding the anti-mouse IgG. Control over concentrations of IgG and the functionalised nanorods determined the structure of the gold nanorod chain.[148]

1.4.3. Optical applications of nanoscale gold structures

The optical properties of nanostructured materials often depend upon shape, composition, and the surrounding medium. This has motivated much of the interest in

using nanolithography to produce precious metal structures. In this section some of the applicable nanoscale precious metal structures that have useful optical properties are briefly reviewed. Also included is a brief description of some of the reported nanoscale gold devices and optical applications that require sub-wavelength lithography for their realisation.

1.4.3.1. UV-Visible and IR optical absorption filters

Optical absorption filters are used in fields as diverse as sensors and detectors for astronomy or to window coatings for thermal protection. It is of particular interest when the filter is spectrally selective such that the desired wavelength range is selected to either absorb or transmit whilst the opposite occurs at unwanted wavelengths. The following section describes optical filters as well as materials that could be used as an optical filter.

Manufacturing filters that block near-infrared radiation but transmit shorter wavelengths is a challenging task that has attracted some interest.[66] Metallic grids fabricated by Jefimovs *et al.* were designed to screen an X-ray detector from incoming heat. The grid structure (Figure 1.16) is made of 200 x 200 nm square voids separated by 100 nm of metal in each direction. The transmittance of the gold grid is shown in Figure 1.23. Transmittance of wavelengths longer than 900 nm is low although the transmission observed at visible wavelengths is much lower than theoretical models predict.[66] Interestingly, the square aperture grid structure showed 10% higher transmission compared to the grid with circular apertures.

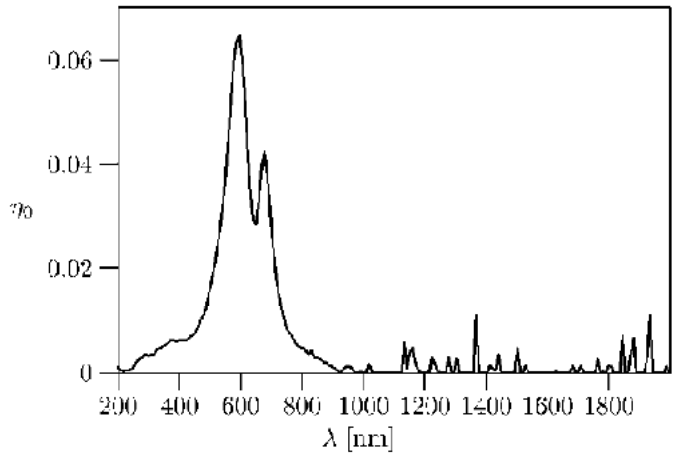

Figure 1.23: Measured transmittance of the fabricated gold grid.[66]

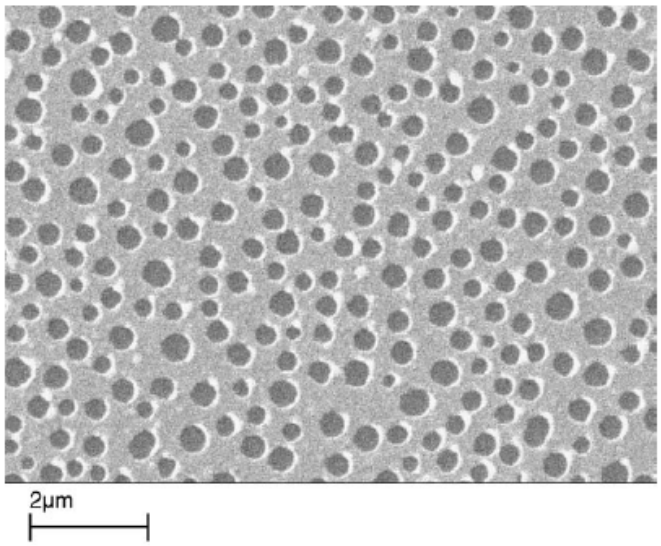

Figure 1.24: SEM image of perforated metal film (Ag) on a glass substrate.[67]

Similarly, Green *et al.* measured the transmission spectra of perforated thin Ag films prepared using island lithography (see Section 1.4.1.7. Island lithography).[67] Figure 1.24 shows the voids in the film where the hemispheres were removed. The transmission of the perforated films was much higher than the transmission of solid films of similar thickness. Disordered arrays of sub-wavelength diameter cylindrical holes have total transmission efficiencies approaching unity, therefore it was concluded that light can couple efficiently to the surface plasmons.[67]

Johannsmann and Lemke reported an IR resonant filter in the wavelength range of 30-200 μm for use in a space-based telescope.[68] The process and structural properties are very similar to Jefimov's work discussed above. Several different meshes were prepared with variations in the dimensions of the cross shapes and their spacing. These structures allowed transmission of specific broadband wavelengths at ~80% transmission. Changing the size of the crosses and their spacing allowed the structures to be tuned for a specific wavelength and also for the transmittance peak to be broadened or narrowed accordingly.

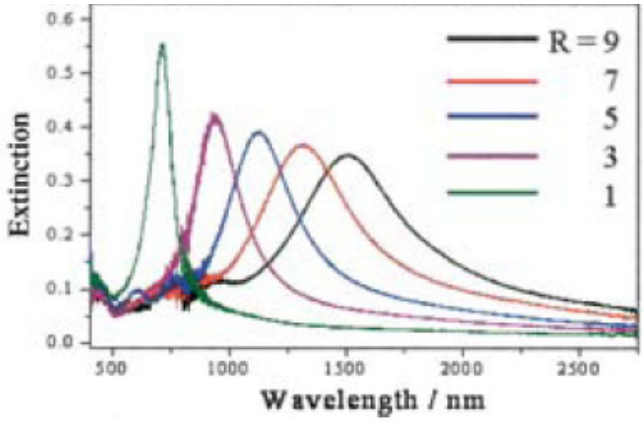

Figure 1.25: Extinction spectra of gold nanoblocks with different aspect ratios (R) for light polarized parallel to the direction of the rectangular blocks' elongation.[60]

Ueno *et al.* fabricated gold nanoblocks with aspect ratios varying from 1 to 9 onto a glass substrate using EBL. The transverse and longitudinal plasmon absorption bands were sensitive to the rod size, aspect ratio, and alignment.[60] For example, blocks with an aspect ratio of 9 have a broad absorption band at ~ 1500 nm whereas blocks with an aspect ratio of 1 had a much narrower, more intense absorption band with a peak at ~ 700 nm. Figure 1.25 shows the absorption spectra for rods of different aspect ratio. This figure also shows aligned rods of set aspect ratio hold great potential as an optical absorption filter.

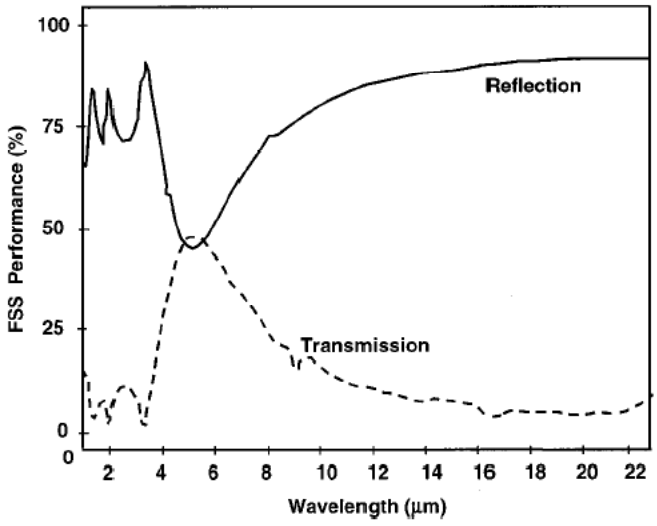

Figure 1.26: Performance of gold FSS at normal and near normal incidence.[61]

A frequency selective surface (FSS) structure was fabricated that could function as an optical filter. Fabrication was achieved using UV lithography with the use of a phase shift mask.[61] The phase shift mask allowed for resolution enhancements to fabricate

feature sizes as small as 50 nm. The structure contained circular or hexagonal shaped cylinders within a gold layer. Figure 1.26 shows the optical properties of the structure. The resonant wavelength, observed at about 5 μm, can be altered by changing the structure and dimensions of the cylinders or the thickness of the gold film. It was suggested that it is possible to increase the transmission at the resonant wavelength above 50% by changing from silicon to a more transparent substrate.[61] This structure is potentially useful in the communications industry as it filters almost all radiation except for that of the resonant band.

Colloidal lithography was used by Hanarp *et al.* to fabricate short range, ordered arrays of nanometre sized gold disks. The dimensions of the gold disks and spacing between the disks combine to vary the optical properties of the material. With increasing aspect ratio, a linear increase in plasmon resonance wavelength and an approximately constant peak-width was observed.[69] The sensitivity of the plasmon resonance wavelength to changes in surrounding refractive index is substantially increased for more elongated disks, suggesting that these structures may have potential use in sensors based on the localized surface plasmon resonance change with refractive index.[69]

These examples of optical filters typically work by absorbing a small wavelength range whilst leaving the majority of the remaining spectrum untouched. Metal nanoparticles are very promising for use in optical absorption filters as some metal particles including gold, silver, aluminium, copper, manganese, potassium and sodium have strong discrete peaks which provide strong absorption over their surface plasmon resonance wavelength (see Section 1.3. Surface Plasmon Resonance).

1.4.3.2. Diffraction gratings and photonic crystals

Photonic crystals are periodic materials that allow light to be controlled and manipulated. The utilization of an optical band-gap for optoelectronic applications is believed to require three dimensional photonic crystals that permit full directional control of the light, which holds information. Nanolithography has the potential to create photonic crystals although fabrication may take longer than other methods.

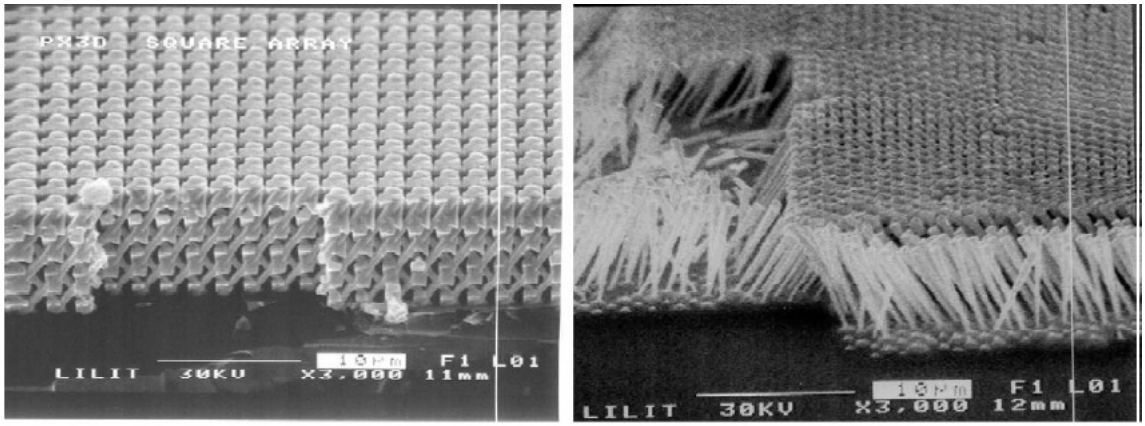

a b

Figure 1.27: SEM image of a (a) 3D nickel lattice structure obtained by fourfold X-ray exposure of a square pattern array. (b) Yablonovite gold lattice obtained by threefold exposure of a triangular pattern array.[62]

Romanato *et al.* utilised X-ray lithography to fabricate three dimensional photonic crystals using gold and nickel (see Section 1.4.1.4. X-ray nanolithography). Soft X-ray lithography was used as it provides a high lithographic resolution. A tilted illumination of a symmetric array pattern (through a mask) generates an array of tilted pillars. When another exposure is performed after a rotation of the mask and sample system, a second array of pillars is generated. If the rotation angle is an angle of symmetry, the second pillar array intersects the first one at 3D lattice points.[62] Repetition of this procedure over the entire mask pattern results in the generation of the full three dimensional lattice.[62] For example in the case of square symmetry four exposures in 90^{o} steps generate a cubic lattice. Figure 1.27 shows two patterns created by this technique. Figure 1.27 (a) shows a SEM image of a cubic nickel lattice. Figure 1.27 (b) shows the Yablonovite gold structure, generated by three 120^{o} step exposure of an equilateral triangle mask array. Preliminary optical characterisation of a cubic metallic lattice showed the presence of resonance features, which are likely to be associated with the excitation of the 3D photonic bands of the metallic sample.[62]

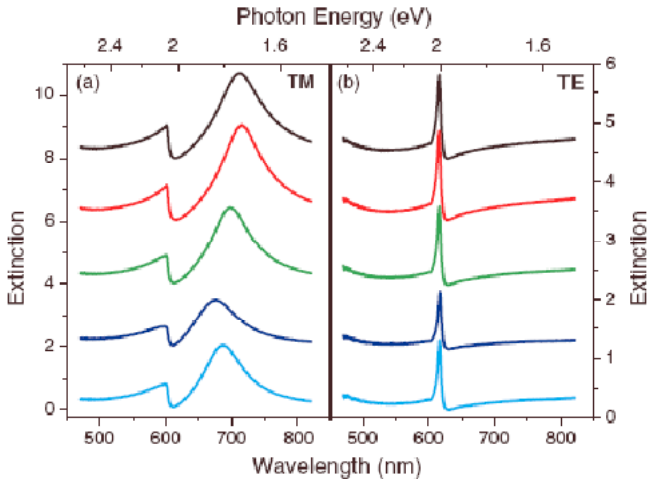

Figure 1.28: Extinction of a gold grating, taken at different positions on the sample (a) TM polarization, (b) TE polarization.[105]

Guo *et al.* recorded the optical spectra of gold diffraction gratings. It was possible to excite a particle plasmon (see Section 1.3. Surface Plasmon Resonance) only when the incident light polarization was perpendicular to the grating lines (Transverse Magnetic (TM) polarisation). Hence, the coupling effect between waveguide mode and gold-particle plasmon resonance appears only in TM polarisation. The waveguide in this case is the ITO layer beneath the gold diffraction gratings. For Transverse Electric (TE) polarisation (parallel to the grating lines) only the waveguide can be excited.[105] These effects are evident from the data shown in Figure 1.28. Increasing the period of the gold grating structure shifts the lower polarisation branch peak (the longer wavelength peak in Figure 1.28 (a)) towards a longer wavelength due to the larger wire width. The extinction characteristics investigated by Guo *et al.* indicate that strong coupling exists between waveguide mode and particle plasmon appears when the waveguide is tuned into the plasmon resonance.[105]

Lamprecht *et al.* investigated the influence of grating effects on plasmon excitations in gold nanoparticles produced by EBL. Results show an increase in plasmon damping in the transition region from evanescent to radiative fields (500 nm – 600 nm grating distance) of the first grating order on the substrate side. A strong red-shift of approximately 50 nm in the plasmon resonance wavelength was also observed in this transition region. The shift and broadening of the plasmon resonance are fundamentally determined by the periodicity of a square array.[81] The dipolar fields of neighbouring particles are superimposed with their respective phase shifts, which depend on the distance between the particles. Thus the geometrical arrangement of resonant metal

nanoparticles in their respective far field regions significantly affects the individual particle plasmon and thus the plasmon near-field characteristics.[81]

For single layer sub-wavelength metal grating polarisers with fixed periods, polarisation anisotropy increases as the wavelength increases.[120] Yu *et al.* fabricated a dual layer grating which shows an extinction ratio maximum in the visible region, indicating resonance occurs between the two metal grating layers. Resonance between the layers helps to enhance the polarization selectivity for wavelengths close to 630 nm. Due to resonance effects, high polarization extinction ratios at certain wavelengths can be more easily achieved with a double-layer metal grating structure.[120]

1.4.3.3. Waveguides

Planar waveguides enable integrated optical components by controlling and directing the propagation of light. The geometry of planar waveguides is limited because of radiation leakage that occurs at sharp bends.[79] Plasmon waveguides guide electromagnetic energy in the visible and near-infrared region of the electromagnetic spectrum. Excitation at or near plasmon resonance allows radiation to couple to nearby particles. In the case of plasmon waveguides there is a line of nanoparticles that can transfer the energy from one particle to another.

Maier *et al.* used EBL and AFM manipulation to construct functional plasmon waveguides. Figure 1.29 (a) shows a 60^{o} corner structure fabricated using EBL on ITO-doped glass. The gold particles are 50 nm in diameter and are separated by 75 nm (centre to centre). Figure 1.29 (b) shows a linear plasmon waveguide using 30 nm colloidal gold nanoparticles. The line was constructed by aligning randomly deposited gold nanoparticles using an AFM tip.[79] These plasmon waveguide show potential for use in nanoscale integrated optics.

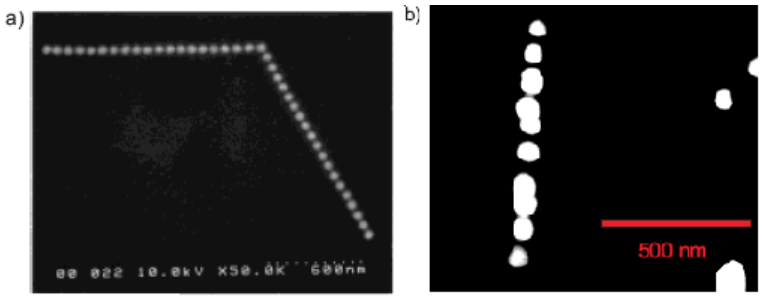

Figure 1.29: (a) SEM image of 60^{o} corner in a plasmon waveguide fabricated by EBL. (b) Straight plasmon waveguide assembled using contact mode AFM and imaged using non-contact AFM.[79]

1.4.4. Conclusions

Lithography techniques play an important role in the fabrication of functional devices based on nanoscale structures of the precious metals. Once a pattern or design has been identified by simulation or calculation, it can be fabricated using one or more of the technologies that described here. Each of the lithography systems is based on fundamentally different physical properties, implying that each technique will exhibit unique properties. Gold is a good choice of metal for use in nanoscale optical devices as it is relatively inert, easily deposited, and has surface plasmon resonance that can be tuned by dimensional control from the mid-visible to the near-infrared.

1.5. Conclusions

Gold nanostructures are one of the most versatile materials at the nanoscale. Gold nanorods in particular warrant further study as they contain useful optical properties with the option of absorption peak design. Potentially, gold nanorods allow a large range of optical applications and optical based devices. Gold nanorods of specific aspect ratios are consistently produced, using either wet chemistry or physical vapour deposition means.

Windows are responsible for the majority of energy transfer into or out of a building. Insulation is placed on walls, roofs, and recently coatings have been added to windows to increase or decrease energy transfer. These coatings have a huge market; the majority of new commercial buildings, and many residential windows include some sort of energy saving coating. There are many different types of energy saving coatings that have different performance characteristics that have been designed for various climates. More efficient window coatings have significant potential as a commercially viable product and thus require research into potential spectrally selective materials.

Due to their controllable optical properties, gold nanorods have great potential for use as an energy saving window coating. This thesis looks into the effectiveness of gold nanorods as a basis for a novel energy saving window coating.

Chapter 2:

Computational Modelling of the Optical Properties of Gold Nanostructures

Chapter 2: Computational Modelling of the Optical Properties of Gold Nanostructures*

2.1. Introduction

This chapter presents the results of computational modelling of the optical properties of various gold nanostructures. Computational modelling is often used to predict and understand experimental results. In this chapter that is also the case and the optical properties of various gold structures are investigated experimentally in Chapter 3. In this chapter, the calculated optical properties of gold nanostructures are presented and the surface plasmon resonances and the resulting electric and magnetic fields of the nanostructures are investigated.

There are numerous computational modelling programs available but the software should suit the problem at hand. For example, exact solutions can be found using Mie scattering and by analytically solving Maxwell's equations for the scattering of electromagnetic radiation by special geometries; spheres, shells and small ellipsoids. However, there is no generally applicable analytical solution for arbitrary-shaped nanoparticles. For more complex shapes the exact solution becomes too complex and it is common to resort to numerical calculations, often based on the discrete dipole approximation (DDA).[154-156]

The software chosen for the current work; the DDSCAT software of Draine and Flatau[154,155,157] (DDSCAT: Discrete Dipole Approximation for Scattering and Absorption of Light by Irregular Particles) which applies the DDA to calculate the scattering and absorption of electromagnetic waves by targets with arbitrary geometries and complex refractive indices. The DDA approximates the target by an array of polarisable points over which the electromagnetic scattering of an incident periodic wave is essentially solved for each of these points.[155,157] The target geometries that the

* Sections of this chapter have been published. (M. Cortie, N. Stokes, A. McDonagh, 2009, 'Plasmon resonance and electric field amplification of crossed gold nanorods' *Photonics and Nanostructures – Fundamentals and Applications*, **7**, 143)

program supports include ellipsoids, regular tetrahedra, rectangular solids, cylinders, hexagonal prisms and more. The primary advantage of the DDA is that it is completely flexible regarding the geometry of the target, limited only by the interdipole separation and the wavelength. The volume of solid material in the targets processed by this software is expressed in the form of an effective radius, a_{eff}, defined as the radius of the sphere with the same volume as that of all the solid material in the target. Agreement between calculation and experiment is good, provided the dipole spacing is very small relative to the wavelength.[158-162] The quality of the DDA is determined by the density of the dipole array, and a compromise is sought between accuracy and computational expense. DDSCAT calculates (i) the absorption efficiency factor, (ii) scattering efficiency factor, (iii) extinction efficiency factor, (iv) phase lag efficiency factor, (v) 4x4 Mueller scattering intensity matrix, (vi) radiation force efficiency vector and (vi) the radiation torque efficiency vector.[155,157] The current version of DDSCAT (7) is also able to calculate electric and magnetic fields at specific locations.[155]

2.2. Experimental Methods

2.2.1. Target selection and design

The first stage when calculating the optical extinction properties of a material is to select and design the structure to be investigated. In this work rods of different aspect ratios, background and effective radii are investigated along with more complex structures comprised of two intersecting rods in an X or V-shaped configuration.

Each target structure requires a text file that lists the positions of the dipoles and a parameter file that describes the DDSCAT parameters including the number of dipoles, wavelengths, size and polarisation to be calculated. Also required for any calculations is a dielectric table showing the refractive index of the desired material in whichever background is selected. Most of the structures in this work contain gold in a vacuum or in water.

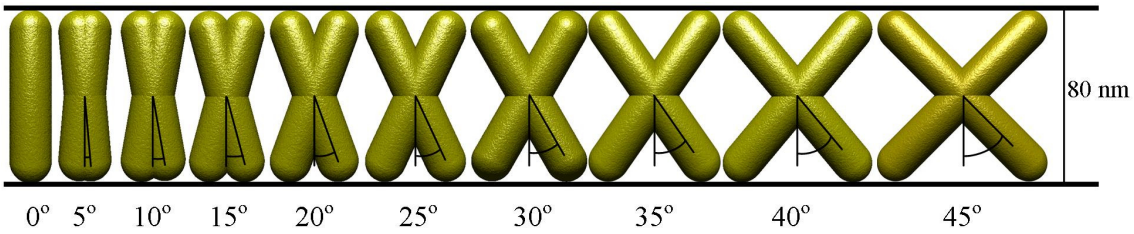

Figure 2.1: Diagram of the generated X targets showing the increase from left to right of the rod length and angle.

A range of generated targets is shown in Figure 2.1. The shapes consist of crossed pairs of rods that were fused at their centres with an angular rotation 2α away from parallel alignment. The length of each of the crossed-rod shapes was 80 nm, and the constituent rods had a diameter of 20 nm. It can be seen that as the angle between the crossed rods is increased the length of the rods that make up the target also increase. The exact geometries are listed in Table 2-1. Comparing the X structures to the rod shaped structures requires several different rod aspect ratios due to the increasing arm lengths as the angular rotation is increased. The visible and near-infrared spectra of crossed-rod structures were calculated for the full range of α (0° through 45°). The nature of the plasmon resonances that occurred was further investigated using animations of the dipoles and calculations of their internal and external electric fields.

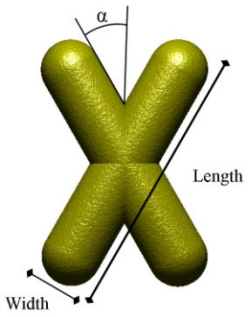

Figure 2.2: The different aspects of the X structures.

Table 2-1: Dimensions of the single rods, which make up the X structures as shown in Figure 2.2. All rods have a width of 20 nm.

Angle, α	**0°**	**5°**	**10°**	**15°**	**20°**	**25°**	**30°**	**35°**	**40°**	**45°**
Length, nm	80	80.3	81.2	82.8	85.1	88.3	92.4	97.7	104.4	113.1

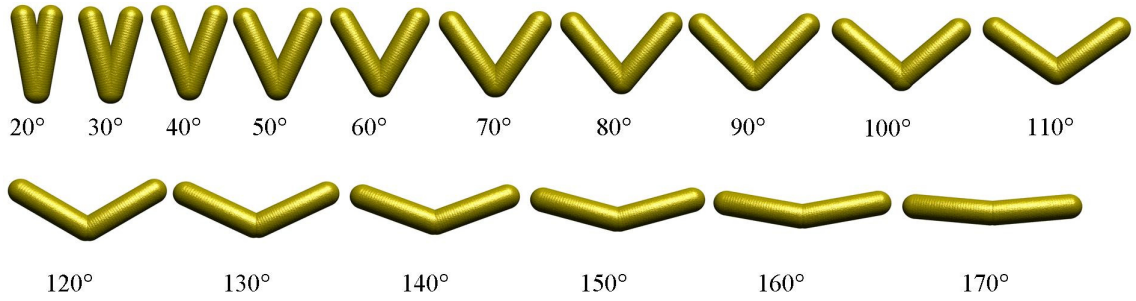

Figure 2.3: Designed V structures, with increasing angle. Individual arms are 80 nm by 20 nm.

Another type of crossed rod structure considered was the V shaped structure with both arms acting like individual rods joined at the apex. Figure 2.3 shows the different angles of V structures made. The angle between the rods was increased in 10° steps between 0° and 180° to investigate the optical extinction properties across the all possible ranges. These structures were investigated in a water background. It should be noted that a specific V structure has been modelled by Stockman *et al.* to investigate the spaser excited electric fields, perpendicular to the structure plane.[163,164]

DDSCAT was then used to calculate optical extinction properties. Figure 2.4 shows several different orientations of the X targets that are possible with respect to the incoming wave vector, ***k***, the direction of electric field, ***E*** and the direction of incoming

magnetic field, ***B***. A longitudinal resonance (Figure 2.4 (a) and (b)) would be most prominent when the long axis of the structure is perpendicular to the ***k*** vector and parallel to ***E*** while a transverse resonance (Figure 2.4 (c) and (d)) would be most prominent when the long axis of the structure is parallel to the ***k*** vector of the light. There is also the possibility of aligning one of the arms of the target with the electric field (Figure 2.4 (e) and (f)) and, finally, polarizing the electric field perpendicularly to the plane of the target (Figure 2.4 (g) and (h)). Note that there are two options for ***k*** and ***B*** for any given orientation of ***E***. In general, however, the extinction efficiency of a nanoscale target depends almost entirely on the orientation of ***E***, with the direction of ***k*** and ***B*** being comparatively unimportant.[165]

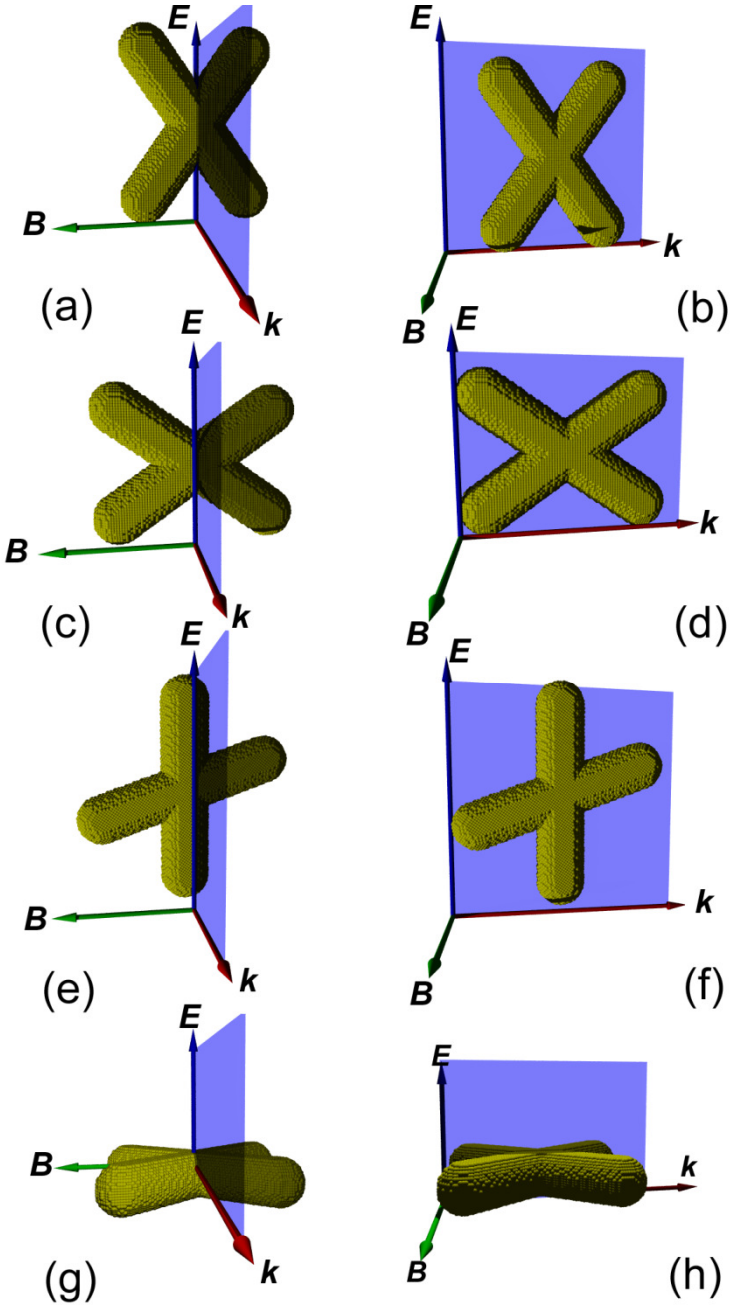

Figure 2.4: The different orientations of the electric and magnetic field that are possible for a crossed-rods shape. (a) longitudinal resonance with ***B*** in the plane of the target (b) longitudinal resonance with ***B*** out-of-plane of the target, (c) transverse resonance with ***B*** in-plane (d) transverse resonance with ***B*** out-of-plane, (e) electric field oriented along one arm with ***B*** in-plane (f) electric field oriented along one arm with ***B*** out-of-plane (g) short transverse resonance with ***B*** in longitudinal direction of target (h) short transverse resonance with ***B*** in transverse direction.

The orientations investigated for the V targets are shown in Figure 2.5 with the applied electric field, ***E*** (a) out of the structure plane, (b) across the V structure and (c) along the V structure.

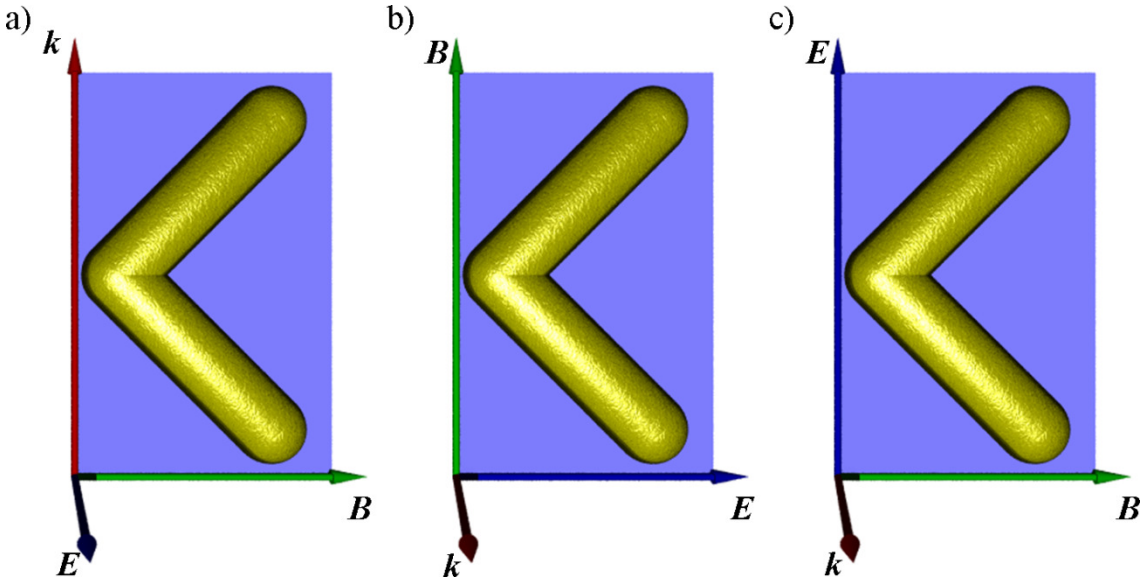

Figure 2.5: The different orientations of the electric and magnetic field possible for a V-rods shape. (a) ***E*** coming out of the page, (b) ***E*** traversing the structure and (c) ***E*** along the longitudinal aspect of the structure.

The method and implications of DDSCAT calculations with respect to multipole resonances is worth considering. While convergence at wavelengths at which a single dipole resonance occurs is readily established with the formation of a single extinction peak at each resonance, Figure 2.6 (a) and (b), convergence was slow at the wavelengths at which two or more resonances were simultaneously active, unless an exceedingly fine dipole spacing (for example <0.5 nm) was used. The presence of a spurious bifurcated extinction peak for complex targets in which two resonances were simultaneously active, and their fusion into a single peak when smaller dipole spacings were used, Figure 2.6 (c), was one of the symptoms of a lack of convergence. The reason for this phenomenon is that *individual* dipoles in the target can only take on a *dipole*-type harmonic oscillation (by definition) in the numerical method used. Therefore, the only way in which the numerical method used can simulate a *multipole* resonance is by mixing domains of different dipolar resonances together so that the ensemble generates the appropriate response. In the present targets these domain mixtures take the form of alternating layers of dipoles, each corresponding to one of the components of the multipole resonance, and with differing phase and amplitude with

respect to the planar wavefront of the exciting radiation. Such dipole domains, Figure 2.6 (d), are absent from simulations of simple dipole resonances, Figure 2.6 (b). It is the collective interaction of these domains that simulates the multipole electric field oscillation external to the target. Therefore, stable convergence of the numerical solution for multipole resonances requires smaller dipole spacing's than would be the case for simulations of simple targets, such as nanorods.

Initially the X structures were run at different aspect ratios, and as such had different effective radii and ultimately different gold volumes. However, in later work the effective radii for selected samples was adjusted such that the gold volume was the same. Other calculations run include a single rod from all the X structures, allowing comparison of rods with X's. The interaction between 2 rods (AR4) end-to-end and side-to-side was also investigated.

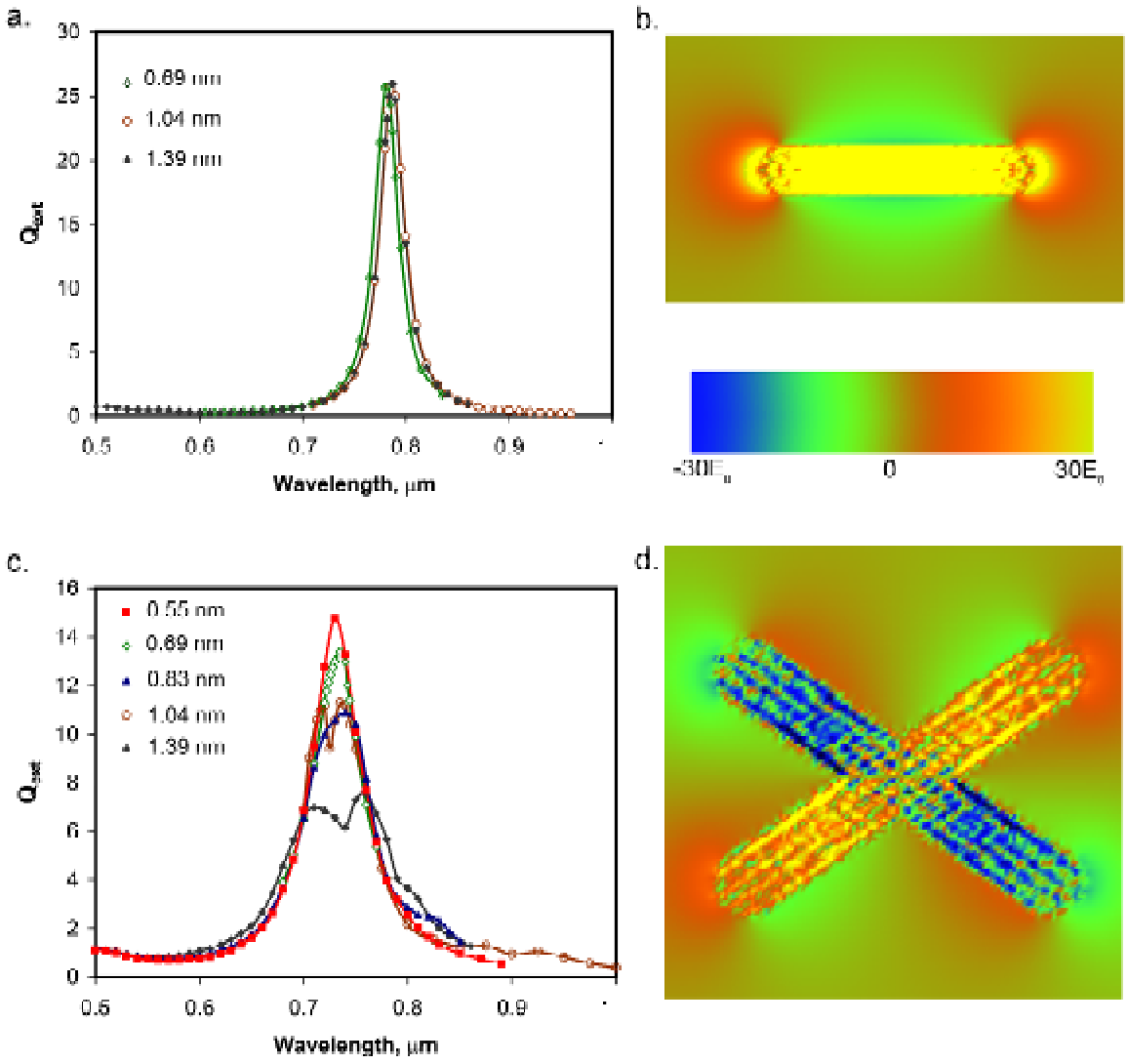

Figure 2.6: Effect of dipole spacing on the convergence of the DDA calculations, (a) dipole resonance in a rod of 98 nm length and 20 nm diameter inclined at 35º to *k*, simulated using dipole spacing's of 0.69, 1.03, and 1.40 nm, showing that calculations performed with a dipole spacing of <1.4 nm produce an extinction peak at 785 ± 3 nm, (b) *x*-component of electric field at θ=90º and λ=782.5 nm for the simple rod shown in (a) revealing the absence of dipole domains, (c) multipole resonance obtained from two of the rods shown in (a) fused together at a half angle of 35º showing that convergence now requires a dipole spacing <0.58 nm, (d) *x* -component of electric field at θ=90º and λ=735 nm for crossed rod target with α=35º showing how the internal field of the target with the multipole resonance contains alternating domains of dipoles. The same dipole spacing (0.69 nm) and colour scheme for the field intensities was used for both (b) and (d)).

2.2.2. Target modelling

Following the generation of target files, the models were investigated using three versions of the DDSCAT program according to the desired output. Standard DDSCAT 6.0 was generally used to produce the optical extinction properties of the specified target. A dipole version of DDSCAT 6.0*, which was edited such that the dipole vectors generated within the program were also produced as an output allowing investigation of dipole movements with respect to the phase of the incoming light. DDSCAT 7.0 was used for the generation of electric field and magnetic field properties surrounding the target as well as extinction properties for very small dipole volumes and higher resolution calculations. The simulation of periodic (1D) arrays of targets was achieved using a version of DDSCAT 7.0 modified by M Cortie to accept an arbitrary periodic target.

The initial step was to run a series of calculations using wavelengths between 300 and 1000 nm in steps of 10 nm. This wavelength range covers the visible and near-infrared spectrum, and features such as absorption maxima can be identified for further investigation. Using a dipole volume of ~1 nm^3 allowed a relatively quick calculation to determine the approximate optical spectra. Further investigation of the peaks was undertaken if required using smaller wavelength steps or reduced dipole volume along the peaks. Also, the initial spectra may show that further investigation is required at wavelengths beyond 1000 nm. The initial spectra were designed to stop at 1000 nm due to the increasing time constraints on the calculations at longer wavelengths.

Targets with potentially more interesting optical properties were selected and if required re-run (particularly across the longitudinal plasmon peak) with more dipoles allowing convergence to occur. For the X structures, the rod (0°) and X's (15°, 25°, 35°, 45°) were selected to cover a good range with much smaller dipole volume. The V structures on the other hand, were selected to cover a number of possible angles; acute angle (60°), right angle (90°), obtuse angle (120°) and very obtuse angle (150°). The structures often had to be re-run with increasing numbers of dipoles for a particular polarisation before convergence occurred. After convergence had occurred for all

* Edited by Mr Martin Blaber and Prof. Michael Cortie at the University of Technology Sydney.

targets, correct peak maximums were found and used as the input wavelength for both dipole movement calculations and electric field calculations.

2.2.3. Data processing

Some processing of the calculated data was required although the calculated optical extinction properties required no further processing. Calculated dipole data was processed using a custom program,* which determined all the dipoles in a set 2D plane and then rendered each dipole's orientation and length at a specific phase value of the incoming monochromatic light wave. To generate sufficient information about the dipole motions a range of phases is required. Different images were generated of the position of the dipoles in 10° phase steps, allowing for collation into a movie showing dipole movement and the different multipole resonances that occur.

Similarly, the electric field calculations were processed using a program* to obtain electric field intensity plots over different applied phases. Compilation of a selection of these images (minimum every 10°) produces a movie showing the magnitude of the external electric field with regard to the incoming wave.

* Developed by Prof. Michael Cortie at the University of Technology Sydney.

2.3. Results and Discussion

2.3.1. Calculated properties of rod shaped structures

Rods are one of the most widely used and investigated structures and, as such, they are useful as reference shapes for experimental investigations (see Chapter 4 and 5) or to investigate basic optical effects of structure distances, gold amount and orientation. Rods were also chosen to compare both X and V structures as they are the basis from which the more complex structures were made.

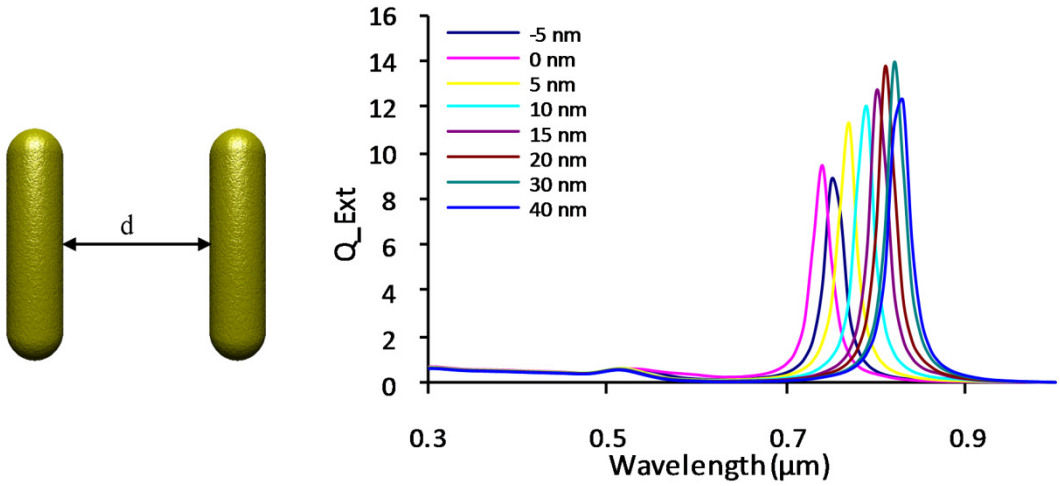

Figure 2.7: Optical extinction spectra for two rods aspect ratio (AR) 4 at the side-by-side separation distances listed. Each rod is 20 nm wide, 80 nm long and the hemispherical end radius is 10 nm.

Figure 2.7 shows the optical extinction spectra of two rods side-by-side separated at various distances. The optical properties agree with previous reports[36] such that as the rods are side-by-side, d = 0, the plasmon resonance couples between the rods making the two-rod structure act as a single rod with twice the width and AR2. As the separation distance between the rods increases, the amount of coupling between the rods decreases and the apparent rod aspect ratio increases from 2 to 4 resulting in the longitudinal plasmon resonance red shifting. Theoretically, when d = -5 nm (corresponding to a 5 nm overlap) then the width of the rod structure is less than when d = 0 resulting in an increased aspect ratio and the longitudinal plasmon resonance red shifts.

Figure 2.8 shows the plasmon coupling effect of two rods separated end-to-end at varying distances. The general trends shows that as the rods come closer together the longitudinal plasmon resonance couples between the rods and the peak is red shifted. Similarly to the side-to-side coupling, as the rods become closer together they couple to form a much longer apparent rod which increases the apparent aspect ratio and causing the longitudinal peak to red shift. Figure 2.8 shows that the peaks for the separation distance of 20 nm is red shifted compared to the 15 nm separation and a similar occurrence for the 40 nm and 30 nm separation. It is thought that this occurs due to differing numbers of dipole layers along the ends or sides due to geometric sampling at the dipole spacing used and not due to convergence problems.

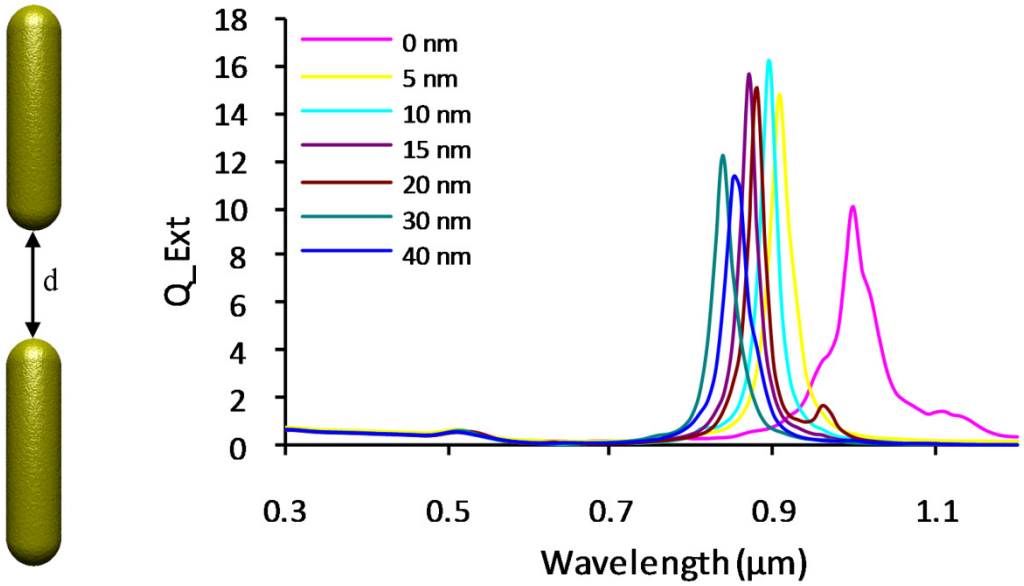

Figure 2.8: Optical extinction spectra for two rods (AR4) placed end-to-end at the distances listed.

Figure 2.9 shows the effect of rod aspect ratio on the position of the longitudinal plasmon resonance peak. The aspect ratios investigated are consistent with the X lengths shown in Table 2-1. In agreement with published work,[32] the longitudinal plasmon resonance red-shifts with increasing rod aspect ratio.

The optical properties of the rods corresponding to the X rod orientations, listed in Table 2-1, are shown in Figure 2.10. Rods with angular rotation, α, of 0°, 10° and 15° all correspond to the peak overlapping the AR4.14 longitudinal plasmon peak which corresponds to the α=15° rod. The longitudinal plasmon resonance is not normalised in Figure 2.10, and as such the orientation of the rods causes the optical extinction properties to vary according to the relation to the incoming light polarisation. In this

case, the polarisation investigated had maximum optical extinction properties for the investigated rods at 45°. It is also shown that the rods angled at 0° do not have a longitudinal plasmon resonance at the polarisation investigated.

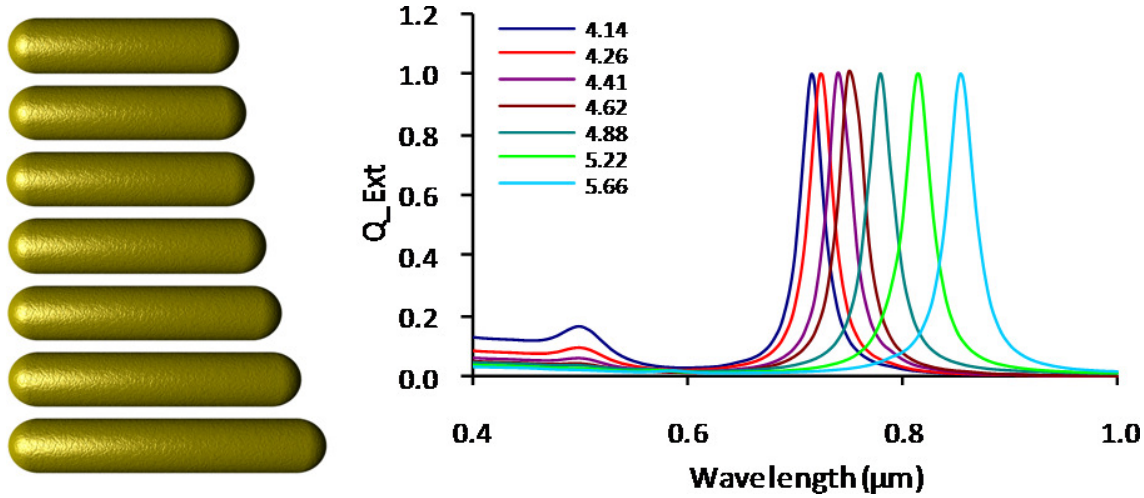

Figure 2.9: Normalised optical spectra of gold nanorods with different aspect ratios.

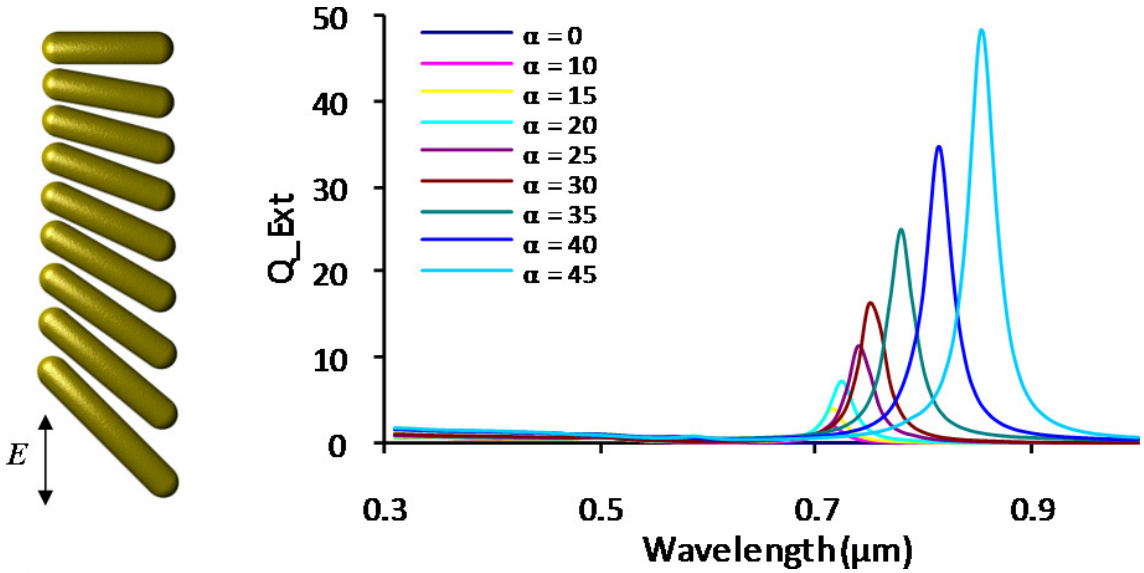

Figure 2.10: Single rods with the same angle and direction as in the X structures in Figure 2.1 with polarisation applied along the α=45° structure.

Calculations were undertaken to model structures that could be fabricated by experimental methods. Electron beam lithography (see Chapter 3.) was used to prepare rods with varying aspect ratios. Rods produced using EBL differ from wet chemistry produced rods in that the edges are not rounded and the shape is more accurately described as a rectangular prism. For this reason a rectangular prism was investigated for comparison with the optical properties of the produced EBL gold nanorod arrays. The structure is shown in Figure 2.11 with dimensions identical to average dimensions

found from the SEM image of EBL produced rods shown; 175±5 nm long, 41±3 nm wide and 20 nm thick. The calculated optical properties are also shown with the longitudinal peak positioned at 950 nm which coincides within the desired range of infrared light absorption for window coatings.

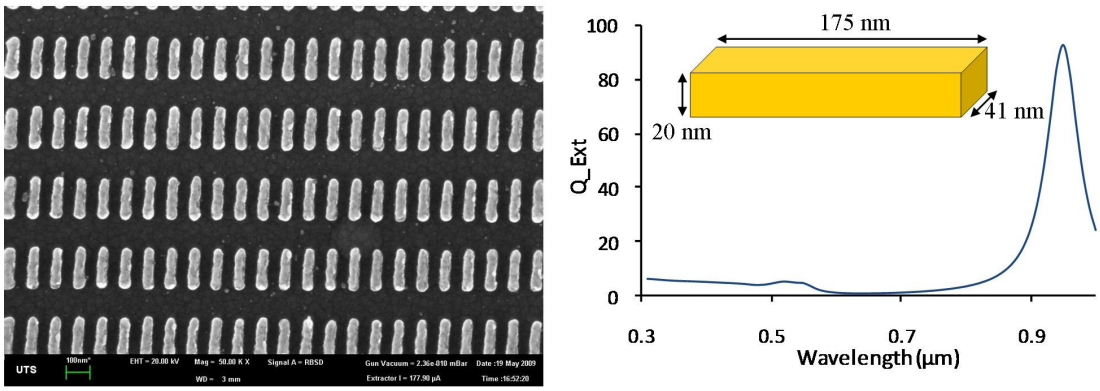

Figure 2.11: SEM image of the gold nanorods produced by EBL (see later) with the average dimensions shown on the schematic, and the corresponding calculated optical extinction properties.

Computational modelling of rods was also used to investigate the accuracy of both the ranges of rod aspect ratios and the optical properties of wet-chemically produced monodisperse solutions. A selection of wet-chemically produced rods was imaged using a SEM and the aspect ratios were measured. Comparison of the experimental optical data with calculated extinction spectra for gold nanorods of different aspect ratios revealed that the measured extinction bands are much broader than that expected for a monodisperse sample of rods. The full width half maximum of the longitudinal peak of the measured spectrum was more than five times greater than for the single simulated rod. To investigate this, the measured spectrum was simulated by combining the weighted average of five rod aspect ratios initially and increasing the amounts of each until summation of the calculated spectra reproduced the experimental one. The measured rods were initially separated into five different aspect ratios ranges, and the average rod dimensions within this range were calculated for the optical properties. The optical properties were then weighted according to the number of rods measured within each range allowing the optical spectra to serve as a comparison with the measured spectra of the initial rod solution. The calculated optical spectra are shown in Figure 2.12. The longitudinal peak consists of five peaks corresponding to the five rod aspect

ratios calculated. This indicates that the rod aspect ratio groupings are too large and require more than five shapes of rods to approximate the overall peak size and shape.

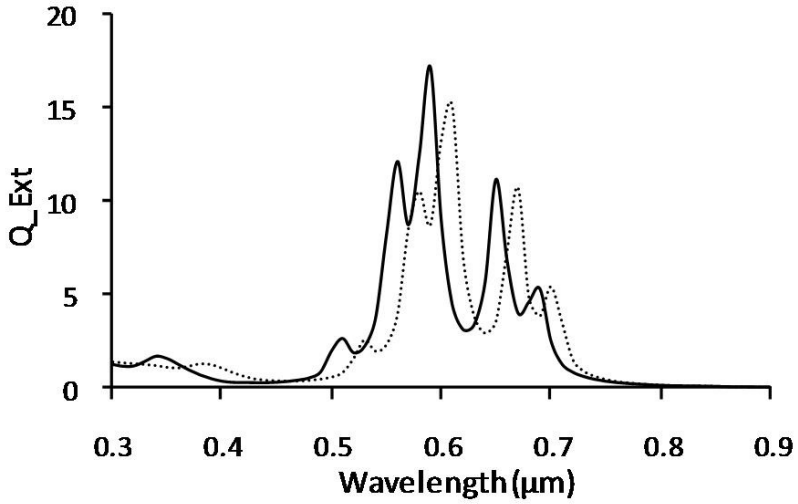

Figure 2.12: The weighted optical extinction spectra of 5 rods of different aspect ratio in water (dotted line) and poly vinyl alcohol (solid line). The 5 main peaks correspond to the longitudinal peaks of the 5 different aspect ratio rods.

As the number of spectra increases, the minima in Figure 2.12 are filled producing more realistic spectra. Twenty five rod aspect ratios were required to produce the smooth spectrum shown in Figure 2.13. Figure 2.13 shows the simulated spectrum together with the experimental spectrum. The calculated extinction (dashed line) is in close agreement with the measured extinction spectrum. More simulations are required outside the aspect ratio range used for complete accuracy; however, the peak position and shape are accurate.

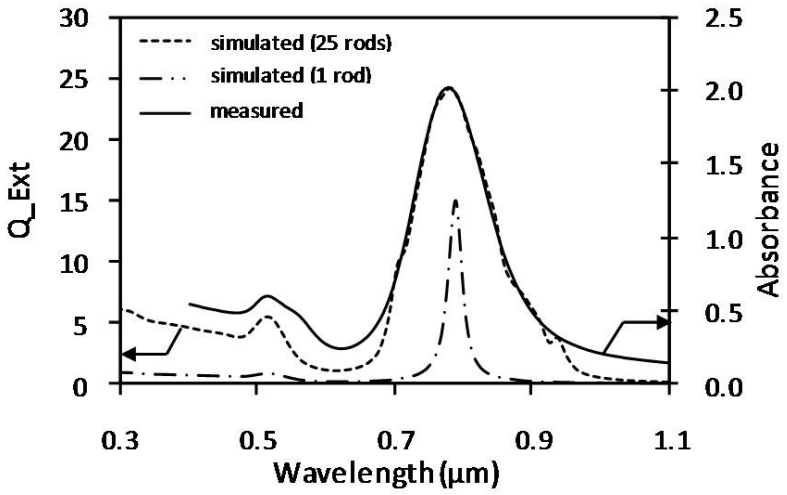

Figure 2.13: Comparison of optical properties between a gold nanorod solution and calculated optical properties of many rods.

The peak wavelength of the simulated rods longitudinal plasmon resonance can be seen in Figure 2.14 as a comparison of the aspect ratio. There is a strong linear relationship between the aspect ratio and longitudinal peak position with very little variance. Therefore precise control over rod aspect ratio allows for mixtures of different aspect ratio rods to absorb over a desired wavelength range.

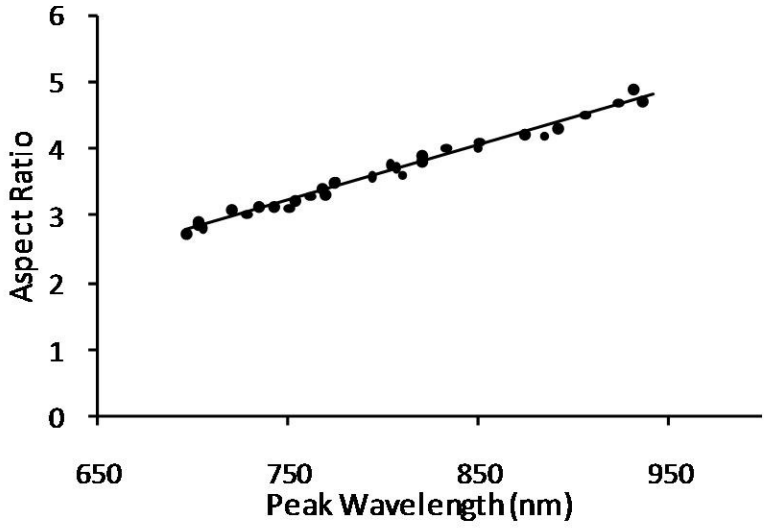

Figure 2.14: Calculated peak position compared to the rod aspect ratio.

2.3.2. Calculated properties of X structures

Optical extinction properties were investigated using two polarisations allowing for investigation of all possible surface plasmon resonances. Samples were calculated for wavelengths in the range 300 nm to 1 µm, with selected examples calculated to 1.1µm. The extinction properties are shown in Figure 2.15 for X structures in a water medium. There are at least two main resonances for each structure and as the angle between the component rods, 2α, increases, the largest plasmon resonance peak red shifts. To further understand the plasmon resonance, investigation of the structures with a single polarisation was required for each orientation. This also helped to confirm that convergence had occurred by removing peaks from other polarisations.

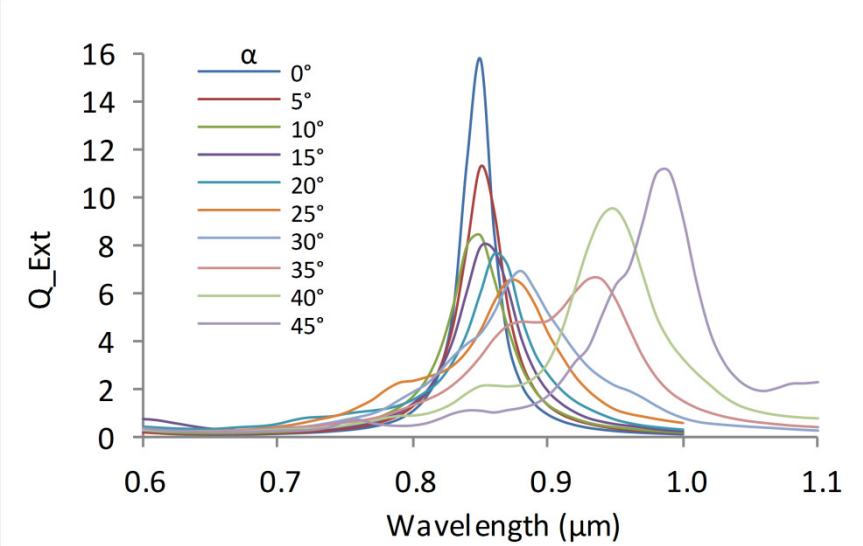

Figure 2.15: Optical extinction properties for all polarisations and all X angles investigated in water with the angle listed corresponding to half the angle between the two arms.

Figure 2.16 shows the investigation of the optical extinction properties of four specific X angles in a vacuum. By changing the surrounding medium from water, Figure 2.15, to a vacuum, Figure 2.16, all the peaks have been blue shifted in comparison but the changes due to the varying structure remain the same. Figure 2.16 (a) and (b) shows the optical extinction properties calculated at the orientations shown in Figure 2.4 (b) and (d) where ***E*** is directed along and across the long axis of the target structure respectively for selected instances of the crossed-rods shown in Figure 2.1. The first peak in Figure 2.16 (a) is generated by the simplest of the structures, a gold nanorod with an aspect ratio of 4 and a length of 80 nm. As the angle between the component rods, 2α, is increased for targets where ***E*** is directed along the long axis of

the structure, Figure 2.16 (a), the resultant plasmon resonance red-shifts and decreases in efficiency. The efficiency decrease is caused by the resonance along the arms being increasingly rotated away from the longitudinal orientation.

When ***E*** is directed across the long aspect of the target structure, Figure 2.16 (b), the extinction of the rod target is negligible due to ***E*** applied along the transverse aspect of the rod. The first peak shown in Figure 2.16 (b) corresponds to a crossed rod target with α=15º. As α is increased a new resonance appears at approximately 650 nm in targets where ***E*** is directed across the long aspect of the structure. This new resonance increases in efficiency and red-shifts as the arms of the target are rotated towards the longitudinal orientation.

Both resonances red shift as α is increased towards 45º, and converge to become identical at α=45º. A part of the red shift is clearly produced by the fact that the aspect ratio of the rods increased as α is increased, for purely geometric reasons (the length of the target in the *x*-direction is set at 80 nm, so when α=45º the rod will be $80\sqrt{2}$ nm, i.e. 113.1 nm long). This can be seen from the position of the peak wavelengths for individual rods of the relevant aspect ratio, superimposed on Figure 2.16, which also red shift. Importantly, the peak extinction of the crossed rods is always blue-shifted relative to single rods of the same aspect ratio. This last result can be contrasted to the result reported by Jain et al.[36] for adjacent, *non-intersecting* rods crossed so that α=45º. In that case the longitudinal resonances of the individual rods did not interact. The situation is different in the current case because the rods are fused together and the electric charge oscillation can freely propagate between the arms of the target.

The positions and origins of the transverse and longitudinal peaks on the sample with α=0º (the simple rod) are consistent with previously reported results,[7,135,136,140,166,167] with a transverse resonance at ~520 nm visible when ***E*** is directed across the long axis of the rod, and a longitudinal resonance at 700 nm when ***E*** is directed parallel to the long axis.

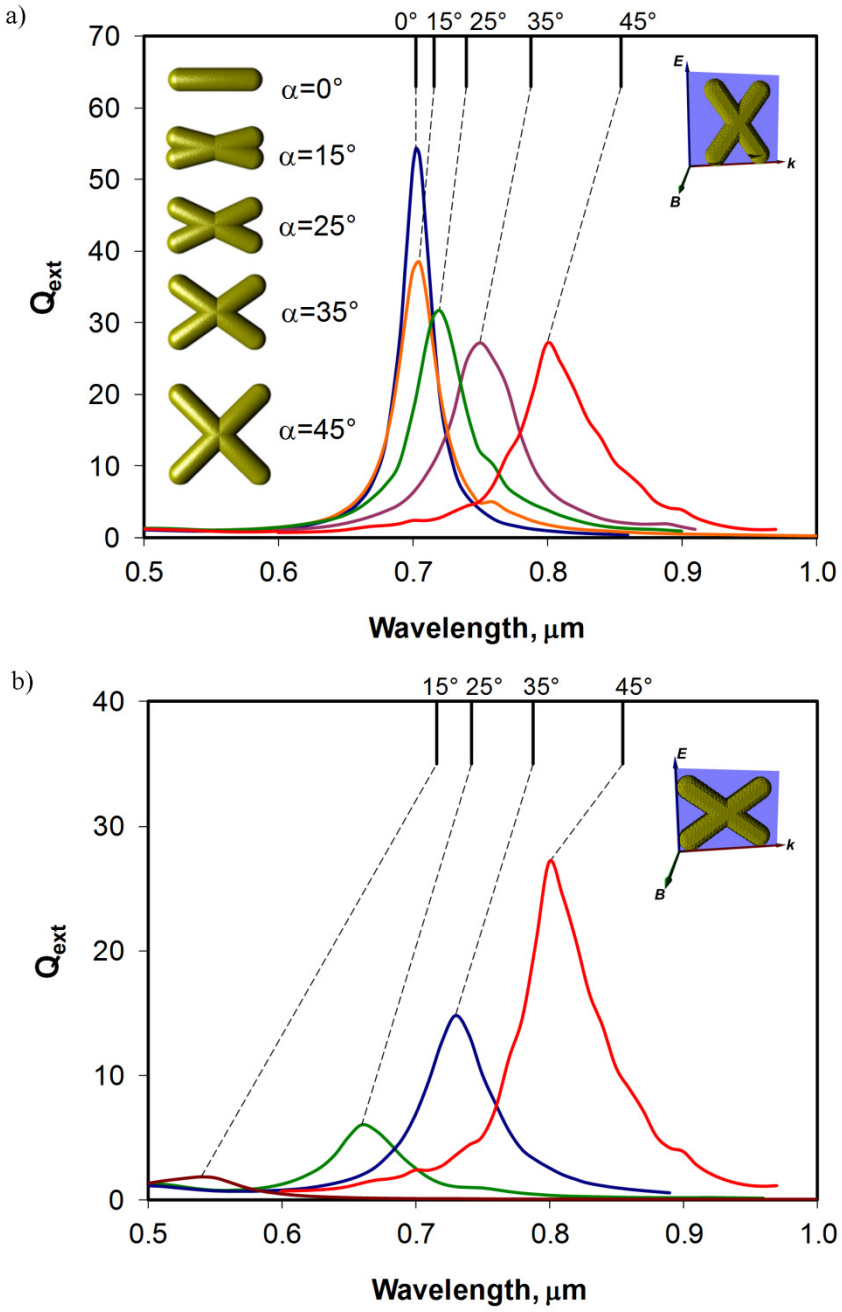

Figure 2.16: Effect of α on the calculated extinction efficiencies of X-rod targets in two different orientations in vacuum. (a) Orientation (Figure 2.4 (b)) and targets shown as inserts, (b) same targets as in (a) but with different orientation (insert Figure 2.4 (d)). Also shown on the graphs are the peak positions of the corresponding isolated, single rods.

Dipole and electric field animations were calculated for the relevant targets in order to elucidate the nature of these resonances. The 45° resonance will be considered first,

as it is in a sense the end member of the series and, furthermore, identical for orientations Figure 2.4 (b) and (d). Figure 2.17 (a)-(e) only shows snapshots of the field taken at a phase angle (θ) of 90º, *i*.e. ¼ of the way through a cycle. It is clear that the overall direction of the dipoles is back and forth along the direction of $\boldsymbol{E}$ (aligned here in the *y* or vertical direction). This produces an approximately dipolar field in each individual arm of the target and the *x*-components of the field must point in opposite directions in each of the arms, Figure 2.17 (a), since as charge flows upwards it must flow to the left in one arm and to the right in the other. The *y* components on the other hand all point the same way, Figure 2.17 (b). There was a negligible $\boldsymbol{E}_z$ component, and it is not shown. The overall magnitude of the $\boldsymbol{E}$-field is shown in Figure 2.17 (c). Overall, the resultant dipole vectors can be interpreted as shown in Figure 2.17 (d) for a phase angle of 90º. However, there was also a multipole component which was strongly developed in the vertices of the target. To visualise this in a quantitative sense we placed probe points at the positions shown in Figure 2.17 (e), and then graphed the overall field strength at the four probe positions as a function of time, Figure 2.17 (f). The resonances at position 4 lags that at position 1 by 19º (corresponding to 0.14 fs) due to time taken for the planar wavefront to cross the target from left to right. However, the fields at positions 2 and 3 are out of phase by 17º and 34º respectively with reference to that at position 1. Furthermore, by far the strongest component is aligned along the *y* direction. Overall, the extinction peak of the complete resonance is considerably blue-shifted compared to individual rods of the same aspect ratio. It is clear that the resonance observed is a new, hybridized multipole oscillation that developed from the superposition of the two individual resonances.

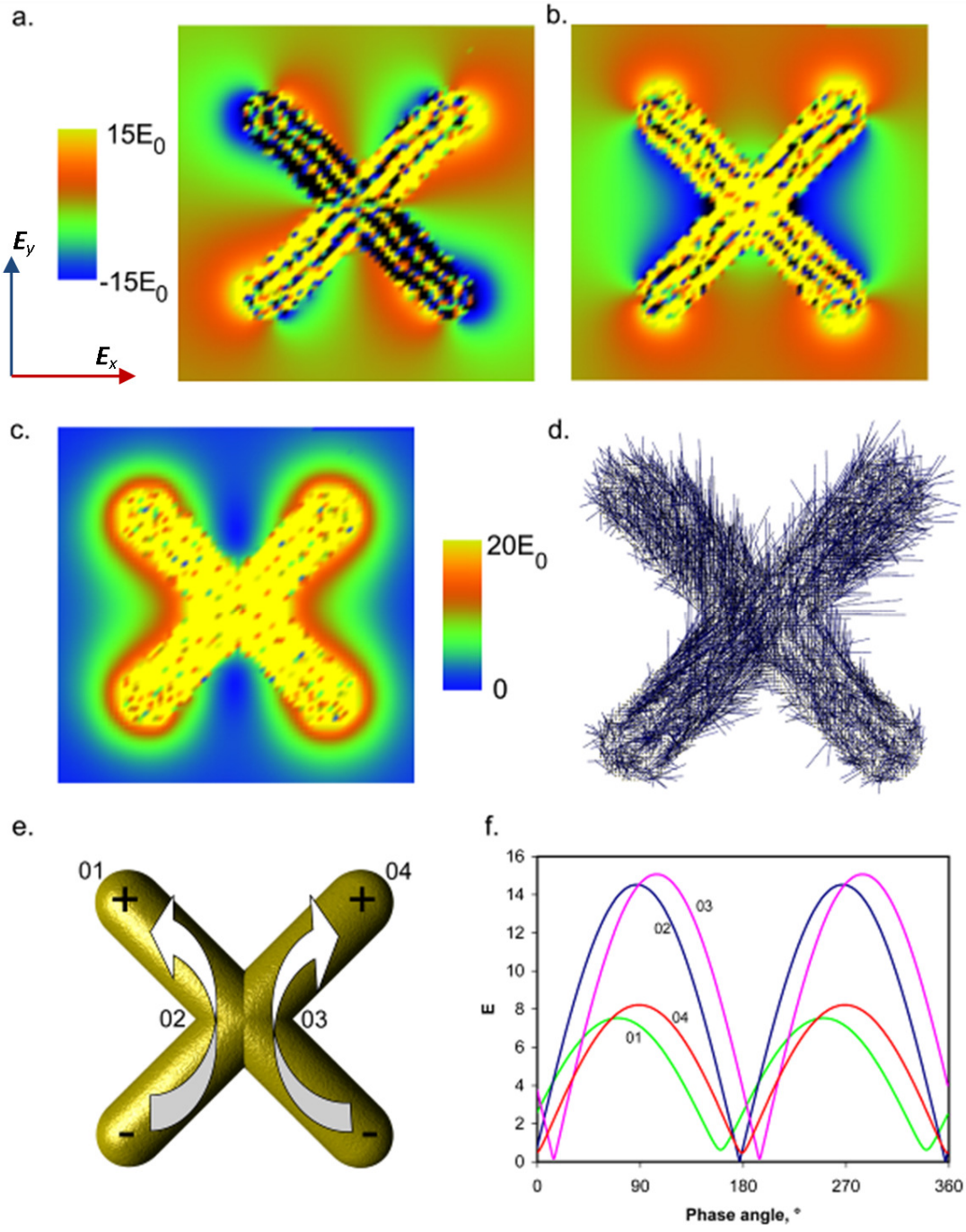

Figure 2.17: (a) $\boldsymbol{E}_x$ (direction shown) at phase angle of 90º, on average the field points right in one rod, and left in the other. The 'stripes' within the target are an artifact of the numerical solution, in which layers of dipoles take up one or other of the two resonances being hybridized, (b) $\boldsymbol{E}_y$ (direction shown), (c) $|\boldsymbol{E}|$, (d) dipole vectors at a phase angle of 90º, (e) schematic illustration of dipole resonance, also showing probe positions 01 to 04, (f) variation of $|\boldsymbol{E}|$ with time at four probe positions.

Next the nature of the resonances possible in a target with $0<\alpha<45^{\circ}$ is considered using the example of the $\alpha=35^{\circ}$ structure as a case study. Unlike the case for $\alpha=45^{\circ}$, these structures have a defined longitudinal and transverse orientation and, as shown in Figure 2.16, these produce different resonances. The oscillation in these targets could also be considered to be the result of a superposition of a transverse oscillation (in the direction of $\boldsymbol{E}$) combined with a counter-current longitudinal component running down the length of the two rods. However, the resonances are subtly different for the two orientations. In particular, the resonances in the $\alpha=35^{\circ}$ target develop a stronger longitudinal aspect when in the orientation shown in Figure 2.4 (b).

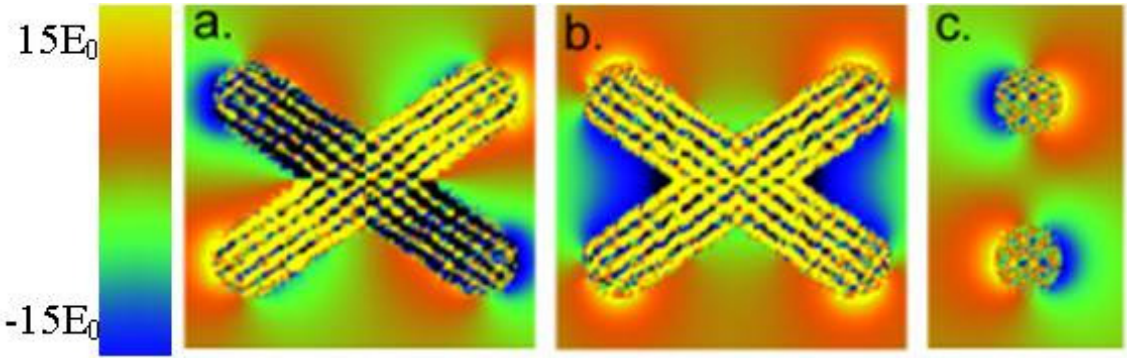

Figure 2.18: Resonances in target with $\alpha=35^{\circ}$ between arms at a phase angle of 90° and with the target orientation shown in Figure 2.4 (d), (a) $\boldsymbol{E}_x$, (b) $\boldsymbol{E}_y$ (c) $\boldsymbol{E}_z$ side view.

When $\boldsymbol{E}$ is oriented along one of the arms of a rod in, for example, the orientation shown in Figure 2.4 (f), Figure 2.19, a strong dipolar longitudinal resonance occurs on one arm of the target, while there is a less intense arm-to-arm resonance elsewhere. This latter resonance peaks at a phase angle that is 20° later than the first. Movies of the internal target dipoles and the external electric field are included in the Appendix for the X35 resonances.

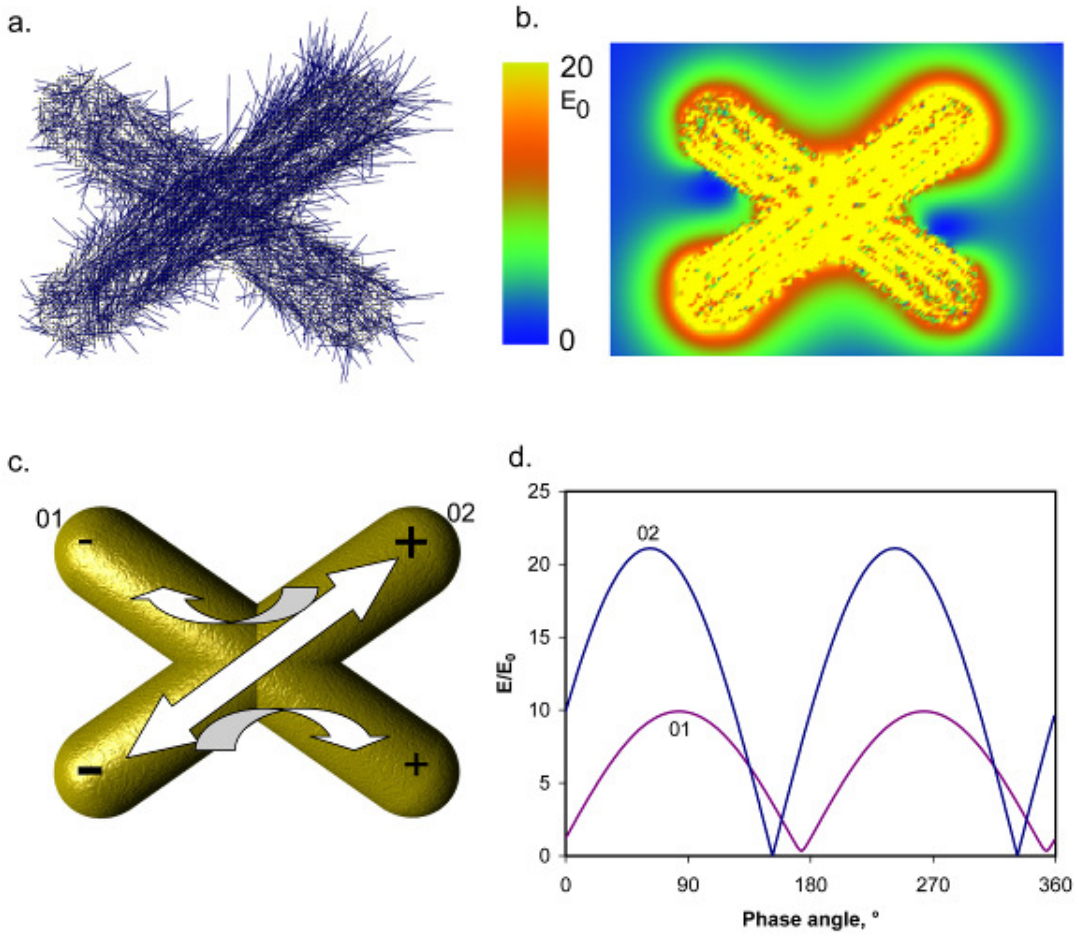

Figure 2.19: Effect of placing target so that ***E*** points along one of the arms, as shown in Figure 2.4 (f). (a) dipole depiction of resonance at θ= 90º (b) electric field at θ=90º, (c) diagram showing the nature of the resonances and probe positions, (d) variation of |***E***| at the probe positions, showing how the weaker resonance lags the stronger one by 22º.

In these calculations, as the inter-rod angle increases, the amount of gold within the target also increases, due to the decreasing overlap of the crossed rods and to the greater length of the rods as α increases. Therefore the effective radius (a_{eff}) parameter of the targets also increases as the inter-rod angle is increased. This change has an additional small red-shifting influence of its own, moving the extinction peak a few tens of nanometres as the size is increased for a fixed value of α (Figure 2.20). However, the primary red-shifting effect in Figure 2.16 is due to the increase in inter-rod angle rather than to the small increase in a_{eff}. Figure 2.21 shows the effect of keeping the a_{eff} (gold amount) constant across geometries 0°, 15°, 30° and 45° and with a comparison to the prior constant of 80 nm structure length shown in Figure 2.1. The a_{eff} is listed for each peak and the largest change in peak position and intensity is the rod structure which is

also consistent with the largest possible change in aspect ratio. Structures with α=15°, 30° and 45° do not have a significant change in peak position or intensity as a function of size, indicating that the red shift of the crossed rod structures is due to the crossed rod angles and not the change in a_{eff}.

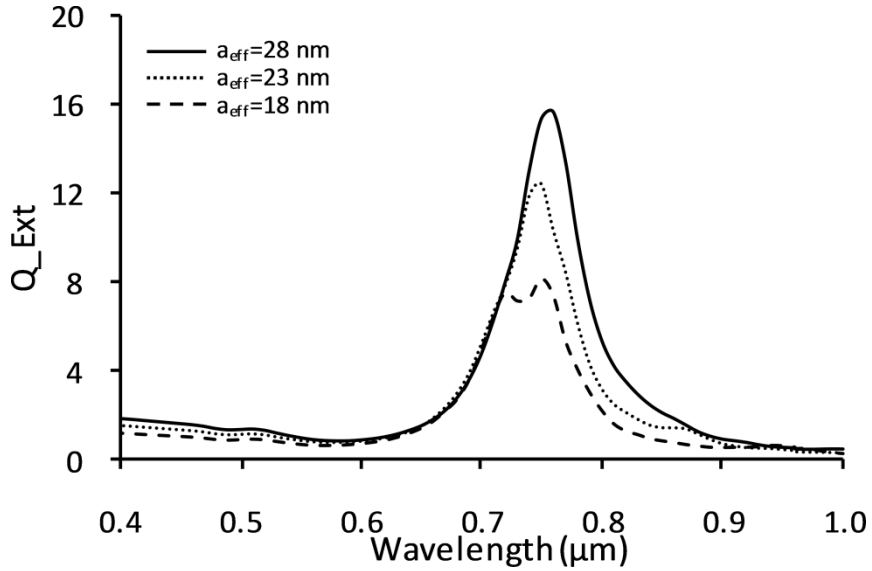

Figure 2.20: Effect of target volume on the extinction efficiency of a target with α=35° in orientation Figure 2.4 (d). There were insufficient dipoles in the smallest target to ensure the full hybridization of the two resonances.

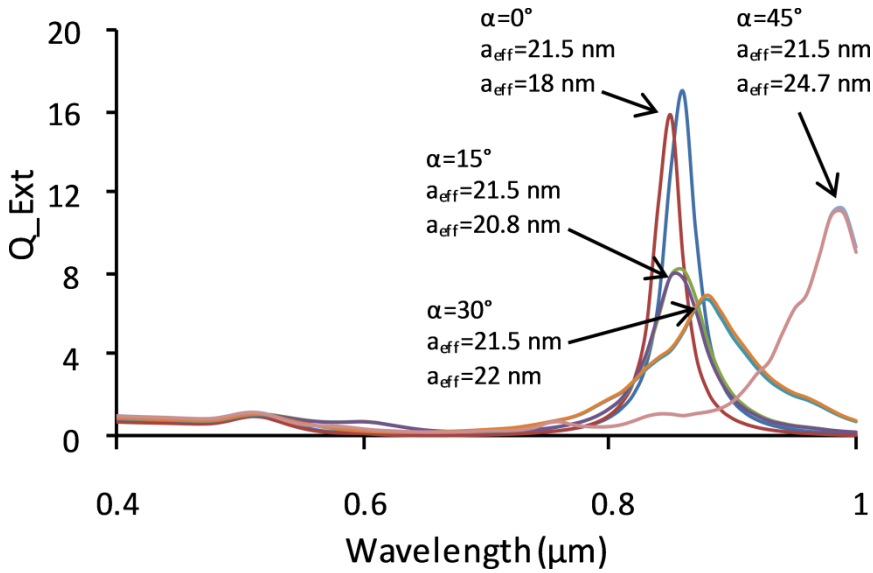

Figure 2.21: Effect of gold volume on the peak positions for target geometries α=0°, 15°, 30°, 45°.

The preceding discussion described the properties of individual structures. The effects induced by placing structures into infinite, 1D periodic arrays are now discussed.

Two orientations of the electric field with respect to the array are important. In the first, the electric field is directed along the length of the array, in the other is perpendicular to the array. Simulations of the optical properties are shown in Figure 2.22 for these two polarizations and for various spacings of the targets. In the first case the extinction maxima are red-shifted and in the second polarization the extinction maxima are blue-shifted and broadened. The effects become stronger as the targets are placed closer together. The result in both cases is due to coupling of the plasmons of the individual particles but it is obvious that the coupling takes a different form for the two different polarizations. The results are qualitatively similar to those obtained with simple nanorods. In that case the red-shifting effect was identified as being due to coupling of the plasmons of adjacent particles to form a new lower energy, symmetric plasmon while the blue-shift resulted from coupling to produce a higher energy, anti-symmetric plasmon.[36] It is believed that a similar explanation will apply in the present instance.

Another important periodic feature investigated is the effects of the electric field when applied along a periodic array formed by alignment of the long aspects of the X35 structure. These effects are shown in Figure 2.23, and red-shifting occurs when the periodic spacings between the X structures are reduced. The amount of red-shifting of the long periodic aspect is less than the short periodic X aspect, however the optical extinction intensities remain higher.

Figure 2.24 shows a comparison of the optical extinction properties of a 1D array with the X35 structures aligned along the long and short aspect. The electric field is applied along the array. A constant spacing of 44 nm between the X structures is used, which corresponds to a periodic spacing of 124 nm for the long aspect and 75 nm for the short aspect. Both resonances observed have red-shifted in comparison to the isolated X structure. However, the red-shift of the short X aspect resonance peak is 110 nm, compared to 40 nm for the long aspect, resulting in the short X aspect having the plasmon resonance with the lowest frequency. Although the order of the plasmon peaks has been reversed within the periodic array, the intensity of the long X aspect resonance remains larger than the short X aspect resonance but there is some loss of signal for both resonances during the plasmon coupling process.

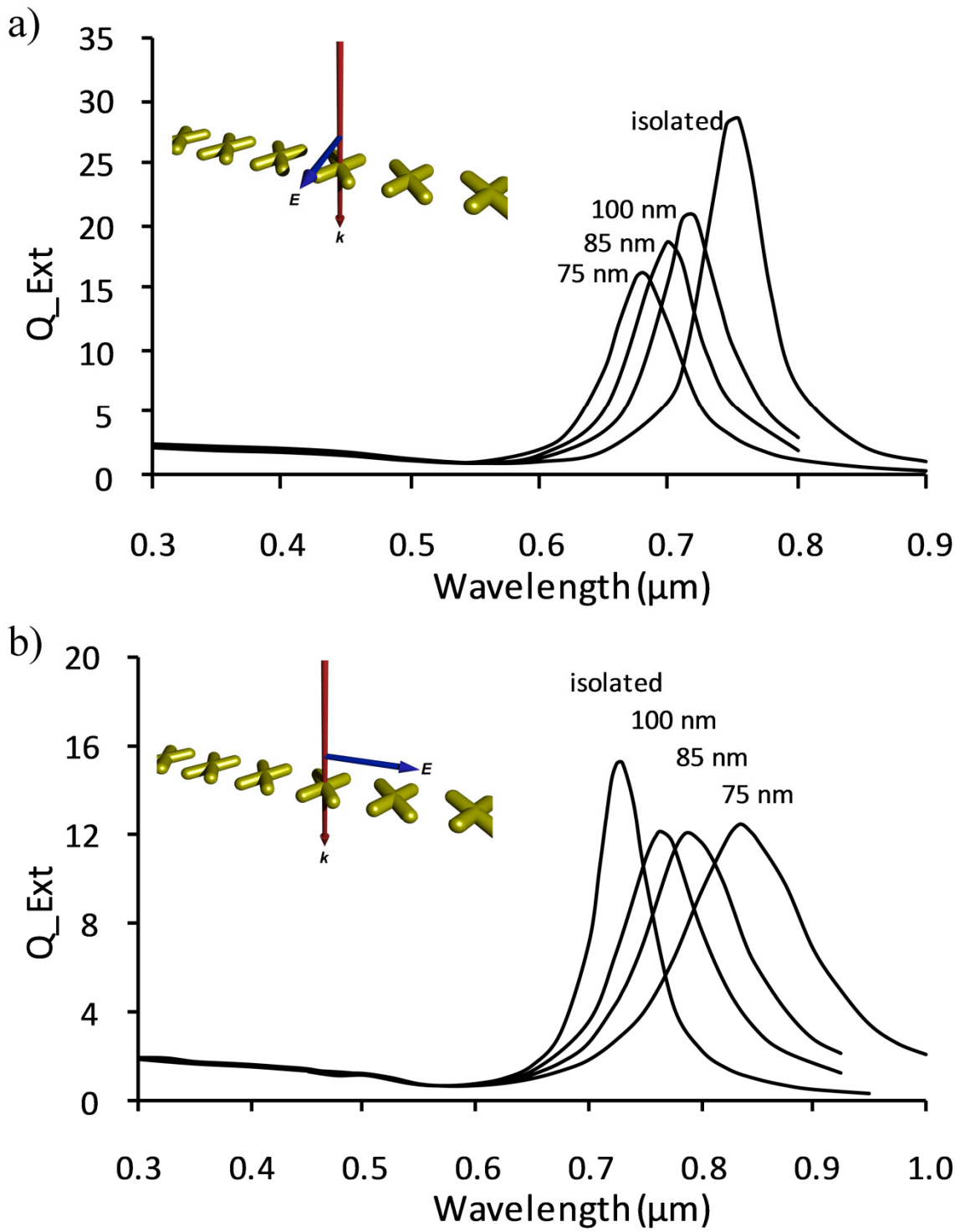

Figure 2.22: Simulated optical properties of arrays of crossed rods at various periodic spacings. In this case the rods with a 35° half-angle have been used to illustrate the point. Electric field directed (a) perpendicular and (b) parallel to the array, with periodicity as shown.

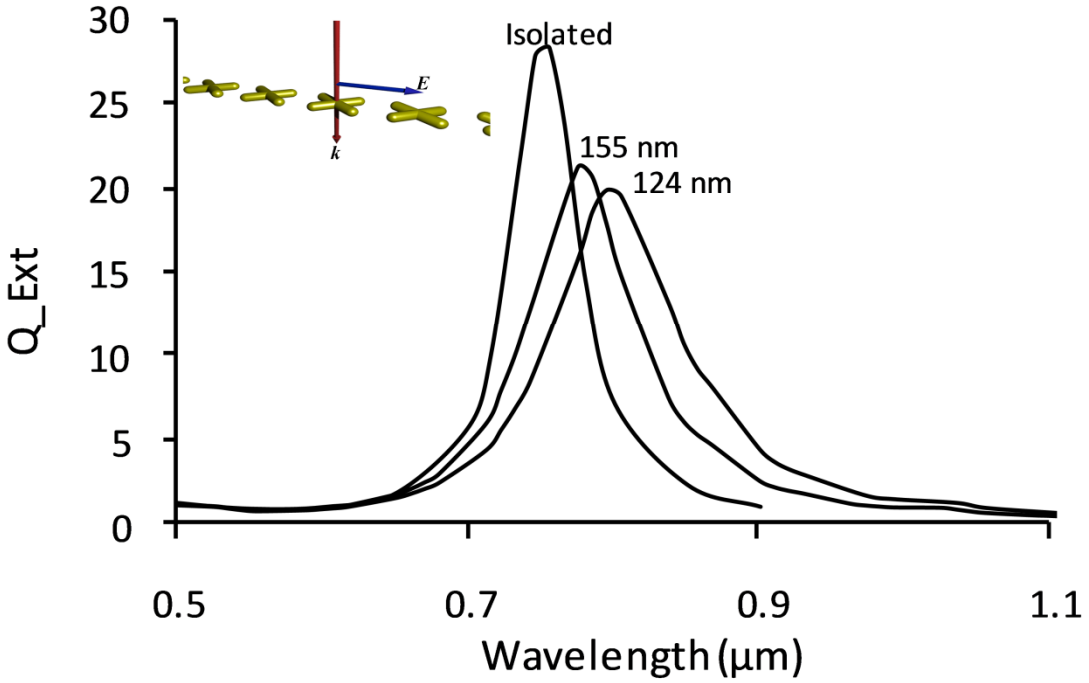

Figure 2.23: Simulated optical extinction properties of arrays of X35 structures with periodic spacings shown. The periodic spacings correspond to air gaps of 44 and 75 nm.

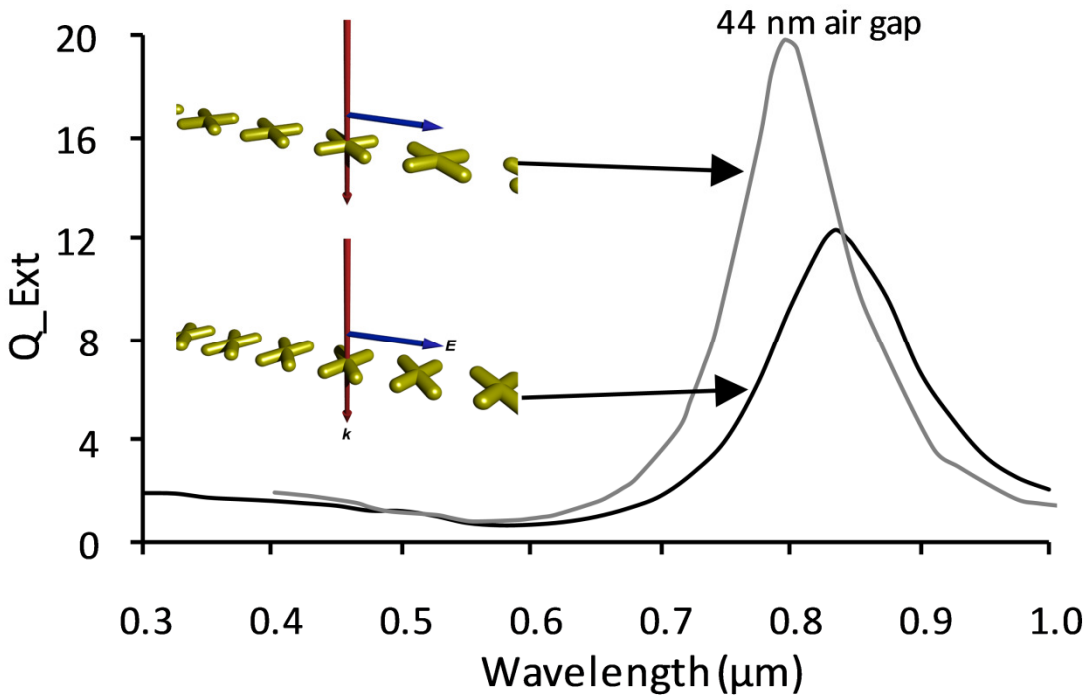

Figure 2.24: A comparison of the optical extinction properties of a 1D array of X35 structures with a 44 nm air gap with the applied electric field in the array direction, along the long and short aspect of the X structure.

An important question to consider is whether 1-D arrays of crossed rods would possess optical properties that are different to those of coatings of randomly-oriented nanorods, in particular for light incident with the TE polarization (that is, light with ***E*** oriented in the plane of the target) onto the coating. The transmission spectra of both types of coating will be characterized by a strong absorption peak, the position of which is tunable, as shown here for the crossed-rods and elsewhere e.g[168] for the randomly oriented individual rods. However, a coating of rods or crossed rods that are aligned will additionally show sensitivity to the direction of both the electric and magnetic fields of the light, while a coating made from randomly oriented rods or crossed rods will not. Although spectral selectivity can be obtained by mixing together ordinary nanorods of different aspect ratio, which may have applications in solar screening,[168] crossed-rod structures may be attractive in applications that engage with some aspect of the polarization of the incident light or the electric field generated around the targets. For example, a polarizing filter created by a crossed-rod array would have the attributes of being active over only a narrow range of wavelengths, and also have a rotational sensitivity that varies at double the rate of conventional polarizing filters.

The enhanced electric field around such arrays may possibly be even more interesting since it can be exploited, in principle, to amplify either single photon or two-photon fluorescence in suitably located dye molecules. The intensity of the electric field as a function of distance from the surface of the targets is shown in Figure 2.25 for two transects. It is clear that there is a strong and extensive amplification of the electric field between the arms of the target. This is of particular relevance as two photon phenomena are dependent on $|\boldsymbol{E}|^2$ rather than $|\boldsymbol{E}|$. However, excitons that are too close to a metallic nanoparticle are likely to be quenched[169] so the enhanced electric field near the metal surface would only yield useful fluorescence enhancement for dye molecules located at least 10 – 20 nm from the surface.[169]

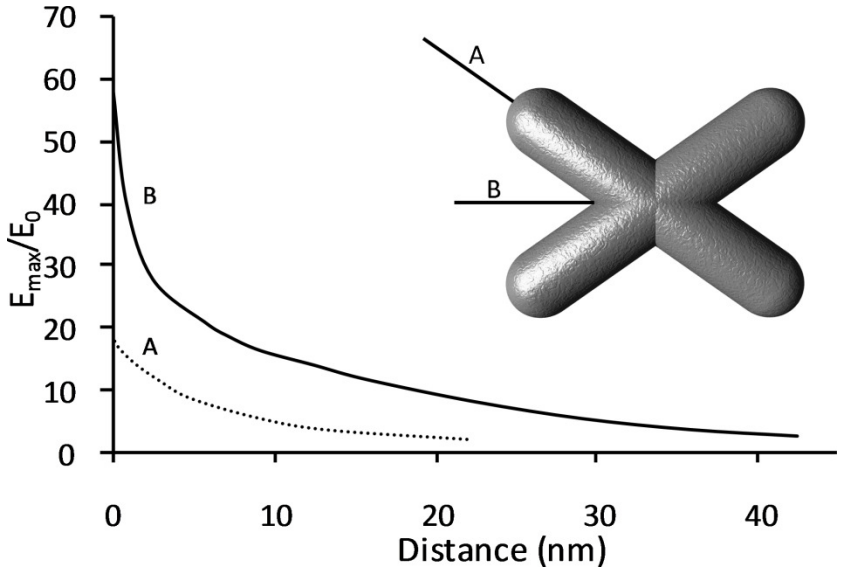

Figure 2.25: Variation of electric field intensity as a function of distance from target surface for two transects (A and B) in neighbourhood of crossed rod target with α=35° and in orientation Figure 2.4(d).

2.3.2. Calculated properties of V shaped structures

Optical absorption properties calculated for V structures are shown in Figure 2.26 for gold in water. The calculations were performed with a dipole spacing of approximately 1 nm. There are two longitudinal resonance peaks; the first corresponds to resonance back and forth along a single arm and peaks ~750 nm, which mimics to resonance from a single rod of ~ AR4. The second corresponds to resonance from one rod around the apex and along the other rod. This resonance peaks at ~1100 nm and closely resembles the resonance of an AR8 nanorod. The extinction peak wavelengths were calculated to be at 710 nm for AR4 and 1210 nm for AR8 for isolated rods. This means that all V structures shown in Figure 2.26 are red-shifted compared to the rod AR4. For more acute structures, less resonance occurs around the vertex and more is reflected back and forth along each arm of the V compared to more obtuse structures. The opposite also holds true. A lack of convergence is observed for structures with the arm angles close to right angles, V70 – V110, these require a large number of dipoles, or a small dipole volume, to essentially follow the resonance around the sharp corners. Convergence does not occur where either of the main peaks becomes multiple peaks. V90 for example, has 2 peaks at ~730 nm and 4 at ~1100 nm and when convergence occurs the split peaks combine into a single peak. The structures closest to either rod (AR 4 or 8) converge

and therefore do not require reduced dipole spacings. Convergence can be clearly seen in Figure 2.27 for V90 with orientation as seen in Figure 2.5 (c).

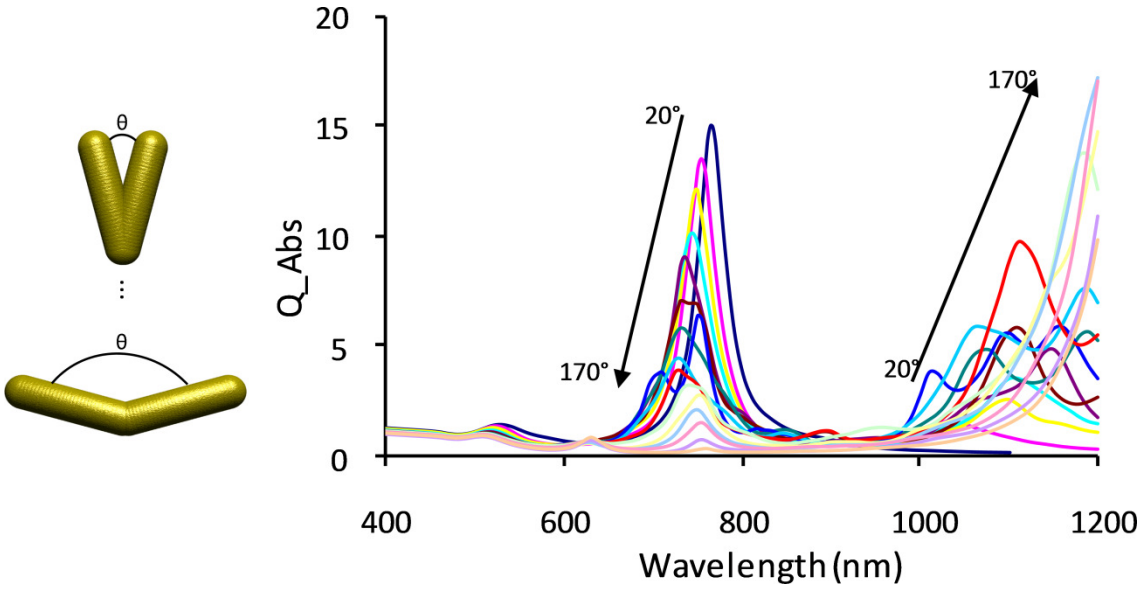

Figure 2.26: Optical absorption properties of V structures with arrows showing the trends of the angles between the V.

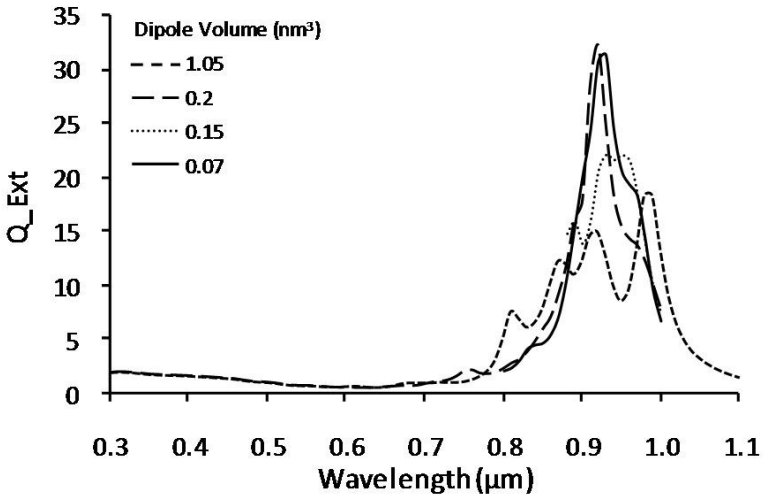

Figure 2.27: Convergence of V90 with the corresponding dipole volume used.

The interaction between rods close together side-to-side is similar to the effect of the small angled crossed rods in the X and V structures. With small angle X and V structures the arms are particularly close to each other such that resonances occurring along the arms may couple between the arms causing a slight blue shift of the resonance peaks. Most of this resonance blue-shift is drowned out by other factors influencing the plasmon resonance including different structure shape, size or mass of gold.

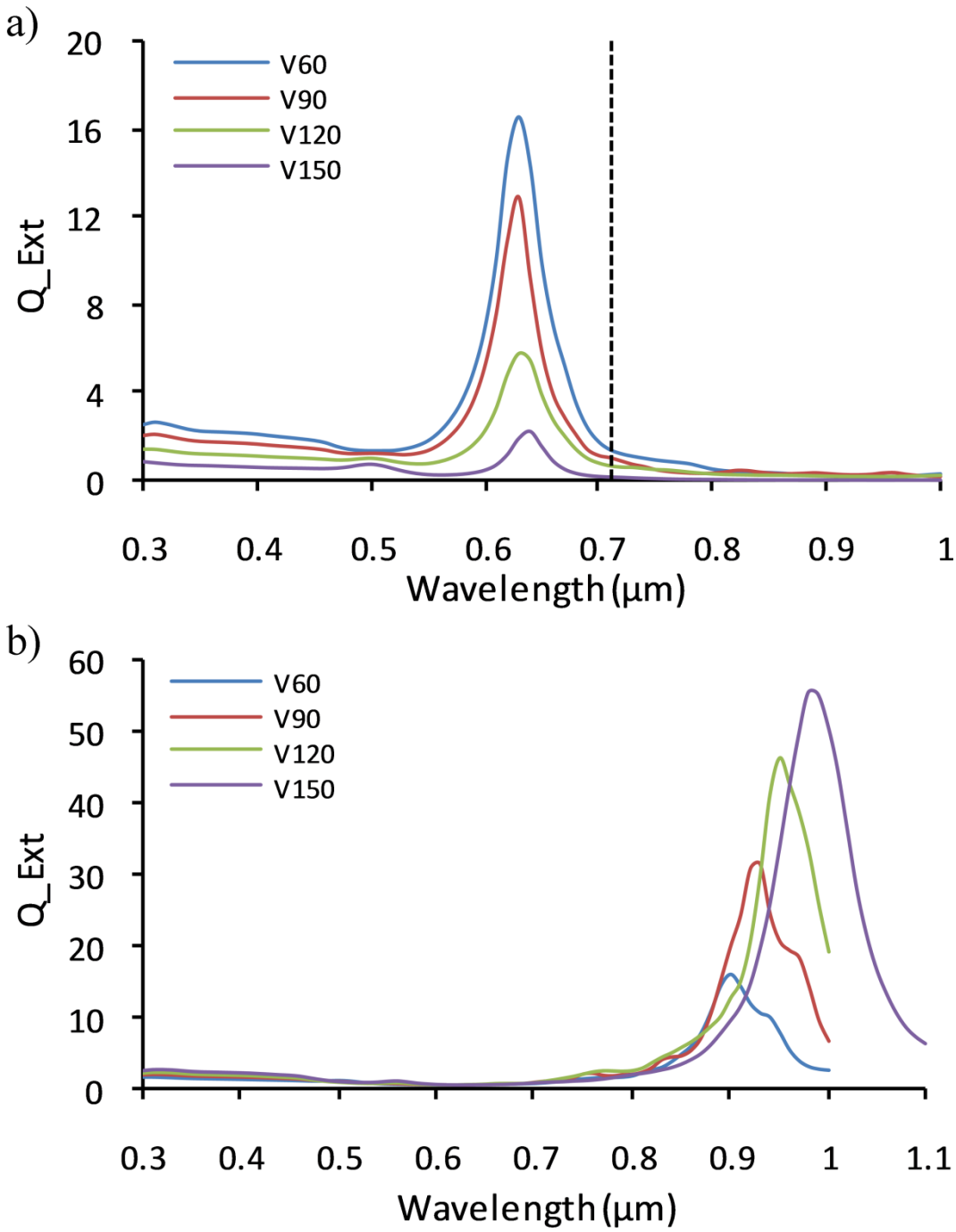

Figure 2.28: Calculated extinction properties of V60, 90, 120 and 150 for the resonances with ***E*** (a) across and (b) along the extended targets. The dashed line in (a) corresponds to the peak position, 710 nm, for an AR4 rod, or the V structure with θ = 0°.

A selection of V structures was investigated with the angle, θ, smaller, equal to, and larger than the rods intersecting at right angles. Figure 2.28 (a) and (b) shows the two main extinction peaks for structures with orientations equivalent to Figure 2.5 (b) and (c) respectively. It follows that for small angles, structures exhibit similar spectra to that

of a thicker rod which lowers the aspect ratio and blue shifts the plasmon longitudinal peak relative to that of a constituent rod. Similarly, when the V structure is extended to 180°, the structure acts like a rod with AR8 and the peak position is at 1.21 µm. V structures with larger angles cause the plasmon resonance peak at ~630 nm to be reduced in intensity and slightly red shifted. Further to this the longitudinal plasmon resonance, in Figure 2.28 (b), increases in intensity and also red shifts with increasing V angle.

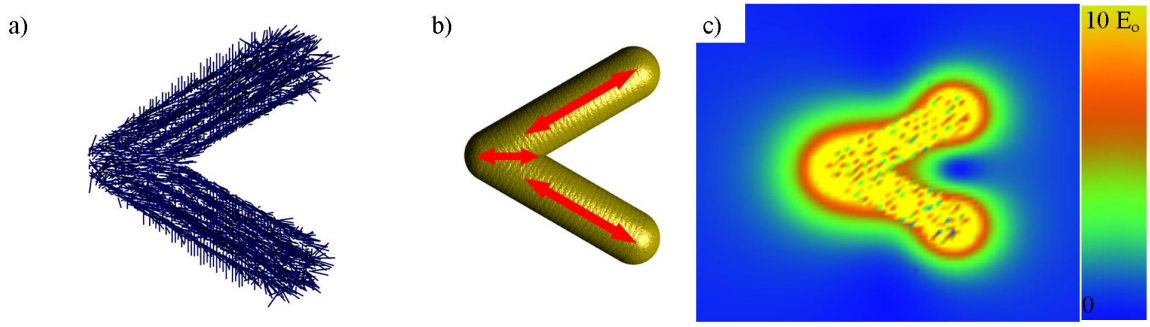

Figure 2.29: Calculations of the (a) dipole resonance at phase 90°, (b) schematic of the dipole movements and (c) interacting electric field at phase 90° from V60 in Figure 2.28 (a) and with orientation of Figure 2.5 (b).

The 630 nm peak for V60 structures was investigated and can be seen in Figure 2.29. Movies of the internal dipole moments and the external electric field intensity are included in the Appendix. The dipole resonance was recorded across the entire incoming wavelength in steps of 10°. The dipole resonance at a phase angle of 90°, which corresponds to the incoming light maximum, can be seen in (a). Investigation of the entire resonance range allowed for the multipole resonance to be determined, with the main resonance patterns shown in the schematic in (b). The electric field interaction through a cross-section bisecting the V structure is shown in (c), with the maximum intensity shown representing 10 times the applied electric field. The areas of the resulting electric field which are largest are sections at the ends of the resonance shown in (b). This indicates that the application of the multipole resonance significantly increases the resulting electric field.

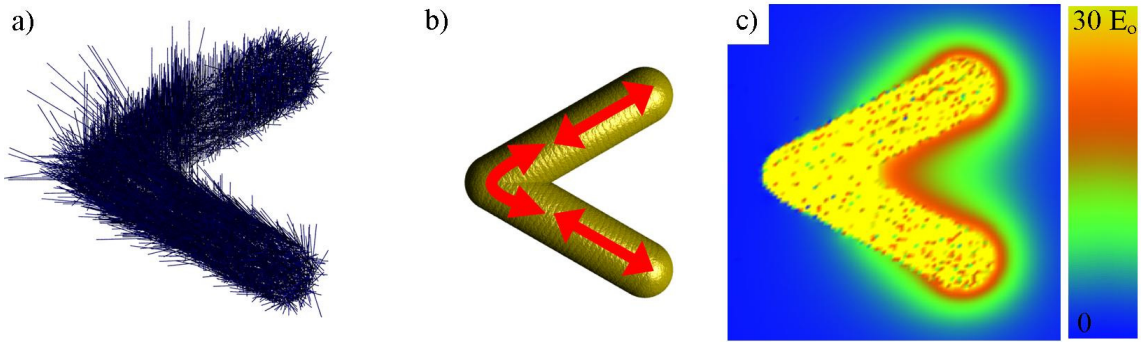

Figure 2.30: Calculations of (a) dipole resonance at phase 90°, (b) schematic of the resonances and (c) interaction of the electric field at phase 90° for V60 in Figure 2.28 (b) and with orientation of Figure 2.5 (c).

The alternative resonance peak for the V60 structure is shown in Figure 2.30. Similarly to Figure 2.29, the phase of the dipole resonances in (a) and the resultant electric field in (c) are all displayed with phase 90°. The dipole size is much larger in Figure 2.30 (a) than Figure 2.29 (a), which is unexpected considering the intensity of the extinction peaks were of similar height. Figure 2.30 (b) shows the directions of the plasmon resonance that occurs at the 900 nm peak. The resultant electric field is of much higher intensity (30 E_o) and spatial extension than that depicted in Figure 2.29 and is mostly situated between the two arms of the V structures.

Alternatively, when the V angle is sufficiently large (greater than 90°) then a high intensity electric field no longer stretches between the arms. Figure 2.31 shows the effect of both dipole movements and electric field intensity for the V120 structure. Figure 2.31 (b) shows how the longer wavelength plasmon 950 nm, with orientation Figure 2.5 (c), does not have a high intensity electric field at phase 90° reaching between the arms. This is different to V60 with the same orientation where there is a minimum of ~ 15E_o at the centre between the arms, which compares to between 5 – 10E_o at the same point for the V120 structure. Both the dipole movements and the movement of the electric fields for the V120 structure are almost identical to the V60 structure.

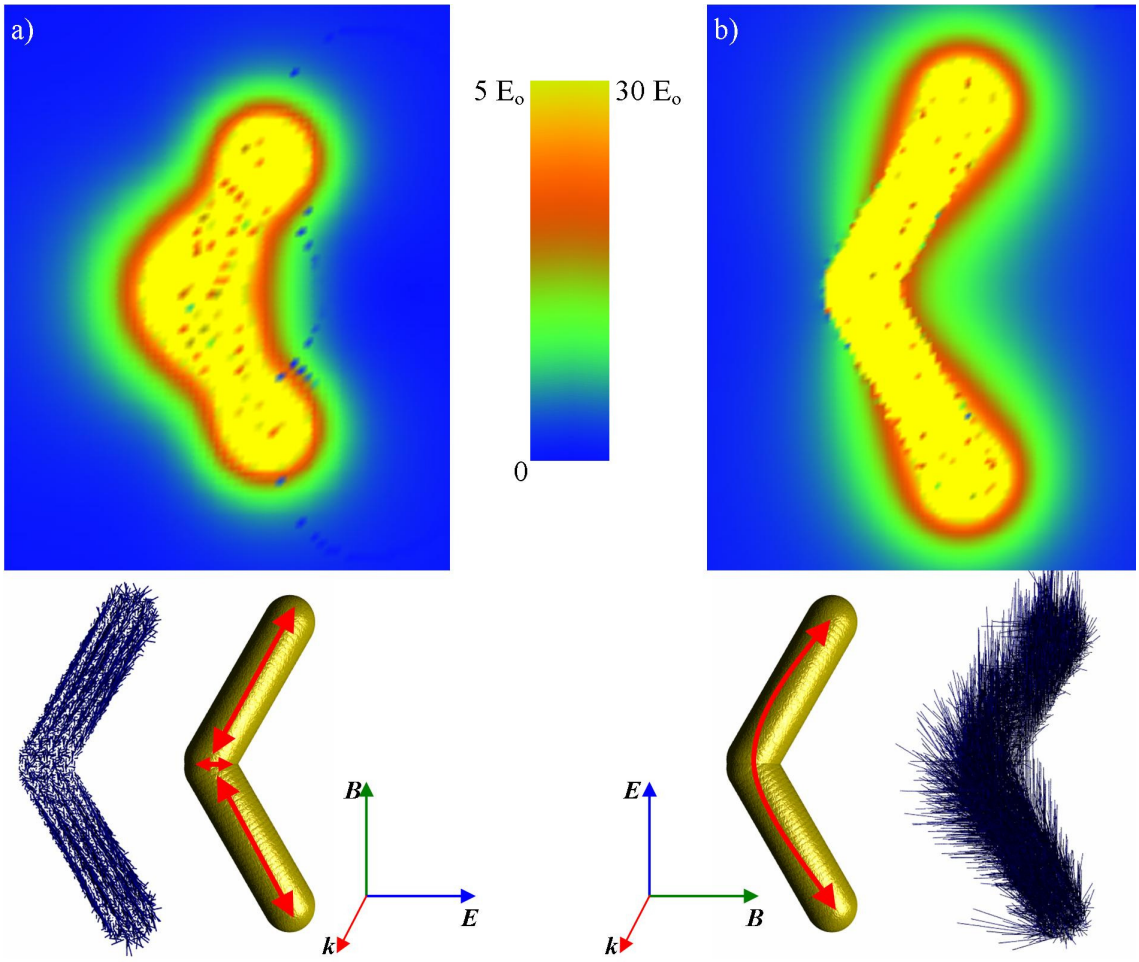

Figure 2.31: Magnitude of the electric field and dipole movement illustrations for the V120 structure with (a) corresponding to Figure 2.28 (a) peak at 630 nm and (b) to Figure 2.28 (b) peak at 950 nm.

The enhanced electric field around individual V structures has been investigated, in a similar process to the X structures. The enhanced electric field can be exploited, in principle, to amplify either single photon or two-photon fluorescence in suitably located dye molecules. The intensity of the electric field as a function of distance from the centre of the target is shown in Figure 2.32 for transect AB. It is clear that there is a strong and extensive amplification of the electric field between the arms of the target and as two photon phenomena are dependent on $|\boldsymbol{E}|^2$ rather than $|\boldsymbol{E}|$ it is of particular relevance. However, as mentioned previously, excitons that are too close to a metallic nanoparticle are likely to be quenched so the enhanced electric field near the metal surface would only yield useful fluorescence enhancement for dye molecules located at least 10 – 20 nm from the surface.[169] This enhancement could be situated between the V

arms and still retain both the enhanced electric field and situated further than 10 nm from the structure edges.

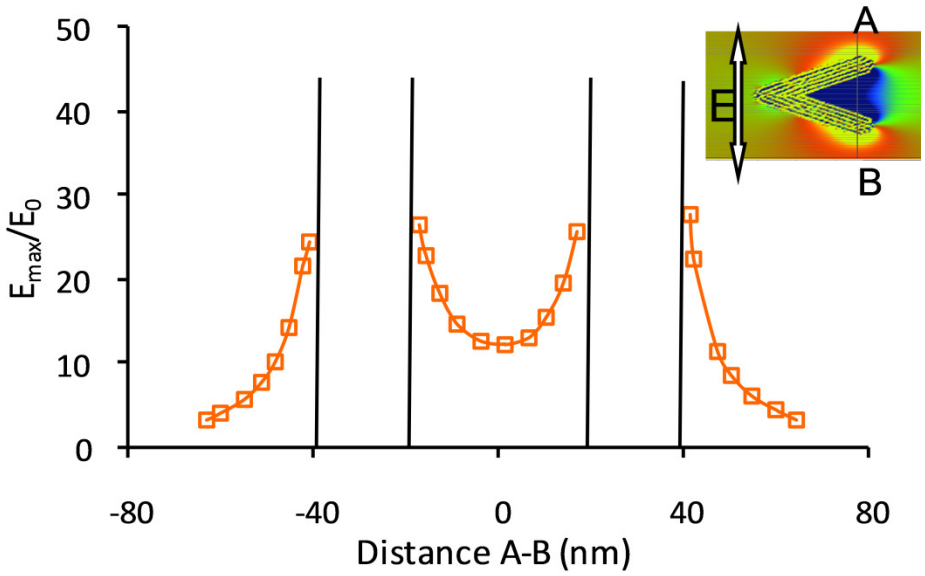

Figure 2.32: Variation of electric field intensity as a function of distance from target centre for the transect AB in neighbourhood of V rod target with α=60º and in orientation Figure 2.5 (c).

The enhanced electric field measured with orientation Figure 2.5 (b) is shown in Figure 2.33. The resultant enhanced electric field was measured along the transect AB which bisects the V60 target. Figure 2.33 has a maximum electric field enhancement of ~15E_o and is a significantly smaller enhancement compared to ~30E_o for Figure 2.32. The maximum electric field enhancement between the V arms occurred at a distance ~ 6 nm from the edge of the structure and the other small peak at ~ 60 nm from the structure is due to the interaction of the two maximums at the end of the V arms. A comparison of the entire region is shown in Figure 2.34 with the size and angle of the lines indicating the direction and intensity of the maximum enhanced electric field.

The enhanced electric fields shown in Figure 2.32 and Figure 2.33 match the significant surface plasmon resonance effects found by Stockman *et al.* who showed that the enhanced fields occurred at the apex for one orientation and running along the V structure for another orientation. Results obtained within this work show enhancements in the electric field directed in the plane of the structure as opposed to perpendicular to the structure plane in the case for Stockman *et al.*[163,164]

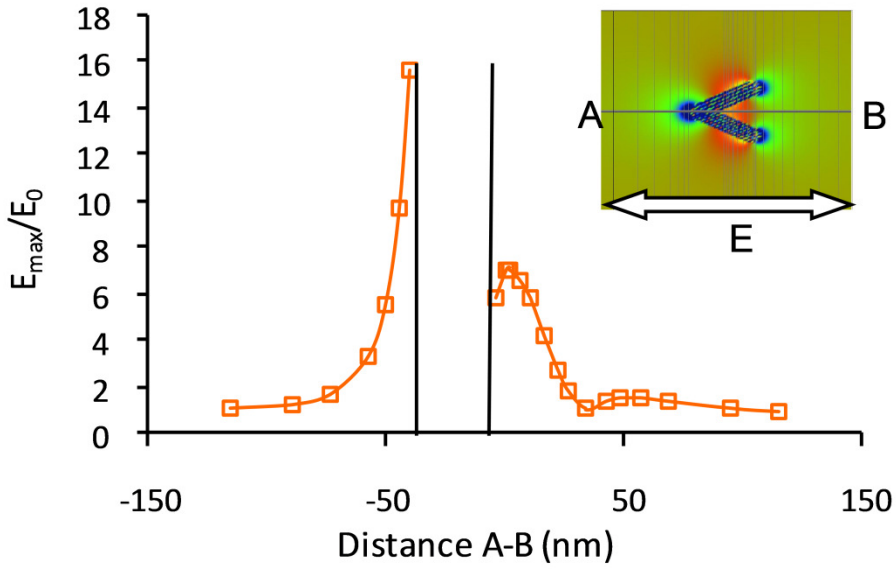

Figure 2.33: Electric field intensity as a function of distance from the V60 target centre along the transect AB and in orientation Figure 2.5 (b).

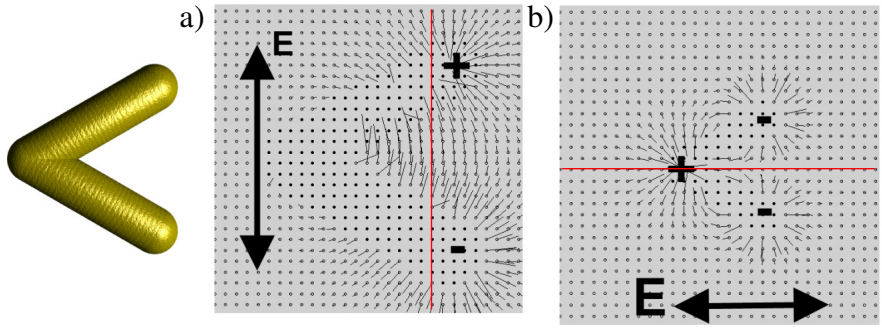

Figure 2.34: A comparison of the enhanced electric fields maxima with two different orientations with the direction of the applied electric field shown. The red lines indicate the measured electric field intensity of transect AB in (a) Figure 2.32 and (b) Figure 2.33.

The optical properties of the V structures suggest that, although they could be used as a window coating, there is no advantage in their optical properties compared to rods. Furthermore, rods can be prepared in solution and are therefore much easier to use. There is, however, potential for their use as antennas for the generation of two photon fluorescence, with the magnitude of the electric field greater than even the crossed rods structures.

2.4. Conclusions

Computer modelling using the discrete dipole approximation has enabled investigations into the optical properties of gold nanostructures with various shapes and dimensions. Modelling of gold rod structures agrees with literature results in that the longitudinal surface plasmon resonance of rods side-by-side blue-shifts as they are situated closer together. Alternatively, the longitudinal surface plasmon peak position of rods end-to-end red shift as the rods move closer together.

A rectangular prism target is preferentially used to model gold nanorod structures produced by EBL over the hemisphere-capped, right cylinder shape used to model wet-chemically produced rods. The actual structure of the prism is more realistic in terms of both the physical shape and the optical properties.

A mixture of rods with a spread of aspect ratios may be utilised to model the spectra of a rod solution. Higher numbers of rod shapes used resulted in more accurate simulation of the optical properties and fewer gaps in the data. Twenty five aspect ratios of rods are sufficient to match the overall shape of the optical spectra with only small aberrations.

Nanoscale crossed-rod structures made of gold provide a tunable and interesting motif to construct spectral and polarization-dependent filters, or with which to amplify two-photon phenomena. Variation of the angle between the rods as well as the aspect ratio of the arms provides a useful means of controlling the frequency of the plasmon resonance. The individual resonances of each rod are hybridized in the crossed-rod structure and blue-shifted as a result. The numerical DDSCAT method may be used to calculate the resonance behaviour using multiple dipole domains, however a mesh size with a spacing of <1 nm is required for accurate results. The electric field distributions in the vicinity of the gold structures are quite complex and have a high intensity and spatially extended nature. This type of structure may be especially useful as a nano-antenna for the generation of two-photon fluorescence in a suitable surrounding medium or for use as enhanced scatterer such as with SERS.

Similarly, crossed rod structures forming V shapes also have potential for the generation of two photon fluorescence. The use of different dimensions of the V structures allows control over the optical properties and also control over the placement and size of the generated external electric field. Acute V angled structures in particular

create high intensity spatially extended electric field between the arms of the structures suitable for the generation of two photon fluorescence or for enhanced scattering with use in SERS.

Having predicted that these nanostructures possess interesting optical properties, the next challenge was to fabricate real examples of these for experimental examination. This topic is addressed in Chapter 3.

Chapter 3:

Preparation of Gold Nanostructures on Glass Using Nanolithography

Chapter 3: Preparation of Gold Nanostructures on Glass Using Nanolithography

3.1 Introduction

This chapter discusses experimental and theoretical aspects involved in the fabrication of novel and interesting gold nanostructures on glass surfaces.

There are many forms of lithography and the relevant techniques were described in Chapter 1.4.1. Electron beam lithography (EBL) is a high precision top-down lithographic technique used to create masks for other mass producible techniques such as X-ray and optical lithography for use in the semiconductor industry,[116] or it may be used in research to prototype new and different shaped structures.[112] EBL is an extremely versatile nanolithography system where structure fabrication is limited mostly by microscope and resist resolution. It does not require a template like optical lithography or have design limitations like interference lithography, and has a resolution greater than or equal to all other lithographic processes. Thus EBL is ideal for fabricating the small quantity of high resolution structures required to investigate the optical properties of the various nanorod structures described in Chapter 2.

The majority of reported EBL uses silicon substrates as silicon is cheap and relatively easy to use, whilst still allowing fabrication of high resolution patterns. However, silicon is opaque in the visible and NIR and therefore of limited use in optical investigations. Thus interest in constructing patterns on optically transparent substrates has led to research into high resolution EBL on glass substrates. Because glass is an insulator, methods to overcome charging problems have been developed including metal layers on top of the glass,[66] using some form of conducting e-beam resist, using conducting glass with indium tin oxide (ITO),[79-83] fluorine tin oxide (FTO) or antimony doped tin oxide (ATO)[71] coatings. Recent work using variable pressure EBL allows glass to be used as a substrate without further development steps.[170] In general, conducting, semiconducting and insulating substrates each require rather different processing steps.

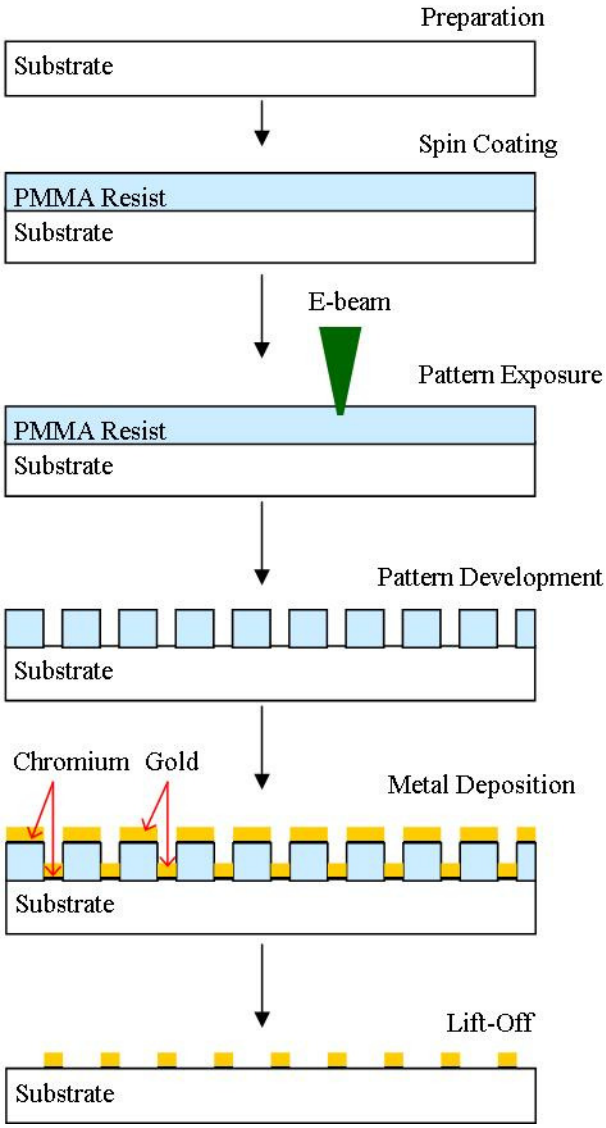

Figure 3.1: Diagram showing the processes used to prepare gold nanostructures. The initial substrate preparation step involves cleaning and is followed by spin coating of the PMMA e-beam resist. The desired pattern is then exposed followed by developing of the pattern. Metal is then deposited; a Cr/Au bilayer was used in this work, and finally lift-off of the remaining resist leaves the metal pattern attached to the substrate.

The fabrication method for structures made using EBL is shown in Figure 3.1. There are a number of variables to consider when conducting EBL, the more common ones include different substrates, resists, chamber pressure, temperature of developer and accelerating voltage.

Initially the type of substrate is selected followed by cleaning the substrate. For best results the substrate must have solvent remnants removed using plasma cleaning or heating techniques prior to resist deposition.

The second step involves the selection and deposition of an e-beam resist using spin coating techniques. An e-beam resist is a material, typically a polymer, which undergoes an irreversible change when exposed to an electron beam. A positive resist is one where exposed regions are removed during the development stage. Alternatively, a negative resist is one where unexposed resist is removed. There are many types of e-beam resists with different properties and consideration of structure design and resist type and resolution can assist with resist selection. A few common e-beam resists are shown in Table 3-1. The type of electron beam resist chosen is based upon the structure design. The structure design accounts for the exposure area and for exposures designed to be voids in a film it is easier to use a negative tone resist where the exposed area is void area which corresponds to a much smaller volume and therefore a much quicker process. The contrary also occurs, when a correspondingly small design requires a small exposure when using a positive tone resist.

The e-beam resists which have good dry etch resistance are generally the better resists for mask manufacturing. The higher resolution resists are more suitable for new designs and small area manufacturing.

Resist thicknesses are determined by the desired thickness of the final structure. A good ratio of initial resist thickness to desired structure height would be 3:1. The resist thickness should be *at least* twice as thick as the final structure thickness because this ensures that the metal coating does not completely cover the resist and prevent the lift-off process occuring.

Table 3-1: Common e-beam resists and their properties. Data from Raith EBL resist information and ref.[171]

Resist Name	**Dose ($\mu C/cm^2$) @ 30keV**	**Resolution (nm)**	**Resist Tone**	**Comments**
PMMA Poly(methyl methacrylate)	~200	<10	Positive	High resolution, poor sensitivity and poor dry etch resistance. Good adhesion and lifetime. Results are very reproducible.
ZEP 520-12	~50	<20	Positive	High resolution resist, 3x faster than PMMA with good dry etch resistance. Poor adhesion and undercut profiles. Results are reproducible.
APEX-E	~5	<150	Positive	DUV resist that works for e-beam. Fast, excellent dry etch resistance, moderate resolution, very sensitive to contamination (spun, written & developed all in a few hours)
UV-III	~10-40	<60	Positive	Good etch resistance, moderate resolution
EBR-9	~20	>200	Positive	Long lifetime, good for mask manufacturing
AZ5206	~20	~250	Positive	High contrast, good etch resistance, good for mask manufacturing
SAL-601	~10	<100	Negative	High sensitivity and contrast, moderate dry etch resistance, short lifetime, poor adhesion, poor reproducibility, bridging between features.
P(SI-CMS)	~10-40	<100	Negative	Good etch resistance, good adhesion, moderate resolution
PN114	~5-40	<60	Negative	Reasonable resolution, moderate etch resistance.
Calixarene	~4000	<10	Negative	High resolution, poor sensitivity
HSQ	~300	<20	Negative	Very good dry etch resistance, good resolution
SU8	~2	<100	Negative	Good for 3D EBL applications, moderate resolution

The third step involves pattern exposure by directing an electron beam onto the electron beam resist and drawing a pattern within the resist. As electrons are fired into a confined area, excess negative charge from the electrons must be removed to reduce beam broadening. A negatively charged area will cause the incoming beam to be repelled resulting in a loss of pattern resolution and definition. Several methods have been used to reduce charging effects; use of a conducting or semiconducting substrate, addition of a conducting layer on an insulating substrate either below[71,79-83] or above the e-beam resist,[66] or to use EBL in a variable chamber pressure[170].

Variable Pressure (VP) microscopy uses a gas, typically N_2, introduced into the chamber at a specific pressure. Beam electrons can strike the gas molecules as they pass through the chamber removing electrons from the molecules leaving them positively charged. These charged molecules are attracted to the negatively charged substrate where they gather the excess electrons from the substrate surface. An advantage of using VP lithography is that the pattern can be written on insulating substrates without extra processing steps.

The accelerating voltage used can be influenced by the type of microscope used, by the resist thickness or by the pattern design. For example, it is normal for an exposure to be undertaken at maximum possible accelerating voltage, which is a limit of a given microscope. This allows for most of the dispersion of the electron beam to occur within the substrate with minimal scattering within the resist layer. Using a lower accelerating voltage reduces the interaction volume, allowing more scattering at the bottom of the resist layer causing greater overhang during development which may improve the effectiveness of the lift-off process. This concept is explained in detail in Section 3.3.4.

The proximity effect is important in EBL and it occurs during exposure where the dose distribution is wider than the scanned pattern due to interaction of the electron beam with the resist and substrate. This interaction causes areas outside the pattern to receive a non-zero dose causing the exposed patterns to be wider than desired. There is software available that calculates dose requirements for each point within a structure. For example, a rectangle should receive a lower dose in the centre, higher dose around the side and the highest dose in the four corners. Alternatively, if the software is not available, the proximity effect can be adjusted for by slightly changing the dose or reducing the pattern size to take into account the desired structure size.

After exposure, the next step is development of the resist. The sample is immersed in a chemical solution specific to the resist which removes either the exposed or unexposed regions. Ocola *et al.* reported the effect of cold development on resolution using resists that work by polymer chain scission, for example PMMA and ZEP 520 resists. It was found that cold development improves resolution and contrast, and can therefore be used to improve the performance of EBL without any extra expensive equipment. The line width reduces from 30 nm with room temperature development to 15 nm with the developer at -4°C.[172]

The next stage in the fabrication of EBL patterns is the application of a metal film. A thin film is deposited across the developed resist, allowing the metal to deposit in the structure holes as well as across the unexposed resist. There are several different methods used to deposit the thin metal films but physical vapour deposition (PVD) is most common. PVD involves the removal of atoms from a solid or liquid by energetic means, and the subsequent deposition of these atoms on a nearby surface. There are several variations of PVD including thermal evaporation, sputtering, laser ablation, arc-based emission, ion beam assisted deposition, and e-beam physical vapor deposition. The deposition methods typically used for EBL are thermal evaporation, sputtering and e-beam physical vapour deposition.[173]

Thermal evaporation involves heating a metal to its melting point and the evaporated metal atoms are deposited on a nearby substrate. Most evaporative systems require good vacuums to operate efficiently since, if the pressure in the region of this liquid source is low, there will be no return or equilibrium of the evaporated vapour flux to the source. The mean free path of the evaporant flux should exceed the distance to the sample, reducing in-flight scattering with the background. The maximum pressure for an evaporative deposition should be around 10^{-5} Torr. At pressures much above this, the evaporant flux will be scattered by the background and the deposition rate will drop. The material to be deposited is stored in a cage or boat constructed from tungsten or tantalum and is then heated by passing a current through the wire cage.[173]

On the substrate surface, the evaporated metal atoms arrive and condense in thermal equilibrium with the surface. As the substrate is typically much colder than the source temperature, a thin film is usually deposited. This thin film is subject to issues related to wetting, nucleation, cluster formation and agglomeration.[173] This means that the binding of the films to the substrate using thermal evaporation is not as strong as sputtering

techniques. One advantage of thermal evaporation for EBL is that it deposits only in line-of-sight, thus the metal deposited into the exposed pattern holes is separated from the metal deposited above the resist.

Electron beam physical vapour deposition (EBPVD) is a very similar process to thermal evaporation, except it uses an energetic electron beam to heat the target metal rather than heating a coil around the target. The electron beam filament is situated adjacent or behind the target, with the electron beam sent to the target by magnetic fields. This results in the filament being out of line-of-sight of the evaporation point. The kinetic energy from the electron beam heats up a point to beyond the melting point. Advantages of EBPVD over thermal evaporation include no contamination from a metal holder and less metal used.

Sputter-based depositions are fundamentally different from evaporative depositions. Sputtering occurs when an energetic particle, typically an inert gas ion, impacts a target surface. The impact of the particle dislodges one or more surface or near surface atoms. These dislodged atoms move deeper into the target and dislodge additional atoms. This process continues until the kinetic energy is spread among the target atoms and the residual energy is insufficient to dislodge additional atoms, at which time the remaining energy is converted to heat. During this process, atoms near the surface may be dislodged with sufficient energy to overcome the surface binding energy and be emitted from the target. These are the sputtered atoms. The mass and energy of the incident particles determine many aspects of the collision process.[173]

There are two methods used to excite the initial particles, using a plasma or ion beam. In a plasma system, ions from a plasma bombard a cathode, the target, and if the conditions are suitable the cathode atoms are sputtered. With a ion beam system, a beam of ions is generated and directed onto the target, and the atoms sputtered.[173]

The energy and distribution of the sputtered atoms is different from evaporated atoms with sputtered atoms tending to have significantly more energy due to the nature of the collision processes. This allows the sputtered atoms to bind more strongly to the surface, and tends to deposit around edges. This presents a problem with sputtering for lithography, where the deposited atoms attach around the edge of the resist causing a problem during the lift-off process.

The next step is the lift-off process and involves the removal of all remaining resist from the susbtrate including any metal deposited on top of the resist. This ideally leaves

only the structures ‘written’ in metal. The lift-off process depends on the type of resist used, but typically the substrate is immersed in a solution that dissolves the resist whilst leaving the deposited structures.

3.2. Experimental Methods

3.2.1. Substrate and resist preparation

The methods of cleaning and resist deposition used here are based upon variations of experimental methods from the Stanford Nanofabrication Facility (SNF),[171] MicroChem Cooperation[174] and the Nanotech User Facility at the University of Washington.[175] Three different substrates were used in the current work; glass, conducting glass (ITO) and silicon. The substrates were initially cleaned by washing and sonicating in isopropyl alcohol (IPA), ethanol and finally MilliQ water. The substrates were subsequently dried on a hot plate at ~200°C for 20 mins to ensure solvent evaporation.

Resists were prepared by dissolving PMMA (950K Sigma Aldrich) in chlorobenzene at a concentration of 2 wt%. The solution was spin coated onto the clean substrate using a Laurell WS-400A-6NPP Lite Spin Coater. The substrate was placed in the spin coater and a vacuum is applied. As soon as rotation commenced 1-2 mL of PMMA resist solution was pipetted onto the spinning substrate surface. The substrate continued to spin at 3000 r.p.m. for the remainder of one minute. The spin conditions were varied to investigate the relationship between rotation speed and film thickness. The substrate was removed from the spin coater and immediately placed onto a hot plate at 170°C for two minutes to dry completely. Drying in this manner is critical as the 'bottom up' solvent removal ensures there are no bubbles in the PMMA. Thickness measurements were obtained by softly scratching the substrate surface and measuring the scratch heights using an atomic force microscope (AFM). The conditions that provide a uniform 100 nm layer of PMMA are; maximum acceleration, 255 ms^{-2}; spin speed, 3000 revolutions per minute (r.p.m.); spin time, 1 min. It is important to note that different substrates may have slight variations (±10 nm) in film thickness as measured using the AFM. Substrates were stored in a desiccator prior to use.

3.2.2. EBL: designing, exposing and developing

3.2.2.1. Pattern design

Patterns were designed using the Raith Elphy plus design program GDSII. Initially a border is defined, and the pattern is written within this area. Individual patterns are designed within a border a few hundred nanometres wide and long. Individual shapes are made with set dimensions and are designed on a single layer, and using a dose factor of 1. The designed patterns include rod, X, + and V shapes and their dimensions are listed in Table 3-2. The 'overlaps out' option is extremely useful and removes any overlaps to a single layer exposure. Large regular pattern arrays are produced by creating a unit cell of the design, which is transformed into an array of the desired 'write field' size using a 'structure reference', which determines the number and spacing of cells in the U and V directions. U and V correspond to the X and Y axis respectively. The write field is the exposure area that corresponds to a magnification at which patterns are exposed. Using smaller writefields has the advantage of higher resolution structures, but requires a lot more patterns to cover a given area. Here, a 25μm^2 write field is used for all structures designed.

Table 3-2: Designed pattern dimensions. Where a single aspect of the structure is an arm; X's consist of two arms crossed at the centre and V's contain two arms joined at the ends.

Pattern	Border UxV (μm)	Structure Dimensions LxW (μm)	Spacing (UxV) (μm)	No. of Structures in 25μm Write Field (UxV)
Rod1	0.05x0.2	0.2x0*	0.1x0.3	250x80
Rod2	0x0.4	0.4x0.1	0.4x0.4	80x40
X	0.2x0.3	0.36x0*/arm	0.3x0.4	79x59
+	0.25x0.25	0.15x0*/arm	0.25x0.25	100x100
X45	0.25x0.25	0.35x0*/arm	0.32x0.3	78x82
V	0.2x0.2	0.22x0*/arm	0.25x0.2	100x125
Continuous V	0.2x0.2	0.22x0*/arm	0.2x0.2	125x125

* 0 corresponds to a single e-beam line, the minimum line width.

3.2.2.2. Pattern writing

A Raith Elphy Plus Nanolithography System attached to a Zeiss Supra 55VP scanning electron microscope (SEM) with a Schottky field emmision gun was used for EBL. Samples were secured onto an EBL stage along with a reference sample called a 'chessy' piece. The stage was then mounted in the SEM and initialised. An accelerating voltage of 20 keV with a 30 μm aperture was selected, which is the highest accelerating voltage usable with the Zeiss Supra 55VP using the In-Lens secondary electron detector. The electron beam was allowed to stabilise up for a minimum of 20 minutes.

The write field was then aligned using the chessy piece. The align write field procedure was undertaken using a 25 μm width of field for all pattern exposures, while the 100 μm write field procedure was used for the standard 'dose test'. This write field allows the pre-made dose pattern to be run, allowing approximate dose requirements to be clearly found for any exposures used with different experimental conditions. The origin was then set at the bottom left corner of the sample. Adjusting the UV global rotates the patterns so they match the alignment of the sample. The 'two point adjust' UV global was used, with point 1 the origin and point 2 the lower right corner. After this stage the beam, stage and sample were all aligned.

The final procedure before exposure was to measure the beam current. The stage was driven to a Faraday Cup and the beam current was measured. The beam current was monitored until the beam stabilised to ±1 pA. The beam current was input into the dose calculation software, and the dwell time for area, line and dot was recalculated.

Table 3-3 identifies the optimum base dose conditions for 20keV accelerating voltages. The beam speed is a dependent variable and changes with altering dwell time. Except for the beam current and dwell times, these conditions were kept constant for all patterns.

Table 3-3: Sample dose conditions for 20 keV accelerating voltage, with 465 pA beam current.

20keV Dose Settings	Area	Line	Dot
Step Size	0.02 μm	0.01 μm	----
Dwell Time*	0.001720 ms	0.001290 ms	0.430107 ms
Dose	200 μAs/cm^2	600 pAs/cm	0.2 pAs
Beam Speed	11.628 mm/s	7.75 mm/s	----

* The dwell time is recalculated for each new beam current.

The equations used to calculate the dwell time are;

$$Area\ Dose = \frac{Beam\ Current \times Dwell\ Time}{Step Size^2} \quad \textbf{(3-1)}$$

$$Line\ Dose = \frac{Beam Current \times Dwell\ Time}{Step\ Size} \quad \textbf{(3-2)}$$

$$Dot Dose = Beam Current \times Dwell\ Time \quad \textbf{(3-3)}$$

Exposure was then performed. The stage was driven to the origin and the beam focused onto the sample, tighter focusing resulted in higher resolution structures. Once focused, the stage was driven to a co-ordinate on the sample and the beam blanker was used to briefly check for satisfactory PMMA coverage and that the surface was free of contamination. The desired pattern was added to the position list, the UV co-ordinates were set, the layer number (0 for default), and the dose factor were entered. The dose factor is a factor of the conditions set previously in Table 3-3. For example, with a 20keV accelerating voltage and a dose factor of 1 the actual dose is 200μAs/cm^2 for an area pattern. If the dose factor is changed to 0.8, then the actual exposure dose becomes 200 x 0.8 = 160μAs/cm^2. By keeping the dose conditions constant and only changing the dose factor, the number of variables is reduced to one.

After one pattern had been prepared, the Select filter, matrix copy option was used to allow for the construction of a matrix of specified dimensions. The dose factors can be set with this option, to either increase or decrease the dose factor of each pattern by an amount specified. Whenever a new substrate or pattern design was used a dose test was required. A typical structure dose test took the form of a 3x3 matrix with the initial dose factor set at 0.8, and the dose increased in the U direction by 0.1 and in the V direction by 0.3, allowing doses between 0.8 and 1.6 to be tested.

After the optimum condition for a particular pattern was determined, the filter matrix copy was then used to create a large area array of the same dose. A 15x15 matrix was equivalent to 375 μm^2 pattern. After exposure, both the dose test and large area patterns require development before inspection.

3.2.2.3. Pattern development

After the sample was removed from the microscope, it was placed in a solution of 1:3 methyl isobutyl ketone (MIBK): 2-propanol (IPA) for 30 seconds. Immediately following this the sample was immersed in a stopping solution (IPA) for an additional 30 seconds and then blown dry with N_2. The sample was then remounted in the microscope and briefly imaged to check the structure and determine the optimum dose for the dose test or full coverage for large area exposures.

3.2.2.4. Other EBL exposure considerations

Other exposure parameters were investigated including the effect of dose using different substrates, different chamber pressures and different accelerating voltages.

The effect of different dose requirements for 100 nm of PMMA on different substrates was investigated, where the minimum structure width was obtained for each substrate and the dose for each recorded and compared. The substrates investigated were gold, silicon, glass and glass coated with ITO.

Using variable pressure (VP) mode with EBL allows for the rapid removal of charge build-up on the surface but is accompanied by a loss of structure resolution. The working distance was set across all exposures to 8 mm. High vacuum (HV) (7.5×10^{-6} Torr) condition patterns were exposed on silicon, glass and ITO glass. Variable pressure (VP) (0.3 - 0.5 Torr) condition patterns were exposed on silicon and glass. The accelerating voltage was set to 20 keV and detection was carried out for variable pressure lithography using variable pressure secondary electron detector (VPSED). The relationship between beam current and chamber pressure was also investigated.

Lower accelerating voltages were investigated due to the smaller interaction volume obtained. They were investigated to determine if any improvement of structure dimensions and, ultimately, in the 'lift-off' process occurred by creating an overhang. An accelerating voltage of 10keV was investigated. The dose conditions used for 10kV

patterns were: Area Dose = 100 μAs/cm^2, Line Dose = 300 pAs/cm and Dot Dose = 0.1 pAs. The step size was the same as in Table 3-3 and the dwell time was varied according to the beam current. The Casino modelling program v.2.42 which uses Monte Carlo simulations to simulate beam-sample interaction was used to model the interaction volume and the energy density of the experimentally used doses. 1.2 million electrons were used in the 20keV model and 0.6 million electrons in the 10keV model. A beam radius of 1 nm was used.

Some samples were plasma cleaned for 1 minute in air prior to metal deposition. This process reduced organics in the holes in the structure and improved metal binding. Final structures with and without plasma cleaning were investigated.

3.2.3. Metal deposition

Two types of metal deposition were used; sputtering and thermal evaporation. Thermal evaporation was undertaken using a Denton DV502 Turbo Deposition System with two sources. These sources were filled with gold and chromium. The samples were placed underneath the two metal sources and the chamber was evacuated to a pressure of 10^{-5} Torr. Some samples had an initial 2-4 nm layer of chromium deposited followed by 50-60 nm of gold at a rate of 1-2 Ås^{-1}. Some samples had only gold metal deposited. Sputtering was undertaken using a Dynavac CE12-14s Evaporation System. Metal thicknesses and deposition rates were measured using an attached quartz crystal microbalance.

An investigation was conducted into the use of gold growth solutions to bridge the gap between the individual gold particles. Four substrates were immmersed into two different concentrations of gold growth solutions and two substrates were heat treated. The growth solutions were made using 0.364g CTAB followed by 10μL of 0.1M $HAuCl_4$ in solutions 1 and 3 and contains 50μL in solutions 2 and 4. 15μL of 0.1M ascorbic acid was then added to solutions 1 and 3 and 55μL was added to 2 and 4. 10μL of silver nitrate was added to 1 and 3 and 50μL of silver nitrate was added to 2 and 4. The composition of these solutions is derived from those used to make gold nanorods by the wet chemical method. Two substrates were heated in a furnace at 200°C for ½ hour and deposited in solutions 1 and 2. The substrates that were not heated were placed

in solutions 3 and 4. All samples were then left in solution for 24 hours before being removed, washed and imaged.

3.2.4. 'Lift-Off'

The 'lift-off' process is the removal of the remaining e-beam resist. Specimens were sonicated in acetone until large areas of gold were removed. Times in solvent varied from seconds to ~20 mins. The sample was then imaged to determine structure shape and dimensions.

3.3. Results and Discussion

Patterns generated in PMMA were used to compare the effectiveness of different EBL techniques. Specifically, these include the use of variable pressure compared to high vacuum on a standard substrate (conducting or semiconducting) and on an insulating substrate, glass. Accelerating voltages of 10 and 20 keV are compared, and the corresponding pattern resolution is determined. The dose requirements are examined for different structures; silicon, glass, gold and conducting glass. The effect of using plasma cleaning to remove surface contamination, and removing PMMA molecules from the pattern surface is investigated. A comparison of different metal deposition techniques and different binding metals is undertaken.

3.3.1. PMMA e-beam resists

The electron beam resist is an important feature in the EBL process. Uniform film thickness permits large areas of substrate to be patterned and cleanliness of substrate allows strong resist binding and a smooth resist surface. Figure 3.2 shows the relationship between rotation speed of the spin coater and the corresponding PMMA film thickness. It was found that PMMA was ~100 nm thick when the ITO coated glass substrate was rotated at 3000 r.p.m. Similar conditions for silicon produced PMMA films of similar thicknesses.

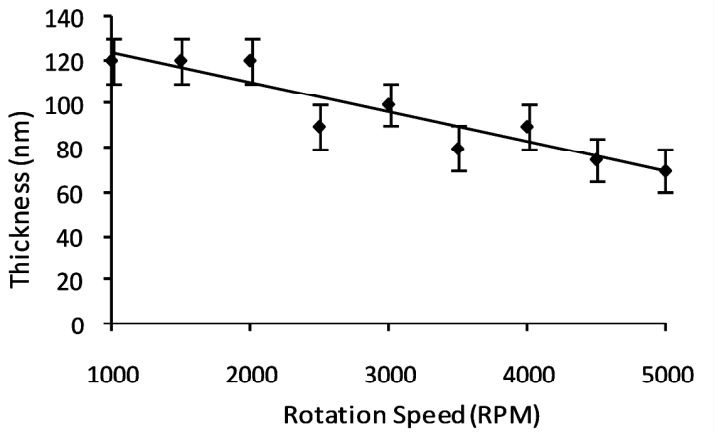

Figure 3.2: Relationship between spin coating speed and PMMA resist thickness using a 2 wt% PMMA in chlorobenzene solution. Film thickness was measured with an AFM.

The lifetime of the resist is of particular interest. A PMMA e-beam resist on a silicon substrate was found to have a lifetime of at least 3 years with no degradation of the sample during this time. Alternatively, PMMA on ITO coated glass was found to have a lifetime of approximately 4 weeks in air after which degradation of the PMMA film rapidly occurs. Degradation was assessed by examining the samples with an SEM, if the sample edges were clear of the resist then degradation had occurred and the sample was unusable, if the sample edges retained a resist covering then the sample remained useable. Also, the application of predetermined dose settings for various patterns produced inconsistent and incorrect structures if degraded resists were used. This problem was solved by storing the PMMA/ITO samples in a desiccator, which indicates that the degradation of the e-beam resist occurs due to the presence of water vapour in air.

Heating the sample before spin coating PMMA and after PMMA deposition has been suggested from several sources.[171,174,175] In the current work, the addition of heat before PMMA coating improved substrate binding and heating after the deposition of PMMA improved the film uniformity and reduced variability's within the resist layer due to different drying rates compared to samples prepared without heating.

Small variations in PMMA film thickness required virtually no change in the exposure dose settings. Indeed there is greater change in the exposure settings when using a different substrate rather than an additional 100 nm of PMMA. This means that if extremely high resolution structures (<20 nm) are not required, the beam can be focused in one spot and that focus can be used to pattern structures over large areas.

3.3.2. EBL structures in PMMA

This section describes the different structures lithographed in PMMA, including test structures and structures designed for their optical properties. The dose requirements and pattern resolution are examined for the purpose of determining suitable dose factors for different substrates.

Figure 3.3, shows two SEM images of the same patterns exposed with slightly different dose factors. The dose test pattern allows users to test seven different dose factors at once and therefore quickly find an approximate dose factor. Figure 3.3 (a) is a

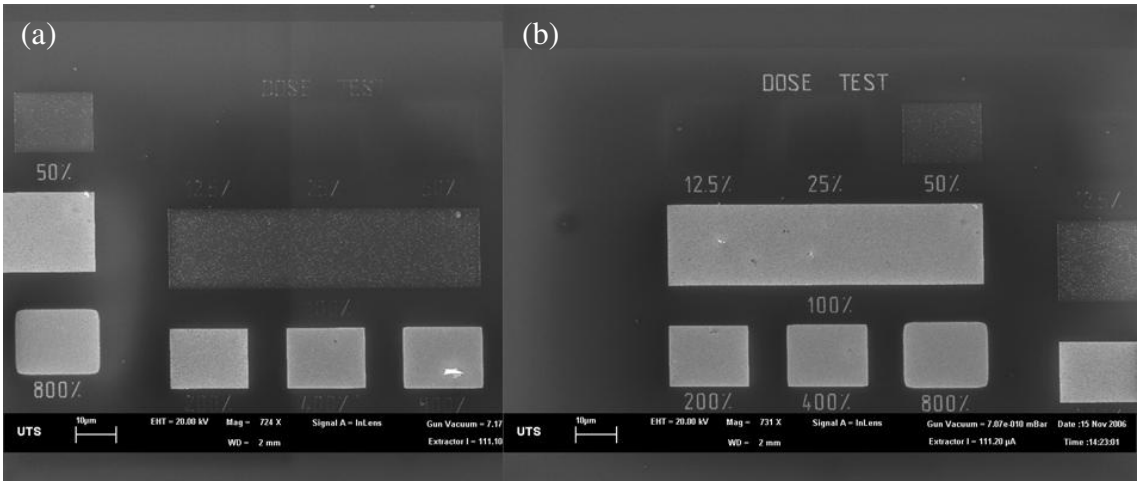

Figure 3.3: SEM images of a 20keV dose test pattern on ITO glass, with a dose factor of (a) 0.5 and (b) 1.0.

dose test with a factor of 0.5 and good quality structures are produced between 200 and 400%. Figure 3.3 (b), which uses a dose factor of 1, confirms this finding and a dose between 100 and 200% is optimal. These images also show overdosed, well- dosed and under dosed structures in the resist. In Figure 3.3 (a), the under- dosed structures are not clearly seen, including the words "DOSE TEST" (which have a dose factor of 1) and rectangles below 100%. The 800% rectangle is overdosed, which results in the curving of the corners and occurs due to reduction in the proximity effect caused by fewer adjacent exposure points at the corners and allowing the corners to be much less exposed compared to the sides. These overdosed and under-dosed effects can also be seen in Figure 3.3 (b), where structures 400% and above are overdosed and structures 50% and below are under-dosed.

Other structures produced in PMMA include line and dot structures, designed to look at the minimum line width and dot size available. Figure 3.4 shows these patterns. The measured line widths are (from left to right) 850 nm, 540 nm, 210 nm, 135 nm, 90nm, 43nm and 31nm. The final line was produced using a pattern design 0 nm wide, corresponding to 1 line with the electron beam. The dots were found to have a minimum diameter of 30 nm.

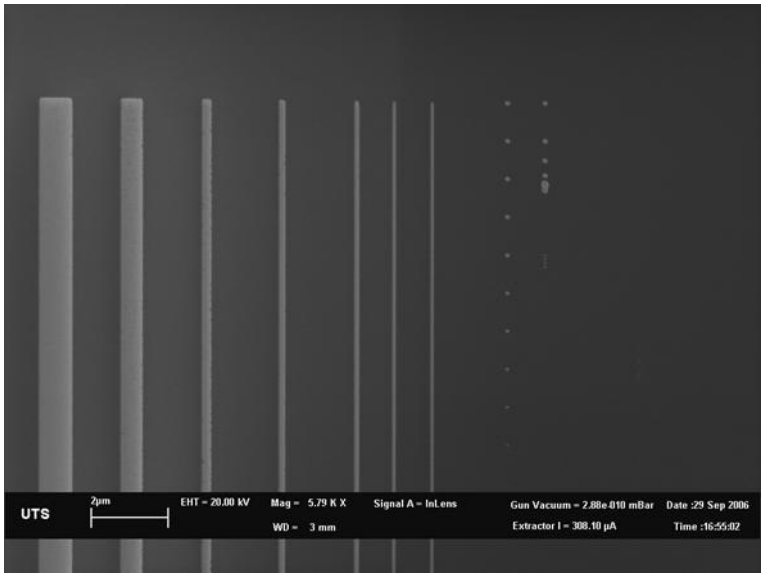

Figure 3.4 Pattern generated to measure the minimum line width and dot size on a 100 nm PMMA/silicon substrate.

Once the operating abilities of the EBL system were understood, structures were produced of more complex size and shape. Figure 3.5 illustrates the shapes produced on ITO glass for the purpose of dose investigation. In later sections, structures on substrates other than ITO glass will be discussed. Figure 3.5 shows the dose investigation for structures comprised of X shapes. These dose investigations must be undertaken before any change in pattern procedure, including design, accelerating voltage or substrate is attempted. After the trial dose structures were produced, the arm widths and lengths of each structure were measured and the complete structure with the lowest dose was typically the desired dose, allowing for production of the smallest possible structures. Figure 3.5 (c) shows an X structure with a dose factor of 1.2, where some of the lower right arms on the X's are not connected to the main body, therefore the dose factor of 1.2 is too low. In this dose test, the X's with a dose factor lower than 1.2 were unsuitable due to incomplete pattern generation, patterns with dose factors 1.3 and 1.4 are complete patterns and therefore suitable for pattern generation. In this aspect a dose factor of 1.3 was chosen to build large area arrays. These large areas are shown in later sections.

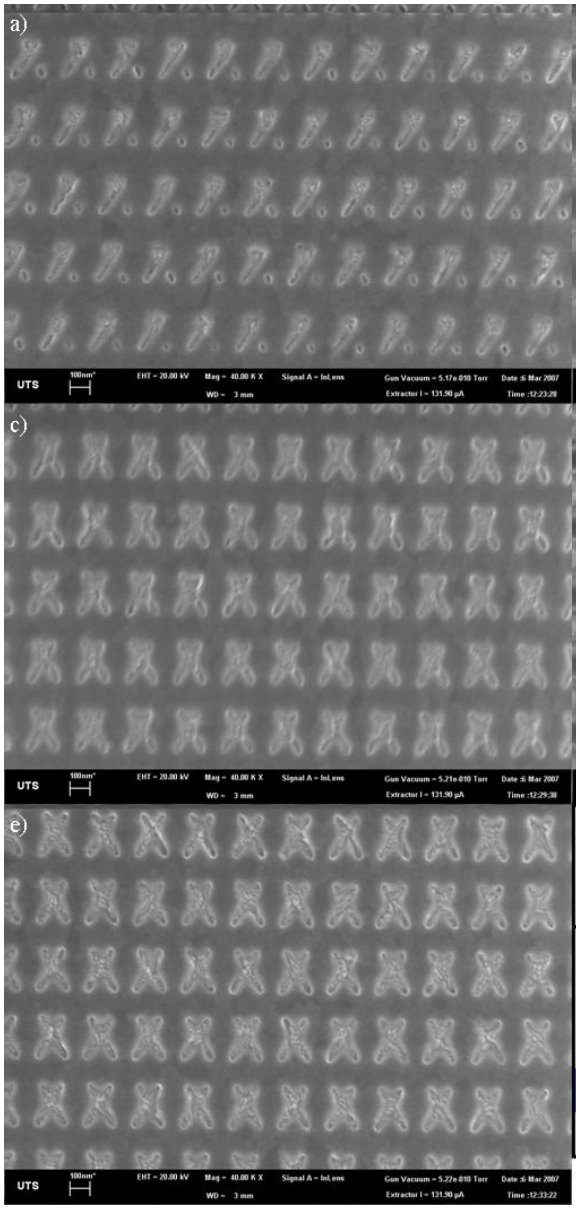

Pattern Type	Dose Factor	Arm Length (nm)	Arm Width (nm)	Complete Structure
X*	0.8	195	25	No
X*	1.0	200	15	No
X*	1.2	240	20	~70%
X	1.3	236	18	Yes
X	1.4	250	27	Yes

* Only complete arms measured

Figure 3.5: SEM images of an X structure dose test. Dose factors are: (a) 0.8, (b) 1.0, (c) 1.2, (e) 1.3 and (f) 1.4. The table above consists of measurements of arm lengths and widths obtained using software tool SmartTiff. The highlighted X structure, with dose factor 1.3 is the most suitable. The scale bars are 100 nm.

Table 3-4 displays the dose factors required for each different pattern, with an accelerating voltage of 20 keV, 100 nm PMMA resist and an ITO glass substrate. These dose factors were obtained using the dose conditions listed in Section 3.2 and the approximate dimensions were obtained using SmartTiff image processing software.

Table 3-4: Optimum dose factors of patterns exposed using a 20keV accelerating voltage into 100 nm of PMMA on an ITO glass substrate.

Pattern	Optimum Dose Factor	Approximate Arm Length (nm)	Approximate Arm Width (nm)
Rod 1	1.0	150	33
Rod 2	1.0	306	40
X	1.3	236	18
+	1.5	160	30
X45	1.2	311	34
V*	0.9	200	25
Continuous V	1.3	200	60

* Longer arm measured

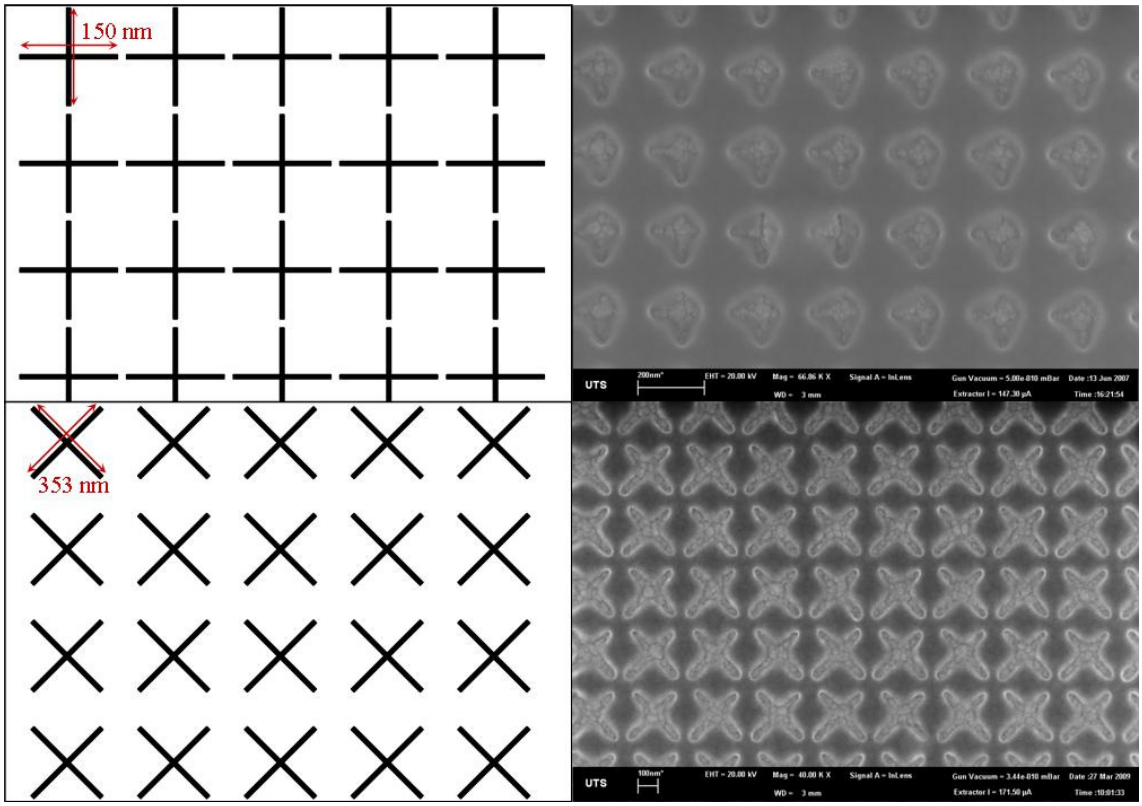

Figure 3.6: Effect of pattern variation on exposed patterns. (a) + pattern design, (b) exposed + patterns, (c) X45 pattern design (+ pattern rotated 45°) and (d) exposed X45 pattern.

It is important to note that the designed pattern is not always identical to the exposed pattern. For example in Figure 3.6 (a) the plus structure (+) was designed to cross in the middle of the two lines, however as shown in (b), the actual crossing point is towards the ends of both lines resulting in a quite different structure than that designed. It is also noted that when exposing the X structure, as can be seen in Figure 3.5, the lines also do not cross exactly in the centre. A new design was tested consisting of the + structure rotated 45°, called X45. This design, seen in Figure 3.6 (c), was produced using the same individual boundary conditions, with the designed lines extended from 150 nm to 353 nm. Figure 3.6 (d) shows that the X45 matches the design more closely than the +. As the only change was the pattern design orientation, and the EBL system can handle the crossed lines well (Figure 3.6 (d)). It is clear that problem occurs within the Raith Elphy Plus software and that it is possible to work around this particular error, as demonstrated by rotation of the structure design. Why this problem occurs is unknown, although because the patterned areas are uniform the problem is not caused by user defined variables and as rotation of the structure fixes the problem it is therefore not due to microscope hardware problems.

Some designed patterns were exposed with their optimum dose shown in Figure 3.7. The optimum dose factors for the majority of these patterns are listed in Table 3-4. Figure 3.7 (a) shows the first rod pattern designed. The surface coverage of rods was very low, with one rod (30 nm thick) every 400 nm. Figure 3.7 (b) shows rod structures, with a higher density of rods and an aspect ratio designed of 4 which, when gold is added, would give a longitudinal plasmon resonance in the near infrared. Both images were taken at the same magnification and the higher density of rods is apparent. Figure 3.7 (c) shows an array of X structures, it is also the only pattern exposed on a silicon substrate. Figure 3.7 (d) shows a sample with a much higher density of the X structures. Figure 3.7 (e) and (f) show the V structure with the ends not touching and touching respectively.

Large areas (greater than 250 μm^2) of patterns were produced in PMMA on ITO coated glass. Figure 3.8 displays several large area arrays. Each of these arrays was designed to be a 15x15 matrix of the 25 μm^2 width of field pattern design. This corresponds to 375 μm^2 of exposed pattern plus an additional micron spacing between each 25 μm^2 exposures resulting in an approximate area size of 390 μm^2 for the entire

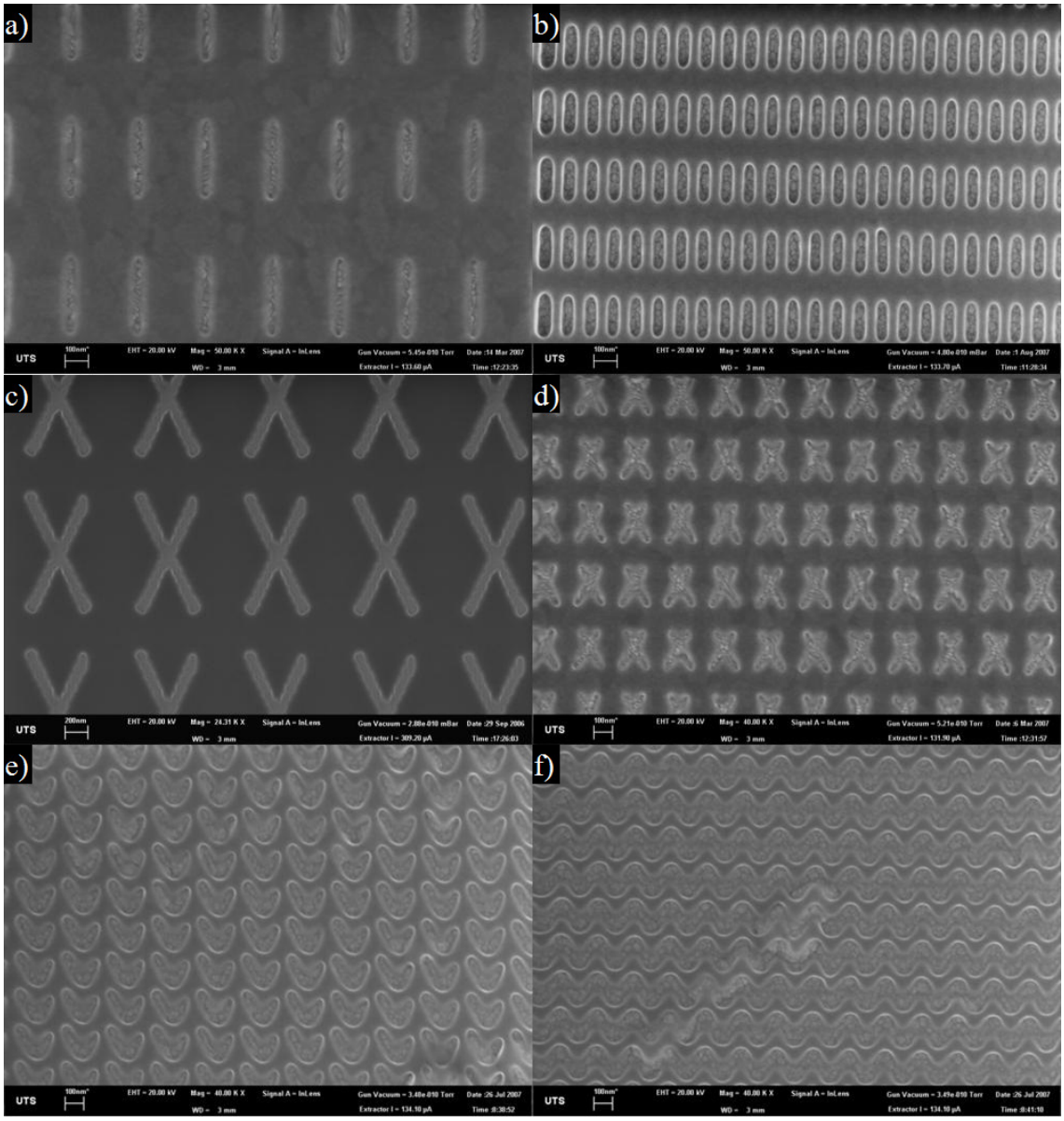

Figure 3.7: SEM images of (a) and (b) rod patterns, (c) and (d) X patterns, (e) V pattern and (f) continuous V pattern. The substrates were 100 nm of PMMA on ITO for all structures except for (c), which was on silicon.

exposure. The micron spacing between each width of field allows for small variations in the stage position, avoiding overlapping exposures. Arrays of this size and larger were chosen as they are small enough to expose in a few hours but large enough to see with the naked eye and easy to find under an optical microscope.

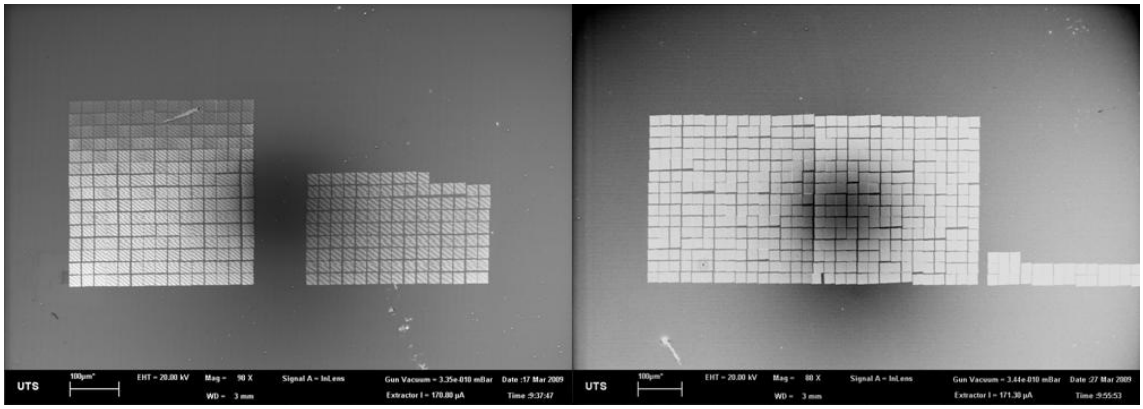

Figure 3.8: Large area exposures; from left to right rods, X's, rods, X45's and V's. The incomplete arrays are only a fraction of the size of the design due to time constraints on the SEM, and the exposures were stopped.

During the large area exposures several issues came to light. These are illustrated in Figure 3.9. These are: (a) pattern stitching miss-matches arising from stage positioning inaccuracies, (b) stage movement failures and, (c) and (d) combinations of these problems. The red box in (a) identifies an area where patterns overlap. The SEM attached to the lithography system uses a mechanical stage, which has positioning accuracy in the micron range. To avoid any significant pattern overlap, a laser interferometer stage with positioning accuracy in the nanometre range is required. It should be noted that the mechanical stage can produce structures without overlap (see Figure 3.8) but there are typically a few overlapped patterns per area. Another problem seen in Figure 3.9 (b-d) is double exposure. This occurs when the stage does not move to the next coordinates after an exposure and then the software does not recognise that the stage has not moved. In image (b) the 25 μm write field patterns were exposed vertically from the bottom left corner and the brighter squares with the red arrows are areas where the patterns are rewritten and always immediately below a exposure void (the blue arrows). Images (c) and (d) have the same problem except the patterns are written horizontally and, as such, the doubly exposed patterns are immediately to the left of the voids. This double exposure problem was mainly due to a software fault and with the latest software update[176] the number of double exposures has been reduced to a maximum of two double exposures in a total of 225 exposures.

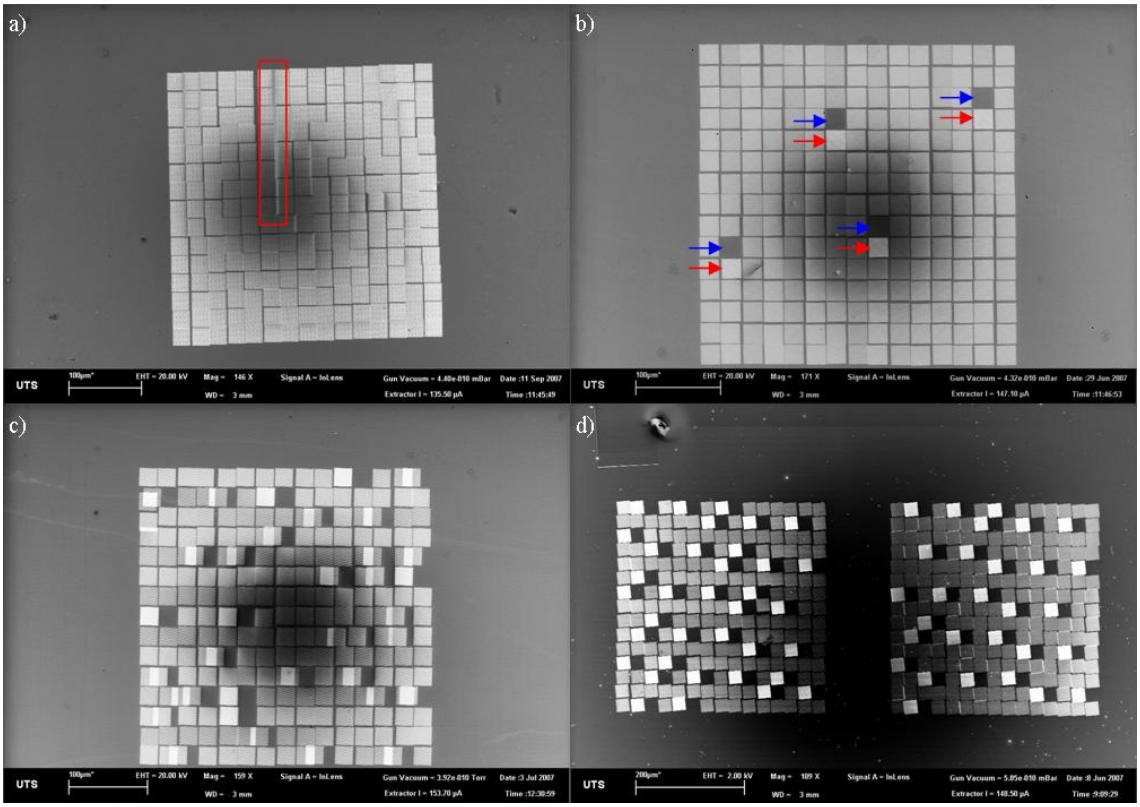

Figure 3.9: Errors with large area arrays, (a) stitching/alignment errors, (b) stage movement errors, (c) and (d) worst arrays produced.

When writing a large area array, the list of exposures was selected and scanned. The stage was then moved to the 25µm write field coordinates and a three second delay was used to ensure stage backlash did not interfere with the final stage position. If the stage was not within the defined position variance then an error was recorded and the software moved onto the next pattern. If the stage was positioned within variance values (± 5 µm) then the pattern was exposed. Occasionally an error may occur during the stage movement process. This happens when the stage movement dialog box stays open even when the stage has finished moving and the whole process freezes. To fix this problem, the stage movement was cancelled and the pattern was rerun. However, preventing this problem occurring has not been solved, but the frequency of this problem has been reduced with software upgrades.

3.3.3. High vacuum (HV) vs. variable pressure (VP) in PMMA

Silicon and glass substrates were spin-coated with 100 nm PMMA. Three different patterns were selected for comparisons between glass and silicon substrates and high

vacuum (10^{-5} - 10^{-6} Torr) and variable pressure (1 - 0.1 Torr) chamber conditions. The exposed designs were carried out twice on the same substrate, once under high vacuum and once under variable pressure. Several EBL runs were carried out to find the optimum dose conditions for each pattern, which are found when the exposed pattern was the same size and shape as the pattern design. Comparisons consisted of evaluations between the same exposed patterns in PMMA, especially the smallest resolvable feature size, resolution, sharpness, accuracy and consistency.

The beam current, the amount of electrons hitting the substrate surface over time, depends upon the chamber vacuum, which can slow electrons according to pressure. Figure 3.10 relates the beam current to the increasing chamber pressure. The graph shows how beam current reduced as the chamber pressure increased. The beam tip used in this experiment was quite old resulting in the beam current being lower than standard. The HV beam current used was ~190 pA. A well set tip will emit a beam current at ~300 pA at 20 keV accelerating voltage under high vacuum. This is much higher than the tip used in this experiment. The main effect of this occurs during lithography when the exposure time will be much longer than normal. Most times this will not be of any great concern unless large areas are exposed. VP-EBL on the other hand has a sharp decrease in the beam current as the chamber pressure increases, and the exposure time becomes noticeably longer, even for small area exposures. A trade-off is required with VP-EBL to achieve the required pressure to avoid charging of the sample and keeping the chamber pressure as low as possible to reduce exposure time.

Figure 3.10 shows that the beam current used for VP EBL was between 20-60 pA for pressures above 0.2 Torr whereas for HV the beam current was between 100-200 pA. Even though more electrons in HV EBL are impacting the surface per unit time it was found that the required dose factors of HV patterns are consistently higher than VP patterns. On the other hand, the lower beam current for VP lithography necessitates an increased beam dwell time.

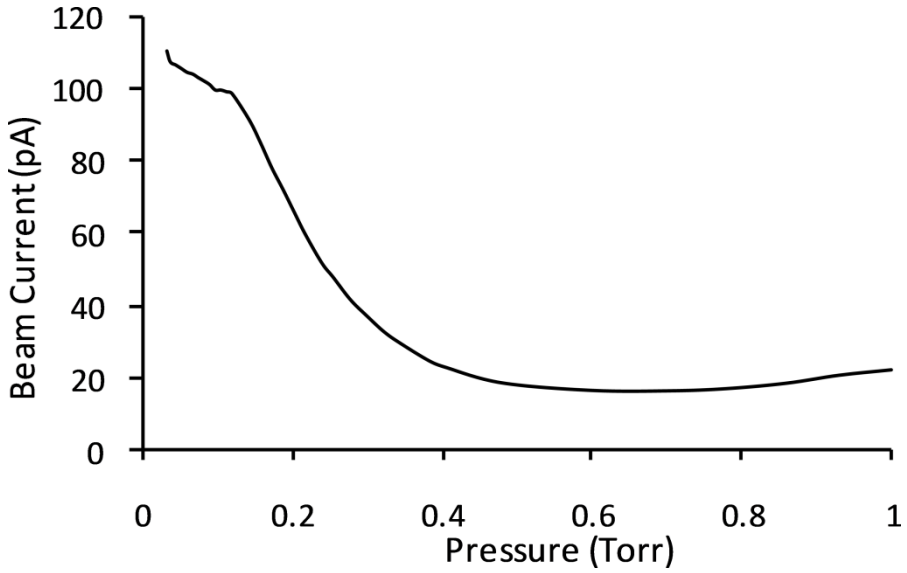

Figure 3.10: Graph of SEM beam current relative to chamber pressure for the variable pressure system.

Patterns were exposed using both HV and VP modes on a silicon substrate with 100 nm PMMA. The samples were developed and imaged under HV with a 20 keV accelerating voltage. Figure 3.11 compares HV and VP EBL with several different patterned arrays under the optimum dose conditions determined to give the highest pattern resolution and smallest structure size. The left column consists of the structures produced under high vacuum and the column on the right under variable pressure at 0.3 Torr. It should be noted that the exposure conditions used for these structures are not the optimum conditions listed in Table 3-3. The corresponding line doses for the HV structures are (a) 255 nC/cm, (c) 191.25 nC/cm, (e) 255 nC/cm compared to VP structures with (b) 127.5 nC/cm, (d) 114.75 nC/cm, (f) 127.5 nC/cm. It should be noted that the HV structures have significantly higher doses that the VP structures. Due to the beam current changing from 190 pA in HV to 37 pA in VP, the dwell time changes from 2.6 ms in HV to 12 ms in VP. Thus the exposure time of a 25µm write field rod pattern takes approximately 1 minute under HV and approximately 2.5 minutes in VP mode. This time difference is significant especially when large area structures are exposed.

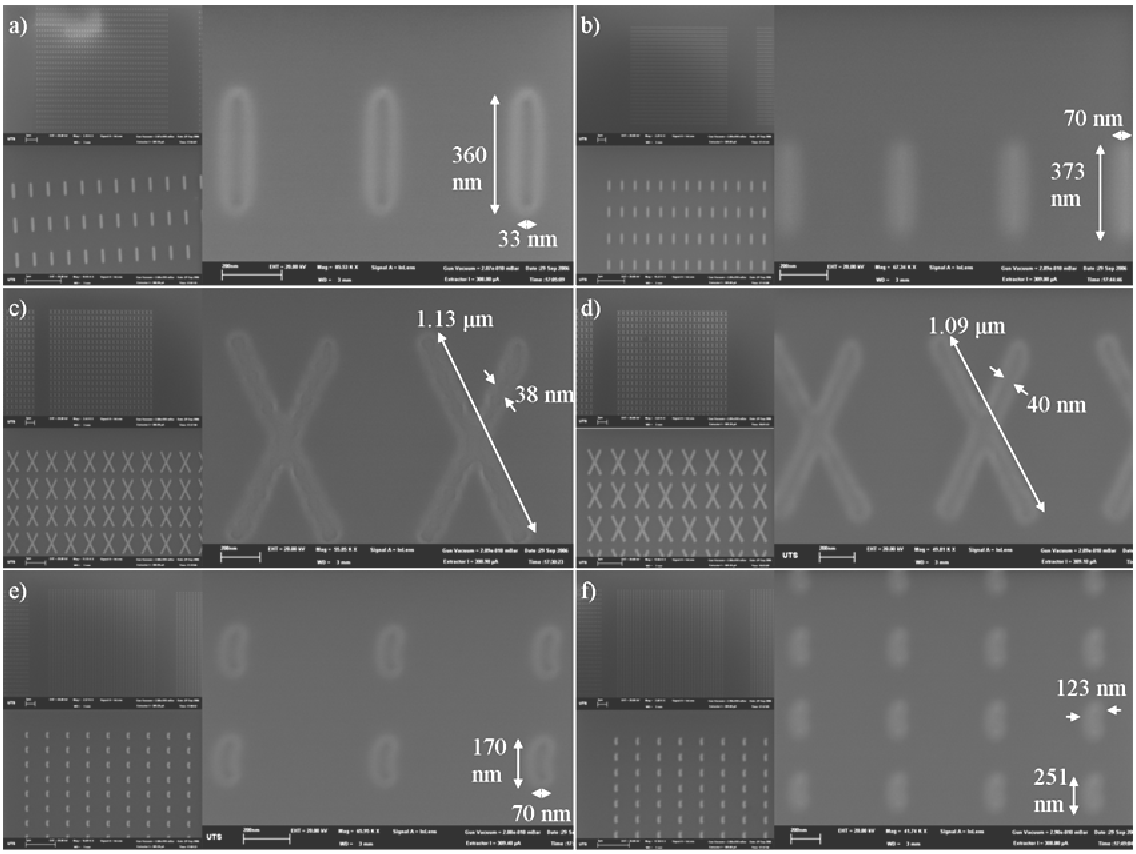

Figure 3.11: Comparison between high vacuum (a,c,e) and variable pressure (b,d,f) for three different structures; rod, X and bent.

Variable pressure lithography was also undertaken on other substrates including glass and conducting ITO coated glass. Figure 3.12 shows dose patterns exposed under high vacuum and variable pressure. The dose conditions used are listed in Table 3-3 and are the conditions recommended by Raith.[176,177] Figure 3.12 (a), HV lithography on ITO glass, shows that between 100 – 200% of the applied dose is required for producing high quality structures. This compares to Figure 3.12 (b), VP lithography on ITO glass, which shows that the 100% of the applied dose conditions produce accurate structures. As mentioned previously, although the required dose is actually less for VPEBL structures, the beam dwell time is considerably longer due to the lower intensity beam current. Figure 3.12 (c) and (d) show HV and VP dose patterns on glass, respectively. The use of 20 keV HV lithography on glass, Figure 3.12 (c), causes significant pattern distortion due to substrate charging. Therefore using EBL on a glass substrate requires some way to dissipate the gathered charge. Figure 3.12 (d) shows the dose pattern exposed under VP conditions on glass, and the resultant structure indicates that the required dose was over 800% for good quality structures. This image was obtained with a variable pressure secondary electron detector (VPSED) and as such is of lower quality

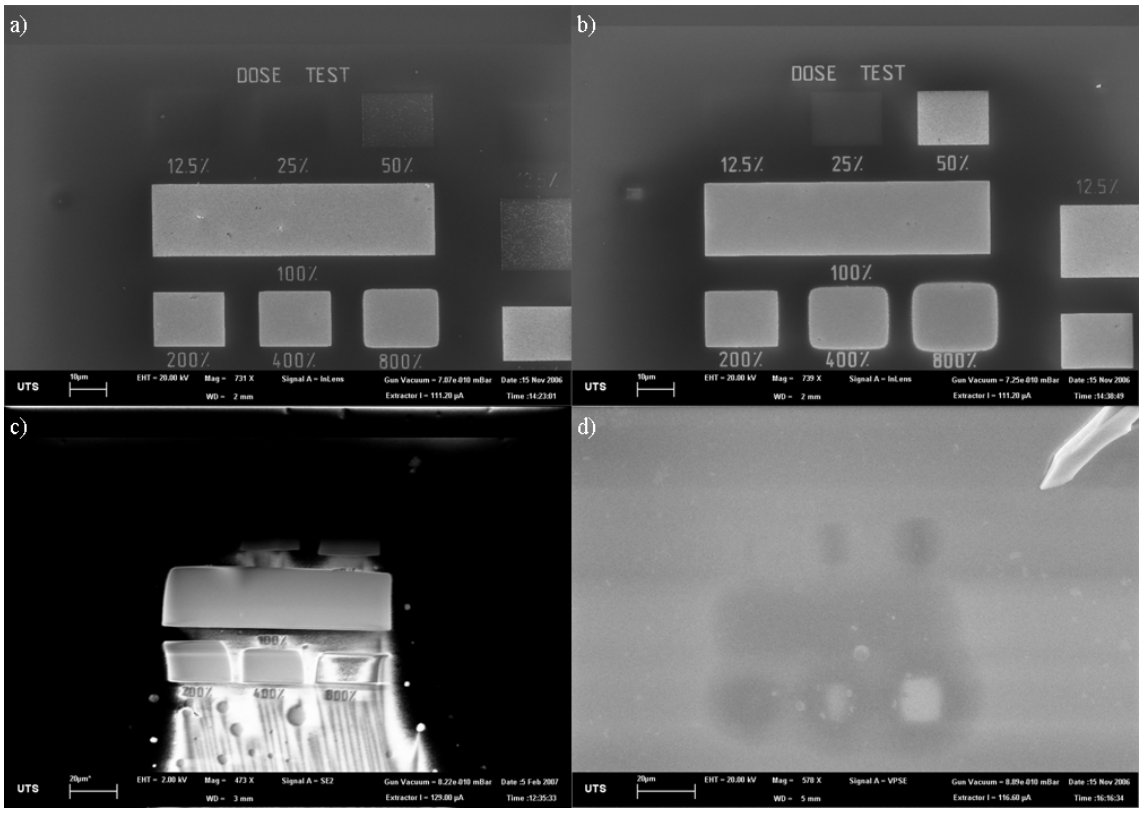

Figure 3.12: SEM images of dose tests on different substrates. ITO coated glass under (a) HV and (b) VP. Glass under (c) HV and (d) VP.

than the other images that were taken with the in-lens secondary electron detector. During exposure of Figure 3.12 (d), focusing was required to be undertaken using the VPSED and resulting in much greater time to (i) align the beam, (ii) align the writefield and (iii) obtain the high magnification focus required before pattern exposure.

After acknowledgement of the greater length of time required undertaking any sort of large area VP EBL exposure, it was decided to pursue methods which utilise HV EBL and a conducting layer to dissipate the charge. From this point the majority of EBL was undertaken using ITO coated glass substrates. ITO was chosen because it is transparent and allows for measurement of the optical transmission of the structures produced.

3.3.4. Accelerating voltage comparison in PMMA

The effect of different accelerating voltages used during exposure was investigated. The accelerating voltages investigated were 20 keV and 10 keV. Different beam accelerating voltages produce different shaped interaction volumes, and therefore

different shaped patterns may be produced. It was hoped to improve the resist overhang and thus improve liftoff. This is discussed further in Section 3.3.8.

All dose settings are changed when exposing patterns with different accelerating voltages, and the exposure conditions used are shown in Table 3-5. Each of the dose values are halved from the 20 keV exposure settings and the beam current drops by about 50 pA. These dose conditions are approximate and pattern dose factor tests are required to determine optimum dose conditions.

Table 3-5: 10 keV dose parameters, with a 280 pA beam current measured.

10keV Dose Settings	Area	Line	Dot
Step Size	0.02 µm	0.01 µm	----
Dwell Time*	0.001429 ms	0.0010714 ms	0.357142 ms
Dose	100 µAs/cm^2	300 pAs/cm	0.1 pAs
Beam Speed	13.996 mm/s	9.337 mm/s	----

* Dwell time recalculated for each new beam current.

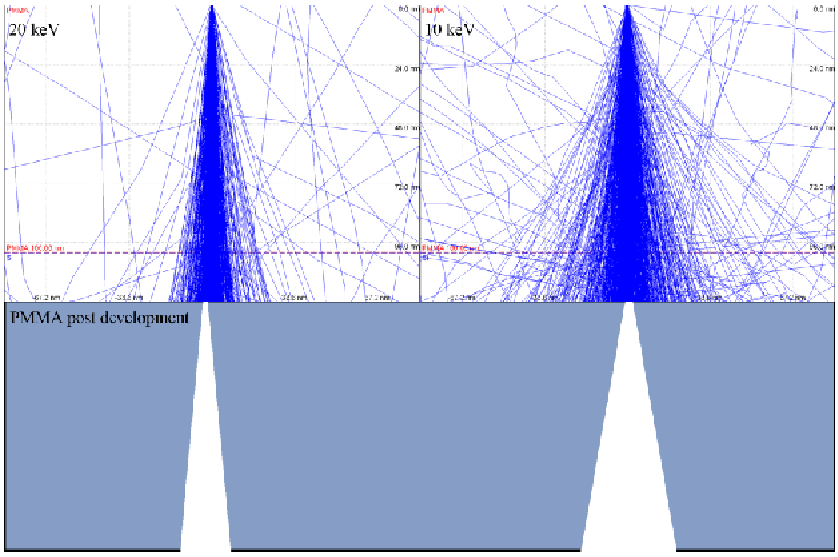

Figure 3.13: Interaction volume simulation into 100 nm PMMA on a silicon substrate with accelerating voltage 20keV on the left and 10keV on the right. The bottom shows the shape after development for the corresponding 20keV and 10keV beams holes.[178]

Figure 3.13 shows a simulation of 2000 electrons with accelerating voltages of 20 keV and 10 keV. Directly beneath the simulation is an illustration of the shape of the post exposure and development of the PMMA. The shapes of the voids correspond to the shapes of the simulation interaction within the PMMA space.

Using the dose values for both 20 keV and 10 keV, the number of electrons hitting the sample at a point was determined to be approximately 1.2 million electrons for the 20 keV exposures and 0.6 million for the 10 keV exposures. These electrons were then modelled using the casino modelling program[178] which uses Monte Carlo simulations to investigate the interactions of the electron beam into the sample. Figure 3.14 consists of the energy distribution of a 20 keV accelerating voltage (a) depth profile and (b) surface profile and a 10 keV accelerating voltage (c) surface profile and (d) depth profile. The depth of the energy distribution interaction is much lower with the 10 keV, showing 535 nm depth for ¼ of the energy remaining compared to 20 keV accelerating voltage with 1765 nm depth for the corresponding energy depth. The beam spot size with 25% energy remaining has a radius of 272 nm for 20 keV and 50 nm for 10 keV. The actual area that is removed in the development processing step is smaller and, as such, needs greater energy than 25% to cleave the PMMA polymer bonds.

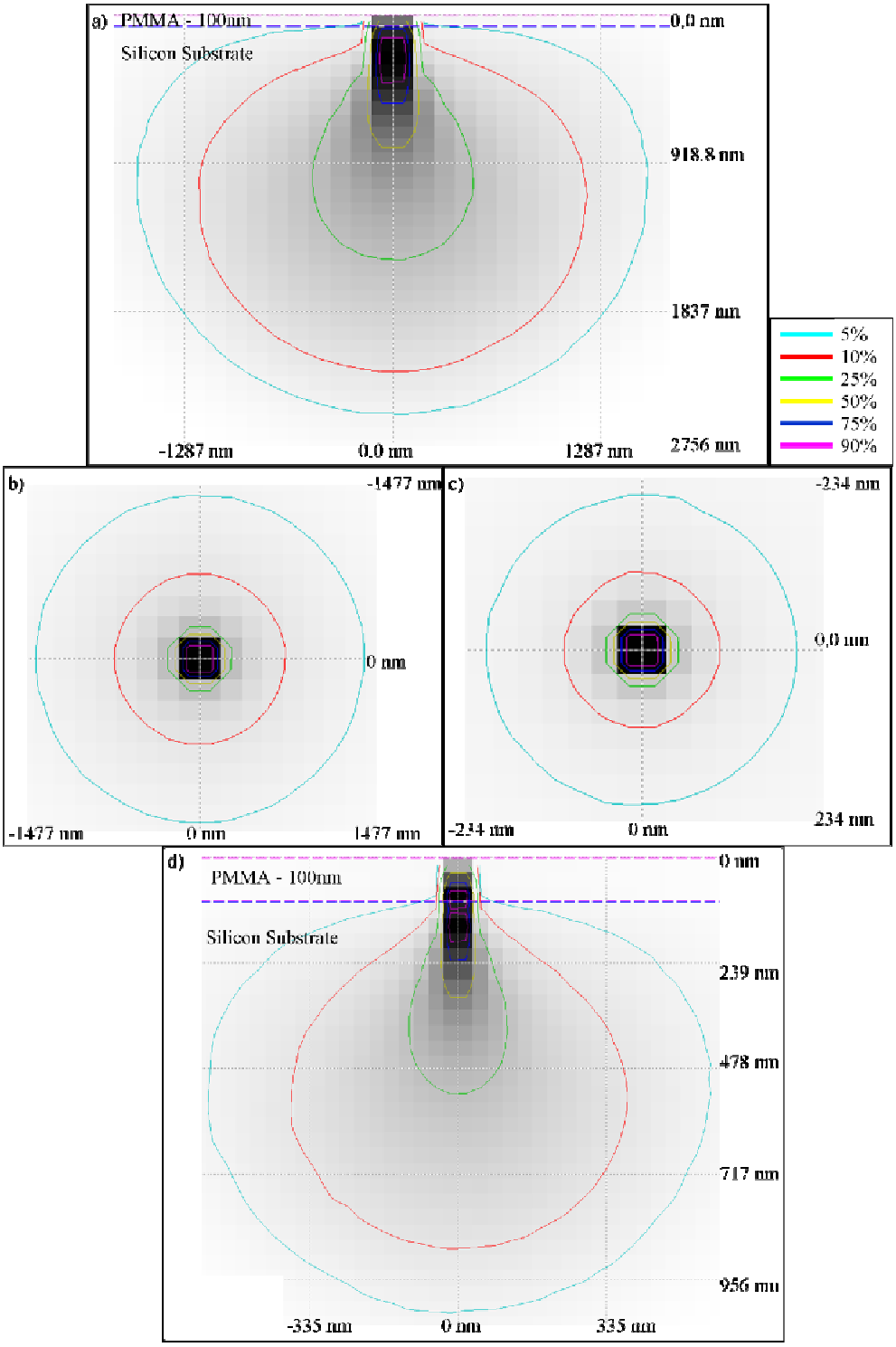

Figure 3.14: Energy distribution of electron beam interaction into 100 nm PMMA on silicon with (a, b) 20 keV and (c, d) 10 keV accelerating voltage using Monte Carlo modelling. (a, d) show the depth distribution and (b, c) show the surface distribution.

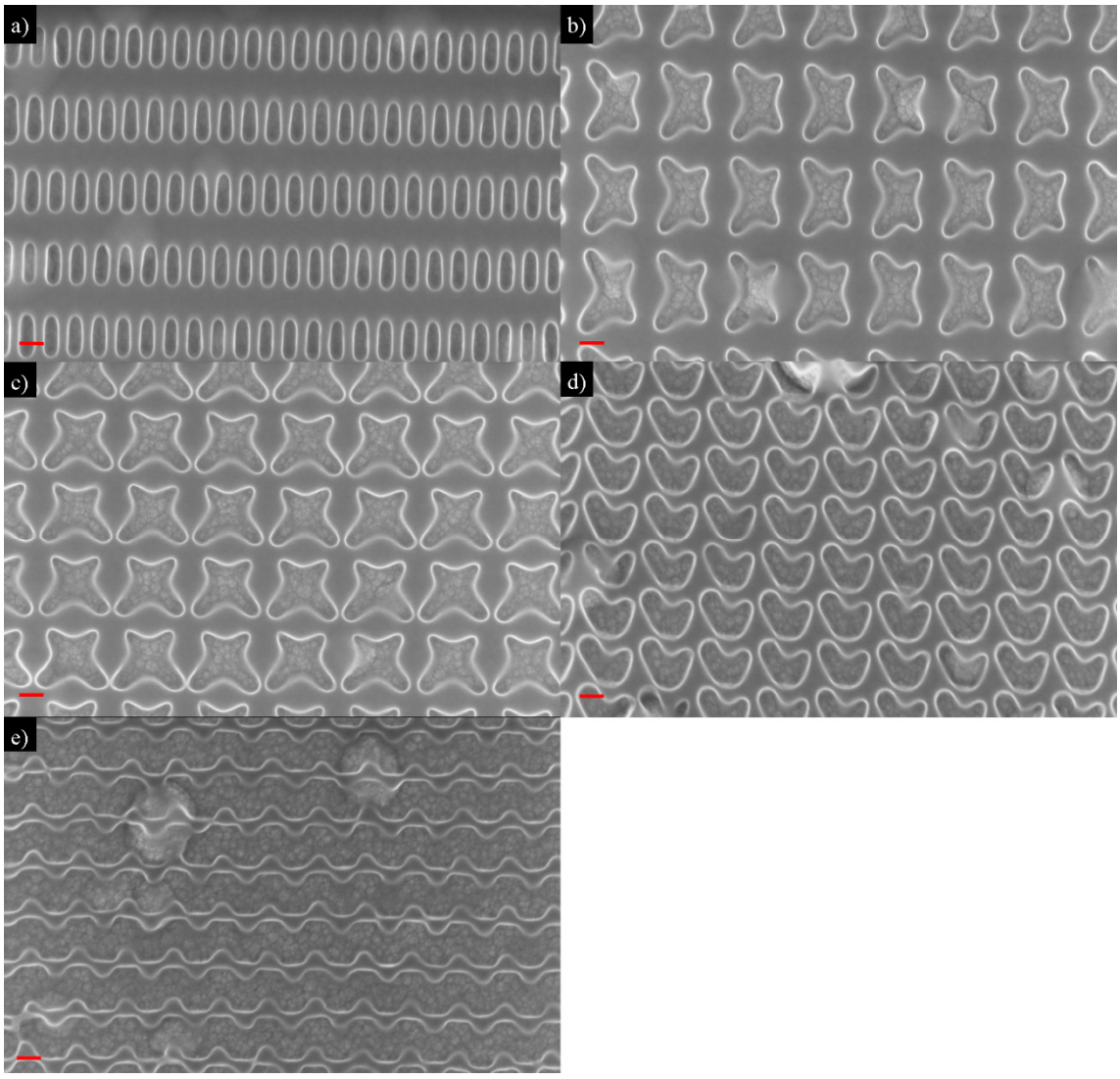

Figure 3.15: Patterns exposed in 100 nm PMMA on ITO glass with an accelerating voltage of 10 keV and under HV. Patterns include (a) rods, (b) X's, (c) X45's, (d) V's and (e) continuous V's. The scale bars are 100 nm.

Some 10 keV exposure structures are shown in Figure 3.15. Examination of these samples reveals some differences compared to 20 keV patterns, shown in Figure 3.7. The rods in Figure 3.15 (a) are less uniform that those fabricated with 20 keV patterns. Figure 3.15 (b) and (c) in particular and to a lesser extent (d) and (e) have corners that are much rounder than 20 keV patterns. This is due to the lower penetration of the beam and more electrons exposing in closer proximity. The proximity effect is much greater when writing with lower accelerating voltages as there is a greater concentration of electrons at or near the surface where the resist is exposed.

Table 3-6: Pattern dose test at 10keV accelerating voltage.

Pattern @ 10 keV	Dose Factor	Dose (nC/cm)	Structure Size (nm)[1]		Structure Size Comparison for 20keV Patterns (nm)[1,3]	
			Length	Width	Length	Width
Rods	1.2	0.36	155	50	-----	-----
	1.3	0.39	160	55	155	45
	1.4	0.42	170	55	175	50
	1.5	0.45	180	60	175	50
X's	1.4	0.42	300	50	250	25
	1.5	0.45	310	50	250	30
	1.6	0.48	310	50	250	35
	1.7	0.51	320	60	-----	-----
	1.8	0.54	330	65	-----	-----
X45's	1.3	0.39	295	50	290	30
	1.4	0.42	305	55	305	35
	1.5	0.45	315	65	315	45
	1.6	0.48	320	70	330	45
	1.7	0.51	325	75	----	----
V's[2]	1.4	0.42	210, 175	75	215, 185	70
	1.5	0.45	215, 180	85	225, 195	60
Continuous V's	1.4	0.42	205	130	240	60
	1.5	0.45	190	115	225	55

[1] Structure lengths have been rounded off to the nearest 5 nm. Measurements were arm length and arm width where appropriate.

[2] Arm lengths are two different lengths.

[3] Doses used are listed in Table 3-3 and multiplied by the corresponding dose factor.

Table 3-6 contains the dose tests for the patterns written at 10 keV accelerating voltage. The dose factors are written as a factor of the dose parameters displayed in Table 3-5. The structure sizes were measured according to arm length and width where appropriate and the highlighted sections are the best quality pattern in terms of both minimum resolution size and pattern uniformity. The corresponding 20 keV patterns are also listed where the patterns were undertaken at that specific dose factor. It is important

to note that although the dose factor might be the same, the exposure conditions were those for the 20 keV exposures.

It was discovered that the patterns on 10 keV exposures were not as uniform and in particular there were areas with bulges in the structures indicative of problems caused by the proximity effect. Also caused by the proximity effect in the 10 keV exposures was the inability to create patterns with sharp points, seen in the X and V patterns; the ends were always significantly more rounded than 20 keV exposures. Proximity effect was more pronounced with the higher accelerating voltage exposures. This may be due to the electrons being dispersed further into the sample with the higher accelerating voltages and more electrons remaining near the surface with lower accelerating voltages. This could be accounted for with either proximity effect correction software or adjustment of the pattern through changing the dose factor at specific points on the individual structure.

3.3.5. Effect of substrate on dose requirements

Different substrates were found to significantly contribute to the variations in required dose characteristics. Patterns on ITO coated glass, gold and silicon substrates were investigated. All substrates were covered with approximately 100 ± 10 nm thick PMMA.

Table 3-7: Comparison of dose factors required for different substrates.

Pattern	ITO	Silicon	Gold
Dose Test	1.0-2.0	1.0	0.5
Rods	1.4	1.0	----
Circles	----	1.5	1.0
Squares	----	1.0	0.4

Table 3-7 compares different dose factors required for the listed patterns on the different substrates. It can be generally observed that the dose requirements for patterns on a gold substrate are typically less than either ITO glass or silicon substrates. The circles are the only pattern which requires an exposure with a dose factor of 1 and this is only required because the circles are deliberately over exposed for all substrates. This was done because at smaller doses a ‘pac-man’ like structure often forms due to the

circles not being completely exposed. These circles can be seen in Figure 3.16 with the 'pac-man' in image (a) and the overexposed circle in (b). The circles are exposed through a series of concentric rings and when the dwell time is insufficient the rings are not completed. To fix this problem the circle pattern is deliberately overexposed so that the proximity effect completes the circle structure. Another option is to manually increase the dwell time for the circle structure. This direction was not chosen so as to ensure the exposure parameters are all consistent with the dose factor the only variable. The silicon substrate has a dose factor of near 1 which is consistent with the fact that the dose parameters recommended by Raith are designed for silicon substrates. ITO coated glass substrate required dose factors higher than those required for silicon substrates.

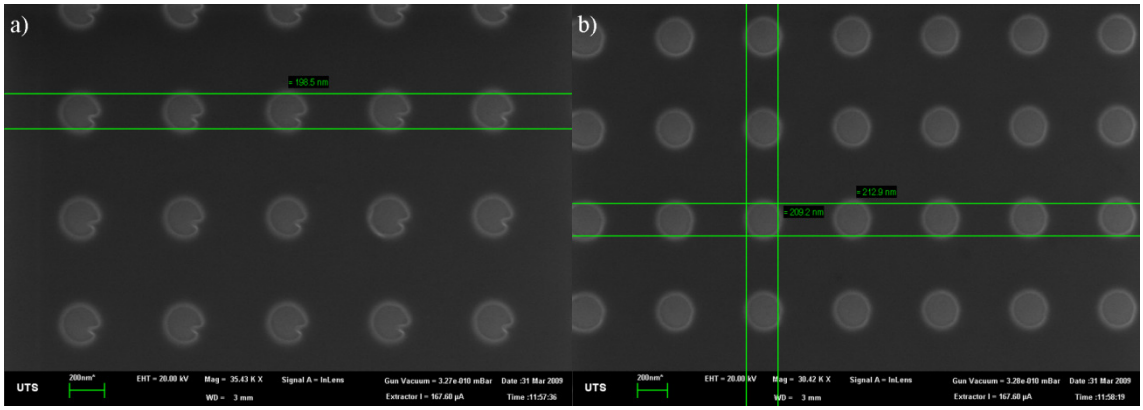

Figure 3.16: SEM images of an array of 200 nm circles using 20 keV accelerating voltage in 100 nm PMMA on a silicon substrate. Image (a) has a dose factor of 1 and (b) has a dose factor of 1.5. The scale bars are 200 nm.

A simulation of 1000 electrons onto different substrates using the Casino modelling program can be seen in Figure 3.17. The substrates are the same as those listed in Table 3-7; silicon, ITO glass and gold. The collisions at the interface between the PMMA and the substrate show that the number of backscattered electrons (BSE) increases significantly as the atomic number of the substrate increases. This is due to the greater possibility of collisions occurring near the surface when the atoms are larger. The gold substrate has by far the most BSE, with a mean BSE coefficient of 0.47, and of high enough density that the BSE contributes to the PMMA chain scission and thus the exposure. This is consistent with the observed required dose whereby the gold substrate required a significantly lower dose. Although the ITO glass substrate has more collisions and greater number of BSE paths than the silicon substrate, near the incident beam where the developed PMMA becomes a hole there is a greater number of

collisions on the silicon substrate than the ITO glass substrate. Thus the ITO dose required was slightly higher than that for silicon.

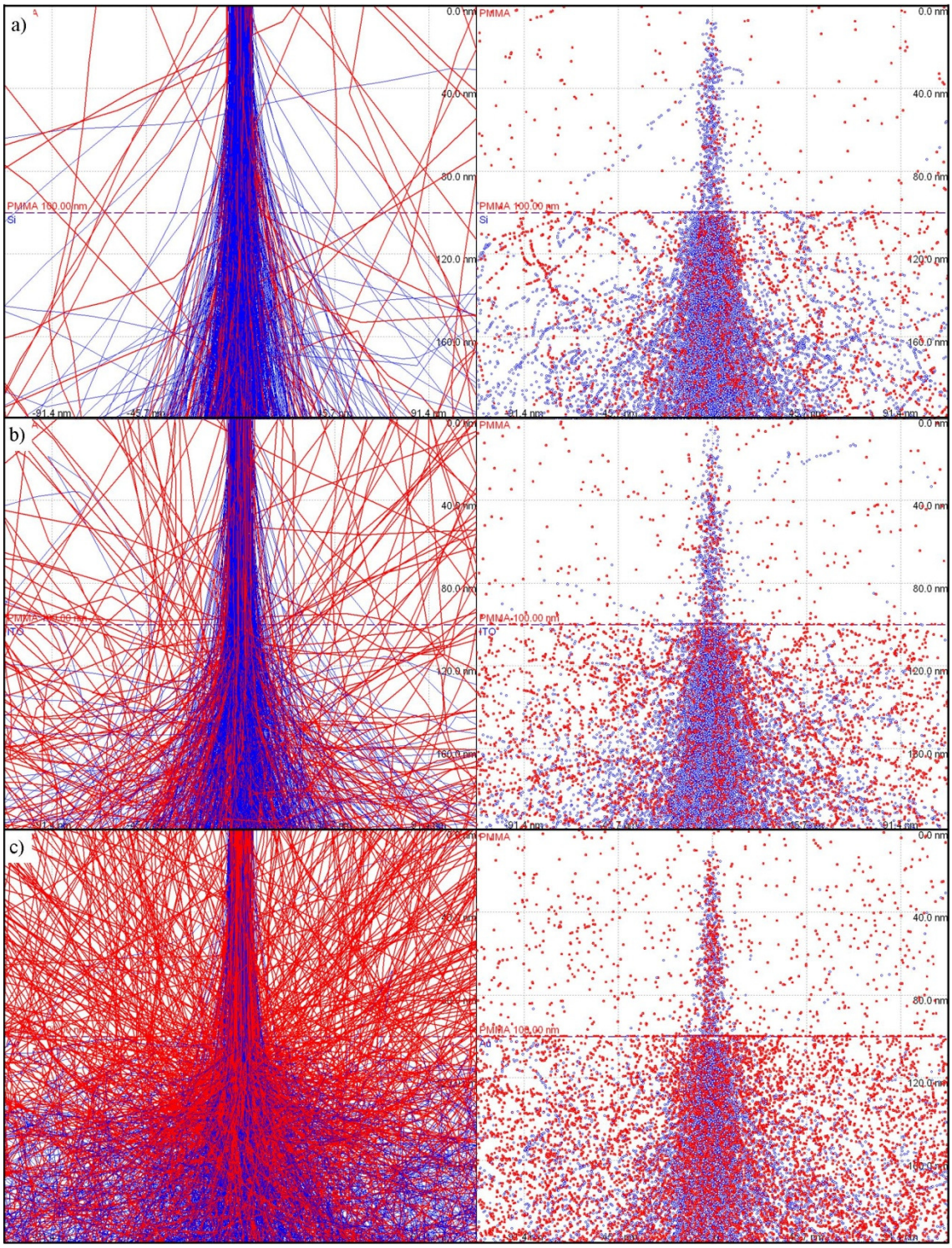

Figure 3.17: 1000 electron Casino simulations into PMMA on (a) silicon, (b) ITO glass and (c) gold. The left column consists of the electron paths with blue the incident electrons and red the backscattered electrons and the right column show only the collision points.

The majority of polymer chain scission comes from secondary electron (SE) interactions with the PMMA film. The secondary electrons are electrons that are excited by the beam electrons (also called the primary or incident electrons). An excited secondary electron is able to excite more secondary electrons and thus expose more of the resist. Therefore for EBL the position of the collisions is more important than the placement of the electron paths. The number of initial electron collisions simulated in Figure 3.17 is similar across all substrates. The effects that the different substrates have are the number of collisions at the interface between the PMMA/substrate and the number of BSE created in the substrate. When the gold substrate is simulated there are significant BSE electron collisions across the entire shown region and where the incident beam strikes the PMMA the number of BSE collisions overshadows that of incident electron collisions. The greater number of collisions in an area results in more SE2 electrons, which are more likely to break down the PMMA.

Different substrates required different dose conditions and when a pattern was exposed on a new substrate dose tests for that pattern were required. Advantages of using higher atomic number substrates, like gold, include the significant reduction in exposure time. For example, the time taken to expose a 25 μm^2 writefield of squares takes 20 – 30 seconds on a gold substrate and about 1 minute on a silicon substrate. Over a large area this amounts to a very significant time saving. Disadvantages due to these substrates include less time required to cause sample damage or unnecessary exposure when setting up a run and less imaging time available to investigate the exposed structures in the polymer.

3.3.6. Effect of plasma cleaning

Plasmas are ionised gases in which a portion of electrons are free rather than bound to form a gas of electrons and nuclei.[179,180] One method to generate a plasma uses a high frequency antenna to inductively couple an oscillating electromagnetic field. Different gases react chemically with different materials. Oxygen plasma is suitable for removing hydrocarbon contamination; the oxygen reacts with the hydrocarbons, converting them to CO, CO_2 and H_2O gas which are pumped out through the vacuum system.[181,182]

Plasma cleaning was investigated in two different aspects. One was to remove beam contamination and determine if contamination had an effect on the deposited gold

structure. The other was to apply plasma cleaning to the developed structures to determine if improved binding resulted from removal of organic material at the base of all structure holes.

Figure 3.18 shows some results from an experiment undertaken to investigate the effects of plasma cleaning with lithography samples. Contamination was deposited onto the samples by focusing the electron beam at high magnification onto the substrate, which allowed the contaminants within the vacuum chamber to be deposited onto the substrate over a period of time. Sample 1, shown in the left hand column, consisted of contamination applied before plasma cleaning, followed by deposition of gold and lift-off of the remaining PMMA. Sample 2, on the other hand consisted of contamination applied after the plasma cleaning step had been undertaken, and was investigated to see if contamination had any effect on the metal binding. Sample 1 shows that 1½ minutes of plasma cleaning removed the contamination from the sample without significantly impacting on the dose pattern in the PMMA. Longer cleaning times can remove the entire PMMA coating and as such there is a time limit of <5 minutes when an EBL structure is desired. Sample 2 shows the structure was not affected by the plasma cleaning and the applied contamination did not have any effect on the metal deposition. Contamination had no effect on the binding ability of the gold to silicon (Figure 3.18 (d)). Although there are areas where the lift-off process has pulled off sections of the pattern, these do not coincide with the contamination areas. Hence, imaging a structure before the metal deposition process has little effect when using a short imaging time. These results agree with the work of Isabell *et al.* who investigated the ability of plasma cleaning to remove contamination spots caused by beam damage.[182]

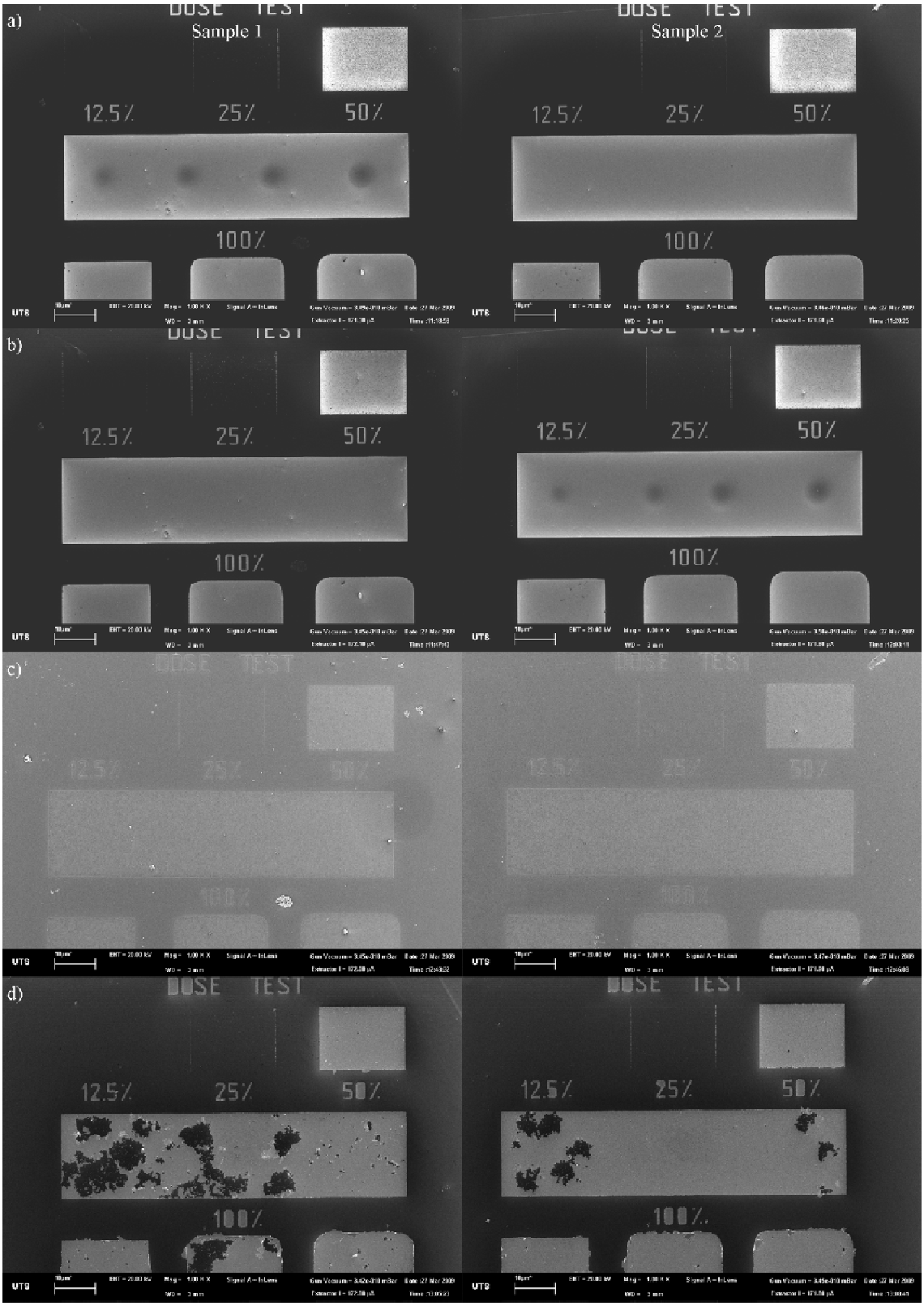

Figure 3.18: Effect of plasma cleaning on EBL samples (a) before plasma cleaning with sample 1 an exposure with contamination applied for 1, 2, 3 and 4 minutes from left to right and sample 2 without contamination. (b) After plasma cleaning in air for 1 minute.

Sample 2 had an exposure for 1, 2, 3 and 4 minutes applied using the electron beam. (c) Deposition of gold and (d) lift-off process.

In general, 30 seconds to 1 minute of plasma cleaning in air after development and before metal deposition was found to do no damage to the EBL structures or the PMMA resist layer. The application of plasma cleaning before metal deposition was found to increase the number of structures remaining bound to the substrate during the lift-off process. Figure 3.19 (a) shows rod structures obtained without plasma cleaning and (b) with plasma cleaning. The areas imaged are some of the more dense structure areas. The rods in (a) have been cut off part-way through the rod, and although there are more structures remaining, there are much fewer complete structures remaining. With plasma cleaning, the rods are able to bind entirely along the structure and thus any structure that is removed in the lift-off process is removed entirely from the substrate. This differs from the sample without plasma cleaning where the rod structures have been pulled off in sections in the lift-off process. It is believed that these sections were areas where PMMA remnants occurred after the development stage. Final structures were of a uniform size when plasma cleaning was applied.

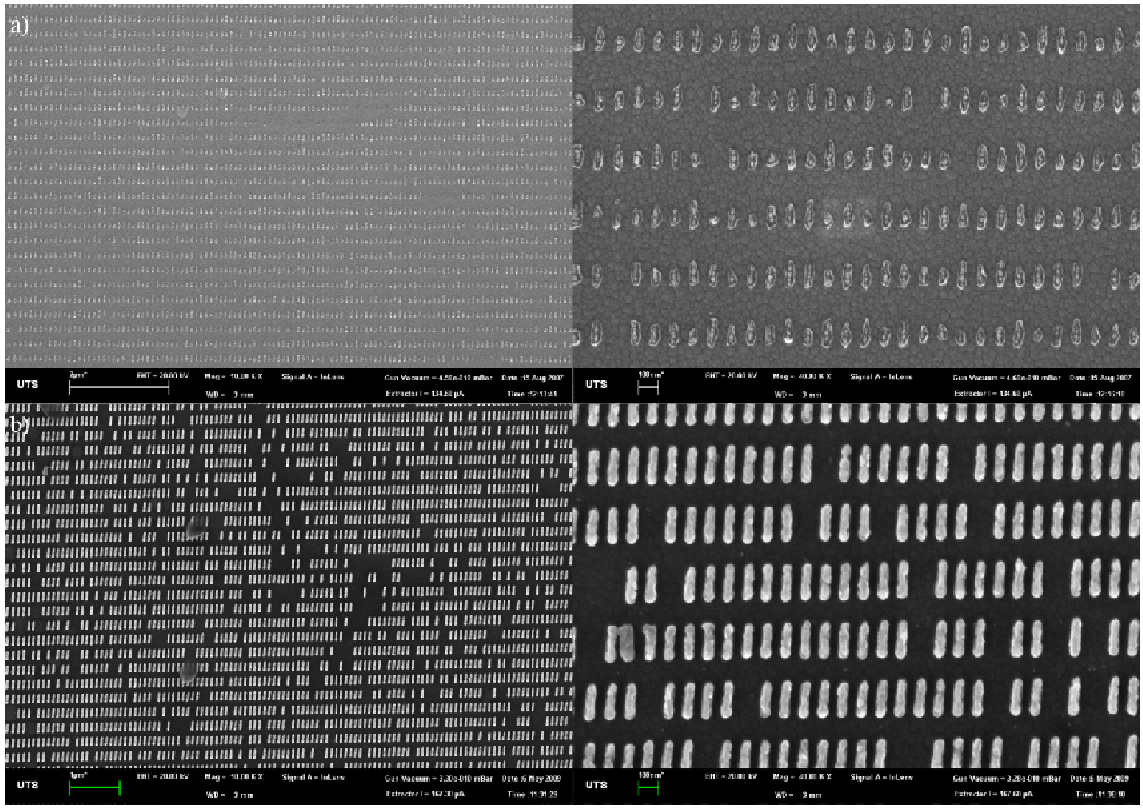

Figure 3.19: Images of Au/Cr bilayer on ITO glass (a) without and (b) with plasma cleaning.

3.3.7. Metal deposition

Gold was deposited onto the lithographic structures by sputtering and thermal evaporative processes. The addition of different metals to improve the binding of gold to the substrate was investigated. Chromium was the metal primarily used, but nickel was also investigated.

Gold deposited onto ITO substrates differs significantly from gold applied onto silicon substrates. Silicon substrates are made from single crystal wafers with a very flat surface, as opposed to ITO glass where the ITO layer is quite rough. As such, metal that is deposited onto the ITO must be able to accommodate the surface roughness. It has been recommended that metal deposition should preferentially be performed using thermal evaporation over sputtering.[177] This is because sputtered gold films can bind along the sides of the PMMA holes and thus may be pulled off the substrate more easily during the lift-off process. Thermal evaporation deposits in line-of-sight and therefore does not coat the sides of the PMMA structures (unless the deposited metal becomes too thick) allowing a more effective lift-off process.

A comparison of sputtering and thermal evaporation deposition onto some exposed patterns prior to lift-off is shown in Figure 3.20. Column (a) shows metal deposited by sputtering and column (b) of metal deposited by thermal evaporation. Each substrate had 2-4 nm of chromium followed by a 30-60 nm layer of gold. It can be seen that the gold structure is only slightly different between the two deposition methods and most of the difference comes from the different deposition rate. Samples inspected with an SEM showed no difference between the deposition methods by analysing the surface structure. The structures are clearly visible as an indent into the metal layer. In column (b) the gold structure can be seen within the structure holes but in column (a) the gold layer is thicker and as such the gold structure cannot be seen within the structure holes.

The metal is typically deposited at a rate of 0.1 - 0.3 $Å s^{-1}$ (monitored using a quartz crystal monitor) to ensure that the size of the deposited gold particles is as small as possible allowing the particles to have a greater likelihood of fitting in the pattern holes.

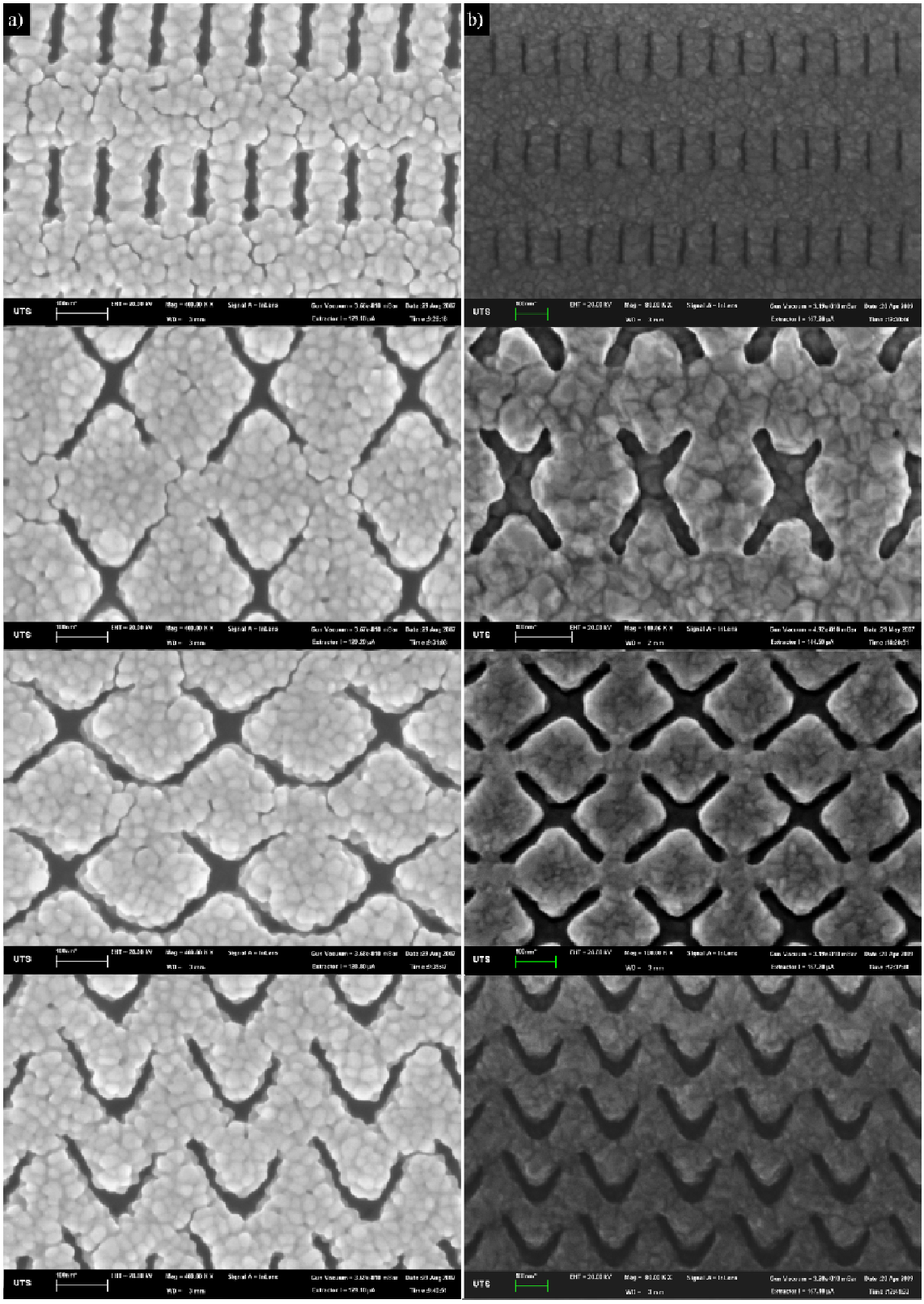

Figure 3.20: Comparison between chromium/gold (a) sputter deposition, and (b) thermal evaporation for rods, X's, X45's and V structures. Scale bars are 100 nm.

3.3.8. 'Lift-off' process

After the exposed patterns have been coated with metal films, a lift-off process was performed. This step is one of the more difficult stages in the EBL process as it is difficult to control the lift-off of high resolution patterns, which may also be lifted off the substrate.

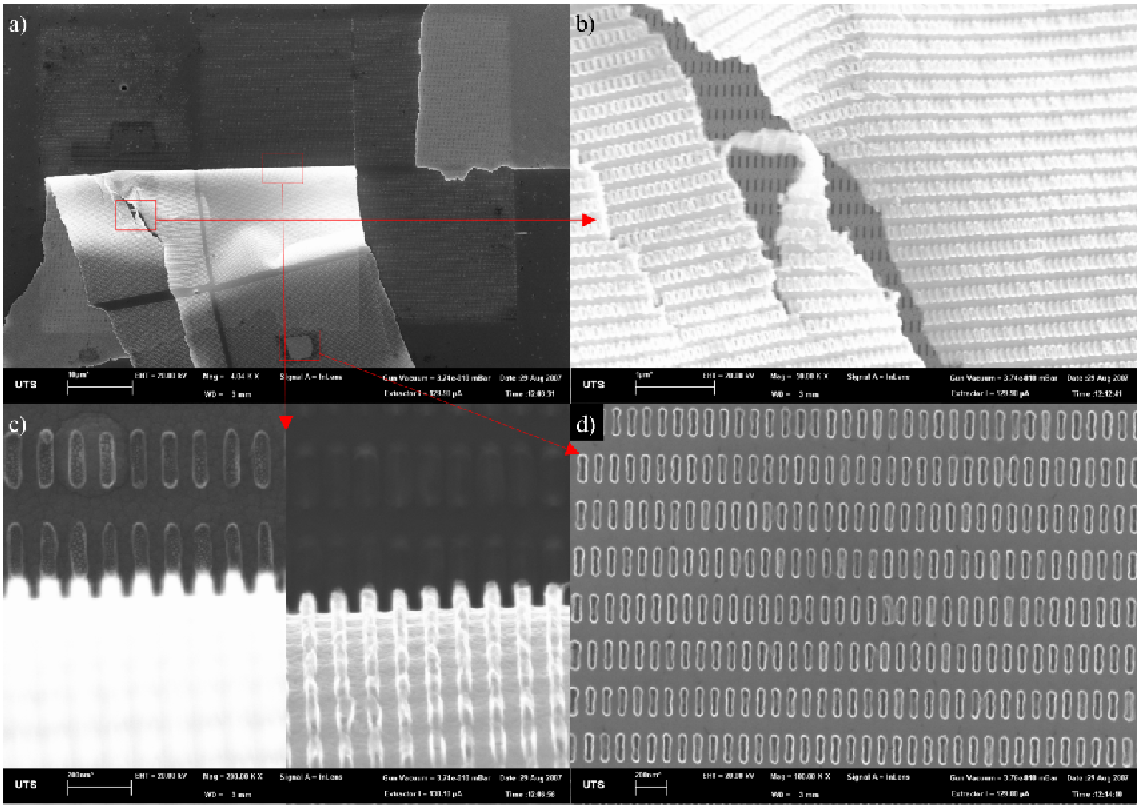

Figure 3.21: SEM images of a specimen part way through the lift-off process. (a) is a low magnification image of the rod array. (b) shows an area where loose gold has folded over a region of gold still attached to the substrate. (c) shows the interface between the lift-off gold and the nanorods. (d) shows a sample of the loose gold film.

In one experiment, the lift-off process was stopped after approximately half of the PMMA in between the patterns were removed, allowing observation of the processes occurring. Figure 3.21 shows the remaining PMMA partially lifted off a surface of rod patterns. The metal deposited was a ~10/60 Cr/Au bilayer. Image (a) shows a low magnification image of a section of the rod pattern and the red boxes indicate higher magnification areas corresponding to images (b–d). The centre of image (b) shows a section where the PMMA has not been removed from the surface and the other sections consist of the PMMA and metal layer folded back from the substrate. Image (c) shows an area where partially removed metal coated PMMA and the substrate are joined. The

left half of the image is focused on the substrate and the right half focused onto the raised metal layer. The metal rods on the substrate consist of mainly the chromium layer and significant quantities of gold can be seen to be lifted off the substrate, which corresponds to the raised sections in image (c). Image (d) shows the raised metal layer and some rod spaces can be seen (dark holes) where the rods have been left on the substrate and other sections (grey rods) show areas where the rods have been lifted off the sample with the PMMA/metal layers, resulting in a gap on the substrate where the rod originated.

Figure 3.22 shows a PMMA/metal layer partially lifted off from an X pattern. Image (a) consists of the entire X pattern and shows how the metal layer has rolled up in the lift-off process from the bottom right hand corner of the pattern. It can be seen that the PMMA is removed preferentially from areas where no e-beam exposure occurs and a number of rolled up metal layers are visible. Image (b) shows the point where the lift-off process had stopped and (c) shows an area where lift-off has yet to occur as well as parts where the metal has peeled off. Image (d) consists of an area of the peeled mask, at the centre of which there is an X structure which has been completely removed from the surface surrounded by empty X shapes.

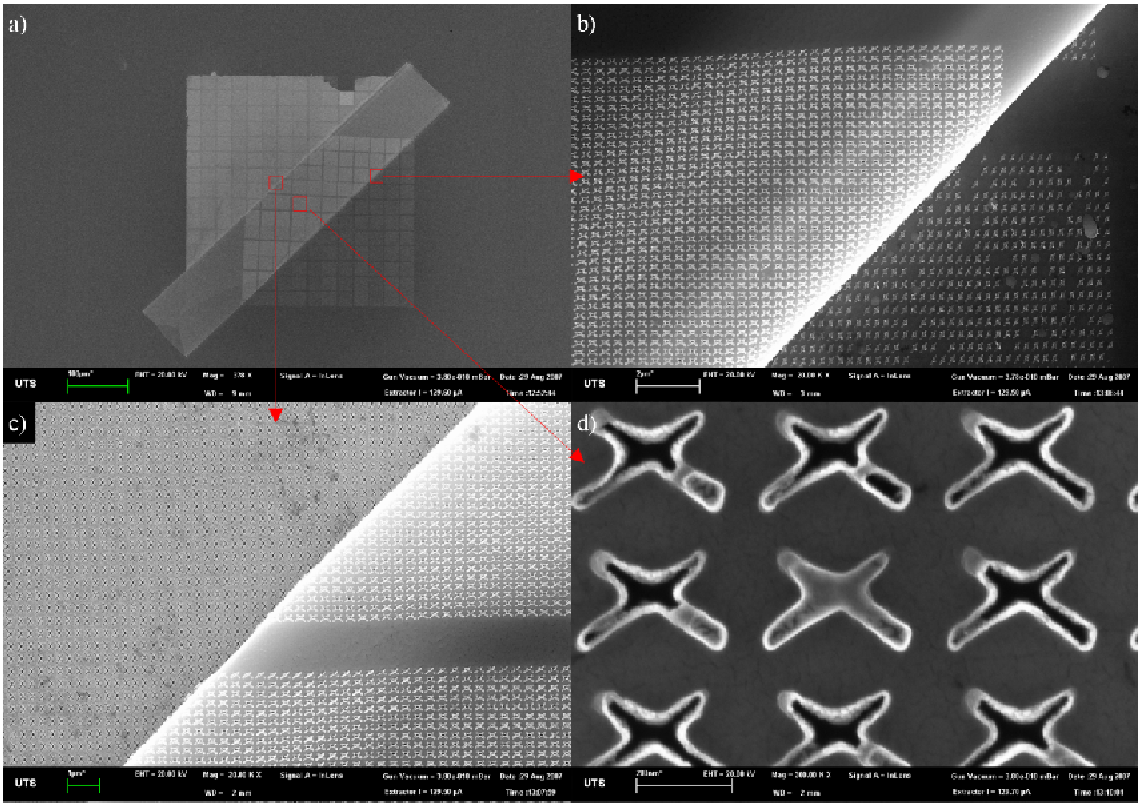

Figure 3.22: SEM images of a specimen part way through the lift-off process: (a) is a low magnification image of an X pattern, (b) shows the interface between the loose gold

of the lift-off region and the final structure array, (c) shows the alternate interface between the loose gold and a region which has yet to be touched and (d) is a high magnification image of the loose gold.

Figure 3.23 shows the lift-off process of V patterns. Image (a) consists of the V structure area with most of the lift-off complete, and only two columns to finish. It also shows that during the lift-off process the gold is being peeled off the substrate in large sheets. Image (b) shows a higher magnification image of the V pattern holes being removed. The substrate areas have missing structures and these correspond to regions on the peeled mask where the V has also lifted off.

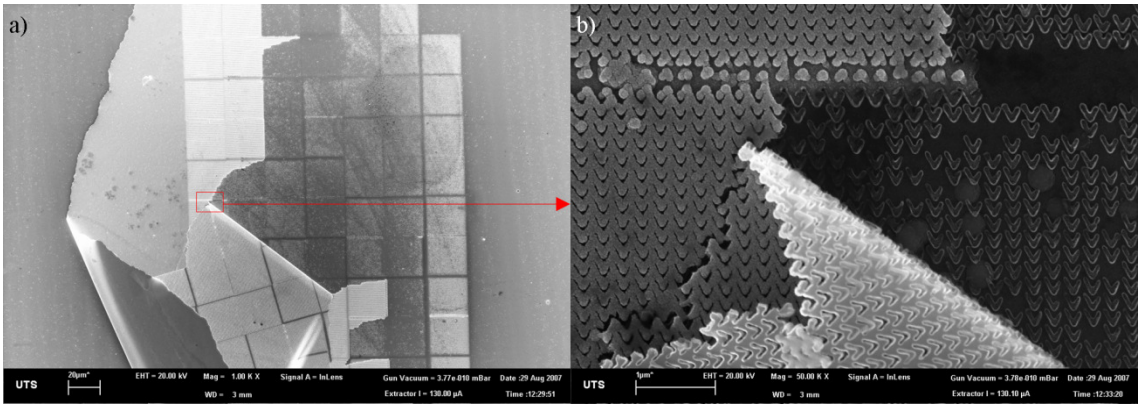

Figure 3.23: (a) a low resolution SEM image part-way through the lift-off process on a V array and (b) an image of a junction between areas which have the remaining resist removed, in the process of being removed and yet to be removed.

In all three previous figures, there are writefield sections where more structures have been removed in the lift-off process (darker squares) and areas where fewer structures have been removed (lighter squares). As the dose and settings were the same for all patterns it is unknown why some writefield patterns worked better than others. Variations in factors such as beam current or metal deposition quantity are not limited to a writefield area either so that is not a viable explanation.

Problems can occur when the lift-off process is not stopped at the point that the excess gold has been visibly removed from the surrounds of the pattern. For example, Figure 3.24 shows that too much sonication removes and/or breaks up the structures on the substrate.

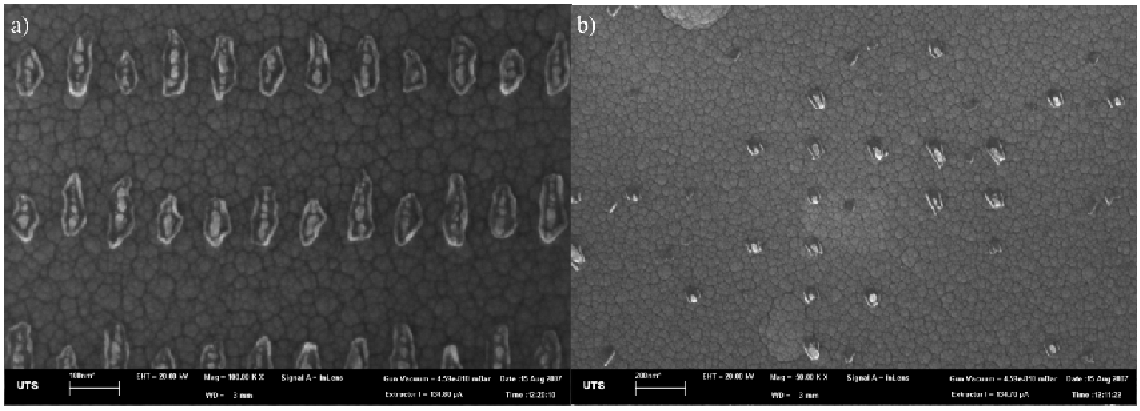

Figure 3.24: (a) rod and (b) V patterns that have had too long under sonication in the lift-off process.

3.3.9. Gold nanostructures

After completion of the lift-off process, the structures left on the substrate are ideally in the same pattern that was designed. This section presents gold and chromium/gold structures prepared by EBL and discuss the pattern coverage and the structure gold concentration.

Figure 3.25 shows gold structures produced on a silicon substrate. Silicon was chosen as a test substrate before investigating the new process on more challenging substrates such as glass. Twenty nanometers of gold was deposited into the patterns before the lift-off process. The dose conditions used in this figure are the 'alternate 20keV dose conditions' given in Section 3.2.2.2. Pattern writing. The dots shown are produced using a dose factor of 1 and consist of a 50 nm diameter dot. The dot pattern was designed using a minimum dot size by setting the diameter to zero. The rods were designed to be 100 x 400 nm and the dose factor used was 0.7 for images (b-c) and 1 for image (d). The rods in images (b-c) are 20-30 nm wide and are very good structures, however, they are not particularly accurate according to the designed physical dimensions. Rods in (b) especially have problems with the ends of the rod where they appear to bend. Rods in (d) are much more accurate with the diameter much closer to the designed values. It can be seen that the rod uniformity in (d) is lacking with the uneven rod sides and sections of rods that have been removed in the lift-off process. At this stage it was decided to focus on producing structures on glass so that the transmission properties could be investigated.

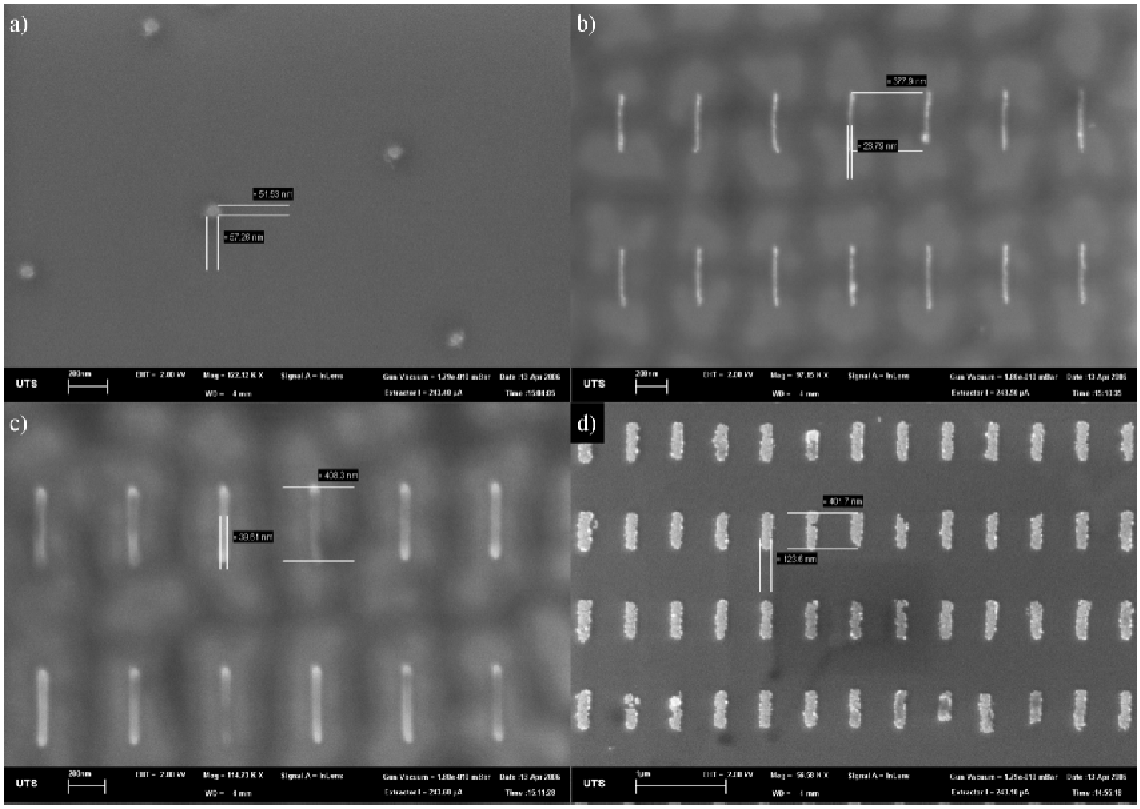

Figure 3.25: SEM images of gold structures on silicon, (a) dots, (b-c) rods at dose factor 0.7 and (d) rods at dose factor 1.

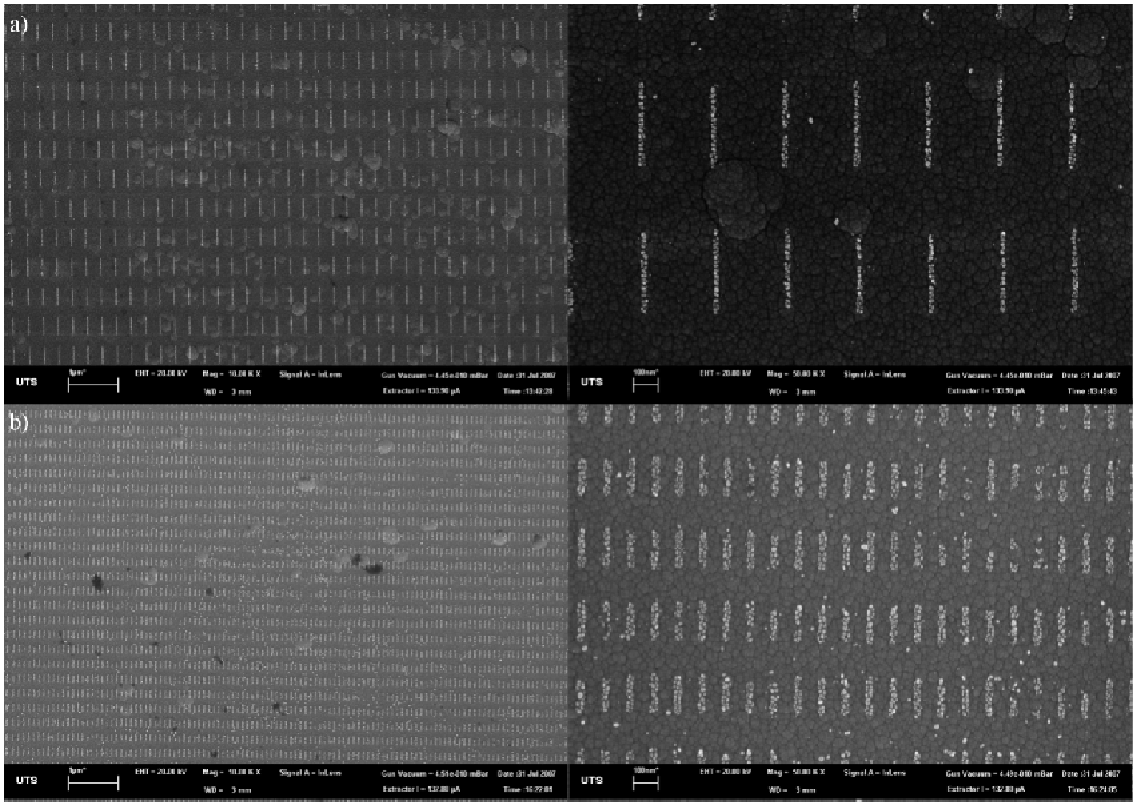

Figure 3.26: Gold rods produced by EBL on ITO glass, (a) low density and (b) high density rods.

Figure 3.26 shows two different rod structures patterned onto ITO glass. These structures consist of small gold particles in the shape of a rod but are isolated from one another. This effect was an artefact due to the underlying ITO surface structure and the bare regions within the structure correspond to areas where the gold was not tightly bound and was removed during the lift-off process. These isolated particles cause potential changes to the desired optical properties where instead of the rod's transverse and longitudinal plasmon resonance, the actual optical properties are due to the plasmon coupling between the closely spaced gold particles. Image (a) consists of the lower density (LD) rod pattern, with low and high magnification images, with design 1 line 400 nm long. Image (b) shows the high density (HD) rod pattern, with design as listed in Table 3-3. The gold rods are 1-2 gold nanoparticles wide as opposed to the HD rods which are 2-3 gold nanoparticles wide. This larger area is due to the proximity effect, which slightly increases the width of the nearest structures.

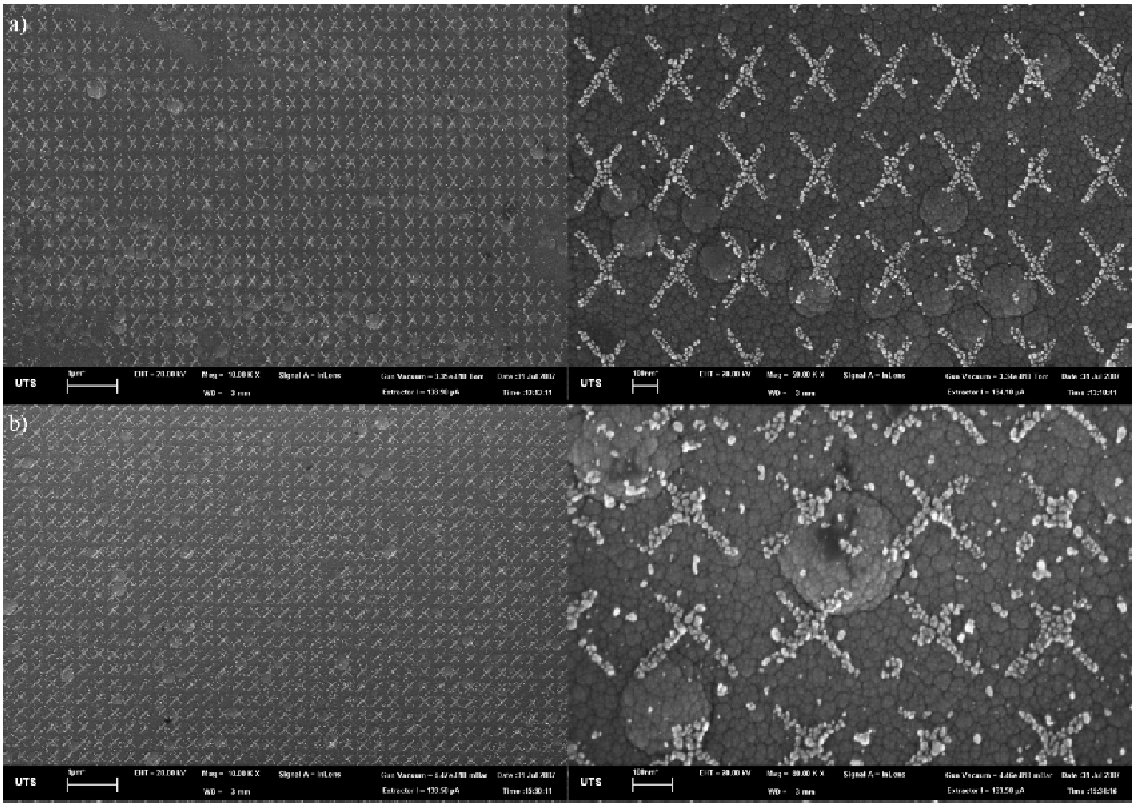

Figure 3.27: SEM images of (a) X and (b) X45 gold patterns on an ITO glass substrate.

Also of interest are some of the more complex shapes. Figure 3.27 shows samples produced by the same gold on ITO glass process but consisting of X and X45 structures. The arms of each of the X structures are 2-3 gold particles wide and only wider at the cross point due to the interaction between the two arms from the proximity effect.

Removing the extra width of the structure centres is possible and would require more work to adjust the dose of individual pixels that make up the structures, for example having the dose factor of points near the centre at ~0.5, gradually increasing the dose as the pixels are further from the structure centre. Image (a) consists of the X structure and (b) of the X45 structure. In these images, extra particles of gold can be seen between the individual structures and are due to the lift-off process where extra gold, which has been lifted off into the lift-off solution, has been randomly deposited as the substrate is removed. Extra washing of the substrates with either clean lift-off solution or clean solvents such as 2-propanol or ethanol is sufficient to remove non-bound gold from the surface.

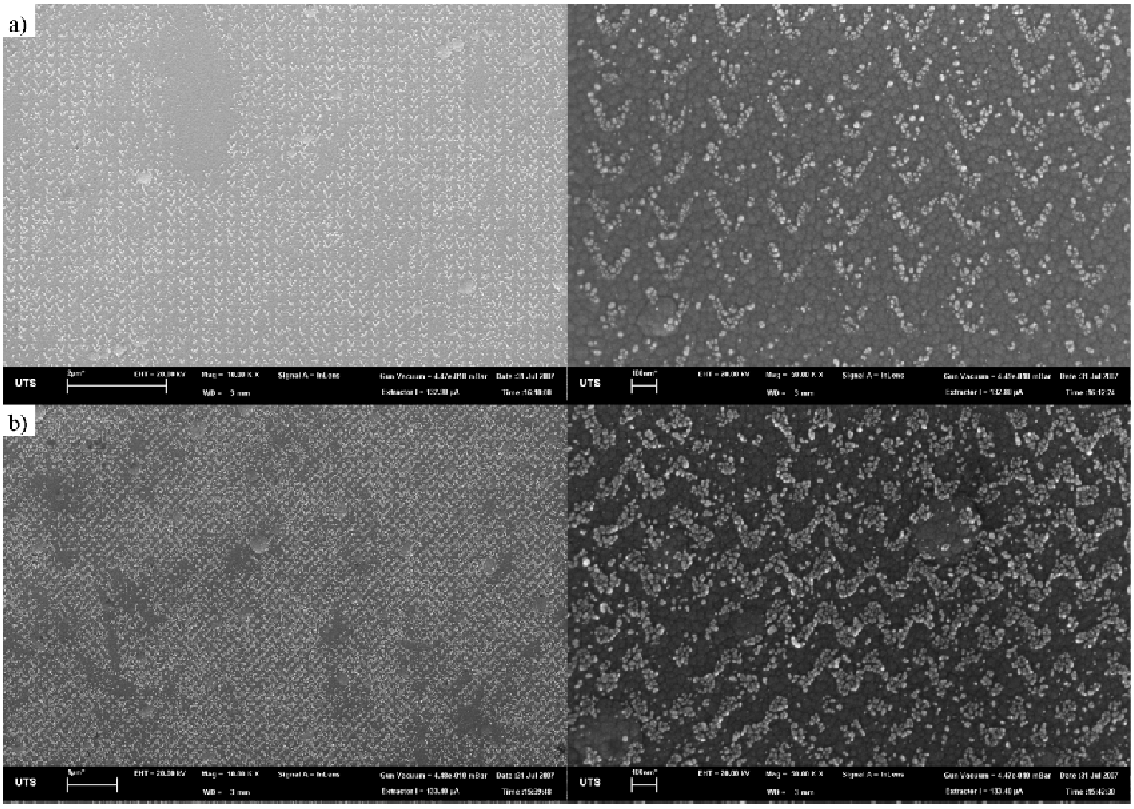

Figure 3.28: SEM images of (a) V and (b) continuous V structures of gold on a ITO glass substrate.

Figure 3.28 shows similar structures where (a) V's and (b) continuous V patterns are produced from gold onto an ITO glass substrate. Again, the width of the V structures is equivalent to 2-4 gold particles. The gold was deposited to a thickness of 60 nm and it can be clearly seen in the higher magnification images that significant quantities of gold have been pulled off the surface. From these results either a much gentler lift-off process should be used or improved binding between the gold and the substrate

achieved, so that relatively defect-free arrays may be fabricated. Also, the gold structures on ITO glass are made from individual and isolated gold particles and, particularly for optical measurement, completely fused structures are preferred. Thus methods to either deposit extra gold between the particles to complete the structures or deposit some material to improve gold binding and reduce structure lift-off were investigated.

The application of a gold nanorod growth solution onto gold structures on ITO glass was investigated to determine if the gold particles could be bridged to form complete structures. In the presence of CTAB, ascorbic acid reduces Au^{III} to Au^{I} via the reaction:

$$AuCl_4^- + 2e^- \rightleftharpoons AuCl_2^- + 2Cl^-$$

This may be further reduced by electron transfer at the surface of the electron-rich gold seeds via the reaction:[7]

$$AuCl_2^- + e^- \rightleftharpoons 2Au^0 + 2Cl^-$$

Two different concentrations of gold growth solutions and four different substrates were investigated. The two gold growth solutions investigated hereafter referred to as (i) 'weak' and (ii) 'strong' and consist respectively of (i) 10 μL of 0.1 M chloroauric acid, 15 μL of 0.1 M ascorbic acid and 10 μL of 0.01 M silver nitrate, and (ii) 50 μL of 0.1 M chloroauric acid, 55 μL of 0.1 M ascorbic acid and 50 μL of 0.01 M silver nitrate. A comparison of the growth effect of substrates with and without ½ hour heat treatment at 200 °C was also investigated.

Figure 3.29 and Figure 3.30 show the effect of a heat treated substrate placed in the 'weaker' growth solution for one day on an array of rods and X patterns respectively. Although a large amount of excess gold surrounding the fabricated structures is observed, it is insufficient to alter the substrate's overall appearance. The structures themselves are continuous but still consist of individual gold particles packed closer together.

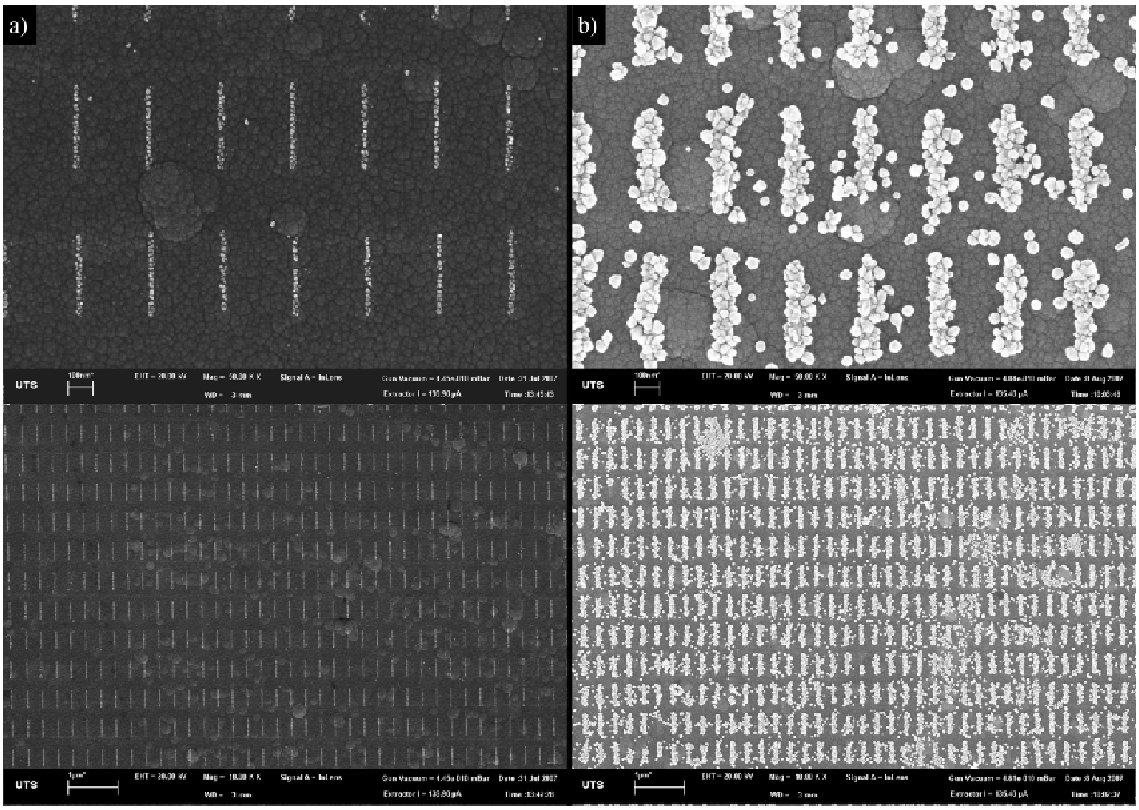

Figure 3.29: Gold rods (a) before and (b) after heat treatment and 24 hr immersion in a 'weak' gold growth solution on an ITO glass substrate.

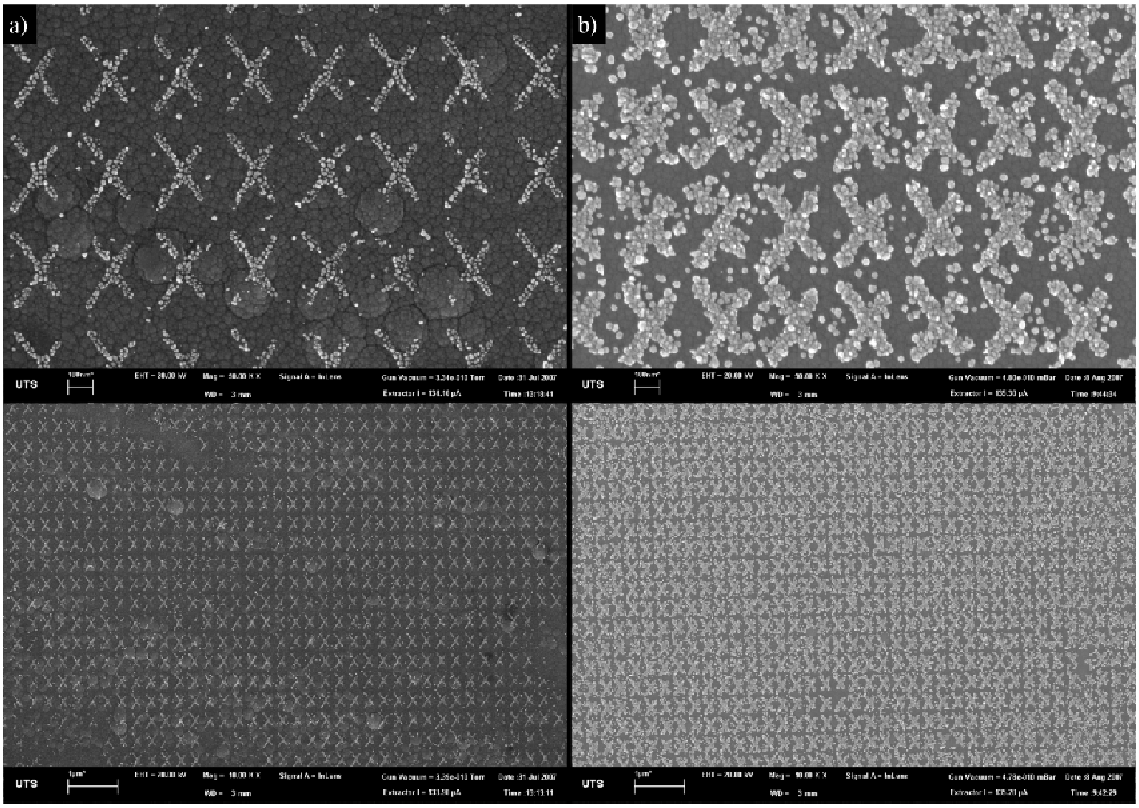

Figure 3.30: X structures (a) before and (b) after heat treatment and 24 hr immersion in 'weak' gold growth solution on an ITO glass substrate.

The following two figures show substrates that have been immersed in the 'stronger' gold growth solution with heat treatment applied to Figure 3.31 and Figure 3.32 without heat treatment.

Figure 3.31 shows four different structures and although there is some ordering or patterning over a larger area, at higher magnifications very few precise structures shapes can be determined. For example, in image (a) the rods have been joined together to form long rows, in image (b) only the occasional structure can be determined and none of these are isolated structures. In images (c) and (d) regular structures can be seen but typically only at lower magnification. This substrate clearly has an excess of deposited gold, and as such a lower concentration of growth solution was tested.

Figure 3.32 (a) shows a rod pattern before (left) and after (right) application of the 'strong' growth solution at the same magnification. It can be clearly seen that the rods after growth solution are not isolated from each other and there is a lot of excess gold on the substrate. Row (b) shows the corresponding images for the X45 pattern. However, the X45 structure is not observed after the growth solution application.

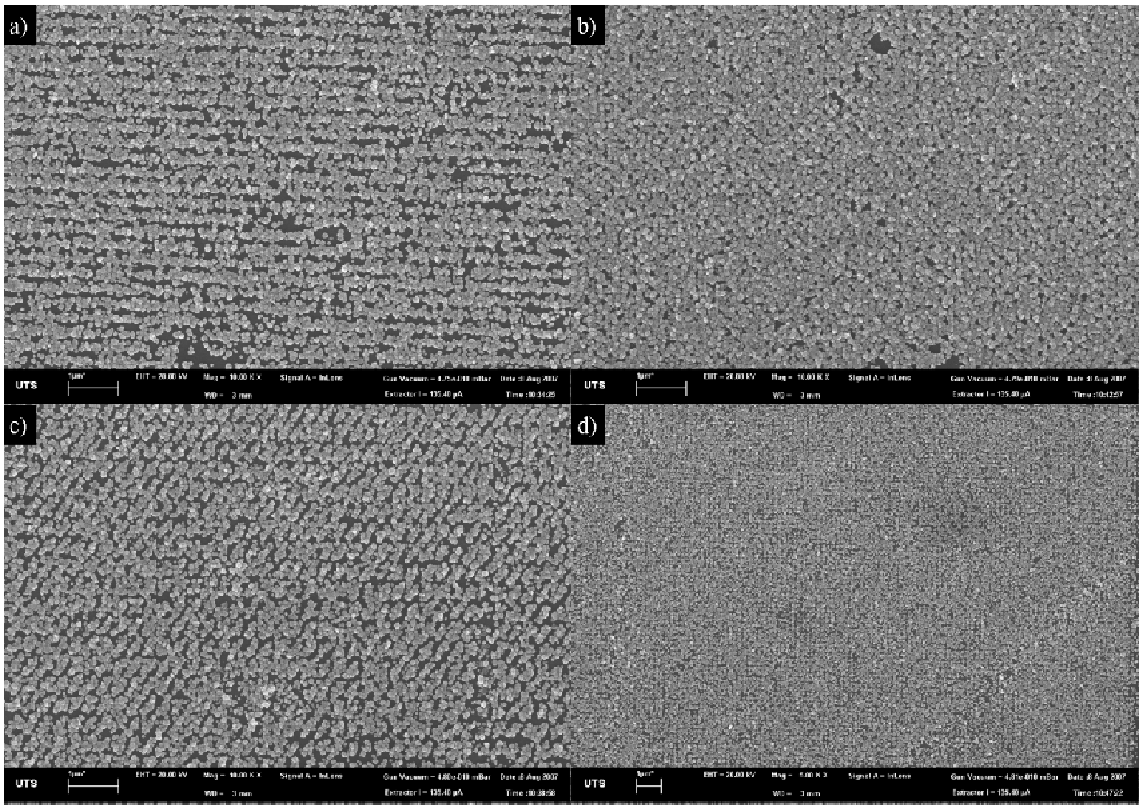

Figure 3.31: Substrate with heat treatment followed by 24 hr incubation in the 'stronger' gold growth solution. Structures shown are (a) rods, (b) X45, (c) X and (d) continuous V structures on an ITO glass substrate.

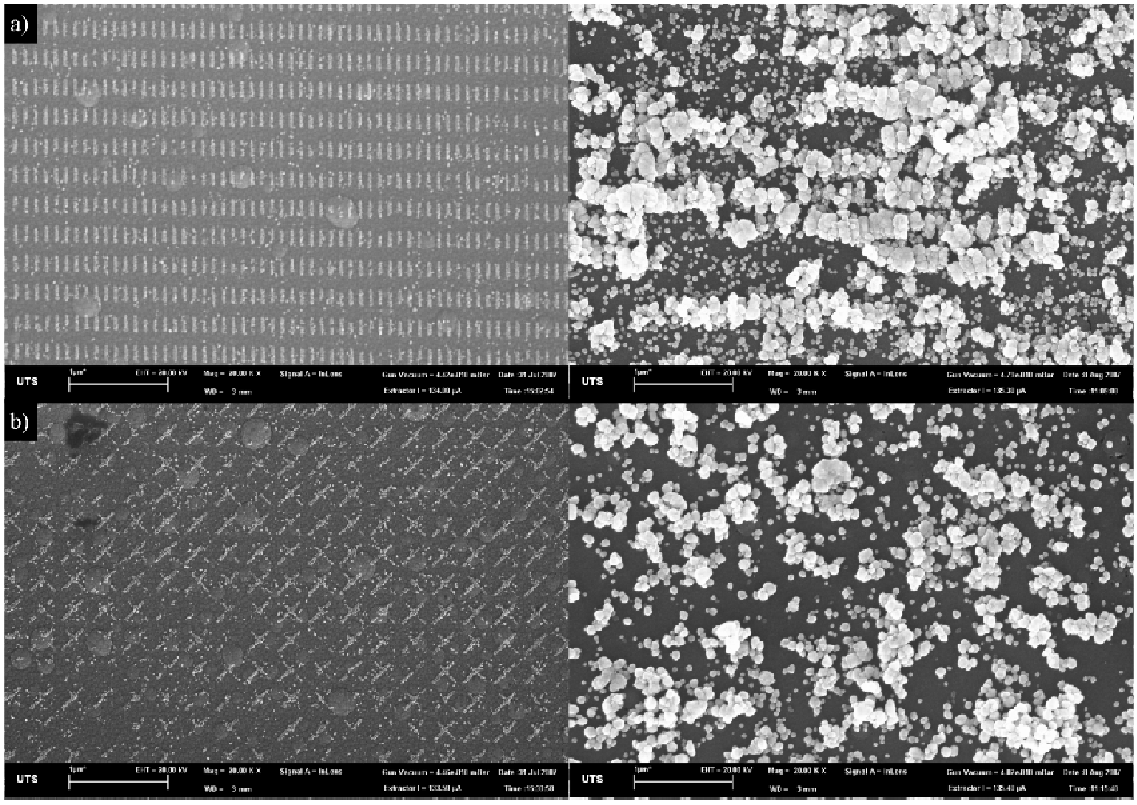

Figure 3.32: (a) Rod and (b) X45 structures before (left) and after (right) 24 hr incubation of the 'strong' growth solution on an ITO glass substrate.

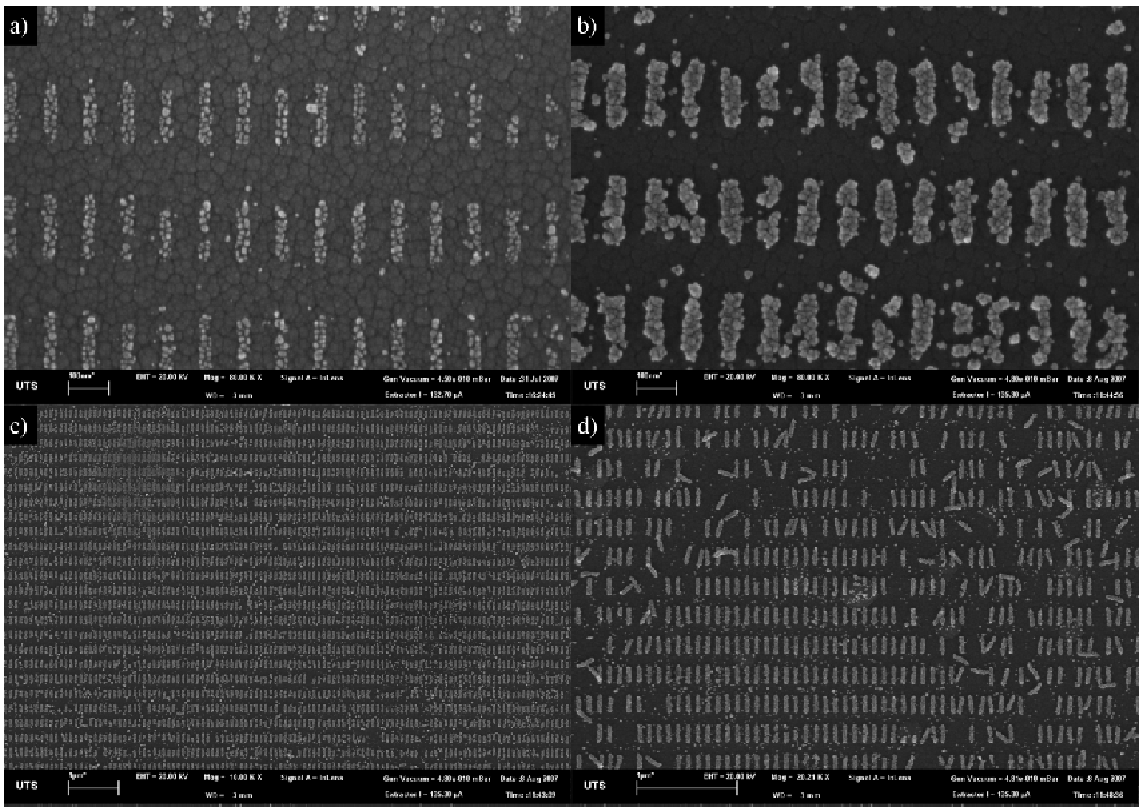

Figure 3.33: Rods (a) before and (b) – (d) after 24 hr incubation of 'weak' growth solution at different magnifications on an ITO glass substrate.

Figure 3.33 and Figure 3.34 consists of rod and V patterns respectively, incubated for 24 hours with the 'weak' growth solution and without heat treatment. Figure 3.33 shows (a) the rod pattern before growth solution and (b-d) after growth solution. The lower concentration gold solution is much more effective in producing isolated structures. Image (d) shows how some of the rods are lifted off the surface during the drying phase after incubation in the growth solution. The rods were fully joined before being unbound from the substrate surface. Although some excess gold was found randomly deposited on the substrates, the surface plasmon resonance of the small gold particles were in sufficient quantities to colour the substrate pink.

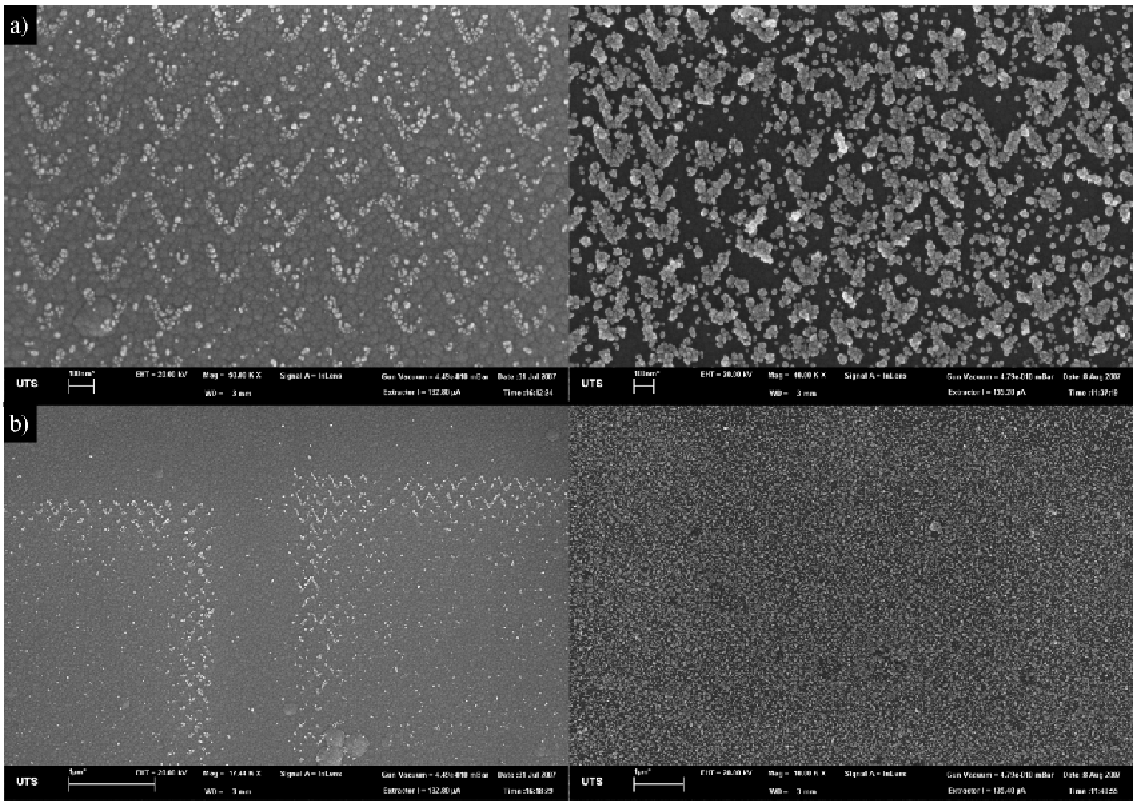

Figure 3.34: (a) V's and (b) continuous V structure before (left) and after (right) 24 hr incubation in the 'weak' growth solution on an ITO glass substrate.

Figure 3.34 (a) shows how some of the complete V structures that were remaining after the lift-off process were joined to form an individual structure whereas areas where incomplete structures were formed resulted in a lot more random deposition of gold particles through the growth phase. This is due to the gold from the incomplete structures being deposited near the designed site and growing under the influence of the growth solution. The continuous V structure, (b), shows that there is insufficient coverage of structures after the lift-off process and is interesting to note that the

coverage is good along the edges of the writefield suggesting that the lower doses at the edges of the writefield perform better during the lift-off process than the centre of the pattern where the proximity effect is higher. None the less, after the application of the growth solution a regular order can be seen from low magnification but as the magnification increases that order becomes much harder to identify.

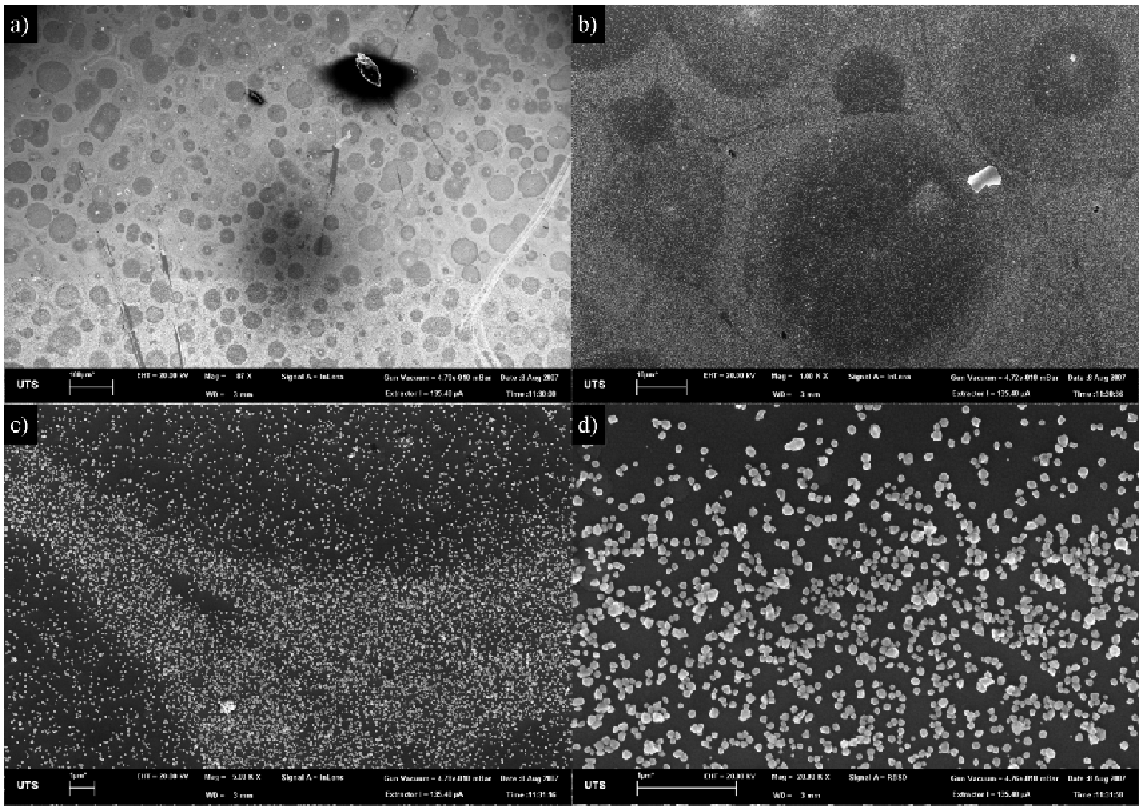

Figure 3.35: Effect on the ITO glass substrate of the 'strong' growth solution at different magnifications.

Three of the four substrates tested appeared pink or pink/purple after the incubation period. Of particular interest was that the heat-treated samples had less gold deposited onto the substrate. The lower concentration gold growth solution sample with heat treatment appeared clear and the high concentration gold growth solution sample with heat treatment appeared pink. The samples without heat treatment appeared darker pink and purple indicating more gold particles depositing onto the substrate. Figure 3.35 shows the deposition of gold particles from the growth solution onto the substrate at increasing magnifications. These images are very similar for all three substrates that appeared pink.

The addition of the growth solutions to the substrates allowed the individual gold particles making up the structures to be joined together to form a complete structure.

However, the final structure shape appears to have been grown with larger gold particles than desired, resulting in a very rough surface and causing much more complex surface plasmon resonances than desired. These results suggest that to produce higher quality structures should be heat treated followed by incubation in a growth solution with lower concentration than the 'weak' growth solution or incubated for shorter times.

Instead, to make the desired structures smoother, a binding layer between the ITO and the gold was investigated. Chromium was chosen to improve gold binding to glass.[60] Figure 3.36 shows rod, X, + and X45 structures after lift-off of a thin chromium layer (2-10 nm) and a thicker gold layer (40-60 nm). The structures are much more uniform and exact than either gold-only structures or gold structures with the application of a gold growth solution. Images (a) and (b) compare the different deposition methods for the rod structures with (a) thermal evaporation and (b) sputtering and images (e) and (f) for the respective deposition methods for the X structure. It is clear that the amount of gold remaining on the structures is significantly more when deposited via thermal evaporation compared to sputtered structures. The large increase in signal (whiter regions) on the top of the structures are the gold sites where the higher atomic number element produces more secondary electrons than either the chromium or the ITO substrate. In the sputtered images (b and f) the strongest signal by far are the edges of the structures, due to the edge effect, and only relatively small amounts of gold remain on the structure's surface. Images (c) and (d) show optical microscope images for rods, X's and +'s from left to right across the images. It is interesting to see that surrounding the large area patterns is gold that has not been lifted off. Further lift-off would cause the structures to lift off as the surrounding gold is also lifted off. Images (e), (g) and (h) correspond to the X patterns, X, + and X45 respectively, deposited via thermal evaporation. It can be seen that there is sufficient gold in the centre of the structures but insufficient gold along the arms. This could be due to two process; (i) the structure in PMMA could be of insufficient width to allow gold to be deposited into the holes along the arms or (ii) the deposited gold may also bind to the PMMA walls and then be removed during the lift-off process.

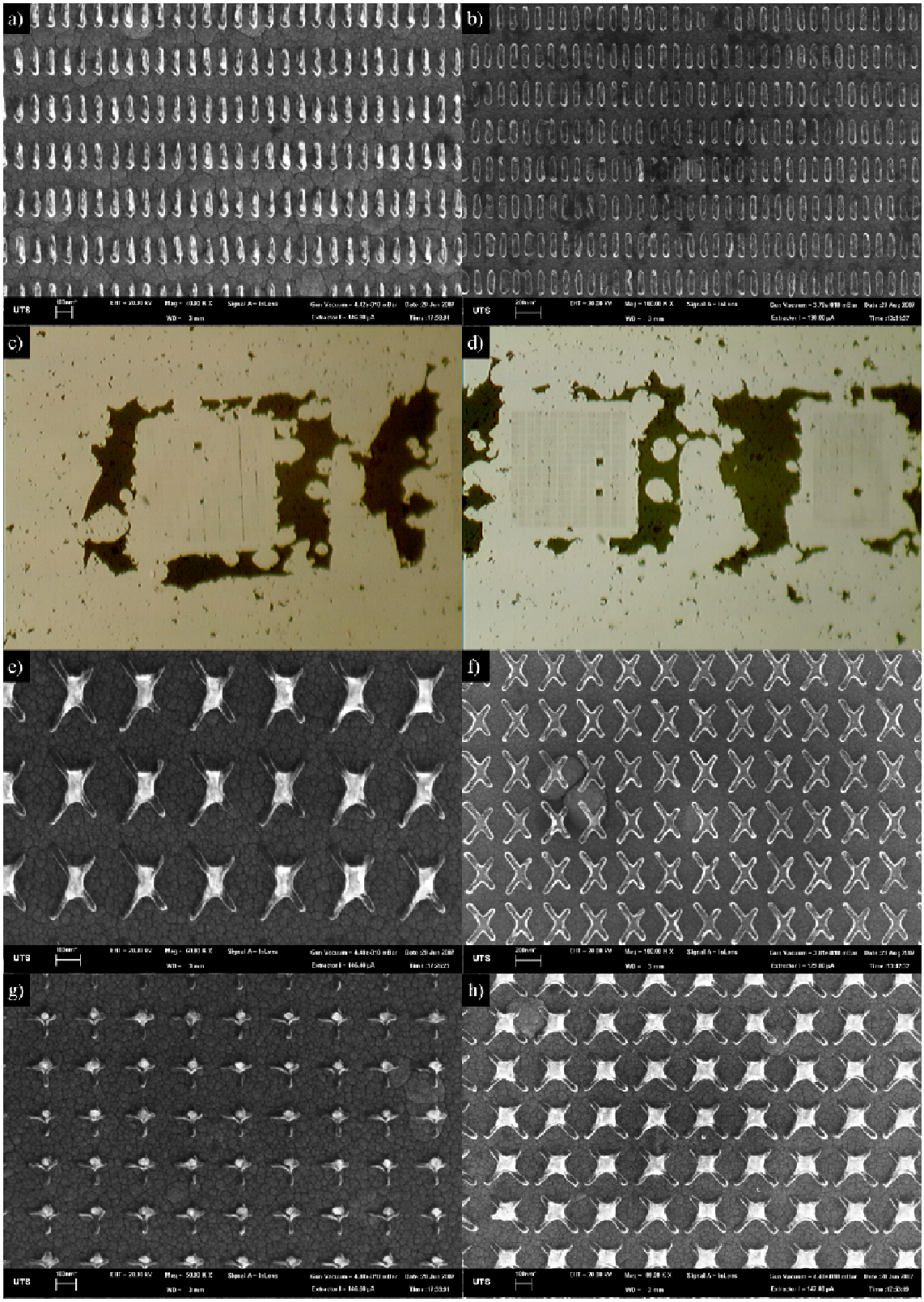

Figure 3.36: Cr/Au bilayers on ITO glass of (a-c) rods and (d-h) X structures. (b) and (f) are deposited via sputtering. (c) and (d) are optical microscope images of the large structure arrays.

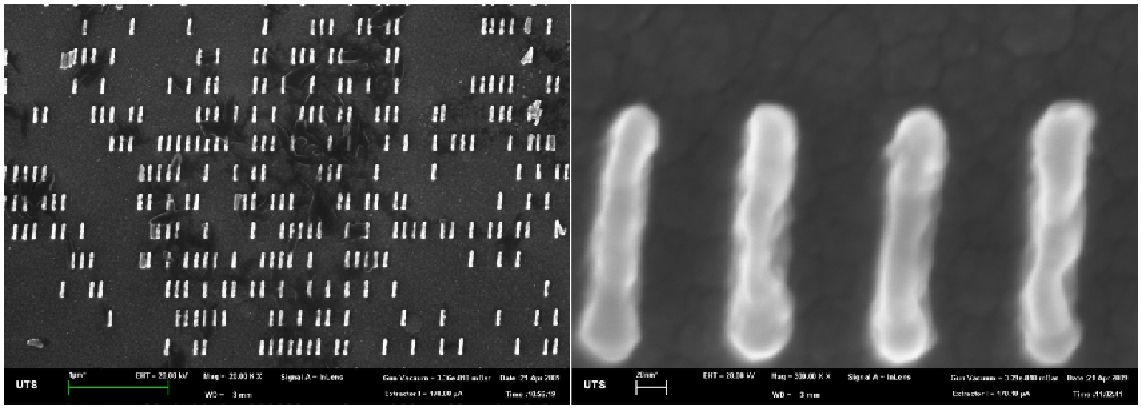

Figure 3.37: Gold rod patterns produced using 30 secs plasma cleaning followed by thermal evaporation of a 2/30 nm Cr/Au bilayer on an ITO glass substrate.

Work was undertaken to reduce the amount of gold removed during the lift-off process. The effect of plasma cleaning PMMA structures before metal deposition, much thinner gold films (20-30 nm), and the effect of increasing development time were all investigated as possible solutions to the lift-off problems.

The plasma cleaning time is typically 30 seconds, sufficient to remove any PMMA remnants at the bottom of the structure holes but not enough to significantly alter the PMMA structure dimensions. Figure 3.37 shows the rod structure made from a 2/30 nm chromium/gold bilayer. The final structure of the individual rods is of much higher quality than all previous efforts. The amount of gold on the structures is considerably more than was left after lift-off from 60 nm gold samples. This figure shows virtually no gold situated between the structures allowing for more accurate optical measurements of the structure. It is also clear that although the structures are exactly as desired, there are lots of spaces from where the rods have been lifted-off.

The same process was used to produce the X45 structures shown in Figure 3.38. Image (a) shows a high magnification X structure with gold visible along the entire length of the arms, which shows that the structures themselves are much higher quality but lower in density than the 60 nm gold deposited structures. The remains of the X45 structures removed during the lift-off process can be seen in image (b). It is clear from images (c) and (d) that (i) there are large areas of X45 structures which have not had the resist removed and (ii) there is a very low density of structures remaining of the lifted-off sections. These images also show why there is such a low density, with the X45 structures very clearly bound to the gold layer that is designed to be removed. Image (d) clearly shows the X45 structures as they are being peeled from the substrate.

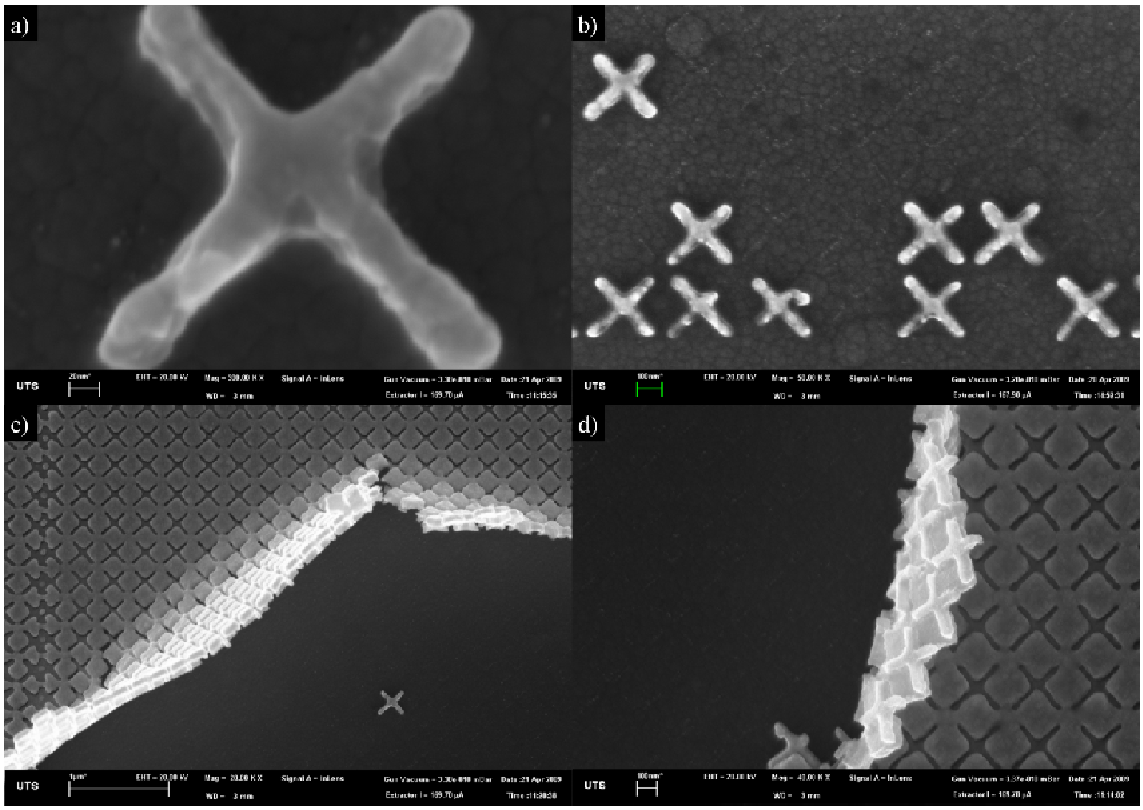

Figure 3.38: X45 structures produced using 30 secs plasma cleaning followed by thermal evaporation of a 2/30 nm Cr/Au bilayer on an ITO glass substrate.

The V structures in Figure 3.39 were produced using the same method. The V structures have the same problems as the X45 structures with significant quantities of structures being stuck to the gold/PMMA layer and being removed during the lift-off stage. Image (a) consists of a high resolution picture of the V structures with gold along the entire structure. Image (b) shows the reduced coverage of the V structures and also the gap between two writefield exposures can be seen as the two vertical lines of partial V structures. Images (c) and (d) show the structures lifting off the substrate with the V structures clearly visible on the underside of the gold/PMMA layer.

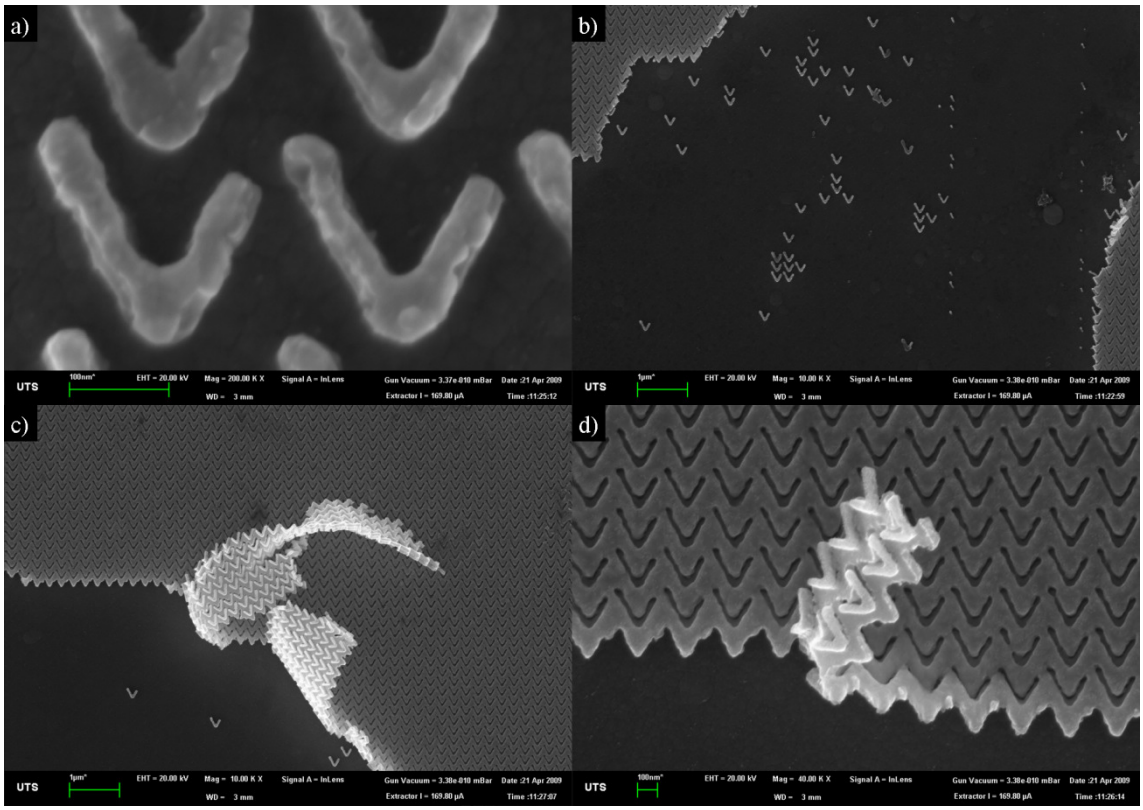

Figure 3.39: V structures produced using 30 secs plasma cleaning followed by thermal evaporation of a 2/30 nm Cr/Au bilayer on an ITO glass substrate.

The next samples that were investigated were structures where the plasma cleaning time was increased to 1 minute for the purposes of improved lift-off stage. Figure 3.40 shows the rod patterns produced with 1 minute of plasma cleaning and a 2/30 nm Cr/Au bilayer deposited. The left column contains images collected after the first lift-off process and the images on the right are after the final lift-off process. Images (a) and (b) show the entire rod array and it can be seen why a second lift-off procedure was required, as ¾ of image (a) has PMMA/gold coating remaining. Image (b) shows the majority of the writefields have the PMMA/gold coatings removed. Image (c) and (d) are the same magnification but image (d) was taken using a 2 keV accelerating voltage and, as such, the chromium remnants can be seen in areas that have had the gold structures removed. Image (d) was chosen as the rods and the holes can be easily seen. Images (e) and (f) are high magnification images showing the gold structure of the individual rods. Both images are taken at the same magnification but image (f) shows significantly more drift with the rods appearing on an angle whereas the image was taken with the rods at the same angle as (e). The extra time spent plasma cleaning before metal deposition does not seem to increase the ability of the gold to remain

bound to the substrate during the lift-off process. In fact, 30 seconds of plasma cleaning produces higher quality arrays than 1 minute of plasma cleaning.

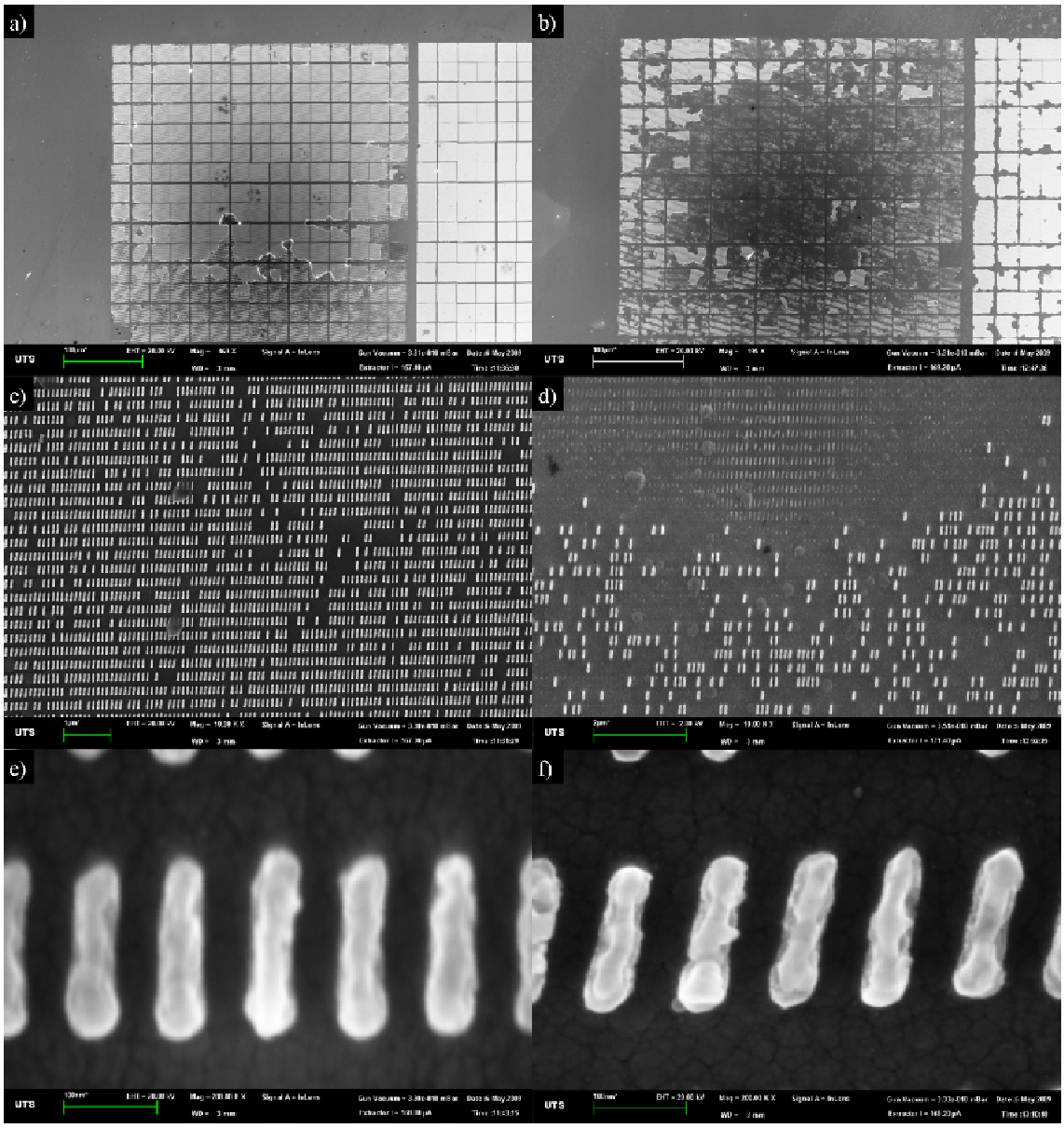

Figure 3.40: Rod structures produced on an ITO glass substrate using 1 minute plasma cleaning prior to deposition of a 2/30 nm Cr/Au bilayer; (a, c, e) are images from the first lift-off process and (b, d, f) are images from the final lift-off process.

A large X array was produced on the same substrate as the rod array above and the lack of lift-off of the X pattern after the initial lift-off process also necessitated the additional lift-off time. The effect of 1 minute of plasma cleaning on the X is shown in Figure 3.41. The additional plasma cleaning time clearly indicates a reduction of efficiency of the lift-off process with additional lift-off time required. It also causes more structures to be completely removed during the extra long lift-off time than

samples with shorter plasma cleaning times. Image (a) shows the large area array and it can be seen that the majority of the array is still covered by the PMMA/gold and cannot be removed without increasing the reduction in quality of the rod array. It is interesting to note that areas that have not been written have been preferentially removed, which has been the opposite of what has been previously observed, for example in Figure 3.36 which shows gold preferentially remaining surrounding the entire pattern. Image (b) shows the corners of four writefields where the PMMA/gold has been preferentially removed. Images (c) and (d) are higher magnification images of areas that have improved lift-off properties. Due to the more complex X shaped structure, the efficiency of the lift-off process is much reduced compared to that of rods. The additional plasma cleaning time does not improve the lift-off efficiency either. Further investigations into methods to create overhangs in the PMMA structure or isolating the deposited gold in the structure hole from the surface gold were required to improve lift-off.

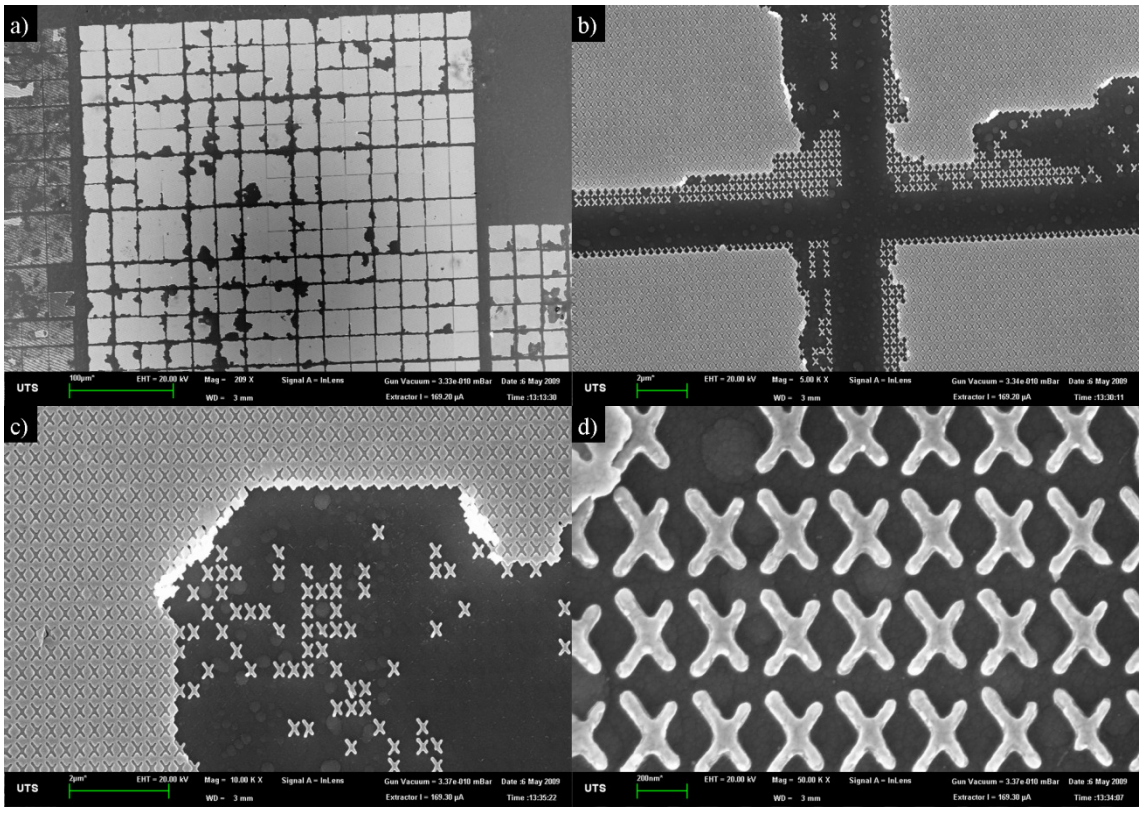

Figure 3.41: The effect of 1 minute of plasma cleaning on the X structure array.

The V structures produced using 1 minute of plasma cleaning are shown in Figure 3.42. It clearly shows that as with the X structure, the V structure also has reduced lift-off efficiency compared to rods. Image (a) shows the large area V pattern and still has most of the gold remaining and requires further lift-off time. However, images (b-d)

show that although further lift-off time is required, the majority of V structures are still lifting off the substrate. Image (b) shows a section of PMMA/gold lifting off the substrate between two writefield patterns and a lot of the V structures can be seen on the bottom of the PMMA/gold film. Images (c) and (d) show some of the areas with more V structures remaining but significantly more structures that have been removed can also be seen. The additional plasma cleaning time does not improve the lift-off process for any of the structures observed (rods, X's or V's).

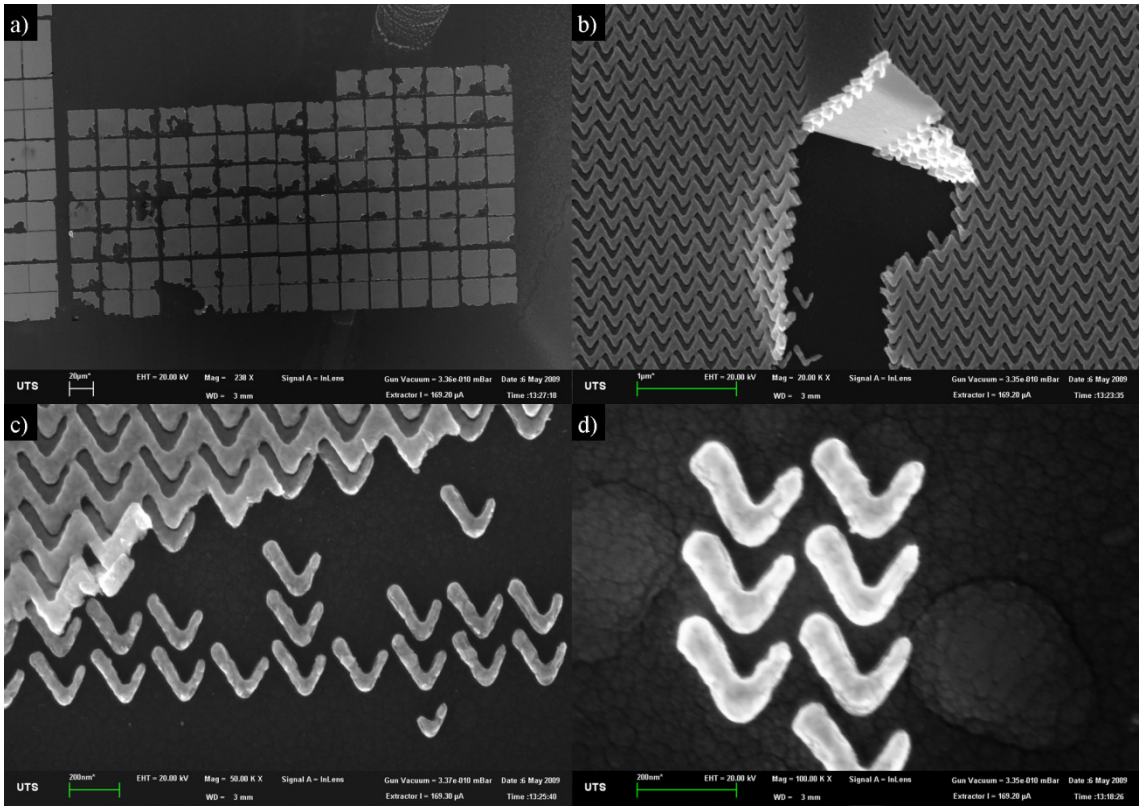

Figure 3.42: V structures produced with 1 minute of plasma cleaning on ITO glass.

The next stage in investigating methods to improve the lift-off process involves increasing the developing time from 30 seconds to 1 minute, the effects of which can be seen in Figure 3.43 for rods and X45 structures and Figure 3.44 for X structures. Figure 3.43 shows the structures that failed with the application of longer developing times. Images (a) and (b) show the rod pattern after the lift-off process. It is clearly seen that although the individual rods can be determined, the majority of rods have insufficient resist between the structures and as such form long rows of joined rod structures. Similarly, images (c) and (d) show the X45 structure which binds at the corners to form the pattern seen in (c). These problems are due to the increased development time, which allows further development of partially exposed areas.

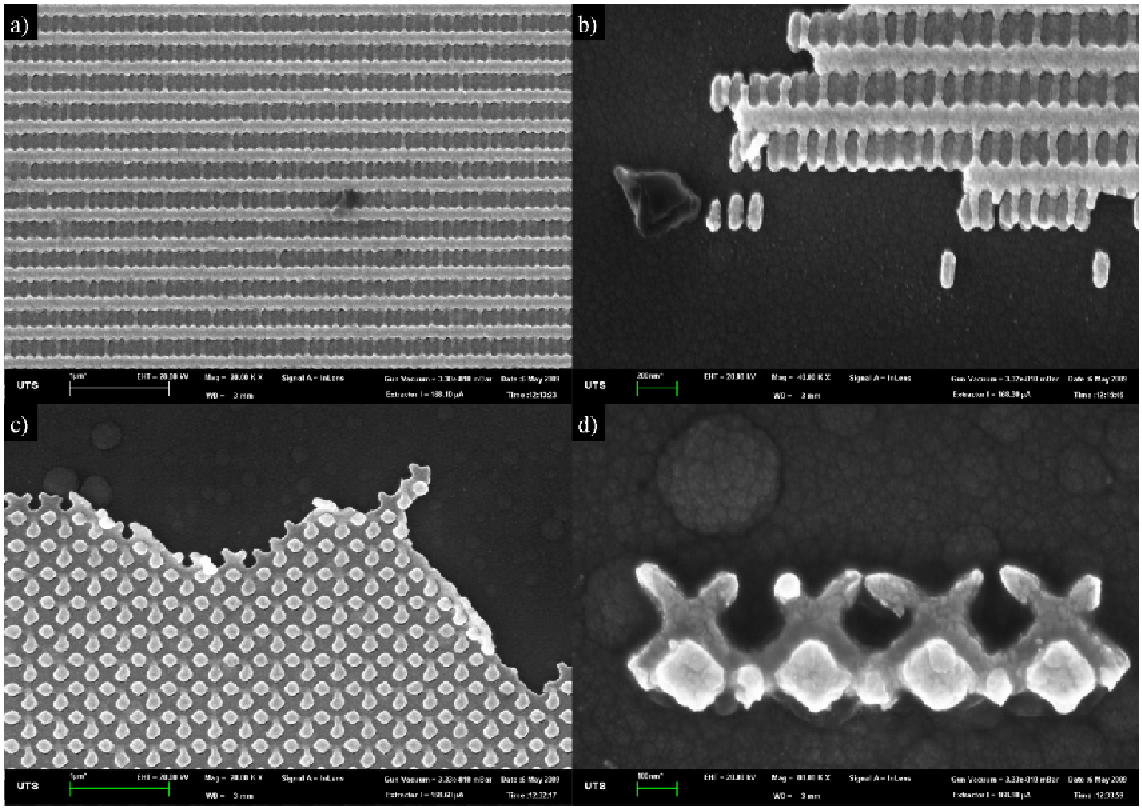

Figure 3.43: (a, b) rod and (c, d) X45 structures produced with 1 minute developing time on an ITO glass substrate.

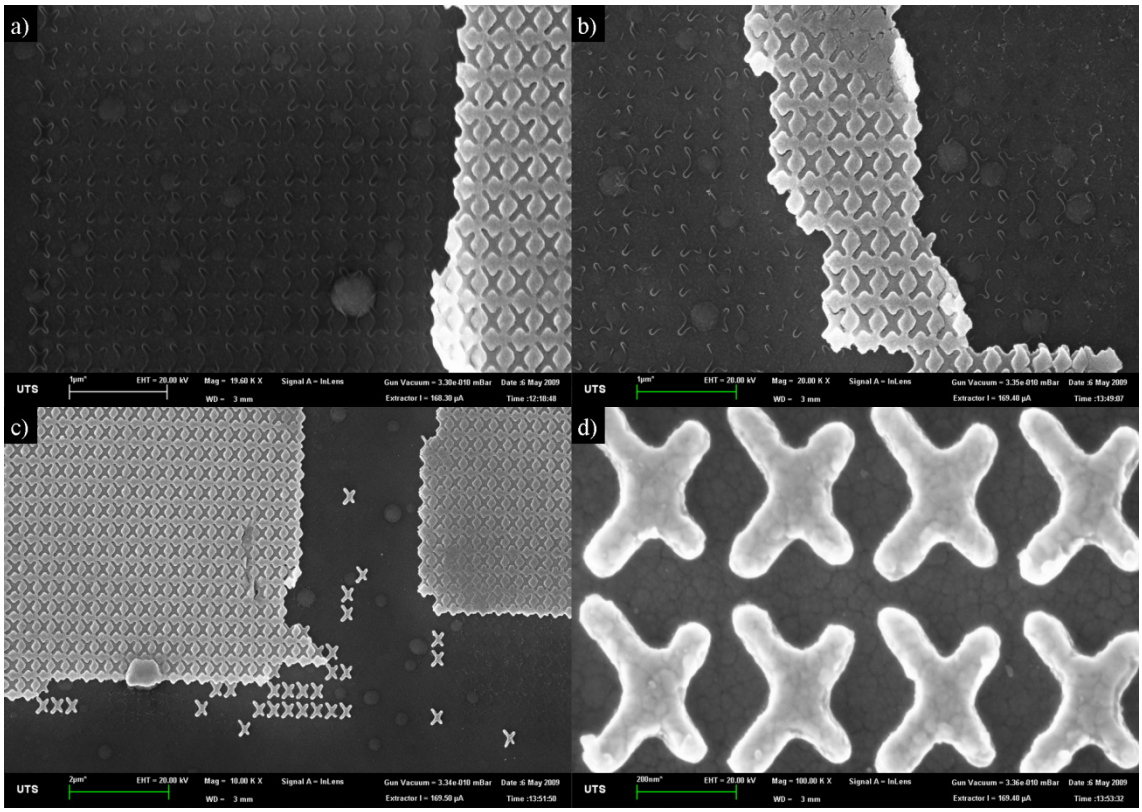

Figure 3.44: X structures produced with 1 minute developing time on ITO glass.

The X structure was the only structure that had sufficient spacing between the individual structures to be unaffected by the increased proximity effect. The effect of 1 minute of developing time on the X structure is shown in Figure 3.44. The additional developing time leads to a less efficient lift-off process with most gold X structures removed from the substrate. Images (a) and (b) show areas where only the chromium layer of the X structures remains and sections that have not completed the lift-off process. Images (c) and (d) show areas where the remaining resist has lifted-off properly. Image (d) shows the effect of the increased development time on the individual structure size. Unlike other methods investigated, longer development times significantly increase the arm size from ~360 x 55 nm to ~375 x 75 nm. There was no increase in the efficiency of the lift-off process with longer development times.

Two different rod arrays are shown in Figure 3.45. Both were produced by applying 30 seconds of plasma cleaning prior to deposition of a 2/20 nm bilayer of Cr/Au. Images (a-e) are from one sample and (f-h) are from the other. Images (e) and (h) are transmission optical microscope images of the corresponding large area rod arrays. The optical images appear to have a reddish tinge where the structures are. The bottom left corner of the pattern in image (e), where the colour matches the background, corresponds to image (c) where large sections of rods have been removed. Images (a) and (b) on the other hand correspond to the coloured part of the array, which shows that much fewer rods have been lifted-off and except for areas which appear to have been scratched during the lift-off process, image (d), there are no large areas of rods that have been removed. By comparing (a) and (c) we can see the major difference between the two patterns is that (a) has a much smoother substrate, and the only missing rods correspond to 'bubbles' in the ITO layer. Alternatively, (c) has a very uneven substrate which seems to provide an increased chance of the rods being removed. The array in (h) was exposed at areas without a visibly rough surface and as such has greater effectiveness in producing bound rods. Although the roughness of the ITO substrate does not mean that structures designed on the large 'bubbles' will definitely be removed during the lift-off process, it does mean that there is a greater probability of removal. Conversely, it also does not mean that rods produced on smoother ITO sections cannot be removed; it does however mean there is a greater probability of sticking to the substrate. The final size of the rods from either sample is approximately 175 x 42 nm which compares to the PMMA structure size of ~ 180 x 50 nm. The final size of the

gold structure is less in both dimensions from the PMMA hole size. There is 155 nm of space between the rows and 55 nm between the columns.

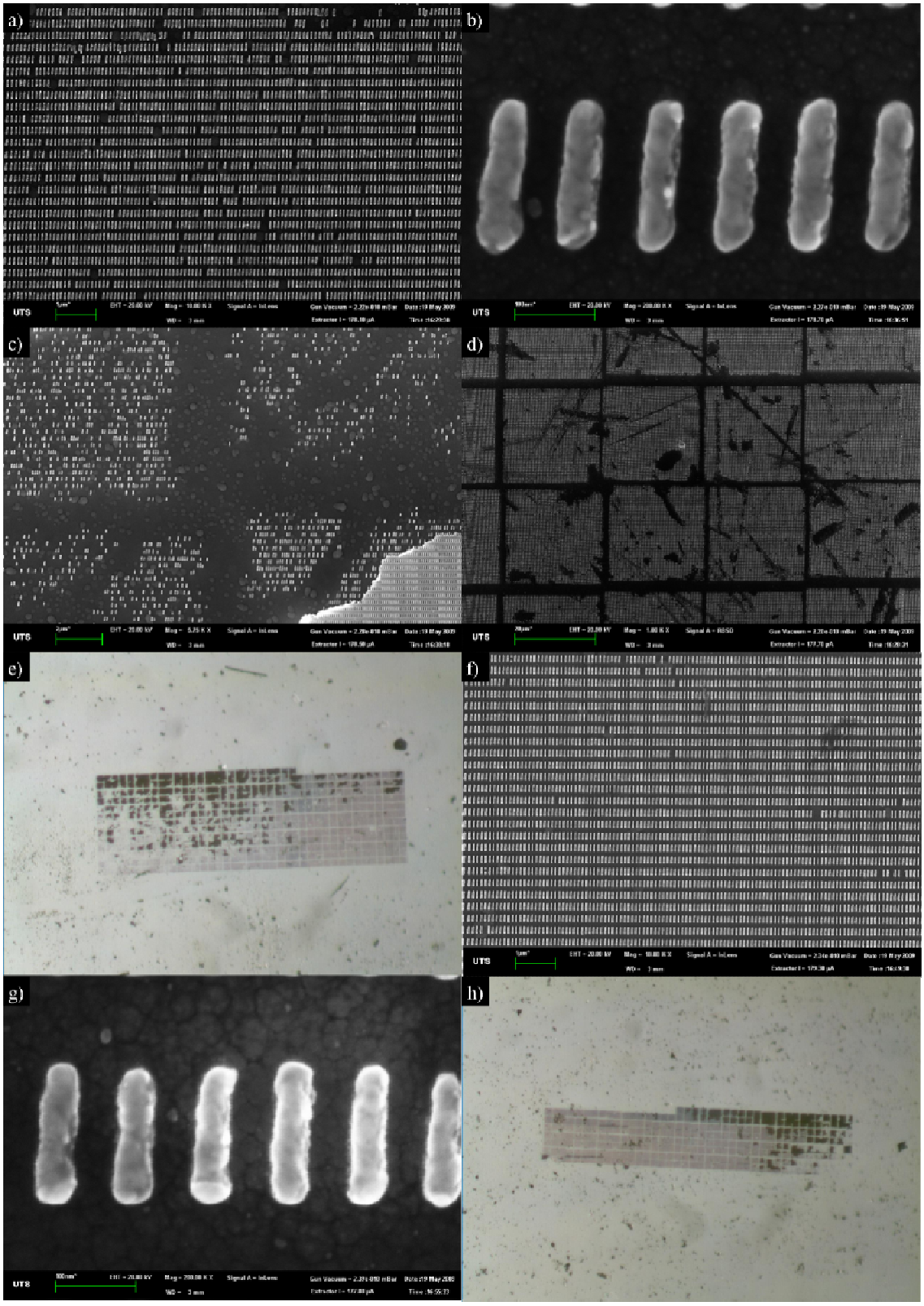

Figure 3.45: Rod structure produced using 30 seconds of plasma cleaning followed by deposition of a 2/20 nm Cr/Au bilayer on an ITO glass substrate.

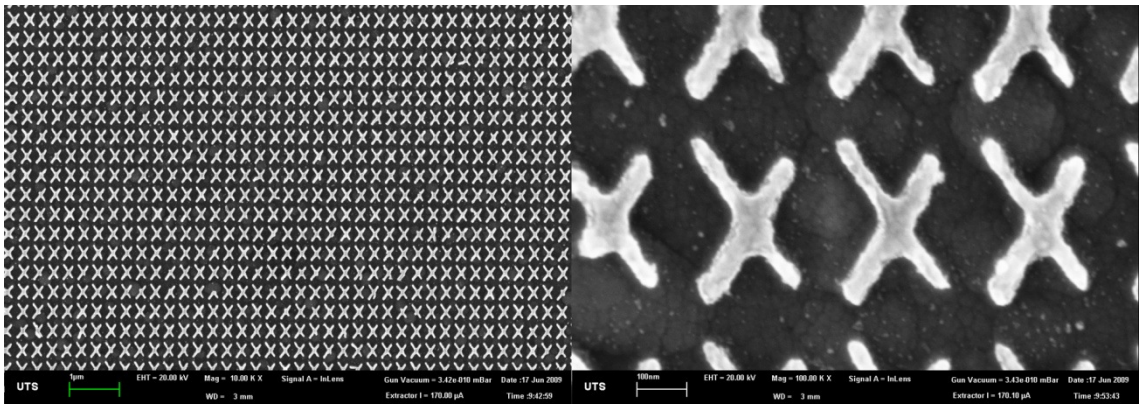

Figure 3.46: SEM images of the completed X array, produced using 30 seconds of plasma cleaning followed by deposition of a 2/20 nm Cr/Au bilayer on an ITO glass substrate.

The completed X structure, shown in Figure 3.46, was produced using the same production method as the completed rods; 30 seconds of plasma cleaning followed by deposition of a 2/20 nm Cr/Au bilayer. Some X structures in either image are missing one of the four arms. This typically occurred where there were bubbles in the ITO layer. Not all the bubbles in the ITO caused loss of structure quality but, in areas with incomplete structures, bubbles where observed. The high magnification image shows there is a large quantity of gold speckles remaining on the surface of the substrate after the lift-off process. On average there is 72 nm spacing between each X structure in both directions.

3.4. Conclusions

There are several conclusions that may be drawn from this body of work, some of which pertain to the particular system used while others are more general. Reported here are the conclusions about the general use of electron beam lithography.

The application of plasma cleaning has significant potential when used in combination with EBL but requires care. Plasma cleaning before the application of the PMMA film allows the removal of solvent remnants and ensures a clean substrate to coat. Short use of plasma cleaning (30s or less), at low energy and after resist development, allows the removal of any remaining PMMA in the structure holes and improves metal binding to the substrate. Longer plasma cleaning times may remove significant quantities of PMMA and can distort the structure dimensions as well as join structures together by removing the intervening PMMA material.

The thickness of the deposited film must, in general, be less than half the thickness of the PMMA otherwise the deposited metal will be pulled off the surface during the lift-off stage. A 20-30 nm thickness of deposited metal with 100 nm of PMMA works well.

The addition of a metal binding layer allows the gold to bind more strongly to the substrate and to create much more uniform gold structures. When a binding layer is not used, the deposited gold structure is affected by the substrate structure. With an ITO glass substrate this gives rise to individual particles (speckles) of gold. The application of a gold nanorod growth solution to a substrate containing individual gold particles was found to (a) not produce rods, and (b) join the structures together using similarly sized particles and thus making rough, non-uniform structures.

Different accelerating voltages can be used to produce structures. A 20 keV accelerating voltage exposure produces higher resolution structures and a faster exposure rate than exposures undertaken with a 10 keV accelerating voltage.

Variable pressure electron beam lithography can be used to produce structures on non-conductive substrates. However, it was found that VP EBL requires exposures at a particularly slow rate due to dispersion of the primary electron beam via the interaction with the gas in the chamber. There is also a loss of structure resolution compared to HV exposures due to (a) lower beam resolution and (b) beam dispersion. It is concluded that for structures requiring a transparent substrate, a conducting glass is more suitable than

ordinary glass on account of having higher resolution structures and faster exposure times.

Substrate dependence was observed for the dose requirements for all structures. Larger atomic number substrates required less dose for the same structure than lower atomic number substrates. In general, the dose requirements were about 0.78 nC/cm for ITO, 0.6 nC/cm for silicon and 0.3 nC/cm for gold. These also varied according to resist thickness and exposure pattern dimensions. Excess dose produced larger structures, and often deformed the corners of the pattern. Insufficient dose reduced the exposed PMMA quantity, and often left some areas of the pattern with only partial PMMA removal.

Large area arrays of rods and X structures have been completed on ITO coated glass substrates following the use of a short burst of plasma cleaning to remove PMMA in the structure holes prior to deposition of a 20 nm thin layer of gold.

Having constructed sufficiently large areas of different types of gold nanostructures, the following challenge was to investigate the optical properties of these arrays. This topic is covered in Chapter 4.

Chapter 4:

Optical Properties of Fabricated Gold Nanostructures

Chapter 4: Optical Properties of Fabricated Gold Nanostructures

4.1. Introduction

In Chapter 2, computational modelling of different gold nanostructures was undertaken to determine the optical properties of different shapes. In Chapter 3, large arrays of gold nanostructures considered to have the most potential for interesting optical properties were fabricated. In this Chapter, the optical properties of these nanostructured arrays are investigated. The accuracy of the computer modelling, the nature of the optical properties of different shapes, and the optimum shape for gold nanoparticulate window coating technologies are considered. Due to the alignment of the nanoparticles in all the arrays, the optical properties under polarised incident light are also discussed.

ITO-coated glass is a useful substrate because it has both good optical transparency and electrical conductivity. However, the electrical and optical properties of ITO are dependent in a complicated manner on the microstructure, which in turn is very sensitive to the deposition conditions and post-deposition annealing. ITO commonly grows with a graded microstructure which introduces grading into the film's optical properties too. The ITO extinction coefficient is lower at the base of the film, suggesting that the film is more conductive near the surface. This is consistent with a graded microstructure. The film is denser at the top and the conduction is enhanced because the film is more continuous at the film-ambient interface.[183] In addition, the use of an ITO substrate gives rise to interference fringes when measuring the optical properties.

The transmittance of ITO films of various thicknesses on soda lime glass substrates are shown in Figure 4.1 which is taken from the literature.[184] The interference fringes due to the ITO can be seen as the peaks particularly focused in the visible and near-visible region of 400-800 nm. As the ITO film thickness increases, the initially broad interference peaks are compressed together, putting more peaks in the same region. In the region 400-800 nm there are two interference peaks for the 0.2 μm film, whereas the 0.7 μm thick ITO film contains five interference peaks. It should be noted that the ITO film thickness used within this chapter corresponds to the 0.5 μm thick film with four peaks in the visible region for the clear ITO substrate. Another effect that alters the interference fringes and therefore the transmission spectrum of the ITO films is the free-electron density, which correlates with the tin doping percentage and the resistivity of the films.[185,186]

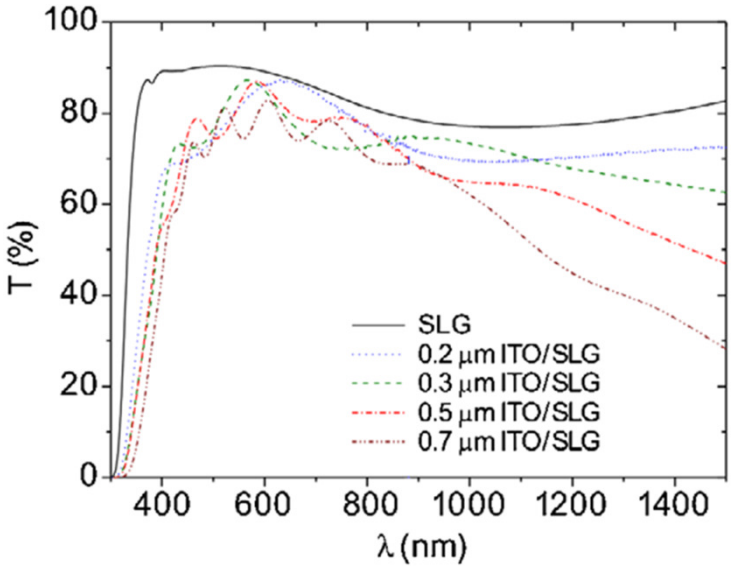

Figure 4.1: The relationship between ITO film thickness on soda lime glass (SLG) and the transmittance.[184]

4.2. Experimental

4.2.1. Collection of optical spectra

Two spectrophotometer instruments were used to measure the optical spectra of the arrays of gold nanostructures produced by EBL. An SEE2100 Microspectrophotometer (Micro Spec) was used as the primary measurement source, due to its ability to focus on the 10 μm^2 sample area, which allowed optical measurement from 360 – 1000 nm of a single writefield. A Perkin Elmer Lambda 950 UV/VIS/NIR spectrophotometer (PE), with wavelength range 300 - 2500 nm, was used to confirm the spectra obtained for the reflectance reference, and both the reflectance and transmission of an ITO substrate.

Transmission, reflectance and absorbance spectra were obtained for ~5 good quality writefields per completed sample, allowing the averages to be obtained over a greater area. A good quality writefield was determined by the lack of continuous gold film and a uniform pale red colour covering the entire area. Measurements were obtained using three different rod arrays and one X array. Transmission and absorbance measurements were obtained using air as the reference, whereas reflectance measurements were obtained using a silver-coated glass slide as the reference. Blank ITO measurements were obtained in the clear areas adjacent to the patterns for each sample. The use of a polariser was also investigated for some transmission and absorbance measurements.

4.2.2. Data processing

A correction factor was required for the reflectance data from the microspectrophotometer (MicroSpec) which was obtained from the measured reflectance of a silver reflective coating using the more accurate Perkin Elmer (PE) spectrophotometer. The transmission and absorption measurements obtained using the MicroSpec used air as the reference and contained some experimental uncertainty. For example, focus adjustment was found to change the intensity of sample spectra, although not the peak positions. As such, using a correction factor to adjust the spectra of the blank ITO samples to match the PE spectra was required. This same correction factor was then used to adjust the sample intensity to more accurately describe the transmission and absorbance intensity.

4.2.3. Modelling optical interference properties of ITO films

The ITO interference fringes were removed from the measured optical properties by simulating the transmission spectrum of an ITO film where the fringes matched the measured spectrum and subtracting out to determine the optical properties of the gold nanostructure. Simulating the ITO-coated glass optical properties was achieved through equation (4-1),

$$T = \frac{\gamma_s}{\gamma_c}|t|^2 \tag{4-1}$$

where T is the transmittance and γ is,

$$\gamma_i = \frac{n_i}{Z_0} \tag{4-2}$$

for incident light, where n is the refractive index and subscripts c, i and s correspond to the cover (air), the coating (ITO) and the substrate (glass) respectively. $Z_0 = \sqrt{\mu_0/\varepsilon_0}$ =377 ohm and t is,

$$t = \frac{2\gamma_c}{\gamma_c m_{11} + \gamma_c \gamma_s m_{12} + m_{21} + \gamma_s m_{22}} \tag{4-3}$$

where m_{jk} are elements of a transfer matrix,

$$\begin{bmatrix} \cos\phi & -(i/\gamma)\sin\phi \\ -(i\gamma)\sin\phi & \cos\phi \end{bmatrix} \tag{4-4}$$

and $\phi = 0°$ for normally incident light.

Transmission and absorbance spectra were modelled for various ITO film thicknesses using equations (4-1) to (4-4)[178] using a custom-designed Excel spreadsheet.* Through trial and error the simulated interference fringes were matched to the measured spectra such that subtraction of one spectum from the other removed or significantly reduced the ITO interference fringes. The refractive index for the ITO film was taken from the literature.[187]

* The spreadsheet was constructed by Prof. M. B. Cortie and Dr M. Arnold, UTS, 2010.

4.3 Results and Discussion

4.3.1. ITO substrate

A MicroSpec instrument was used to collect optical data for the small areas of the arrays. However, to correct for reflectance in this instrument, optical reflectance of a silver reflective sample was first measured using a Perkin Elmer (PE) spectrophotometer between 300 and 2500 nm (see Figure 4.2). The red trace in Figure 4.2 corresponds to the measured reflectance within the measurement range of the MicroSpec. These data were then used to correct spectra obtained from the Microspec instrument.

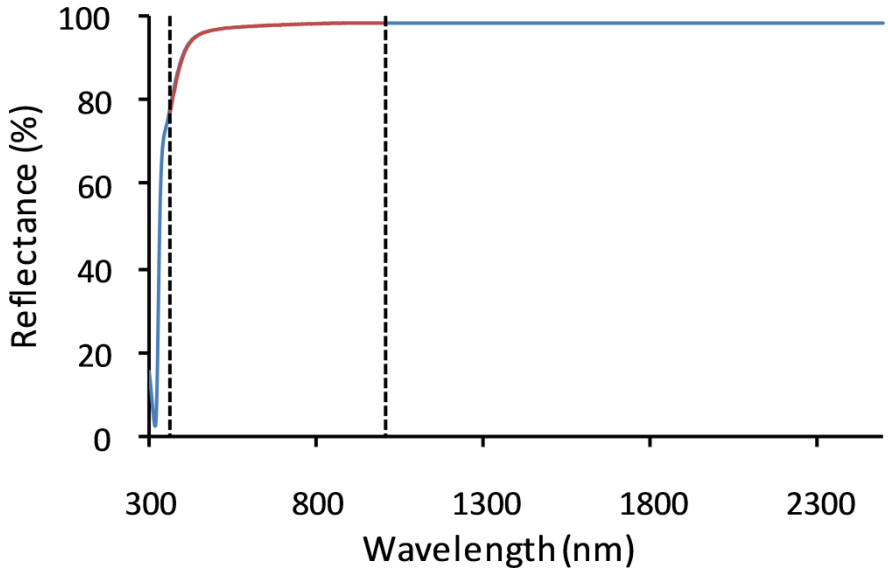

Figure 4.2: Reflectance of silver reflective reference sample. The red line between the dotted lines corresponds to the reflectance correction factor.

Transmittance and reflectance spectra of an ITO-coated glass substrate were measured using the PE spectrophotometer and are shown in Figure 4.3. The area between the dotted lines corresponds to the MicroSpec spectral range. The ITO interference fringes are observed in the range between the dotted lines and consist of five peaks for both the transmission and reflection spectra. These interference regions are similar in peak number and peak height to those shown in Figure 4.1, which were for the same ITO thickness (0.5 μm). It can be seen that a peak in transmittance corresponds to a dip in reflectance and vice versa; clearly the two are related and due entirely to interference effects. The energy remaining after both the transmittance and

reflectance are removed is the absorbance, shown in Figure 4.4. The absorbance is calculated using equation (4-5).

$$A = -\log_{10}\left(\frac{I}{I_0}\right) \quad \textbf{(4-5)}$$

where A is absorbance, I is the intensity and corresponds to the transmission and I_0 is the initial intensity, of 100%. The resultant equation therefore becomes equation (4-6).

$$A = -\log_{10}\left(\frac{T}{100}\right) \quad \textbf{(4-6)}$$

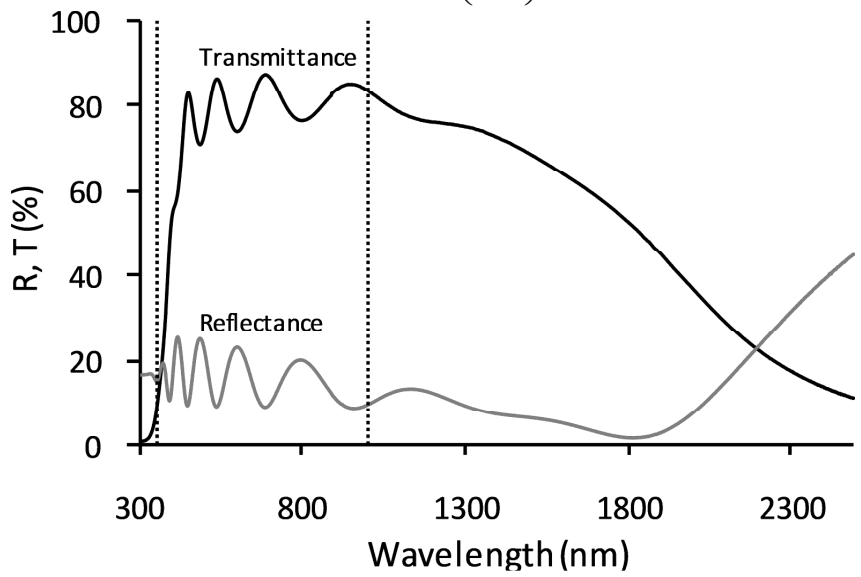

Figure 4.3: Transmission and reflection spectra of an ITO-coated glass sample. Dotted lines indicate the MicroSpec spectral region.

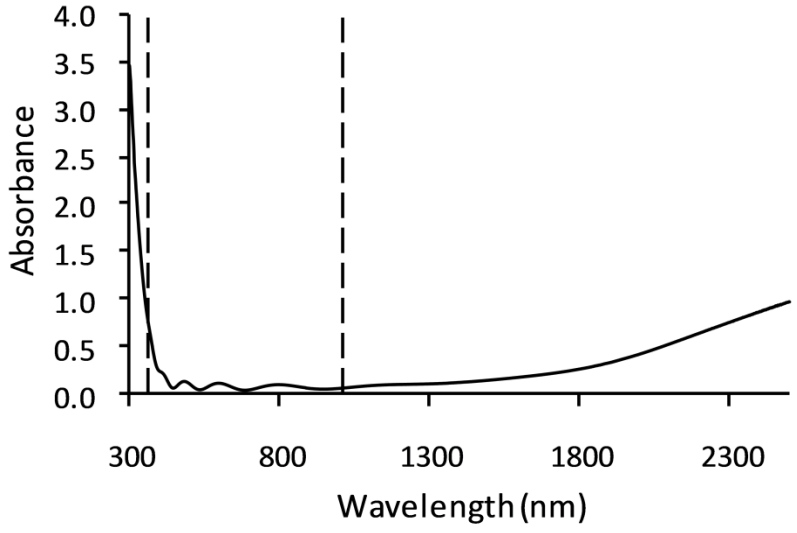

Figure 4.4: The calculated absorbance of ITO-coated glass from the PE transmission spectrum using equation (4-6).

The interference fringes in the transmission and reflection spectra are significantly reduced in intensity in the absorption spectra, and the oscillations that remain are in part due to subtraction errors between the measured *T* and *R* signals. ITO has relatively low absorption in the MicroSpec spectral region and this should allow the optical properties of the gold nanostructures to be more easily observed than in either the transmission or reflection spectra.

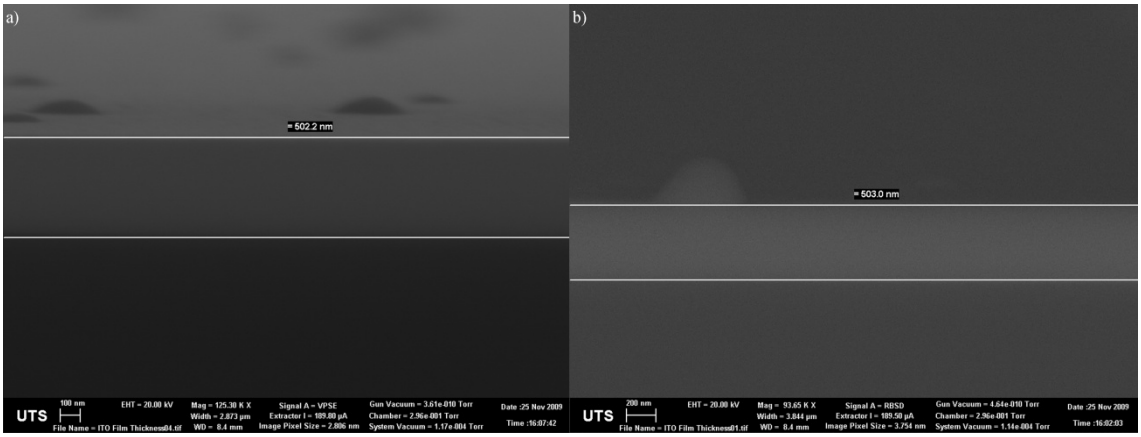

Figure 4.5: SEM images of an ITO-coated glass substrate in cross-section using (a) variable pressure secondary electron detector and (b) electron backscatter detector. The ITO thickness was measured to be 500 ± 10 nm.

Another aspect to consider is the effect of the ITO thickness. The thickness of the ITO cross-section was measured in an SEM and is shown in Figure 4.5. The ITO layer was measured to be 500 ± 10 nm. In Figure 4.1, the data for a 0.5 μm thick film best matched the interference fringes measured in the current work.

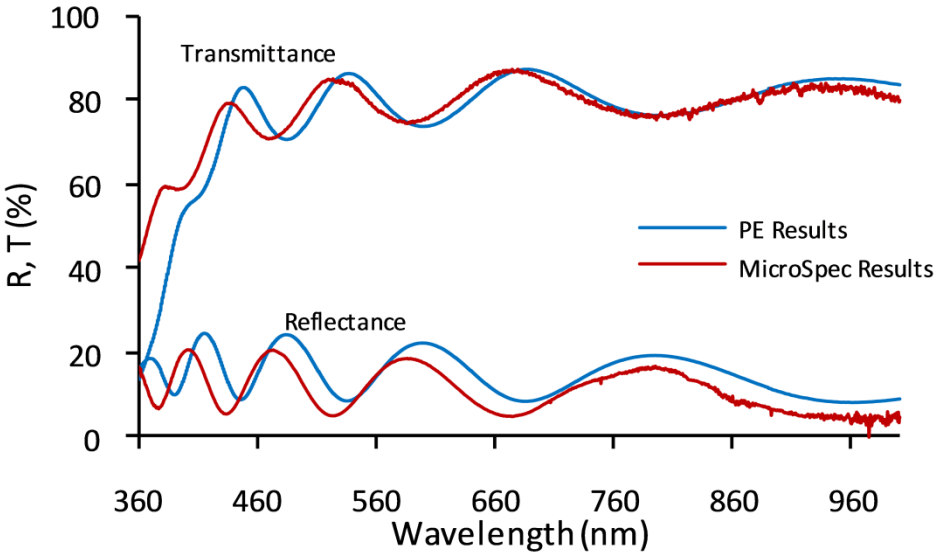

Figure 4.6: Comparison of PE and MicroSpec transmission and reflection spectra for the ITO substrate. A correction factor of 0.715 was used for the MicroSpec transmission spectrum.

A comparison between the ITO reflection and transmission spectra obtained by the Perkin Elmer spectrophotometer (PE) and the SEE2100 Microspectrophotometer (MicroSpec) is shown in Figure 4.6. The reflection spectra obtained from the PE and MicroSpec instruments were corrected using the silver reflective reference data. The ITO spectra obtained via the MicroSpec were averaged over several areas and for three different ITO substrates. The MicroSpec reflection and transmission data exhibited a hypsochromic shift of about 10-15 nm compared to the PE spectra, which indicates that the results obtained using the Microspec have a reasonable uncertainty with regard to wavelength. In addition, the transmission spectra obtained using the MicroSpec contain peaks of up to 120% transmission, and a correction factor of 0.715 was required to match the results obtained using the PE spectrophotometer. MicroSpec absorbance and transmission intensity was found to vary when the microscope focus was adjusted to set the reference sample due to the experimental geometry. Because air was used as the transmission and absorbance reference, the focus was arbitrary, and adjusting the focus altered the incident light intensity. To obtain consistent results, the microscope was focused on the ITO surface at the positions of the gold nanostructure arrays and that focal length was used to obtain the air reference. However, when the ITO coated glass substrate was removed, light was no longer focussed onto the detector and thus transmission values greater than 100% were recorded. By matching the MicroSpec

transmission and absorbance intensity to the PE intensity, a correction factor was obtained, which was then used to adjust the gold nanostructured array spectra, resulting in more accurate transmission and absorbance intensities.

4.3.2. Gold nanorod arrays

The transmittance and reflectance of the rod samples were averaged across five different writefields for each of two samples and the resulting spectra are shown in Figure 4.7. There is, approximately, a 30% drop in transmission between the gold nanostructure arrays and the ITO substrate. Also, the ITO interference fringes shifted when gold arrays were included in the spectroscopic measurements due to refactive index changes. Two major minima are observed for the transmittance of the rods and these match reasonable well with the maxima obtained from the reflectance spectra. These two peaks show roughly the position of the transverse and longitudinal peaks produced by the excited nanorods. The actual peak position of the plasmon resonances would be slightly shifted relative to that currently observed due to the present inclusion of the ITO interference fringes into the measured optical spectra. Some writefields showed differences in the peak positions, which correspond to areas of the arrays at which gold nanorods have been removed or partially removed from the ITO surface. The inclusion of these unusual spectra in the average spectrum allows a more accurate picture of the total sample spectrum.

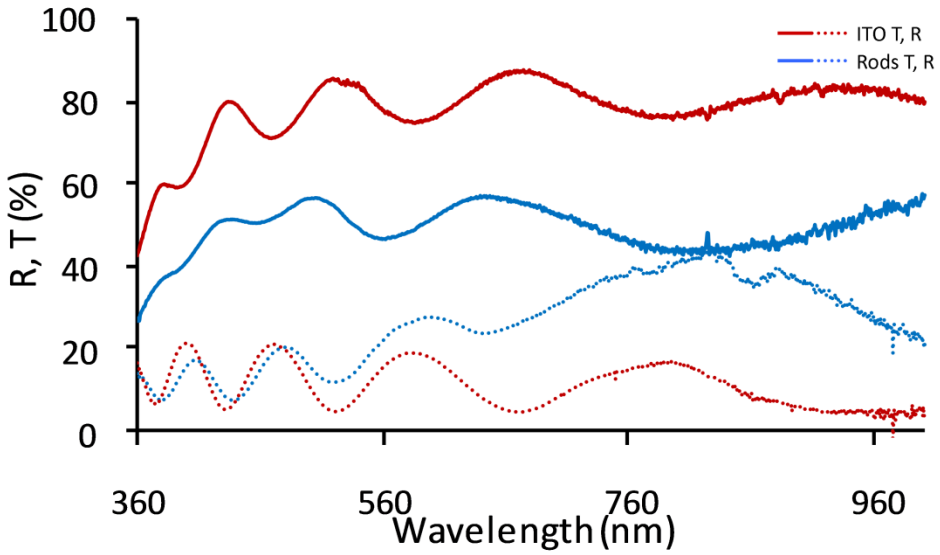

Figure 4.7: Corrected transmittance and reflectance spectra of ITO and gold nanorod arrays on ITO-coated glass. The results are averaged over a total of ten writefields for each spectrum.

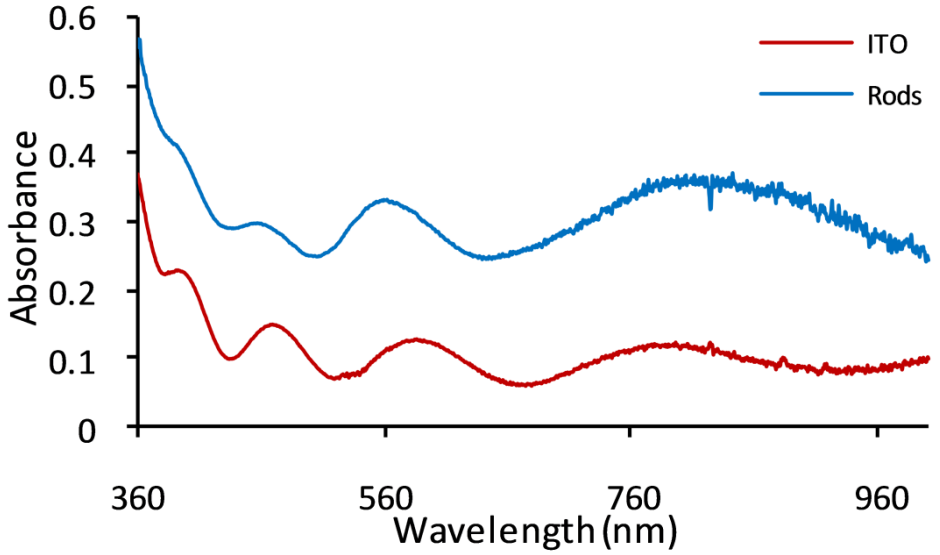

Figure 4.8: Absorbance spectra of the gold nanorod arrays compared to the clear ITO substrate.

The absorbance spectra of the gold nanorod arrays and the clear ITO substrate are shown in Figure 4.8. The peaks at approximately 560 and 780 nm correspond to the transverse and longitudinal surface plasmon resonance peaks of the nanorods. The dimensions of the rods are 175 (l) x 42 (w) x 20 (d) nm such that the apparent aspect ratio of the rods with respect to the incoming light is 4.2. A modelled gold rectangular prism (see Chapter 2) exhibited optical extinction peaks at 500 and 550 nm for the

transverse resonances and 950 nm for the longitudinal resonance. Although the modelled transverse peaks agree with experimental data shown in Figure 4.8, the longitudinal resonance occurs at a shorter wavelength than the modelled prism. While the nanorod structures may be described as rectangular prisms on average, high magnification imaging of the rod surfaces (Figure 3.45) shows uneven widths and thicknesses along each rod resulting in accurate modelling being difficult. Modelling of the gold nanorod separation distance showed very little peak dependence on the rod separation distance.

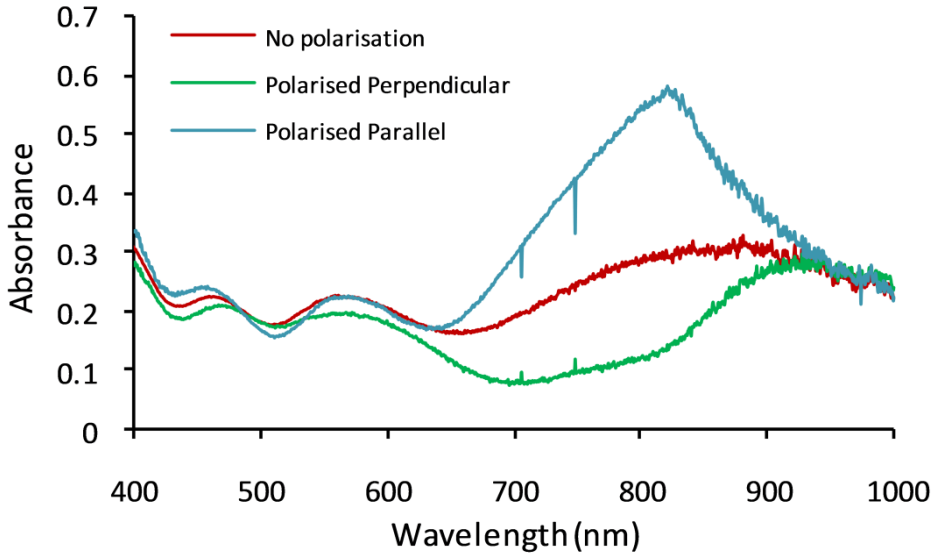

Figure 4.9: Absorbance spectra of polarised and non-polarised light interacting with the gold nanorod arrays. The polarisation direction is relative to the long aspect of the nanorods.

The effects of incident polarised light on the nanorod arrays are shown in Figure 4.9. The incident light was polarised parallel or perpendicular to the long aspect of the rod. The polarised parallel spectrum shows the large longitudinal plasmon resonance absorbance peak at 810 nm. This peak disappears when perpendicular polarised light is applied. The use of the polariser allows the absorbance of the larger plasmon resonance peaks to be raised significantly above the ITO interference fringes, especially for the rod shaped nanostructure.

4.3.3. Gold X arrays

The optical transmittance and reflectance spectra of gold X arrays are shown in Figure 4.10. The largest peak observed begins at approximately 920 nm and increases

beyond the range of the MicroSpec. From both the rod and X arrays it can be seen that the addition of any gold on the surface of the ITO substrate causes the transmission of light through the sample to decrease across all of the wavelengths investigated. The reflectance of the ITO and gold-coated ITO, on the other hand, is comparable up to about 600 nm, and only diverges at longer wavelengths.

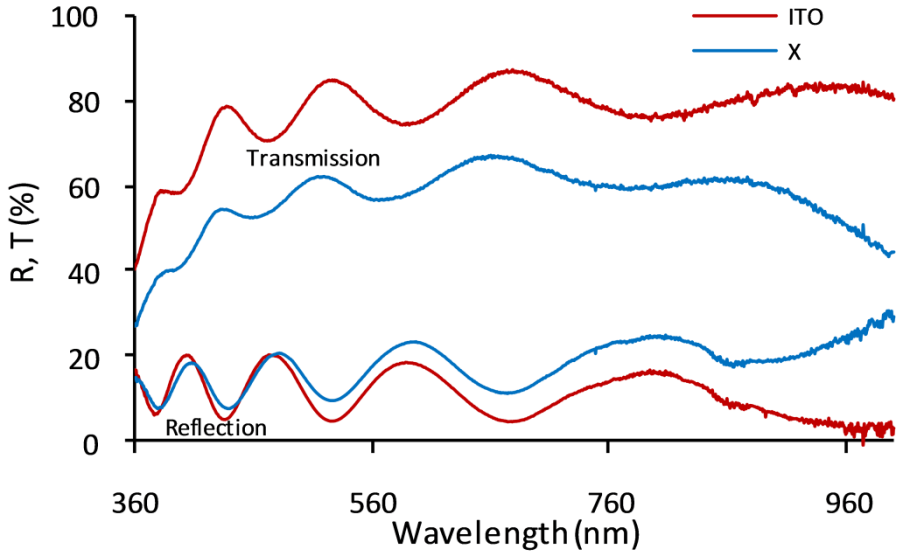

Figure 4.10: Transmission and reflection spectra of the X structured arrays shown with an ordinary ITO comparator.

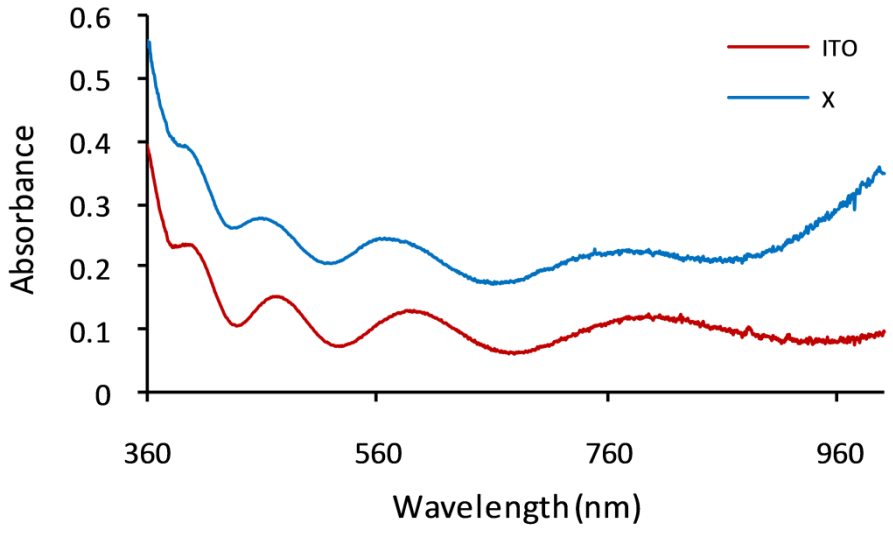

Figure 4.11: Absorbance spectra of X nanostructured arrays, with an ITO comparison.

The addition of gold to the ITO substrate causes an increase in absorption across the entire measured spectrum for both the rod and X arrays. Measurement of the ITO and the X arrays (Figure 4.11) showed that, on average, a 0.13 increase in absorbance

intensity occurred along the entire investigated wavelength region excluding the large absorption peak beginning about 920 nm. The addition of gold also slightly alters the position and intensity of the interference fringes, similarly to that observed for the rod samples. The X arrays measured here are closely related to X35 structure modelled in Chapter 2. The isolated X35 structure was calculated to have two longitudinal resonances along the shorter and longer dimensions of the X structure. The positions of these peaks for an individual X35 structure in a vacuum were calculated to be 720 nm for the shorter aspect and 745 nm for the longer aspect. The spacing between the fabricated X structures were measured to be approximately 72 nm in each direction or, in other words, the periodicity was 393 nm in the long aspect and 288 nm in the short aspect directions. The calculations of the X35 periodic 1D array show that there is a very strong red-shift of the short X aspect resonance when each periodic spacing is 75 nm and the electric field direction of the applied light is along the direction of the array, see Figure 2.22. The main resonance peak was calculated to shift from 720 nm to 835 nm for the 1D array with 75 nm periodic spacings. A 1D array was also calculated when the X structure aligned along the long aspect of the X structure, Figure 2.23, and a red-shift from 745 nm to 775 nm for the main resonance occurred. The largest measured absorbance peak is situated beyond the MicroSpec's wavelength range, above 1000 nm. However, this peak also corresponds to a reflectance peak and may be partly due to scattering. Also, the high magnification SEM images of the X structures (Figure 3.46) show that the edges and surfaces of the structures are uneven, as with the rods. This might also effect the position and width of the plasmon peaks.

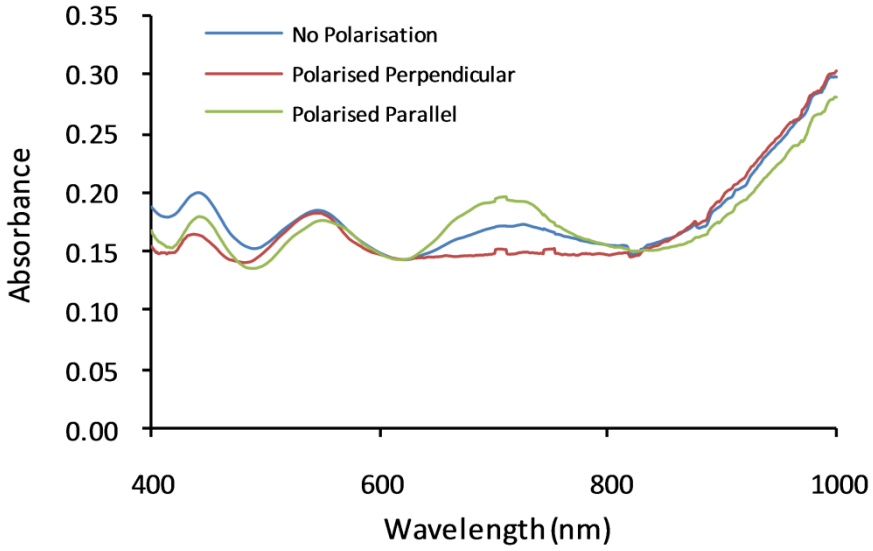

Figure 4.12: Absorbance spectra of the gold X arrays with and without initial light polarisation. Light was polarised parallel and perpendicular to the long aspect of the X structures.

The effect of incident polarised light on the absorbance spectra of the gold X arrays is shown in Figure 4.12. The incident light is polarised parallel and perpendicular to the long aspect of the X structure. When the light is polarised parallel to the long X aspect, the plasmon peak at 700 nm is doubled in height compared to the case for no polarisation. Alternatively, when the incident light is polarised perpendicularly to the long aspect of the X structure the plasmon peak at 700 nm completely disappeared. It is interesting to note that this result differs from the modelled data obtained in Chapter 2, which suggests that the perpendicularly polarised light should also have a maximum at a position slightly blue-shifted compared to that of the parallel polarised maximum. However, the intensity of the plasmon peak where the incident light is polarised parallel to the long X aspect maximum is almost doubled compared to that of the light polarised perpendicular to the long X aspect. Therefore, it is believed that the surface plasmon resonance peak which has been modelled for the light polarised perpendicular to the long X aspect has been drowned out by the ITO interference fringes. The periodic X arrays modelled in Chapter 2 show that the optical extinction of the 1D array polarised parallel to the long aspect of the X structure is also almost twice that of the perpendicularly polarised sample. A red shift is also observed for both polarisations when the structures are in a 1D array, with the same air gap, but there is a much stronger

red shift for the plasmon peak when the electric field of the incident light is applied along the short aspect of the X structure (see Figure 2.24).

The transmission spectra of both the rod arrays and the X arrays show that, although the plasmon resonances from the gold nanostructures are observed, the intensity of these peaks are only slightly larger than the entire region investigated. As initially hypothesised, these results mean that the use of a single layer of gold nanorods, or X structures will not produce sufficient extinction for window coatings. Nevertheless, the aligned gold nanorods may have potential for use in polarisers, optical filters, or plasmonic circuits. Actually, the X structures also have good potential for use in window coatings due to the larger transmission minima in the NIR, if only their overall coverage can be increased. This is also because there are no major transmission peaks or troughs across their entire visible spectrum which means that light transmitted through such coatings would have a relatively neutral colour.

4.3.4. The contributions of gold nanostructures to the measured optical spectra

To determine the contributions of gold nanostructures to the measured optical spectra, a simulated ITO-coated glass spectrum was subtracted from the measured ITO and gold particle spectra. Literature values[187] for the refractive indices for ITO was used and the modelled ITO film thickness was adjusted until the interference fringes of the modelled spectra matched the experimental data (the actual ITO film thickness was measured to be 500 ± 10 nm). It should be noted that between 300 and 500 nm the simulated and measured optical properties did not match exactly, resulting in areas where the fringes were not completely removed.

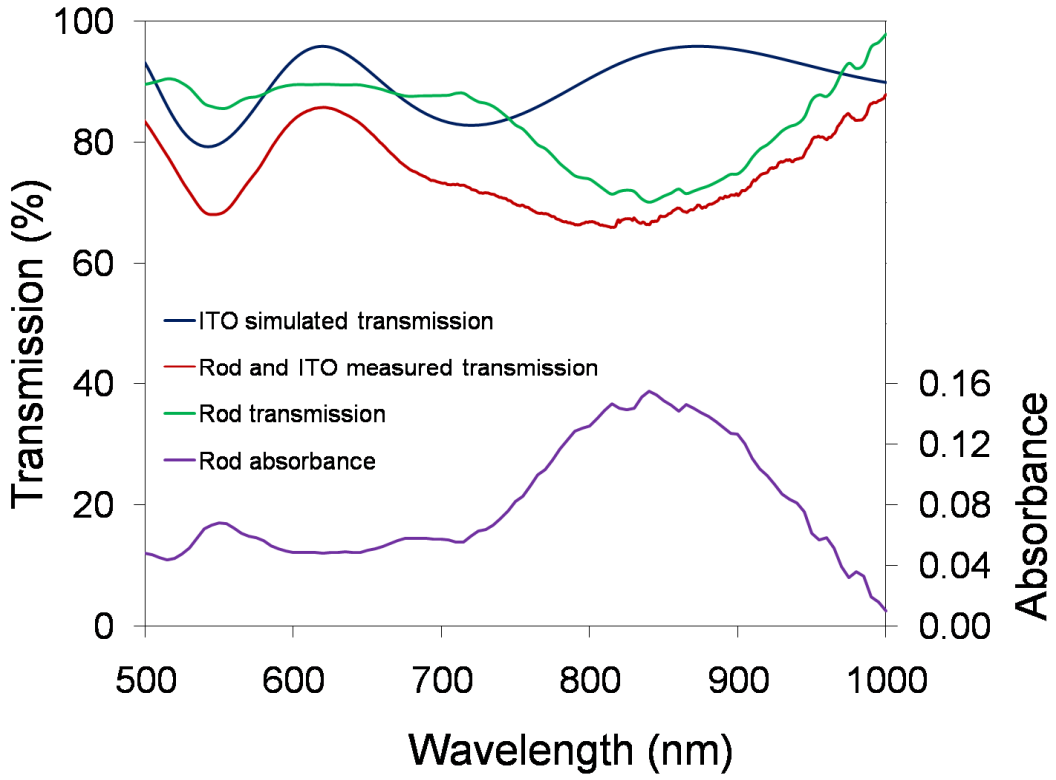

Figure 4.13: Rod transmission and absorption properties with the ITO fringes subtracted. Also shown are the simulated and measured rod and ITO transmission spectra.

The transmission and absorbance spectra of gold nanorod arrays produced by EBL that are deconvoluted from the ITO interference fringes are shown in Figure 4.13. Also shown is the measured rod array transmission spectrum and the simulated transmission spectrum for an ITO-coated glass sample, from which the transmission and absorbance of the gold nanorods was obtained. The transmission spectrum of the 2D array of aligned gold nanorods shows that 90% of light is transmitted through the rod array in the visible spectral region. This decreases, to a minimum at 835 nm of 70% transmission due to the longitudinal plasmon resonance. This transmission minimum in the deconvoluted spectrum is slightly red-shifted compared to that for the experimental data.

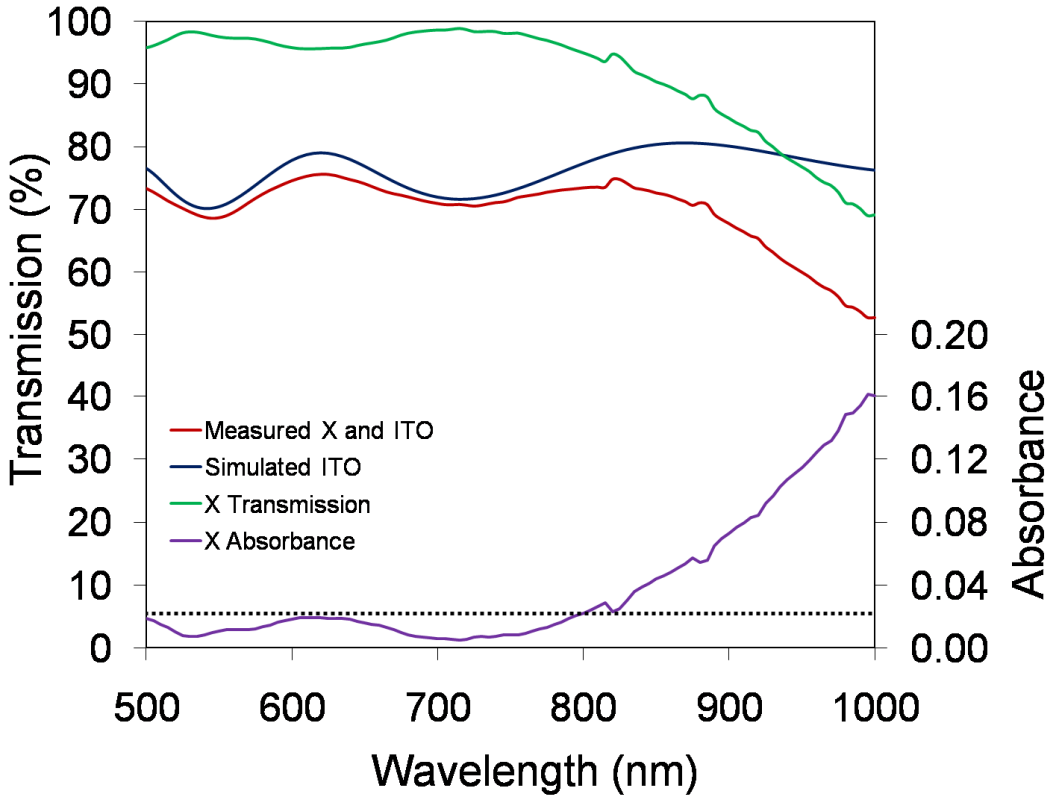

Figure 4.14: The simulated ITO (blue) and the measured X on ITO-coated glass transmission (red) subtract to give the X transmission (green) spectra. The X absorbance (purple) spectrum is also shown.

The transmission and absorbance spectra of the X arrays are shown in Figure 4.14. The measured X on an ITO-coated glass substrate transmission spectra was subtracted from the simulated ITO transmission spectra to acquire the transmission spectrum of arrays of gold X's. This transmission spectrum could be converted to the absorbance spectrum which is also shown in Figure 4.14. The dotted line marks the maximum absorbance region below which noise has an effect. In other words, below the dotted line the maxima and minima of the absorbance spectrum are due to inaccuracies in the optical properties of the simulated ITO spectrum. It should be noted that when simulating the ITO fringes to match the measured X and ITO fringes, two reported ITO thickness were combined to broaden the ITO fringes. The combination consisted of 72% of a spectrum generated by 480 nm thick ITO layer combined with 28% generated by 430 nm thick ITO.

4.4. Conclusions

Surface plasmon resonance has been observed on all complete fabricated gold nanostructured arrays. Optical measurements were undertaken for completed arrays of gold nanorods and X structures.

The results obtained from the MicroSpec required a correction factor due to the experimental geometry, specifically for transmission and absorbance spectra. The correction factor was selected to fit the ITO intensity from the MicroSpec to the PE spectra and was different for each sample.

The use of ITO glass as the substrate affected the optical properties of the samples by introducing interference fringes which were found to alter the position and intensity of the surface plasmon resonance of the nanostructures. In some cases the resonance peaks were drowned out by these fringes. However, the longitudinal plasmon resonance of the gold nanorod and X's could still be identified as a separate peak clear of the interference fringes.

Transverse and longitudinal plasmon peaks were observed with the gold nanorod arrays. The peak positions of these structures were more accurately modelled using a spherically-capped cylindrical rod-shaped structure with aspect ratio of 5.22 rather than the using the measured dimensions to model as a rectangular prism. The longitudinal surface plasmon resonance peaks were sufficiently large to be clear of the ITO interference fringe, however, their macroscopic intensity is insufficient to create any form of efficient window coating. Also, the position of the plasmon peak must be shifted further into the infrared by increasing the aspect ratio prior to use as a window coating. In addition, a practical window coating would require a greater density of rods, removal of the ITO interference fringes through the application of the gold nanostructures onto clear glass, and a spread of aspect ratios to cover a large spectral region.

The arrays of X's displayed a single main plasmon resonance peak that was affected by the incident light polarisation and corresponded to the resonance of the long aspect direction of the X structure. There was a transmission minimum from 920 nm further into the NIR, which is a potentially useful base for designing window coating applications, however the position of the surface plasmon resonance peak needs to be shifted further into the NIR prior to use in the formation of energy efficient window

coatings. Multiple layers of gold structures may be required before sufficient extinction would be obtained.

A comparison of the measured optical properties with the results of computational modelling, Chapter 2, showed that the position of the surface plasmon resonance peaks of the fabricated structures differs slightly to that of the modelled structures. This appears to be due primarily to differences in the structure shape. The trends that were found using modelling calculations are believed to be the same but the peak positions and intensities differ.

Understanding the contributions from the ITO interference fringes allowed the position and relative intensity of the gold surface plasmon resonance peaks to be identified.

Having investigated the optical properties of 2D arrays of gold nanostructures, the next challenge was to investigate simple fabrication methods to produce these structures by wet-chemical techniques. This topic is covered in Chapter 5.

Chapter 5:

Coatings of Gold Nanorods on Glass

Chapter 5: Coatings of Gold Nanorods on Glass*

5.1. Introduction

The investigation of the optical properties of different shapes, positions, dimensions and orientations of gold nanoparticles has been discussed in previous chapters. As well as the theoretical considerations for window coatings, practical aspects are important so that new materials can be utilised through binding to a window surface. This chapter investigates different methods to bind gold structures, primarily nanorods, to glass surfaces. Investigations were conducted into methods to attach gold nanorods to glass by molecular binding and the immersion of gold nanorods into a polymer solution.

Glass is used extensively in buildings because of its aesthetically pleasing appearance and because it permits ingress of daylight. Unfortunately, glass windows are sites for significant heat transfer. A problem in cooler climates is outwards flow of heat during winter while inwards transfer of heat in summer is a significant issue in many tropical and temperate locations. The heat transfer occurs by a combination of conduction, convection and radiant mechanisms and here we focus on the passage of *radiant* solar energy through glass. The comparatively modest conductive and convective heat flux across windows due only to differing internal and external air temperatures is a separate issue that may be readily addressed by double glazing or other barriers to convection.

* Sections of this chapter have been published. (N.Stokes, J. Edgar, A. McDonagh, M. Cortie, 2010. 'Spectrally-selective coatings of gold nanorods on architectural glass' accepted 23rd January 2010, *Journal of Nanoparticle Research,* in press.)

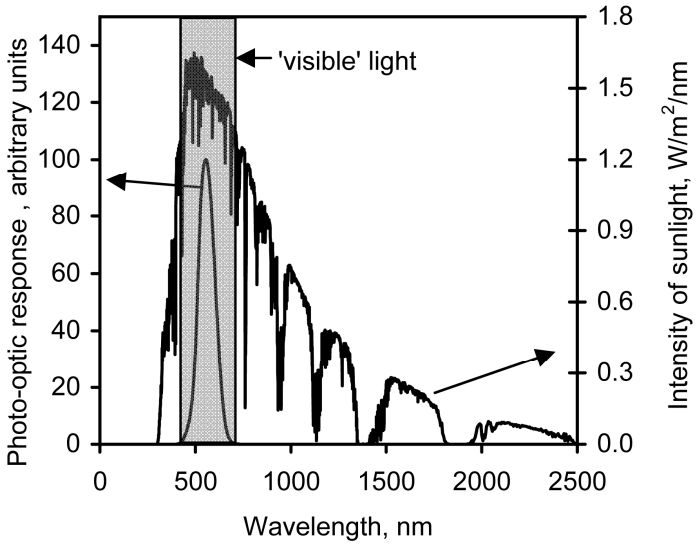

Figure 5.1: The solar energy spectrum at the Earth's surface (hemispherical spectral solar irradiance for a sun-facing surface tilted at 37º, from ASTM G173[188]). The shaded section indicates the visible region. The photo-optic response of the human eye is also shown.

Normal glass is highly transparent to both the visible and infrared components of sunlight, which exacerbates the problem of solar heating in buildings. The sun can radiate up to 1000 W/m^2 in some parts of the world and the heat load on buildings from this source can be significant. The solar spectrum at the Earth's surface is reproduced in Figure 5.1 along with the photo-optic response of the human eye. In warm climates or seasons it is desirable that windows transmit as much visible light (400 to 700 nm) and block as much infrared radiation as possible. Given the nature of the solar spectrum on Earth, it is particularly desirable to attenuate the near-infrared region between 750 and 1300 nm as this contains an appreciable fraction of the invisible solar energy.

Transmittance through high quality 4 mm thick glass[15] is about 90% over the spectral range 300 to 2500 nm but an acceptable level of optical transparency for architectural purposes would be maintained if up to 50% of the incoming visible spectrum was attenuated.[189] To achieve this, coatings may be designed to enhance the amount of radiation *reflected* from the surface of the window or alternatively to *absorb* radiation. A variety of materials have been used or proposed for both classes of coating.[190-192] Thin, reflective metal films have been made using several different vacuum deposition techniques such as sputtering or ion plating, but these technologies are expensive relative to the relatively cheap absorbing materials available. In addition, legislation has

been introduced in some cities that limit the amount of light that can be reflected by a building's facade. For example, in Sydney, Australia, the city council has limited the reflection of visible light from buildings to ~20% of that incident.[16] The motivation is to prevent neighboring buildings being subjected to an increased heat load and/or to prevent glare. It is apparent that absorptive coatings will conduct and convect approximately half of the absorbed heat inwards[193] and thus may be less efficient than reflective coatings but, given the considerations mentioned above, interest in producing more efficient absorptive window coatings has increased significantly.

Absorptive systems involve coatings based on dyes (e.g. perylene or quaterrylene-based molecules) or nanoparticles (e.g. lanthanum hexaboride[192]) that absorb strongly in the infrared. Gold nanorods and nanoshells can be synthesized that absorb in the near-infrared by virtue of their plasmon resonance, and they scatter very little light provided that they are sufficiently small. (Too much scattering of light is generally undesirable in window coatings as it renders the window translucent and hazy.) The comparative merits of gold nanorods and nanoshells for spectrally-selective applications have been analysed elsewhere[156,194] and although nanoshells have been previously considered for solar applications,[195] nanorods are easier to produce in large quantities and have the better optical characteristics. The strongest plasmon resonance in gold nanorods occurs when the conduction electrons within the gold oscillate along the long axis at the same frequency as the incoming light. This is known as the longitudinal resonance and the wavelength of light at which it occurs is dependent on the shape and dimensions of the nanorod.[196] In particular, increasing the aspect ratio (the ratio of length to width) of the nanorod shifts the longitudinal plasmon peak to longer wavelengths. Because gold nanorods can be synthesized with controlled aspect ratios, the inherent tunability of their longitudinal plasmon peak wavelength makes them candidates for use in spectrally-selective coatings.[168]

Xu *et al.* have previously investigated the spectral-selectivity of coatings of nanometre-sized gold hemispheres on glass and found that they screen 17 to 28% of incoming infrared radiation, depending on their optical density.[193,197,198] Modelling showed that a window coating consisting of a mixture of gold nanorods with aspect ratios ranging from 3 to 10 would effectively block light in the 800 to 1500 nm region.[199] Gold nanorods bound to glass have been reported using a binding layer of, for example, poly-electrolytes[144,200] or a monolayer of 16-mercaptohexadecanoic acid on a

gold substrate.[201] Alternatively, Wei *et al.* reported that it is possible to grow gold nanorods on the glass after first attaching gold seed crystals.[202,203] In contrast, Mulvaney *et al.*[204] reported that gold nanorods could be readily dispersed in aqueous poly vinyl alcohol (PVA) from which thin polymer films of reasonable optical density could be obtained. The straightforward preparation and high optical density of the Au/PVA films led us to consider them here for spectrally-selective window coatings. This chapter chiefly explores the performance of Au nanorod/PVA coatings on glass under solar irradiation. Modelled and measured results are analyzed and compared. However, some preliminary test work to attach rods to glass by other means is also described.

Wei *et al.* have used mercaptopropyltrimethoxysilane (MPTS) to grow gold nanorods on a glass surface.[202,203] After the MPTS was bound to the glass surface, the gold seed was bound to the thiol group of the MPTS. Following this the substrate was immersed in a growth solution allowing the seeds to grow into rods on the glass surface. The MPTS molecule and a diagram showing the growth of gold nanorods attached to a substrate is shown in Figure 5.2. Alternatively, Zhang *et al.* reported that when using an ITO glass substrate, more rods were produced when depositing the seed directly on the ITO without using a MPTS binding layer than with.[205,206] Whereas, Taub *et al.* reported a significant increase in the number of gold nanorods generated when attached to mica or silicon via aminopropyltrimethoxysilane (APTS) compared to solution growth process.[207] The processes where the gold nanorods are strongly attached to the substrate have great potential because they can theoretically control the direction of rod growth too. Consequently, an investigation was conducted into the use of MPTS as a binding layer for both the application of window coatings and the straightforward alignment of gold nanorods on a substrate.

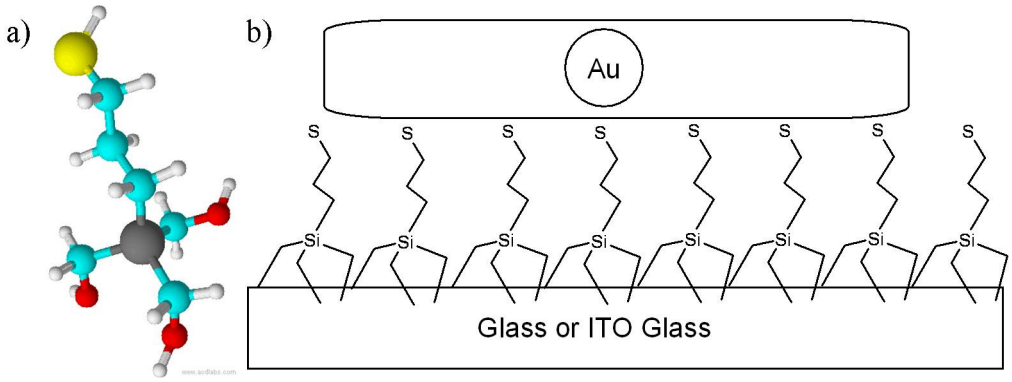

Figure 5.2: (a) Model of mercaptopropyltrimethoxysilane (MPTS) and (b) a diagram showing the growth of surface attached gold nanorods.

5.2. Experimental Methods

5.2.1. Molecular binding

Molecular binding of the (3-mercaptopropyl)trimethoxysilane (MPTS) to glass was investigated using two methods. Glass and ITO-coated glass were functionalised with MPTS by immersion in a refluxing solution containing 100 mL of 2-propanol, 1.9 mL of MPTS and 1.4 mL of water. The substrates were immersed in the solution for 10 mins, rinsed with 2-propanol, dried with N_2, and cured in a 100°C oven for 10 mins. This process was repeated 3 times.[208] Alternatively, glass was functionalised with MPTS using a solution of 10 mL of 2-propanol, 100µL of MPTS and 6 drops of MilliQ water. The substrates were immersed in the solution for 30 mins, with the temperature of the solution just below boiling. Thereafter, the substrates were washed in 2-propanol and dried with N_2.[202,203]

Two methods of rod growth were investigated following the functionalisation of the ITO-coated glass and uncoated glass substrates. Firstly, 1 mL of 5 nm gold seed solution (Aldrich) was diluted with sufficient MilliQ water to immerse a functionalised glass substrate and a reference glass substrate for 24 hrs. After washing, the samples were imaged using an SEM and the observed seed was compared. Alternatively, the MPTS functionalised substrates were immersed in a gold nanorod solution overnight and dried using (i) oven, (ii) desiccator and (iii) atmosphere. Also a comparison between substrates with and without the MPTS functionalisation was investigated.

5.2.2. Polyvinyl alcohol/gold nanorod films

5.2.2.1. General

The following chemicals were purchased commercially and used as received; hexadecyltrimethylammonium bromide (Nanjing Robiot), sodium salicylate (Ajax Finechem), ascorbic acid (Sigma Aldrich), silver nitrate (Sigma Aldrich) and potassium borohydride (Sigma Aldrich), polyvinyl alcohol (Ajax Chemicals). Tetrachloroauric acid ($HAuCl_4$) was synthesized according to published methods.[209] Water was purified by a MilliQ system (18 MΩ cm^{-1}). Glass (4 mm thickness) was manufactured by Viridian and purchased from R & R Glass Services, Australia. Glass panes were cut with dimensions 70 mm x 70 mm. The nanorod aspect ratios were measured using a Zeiss Supra 55VP scanning electron microscope.

5.2.2.2. Preparation of coatings on glass

Gold nanorods were prepared using a variation of the method of Murphy and co-workers.[140,210] Briefly, for aqueous nanorod solutions consisting of nanorods of 3.4 aspect ratio, we used 10.93 g hexadecyltrimethyl ammonium bromide (CTAB) diluted in 150 mL water, 1.5 mL 0.1 M tetrachloroauric acid ($HAuCl_4$), 1.5 mL 0.1 M sodium salicylate, 1.65 mL 0.1 M ascorbic acid, and 2.25 mL 0.01 M silver nitrate ($AgNO_3$), diluted to 300 mL. Nanorods of 3.9 aspect ratio were prepared using 14.58 g CTAB dissolved in 200 mL water, 2 mL 0.1 M $HAuCl_4$, 2 mL 0.1 M sodium salicylate, 2.2 mL 0.1 M ascorbic acid, and 4 mL of 0.01 M $AgNO_3$. This solution was then diluted to 400 mL. Growth was initiated by addition of 1% v/v of seed solution to the growth solution. The seed solution was prepared by adding 0.5 mL of ice-cold potassium borohydride (0.01 M) to 10 mL of a solution containing $HAuCl_4$ (0.125 mM) and CTAB (25 mM). The resultant suspensions were centrifuged and washed with water. The two rod samples are designated as 'R1' and 'R2' hereafter. The aspect ratio of the rods is controlled by the amount of $AgNO_3$ added but larger additions than those used here brought no advantage because they decreased the yield of nanorods.

The initial test coatings consisted of rods were mixed with PVA solutions of 5-15 wt% concentration and applied to glass slides and dried. Initial tests were produced by placing a drop of rod/PVA solution on a glass slide and spreading the solution out by placing another slide on top and sliding it in a single direction with the aim of aligning the rods along the sliding direction. A diagram of this method is shown in Figure 5.3. Several rod PVA solutions were dried sufficiently so that they could be peeled off the substrate and stretched to investigate the effect on the optical properties of the alignment of rods. The applications of successive layers of PVA rods on a glass substrate as well as the use of a screen printer to align rods in PVA were also investigated.

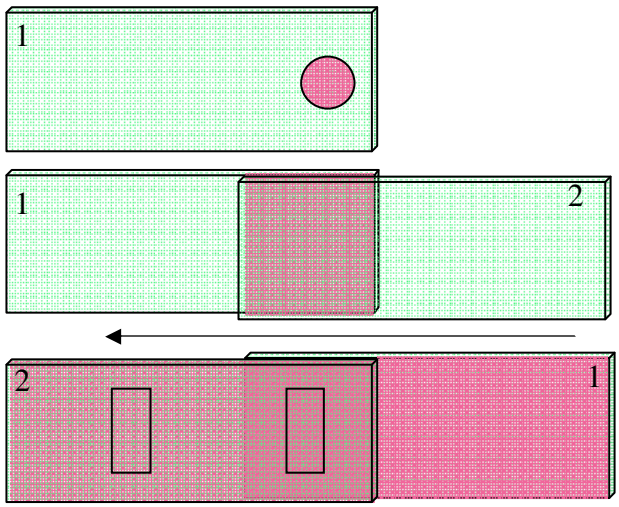

Figure 5.3: Test method for rod PVA solutions. The arrow shows sliding direction and the two rectangles show the sample areas where the optical spectra were measured.

The alignment of gold nanorods in PVA was also investigated. A very thin glass pipette was dipped in a mixture of 7.5 wt% PVA and gold nanorods. Straight lines of the PVA solution were written using the pipette. The samples were imaged using the SEM.

Methods to increase the amount of gold nanorods binding to glass for the purpose of increasing the optical absorption were investigated. Gold nanorods mixed with a 15% PVA solution were applied evenly to a glass surface with a border of adhesive tape to form a shallow well. The samples were dried overnight in a desiccator and the optical properties measured. Additional layers were then added by refilling the well and the optical properties were measured between each additional layer. Samples consisted of 3 to 6 applications of the rod solution.

The stability of gold nanorods in a PVA film was investigated. Two films consisting of rod sample 'R1' (see Section 5.2.2.2.) were mixed with 15 wt% PVA solution and cast into a 2 mm well to dry. The film was then detached from the substrate and one sample was stored in the dark and the other sample was stored on a window sill. The absorbance and transmission spectra for each sample were obtained over several months.

Stretching of films along one dimension was also investigated with particular focus on aligning the gold nanorods within the polymer and the effect of alignment on the optical properties. Rod sample R1 and a 15 wt% PVA solution were preferred for this experiment. The methods used here are based on those reported by Mulvaney *et al*,[204] however, the films in the current work were manually instead of mechanically stretched. The films were stretched along one dimension as far as possible. Over-stretching resulted in holes forming within the film. The UV-visible absorption spectrum was recorded for the unstretched and then stretched sample using polarised and unpolarised light.

Test coatings consisted of a mixture of R1 and R2 into 15 wt% PVA solutions in various ratios and then cast into a 2 mm deep recess on glass panes and allowed to dry to form thin films. The final thickness of the film was ~0.8 mm. The optical densities of these thin films were controlled by the concentration of the initial gold nanorod solutions. Larger area sample coatings were made using R1:R2 ratios applicable for absorptive window coatings determined during the test film stage.

5.2.2.3. Characterization of coatings

Test coatings were characterized by a Shimadzu UVmini 1240 UV-Vis spectrophotometer collecting transmission and absorption data between 300 and 1100 nm.

Reflection and transmission spectra for sample coatings were collected between 300 and 2500 nm using a Perkin Elmer Lambda 950 UV/VIS/NIR spectrophotometer. These data were then convoluted with the standard ASTM AM1.5 solar spectrum[188] to give an estimate of the solar screening efficacy of the coated glass panes. The optical properties of these larger area samples were also tested outdoors in natural sunlight using a thermopile to measure the incident and transmitted intensity. This was considered to give a more realistic simulation of the coating's overall performance than use of lamps

in an indoor laboratory setting. A thermocouple was used to measure the temperature of the glass, film and ambient air. The panes were oriented so that they were normal to the direction of sunlight and measurements were made between the times of 09:00 and 12:00 on two very clear days in June in Sydney, Australia. The solar irradiance was 870 ± 5 W/m^2 at 10:30 am and increased to 885 ± 5 W/m^2 at 12:00 pm. Wind speed was measured using a Digitech anemometer. Average wind speed during measurements was between 0 – 3 km/hr with occasional gusts of up to 7 km/hr recorded.

The thermopile detector, (PMA 2143, from Solar Light Company, USA) provided a linear response to radiation between 200 and 50000 nm and had an angular field-of-view of 9°. Recording the transmission of the film required the thermopile to be set behind the window and the intensity was recorded at 90° to the plane of the glass. Direct reflection, on the other hand, could not be measured due to the shadow cast onto the glass by the thermopile. Instead, reflection data was obtained from the laboratory spectra. The remaining solar radiation was either absorbed by the samples, or re-radiated at high angles (>9º) off the front and back surfaces. Any absorbed radiation will cause the glass to heat up and the energy will thereafter be both convected and re-radiated to the surrounding environment. However, thermal re-radiation at these low temperatures can be neglected and the dominating form of heat transfer from the glass will be convection.

Heat convection from the front and rear surfaces of the glass panes was estimated from

$$q_{convected} = (T_S - T_{Air})A\bar{h} \qquad \textbf{(5-1)}$$

where T_s is the temperature of the window surface, A is the area of the glass and $\bar{h}$ is the average heat transfer coefficient over the pane. The latter can be estimated from

$$\bar{h} = \frac{Nu_L.k}{L} \qquad \textbf{(5-2)}$$

where Nu_L is the average Nusselt number over the glass pane, k is the thermal conductivity of air and L is the height of the glass pane. There are many empirical correlations for Nu_L. In our case we used a generic expression[211] for forced convection over an evenly heated plate:

$$Nu_L = 0.228\mathrm{Re}_L^{0.731}\,\mathrm{Pr}^{1/3} \qquad \textbf{(5-3)}$$

The condition of 'forced' (rather than 'natural') convection was used because the experiment was conducted outdoors with a light breeze. The Prandtl number (Pr, which relates the relative thicknesses of the hydrodynamic and thermal boundary layers) is approximately 0.71 for air at temperatures between 0 and 50ºC, and the average Reynolds number (Re_L, which is related to the transition from lamellar to turbulent flow) over the pane is given by

$$Re_L = \frac{u_\infty L}{\nu} \qquad \textbf{(5-4)}$$

where u_∞ is the fluid velocity. The kinematic viscosity, ν is approximated by

$$\nu = \frac{\mu}{\rho} \qquad \textbf{(5-5)}$$

where ρ is the density of air, and μ is the dynamic viscosity and may be obtained from tables. It is about 15×10^6 m^2/s at 27ºC.[211]

Finally, measured temperatures from the window and surroundings were used in conjunction with the above equations to estimate the heat convected and radiated from the front and rear of the glass panes.

5.2.2.4 Solar heat gain coefficient (SHGC)

The total incident energy can be found from the equation

$$q_{incident} = q_{reflected} + q_{transmitted} + q_{convected(f)} + q_{convected(b)} + q_{radiated(f)} + q_{radiated(b)} \qquad \textbf{(5-6)}$$

where the radiant energy passing through the window is $q_{transmitted} + q_{radiated(b)}$ and the radiant energy shed from the front window face is $q_{reflected} + q_{radiated(f)}$. $q_{incident}$ is a well characterized value as it can be measured or estimated from standard tables. $q_{transmitted}$ and the majority of $q_{radiated(b)}$ can be obtained by measurement (note that the detector used had a field-of-view of 9º, therefore any $q_{radiated(b)}$ at greater angles than this was ignored, and summed instead into the absorbed, i.e. convective, component of the energy balance). Finally, $q_{convected}$, both front and back were estimated from the surface temperature of the glass and the principles of convective heat transfer. Equation **(5-7)** shows the proportion of energy that is transferred to the interior environment. As $q_{incident}$ is solar radiation, $F = F_{solar}$, is the solar heat gain coefficient (SHGC).[212]

$$F = \frac{q_{transmitted} + q_{convected(b)} + q_{radiated(b)}}{q_{incident}} \qquad \textbf{(5-7)}$$

The SHGC of the coated glass panes was determined by two means. First, the transmission and reflection spectra of the samples were convoluted with a standardized solar spectrum and the expected energy balance over the sample calculated. Second, samples were exposed to natural sunlight outdoors and the energy balance over the sample was estimated by consideration of the convective and radiative transfer of heat that took place, and the actual solar irradiance. Naturally, the two approaches would be expected to produce a similar estimate of SHGC.

5.3. Results and Discussion

The ability of gold nanorods to absorb the desired wavelengths of light and their potential for use in novel window coating possibilities has been previously mooted[168] but until the attachment and stability of the rods to glass is achieved the method is not usable in practice. This section discusses methods to bind gold nanorods to glass in sufficient quantities to investigate the optical characteristics of the coatings.

5.3.1. Gold nanorod molecular binding to glass

The molecule MPTS was investigated with the aim to increase the binding of gold structures to the surface of glass. It was also hoped that the lower density of CTAB on the ends of the gold nanorods compared to the sides would lead to preferential binding of the rods by their ends

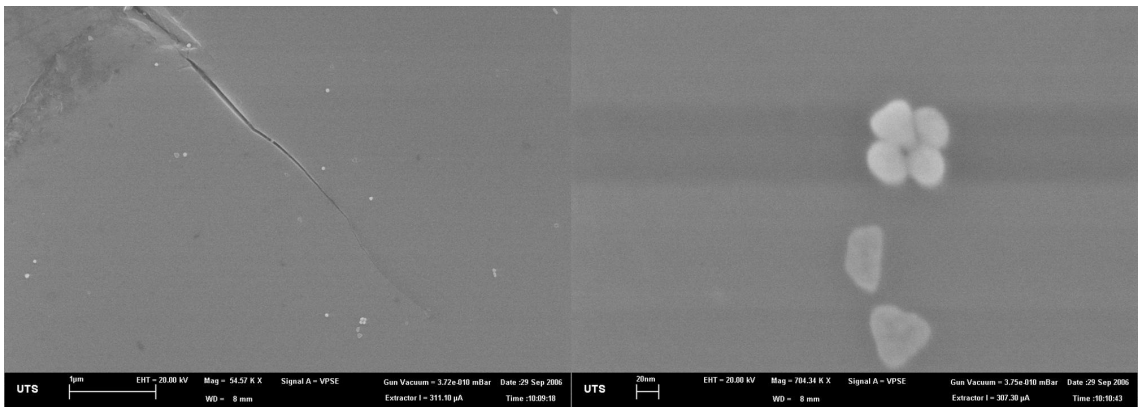

Figure 5.4: Low and high magnification SEM images showing the remaining gold particles on MPTS coated glass after washing.

SEM images of gold nanoparticles on MPTS coated glass and gold seeds on untreated glass showed that very few nanoparticles remain after washing. However, a few particles were still observed on the MPTS-treated sample as shown in Figure 5.4. The particles were obtained commercially and interestingly shapes including triangles, rods and others were observed as well as spheres. No gold particles were observed on the uncoated glass samples. It may be concluded that the application of MPTS to the glass surface increases the binding of the gold particles. However, they are of insufficient quantity to provide a measureable light absorption spectrum even if 100% of the particles could be grown into longer rods.

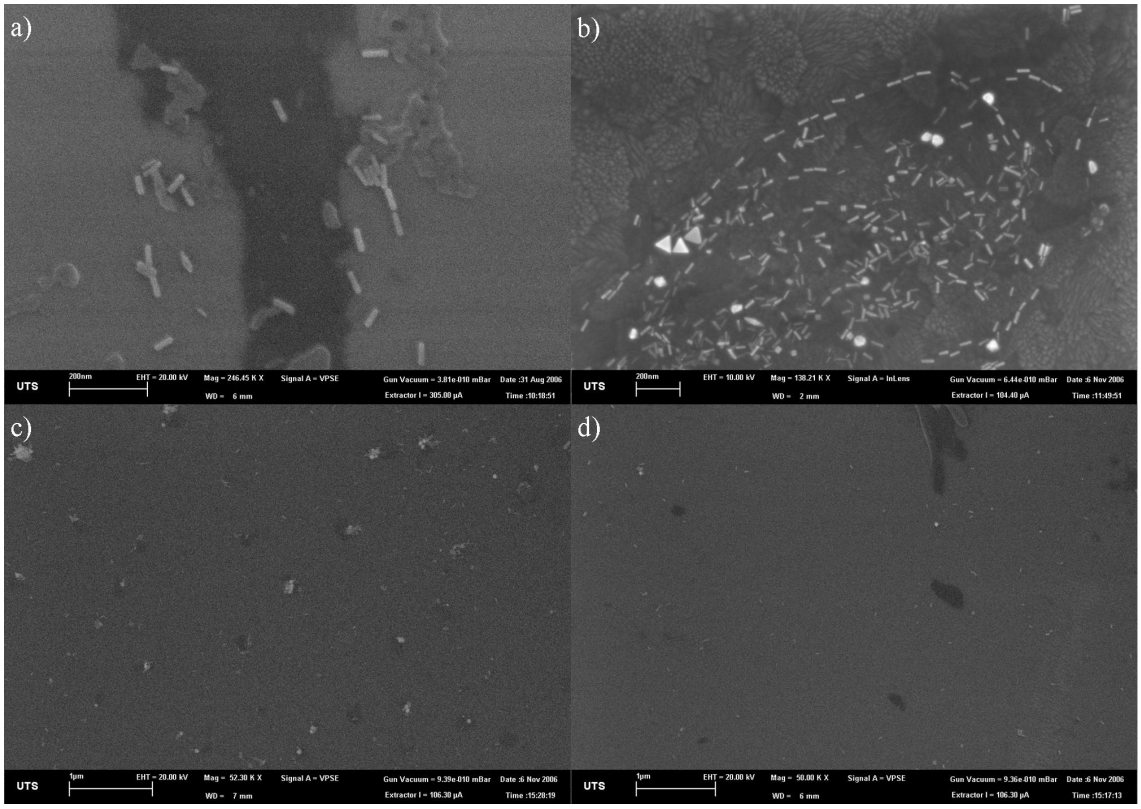

Figure 5.5: Gold nanorod solution dried on MPTS coated (a, c, d) glass and (b) ITO glass (a, b) under atmosphere, (c) in a desiccator and (d) in an oven at 100°C.

Gold nanorod solutions were then applied to MPTS coated glass and three different methods of drying were investigated to determine if different drying rates allowed rods to align as they were dried. Figure 5.5 shows SEM images after three different drying methods; (a) atmosphere, (c) desiccator and (d) oven. There was no significant change in rod alignment or rod coverage across the three drying methods. The sparse coverage of gold nanorods on the samples was primarily due to the rods being removed during the washing step. Figure 5.5 (a) and (b) compare the strength of rod binding to MPTS coated (a) glass and (b) ITO-coated glass. There was little difference in the number of gold nanorods bound to glass or ITO glass substrates. As use of ITO glass made little difference in the number of bound rods attached and was much easier to image in the SEM, it was the substrate of choice for subsequent investigations.

To further investigate the role of the MPTS binding layer, a drop of gold nanorod solution was placed on the surface of ITO glass with and without the MPTS layer. After application, neither of the substrates was washed. The comparison images show the effect of the MPTS layer on an ITO substrate. Figure 5.6 (a) and (b) show gold nanorods on the sample without the MPTS layer, whilst (c) and (d) show the gold

nanorods with the MPTS layer. The addition of the MPTS layer shows that significantly more gold nanorods preferentially group together along the edges of the drop as well as more groupings in the centre of the drop. The substrates without the MPTS layer have groups clumped together in random orientations. Images (b) and (d) show the differences between the gold nanorod groupings, with the MPTS layer causing the gold nanorod to preferentially stick alongside each other whereas the gold nanorods normally bind in random orientations and often either partly overlapping or fully overlapping other nanorods. The large blank areas in Figure 5.6 (a) correspond to CTAB remaining on the surface, as the rods can be seen immersed within. Further centrifugation of the rod solution removes this effect (CTAB was used in excess during the gold nanorod synthesis. The gold nanorods could be separated from the excess CTAB but this caused the gold nanorods to aggregate.) It is interesting to note that 'like' particles tended to stick to one another, i.e. spheres to spheres and rods to rods. The reason for this is believed to be due to a packing effect from the high particle concentration in specific areas as the films dry.

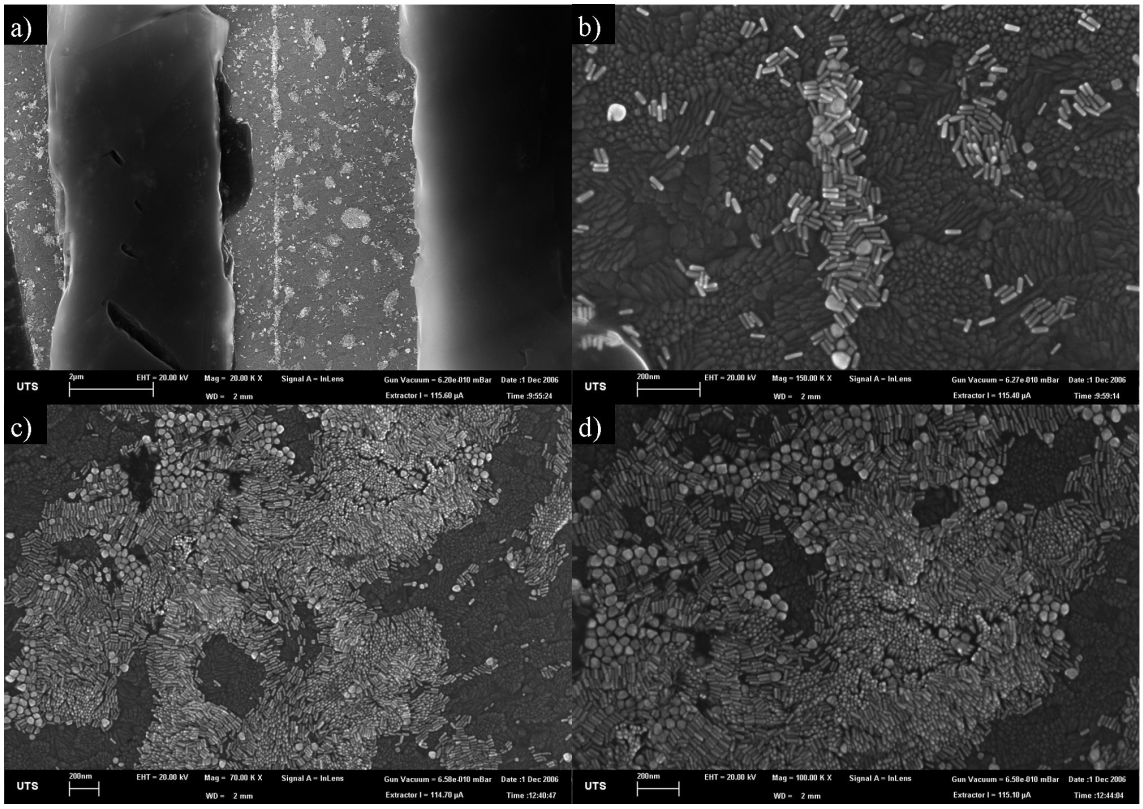

Figure 5.6: Unwashed samples of gold nanorods on ITO-coated glass (a, b) without and (c, d) with the MPTS binding layer.

Figure 5.7 shows a comparison of washed, (a), and unwashed, (b), samples of gold nanorods on an ITO-coated glass substrate. Figure 5.7 (a) was washed by gently applying MilliQ water dropwise to avoid excessive surface damage. Significantly higher quantities of gold nanorods are seen on the unwashed sample than the washed sample. Along the edge of the drop, where the nanorod solution dries initially, a much higher concentration of rods exist for both samples than in the centre regions of the applied drop. Interestingly, the rods preferentially deposited in parallel on the unwashed sample. The washing step removes the majority of excess CTAB dried on the substrate as well as removing quantities of gold nanorods from the surface. It has been reported that upon solvent evaporation the CTAB molecules can assist in drawing the nanorods closer, to share a common layer of counter ions, or through inter-digitation of CTAB tails from neighbouring nanorods.[213]

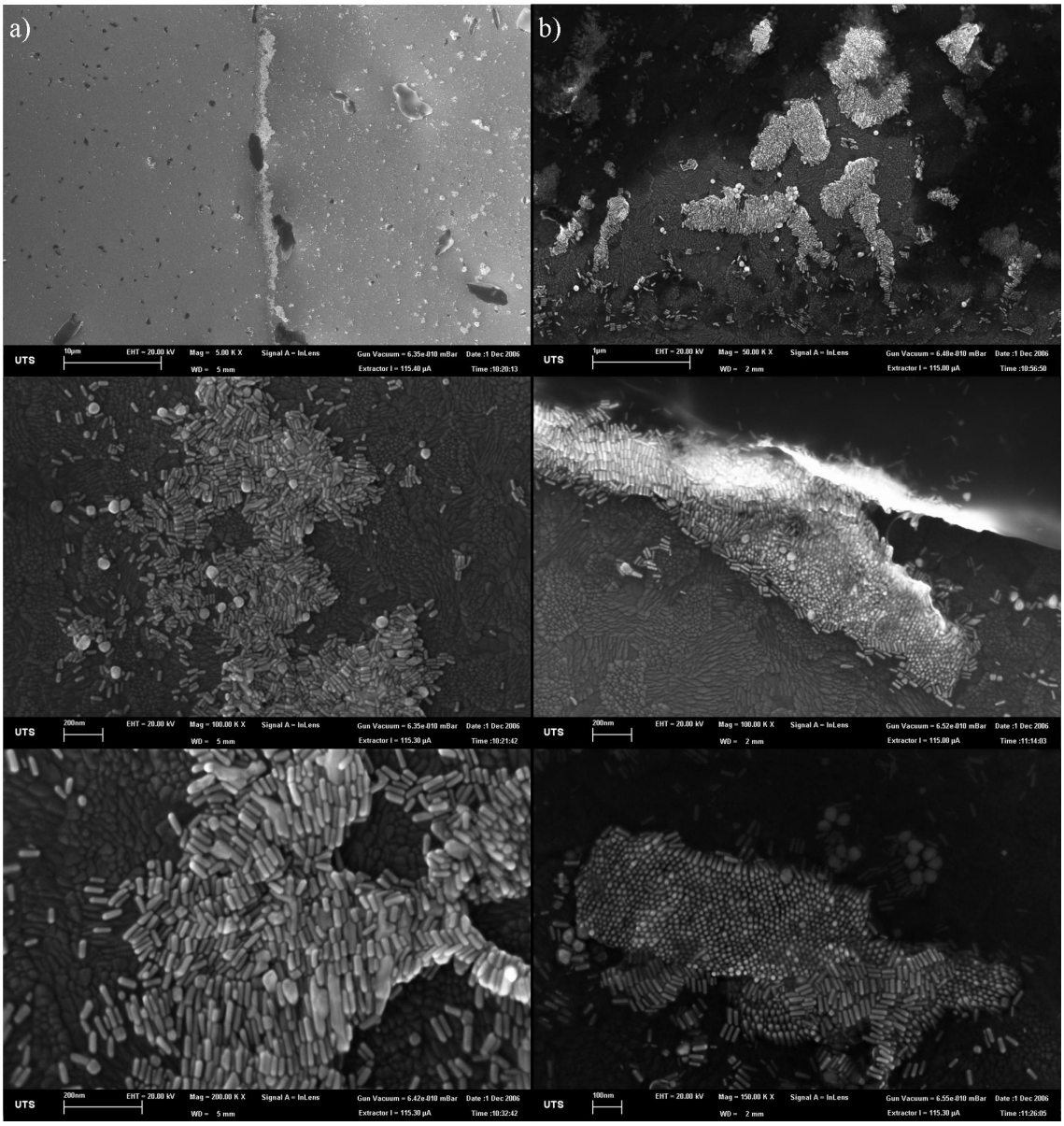

Figure 5.7: SEM images of gold nanorod solution drop dried on ITO both with, column (a), and without, column (b), washing.

After investigating the physical effect of both MPTS and washing the sample, the optical effects were also investigated. Use of MPTS was found to slightly increase the number of gold nanorods binding to the substrate compared to substrates without MPTS. Unwashed samples had more gold nanorods on the surface and more CTAB remaining whilst washing the sample caused some of these rods to be removed and removed some alignment between small groups of rods through either physical means or through excess reduction of CTAB allowing the rods more movement. Figure 5.8 compares the optical absorption spectrum of an unwashed sample of gold nanorod solution on MPTS-coated ITO glass with the spectrum from a sample without the

MPTS layer. The MPTS layer increased the binding of gold nanorods to the substrate so that the longitudinal peak is almost twice the size of the transverse peak, whereas without the MPTS layer the longitudinal peak is only slightly higher than the transverse resonance peak. It is important to note that the transverse peak also contains the resonance from the remaining gold seed particles which did not grow into rods.

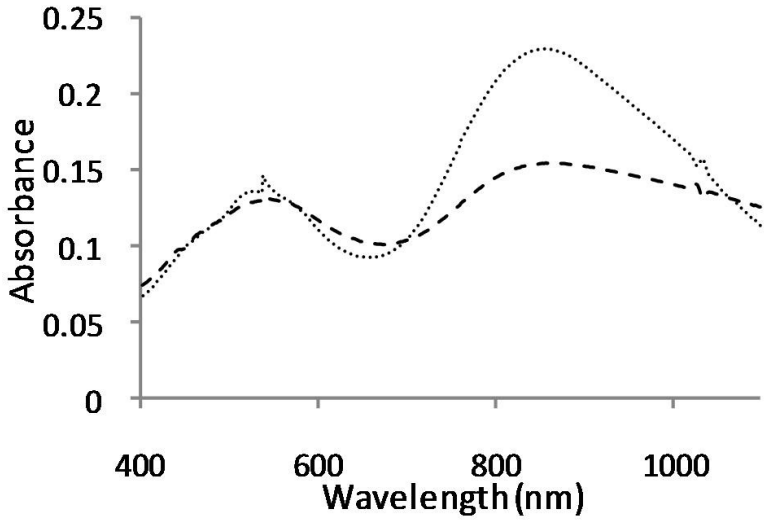

Figure 5.8: Absorbance spectra of gold nanorods deposited from solution on (····) MPTS coated ITO glass and (----) untreated ITO glass. Both samples were dried before measurement.

5.3.2. Gold nanorods in PVA films

This section investigates the stability of gold nanorods in PVA solutions and in aqueous solutions. Also explored were the different methods of drying the gold nanorod PVA films. The stability of the gold within the films was also assessed. Finally, the ability and effect of alignment of rods via stretching of the films was considered.

Gold nanorod solutions were observed to have visible amounts of gold flocculate after long periods of time i.e. months. It was also noted that solutions which had been washed, although easier to use, flocculated at faster rates. This was a result of the excess CTAB stabilising agent being removed from the solution. Mixing the washed gold nanorod solutions in PVA solutions allowed the gold nanorods to remain suspended for longer times even compared to the unwashed gold nanorod solutions. After 6 months very few gold nanorods had flocculated in such solutions, so that the optical spectra of

these solutions changed only slightly. Figure 5.9 shows the normalised absorbance spectra of a gold nanorod solution taken five months apart. Although some nanorods had flocculated prior to the measurement of the second spectrum, there is little difference between the two spectra.

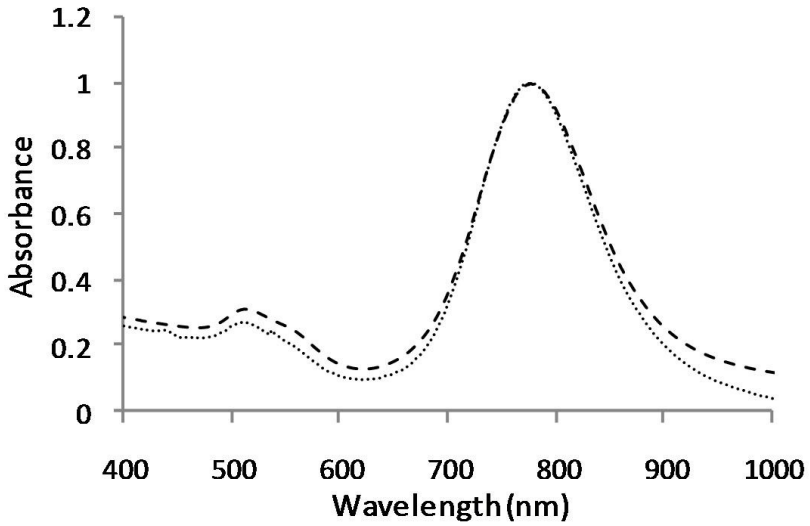

Figure 5.9: Normalised absorbance spectra of gold nanorod solution at (----) 4/05/07 and (····) 18/10/07.

When drops of gold nanorod solution were applied to glass they dried from the outside of the drop inwards and overall the rods next to the edge were aligned parallel to the drop edge. An investigation was undertaken to determine if mixing gold nanorod solutions with PVA and writing the mixture in straight lines on an ITO glass substrate formed long lines of aligned gold nanorods. Figure 5.10 shows the results of writing lines of rod/PVA mixture with (a) displaying the edge of a line and (b) showing the centre of a line. No alignment is observed along the edge of the line and the rods in the centre of the line are seen through a layer of PVA but remain unaligned.

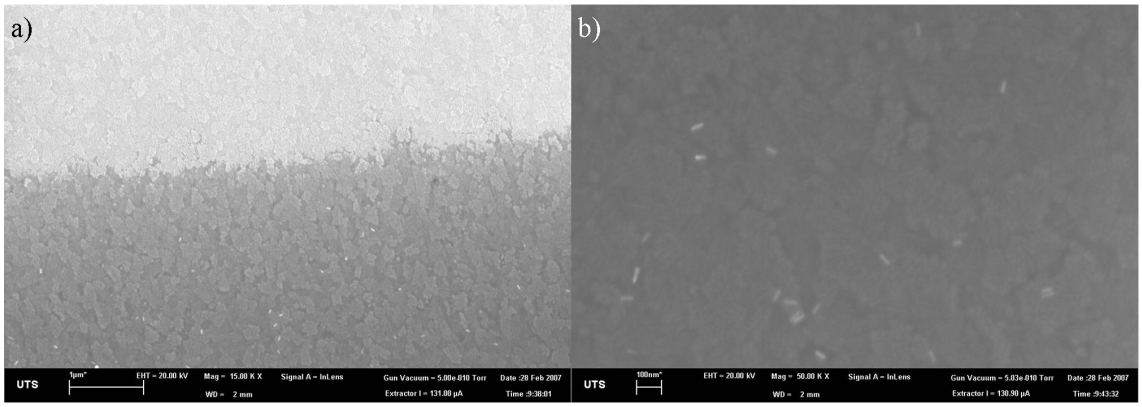

Figure 5.10: SEM images at (a) the edge and (b) the centre of lines of PVA and gold nanorod solution.

Another investigation into the alignment of gold nanorods on glass was conducted using the method shown in Figure 5.3. The movement of the glass slide along one dimension could provide a medium to align the rods along the sliding direction. At low gold rod concentration, (or coverage) a very weak absorption was observed and as such any results showing some sort of alignment were within the error values for the spectrophotometer. Increasing the concentration of the rod solution prior to mixing with the PVA solution was required before significant signal could be obtained. Figure 5.11 shows the absorbance spectra obtained using a more concentrated solution of gold nanorods immersed in PVA. These spectra consist of a smeared solution, an un-smeared solution and polarisation of the smeared sample parallel and perpendicular to the smearing direction. Comparing the smeared and un-smeared sample showed a slight reduction in the rod numbers in the sample area suggesting the action of smearing the glass slides together pushes some rods towards either end. The polarisation data suggests that very few nanorods are aligned through the use of a smearing action.

Some samples were separated into two single slide coatings of uneven thickness and dried separately. It was found that there was no great difference in the amount of signal or alignment compared to the films sandwiched between two slides. Ultimately, it was found that, to be useful as a window coating, significantly more gold needed to be attached to the glass, which could be achieved either with a higher coverage of rods or a thicker polymer layer.

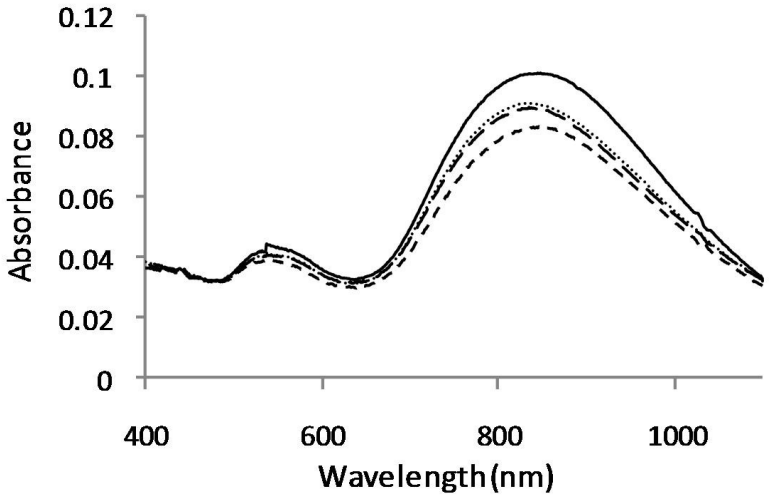

Figure 5.11: Absorbance spectra of gold nanorod PVA solution between two glass slides. A (—) un-smeared sample and a (····) smeared sample with polarisation (– – –) along and (----) across the smeared direction are shown.

Several different methods to dry the PVA films were investigated including oven, desiccator, ambient atmosphere and hot plate drying. The optical properties of the films were investigated and no significant variation was found between the drying methods. Drying in ambient conditions was the slowest method investigated and found to be the optimum method in terms of producing stretchable PVA films. Other drying methods removed too much water from the films such that when stretching the films they cracked rather than stretched.

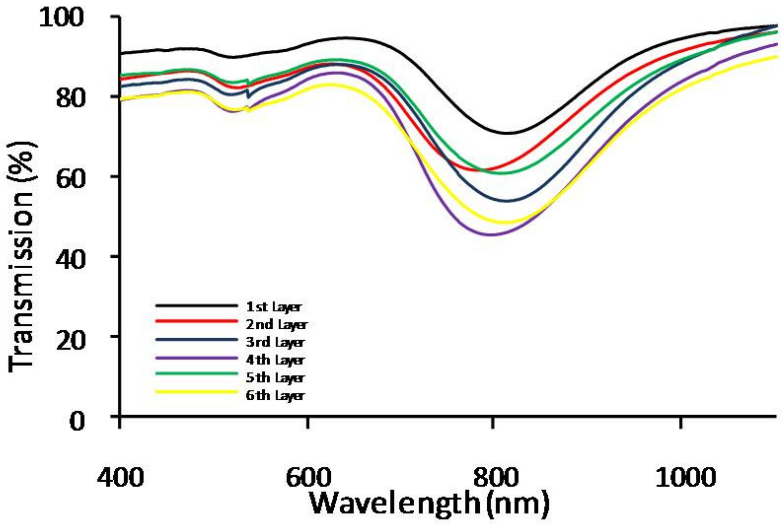

Figure 5.12: The transmission spectrum of multiple layers of a PVA-gold nanorod films.

An increase in the amount of gold nanorods per unit area of glass was required to increase the optical absorption of the PVA-gold films. Multiple layers of PVA-gold rod solution were investigated. Figure 5.12 shows transmission spectra of multiple layers of PVA-rod films on glass. The application of more layers of PVA-rod solution to the glass does not always decrease the transmission through the films. Indeed, layers 1-4 decreased the transmission minimums of the sample but layers 5-6 have reduced intensity troughs compared to layer 4. The applications of additional layers of PVA-rod solution re-wets the layers previously applied and as reported previously, gold nanorods dry preferentially at the edge of a drop or in this case the edge of the layer, and additional layers which wet previous layers cause more and more rods to migrate to the drying edge. Some spectra obtained from samples with several layers had up to 40% difference between the transmission minima at the longitudinal resonance peaks when measured at the centre of the sample (~ 80%) compared to the edge of the sample (~ 40%).

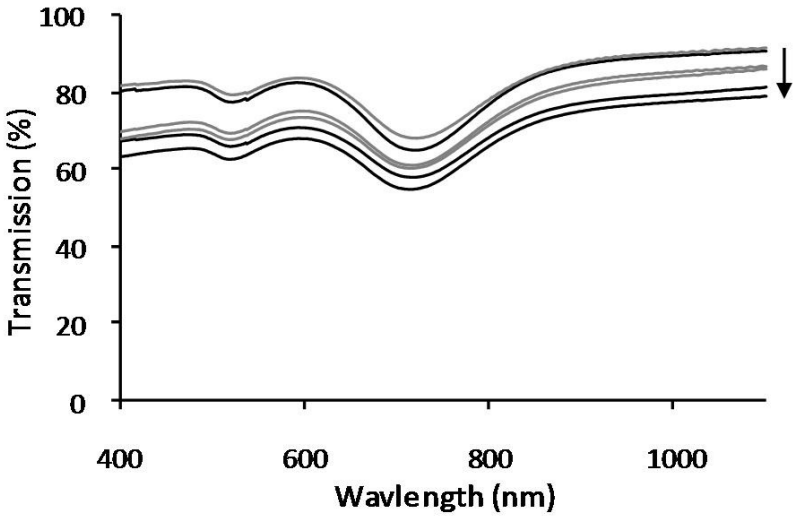

Figure 5.13: Transmission spectra of gold nanorod PVA films over several months. The grey spectra correspond to a film stored in a dark area whilst the black spectra sample was stored in a light area. The arrow points in the direction of time flow, with the initial measurements at the top, followed by 1 month and 3 month measurements.

The stability of the rods in a film was investigated for two samples. One sample was stored over the test period in a dark area whilst the other sample was stored on a window still, under the maximum available sunlight in the laboratory. The absorption and transmission spectra were measured immediately following the drying of the films.

Additional spectra were obtained after 1 month and 3 months. The spectra are shown in Figure 5.13 with the black lines representing the sample placed on the window still, and the grey lines placed in the dark area. The arrow shows the order in which the spectra were obtained, i.e. the initial spectra are at the top and the 3 month spectra at the bottom. For both samples, there was a decrease in the longitudinal peak height particularly between the initial measurement and after 1 month. Over the following two months there was very little change between the obtained spectra. Also observed was the relatively little change between the dark and light samples suggesting that the gold nanorods within the PVA film do not degrade or change shape due to the applied light, or if they do then this occurs only at a very slow rate. This is a very important factor for the use of gold nanorods as a window coating.

The stretching of the rod-polymer films was investigated to determine the stretching requirements in terms of length vs. change in optical properties. Figure 5.14 shows the effect of several different stretching lengths with the amount listed corresponding to the factors of the initial film length. The green line corresponds to an unstretched sample and the red lines indicate a stretching factor of 1.41 whilst the blue lines have a stretching factor of 1.67. When the polariser was parallel to the stretching direction (dotted lines), the longitudinal peak increased compared to the unstretched sample. Conversely, the transverse peak decreased compared to the unstretched sample. When the polariser was placed perpendicular to the stretching direction (dashed lines) the opposite occurred, the longitudinal peak decreased in intensity whilst the transverse peak increased. These results are not as good as those in certain published work where the use of a mechanical stretcher allowed the stretching factor to be several times greater than those used herein and as such allowed the longitudinal peak or the transverse peak to completely disappear when measured using the corresponding polarised light.[204,214] Under unpolarised light the stretched samples had significantly less intense peaks than the unstretched sample. This is due to the process of stretching which thinned the sample and thereby removed some of the gold nanorods from the measurement area. Increasing the stretching factor decreased the peak signal obtained under unpolarised light. Alternatively, under polarised light increasing the stretching factor increased the effect previously mentioned.

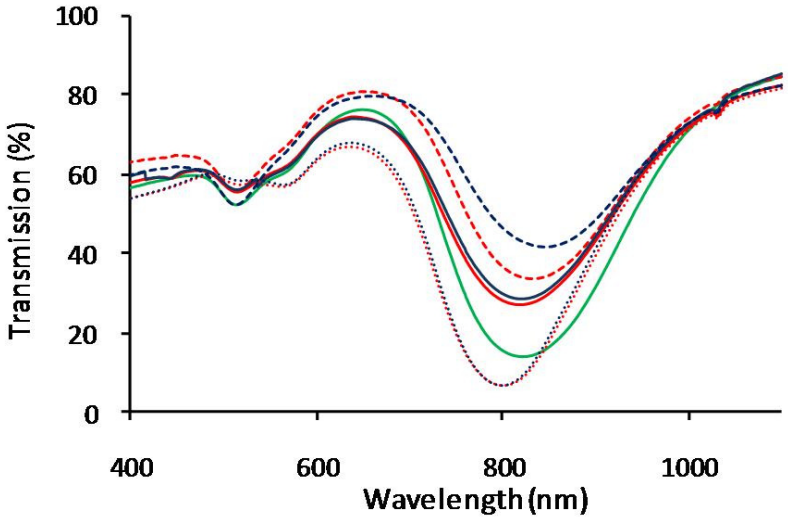

Figure 5.14: Transmission spectra of gold nanorods PVA films with (blue, red) and without (green) stretching. The stretching factors for red are 1.41 and blue 1.67. Measurements are taken in unpolarised light (solid lines), polarised parallel to stretching direction (dotted lines) and polarised perpendicular to stretching direction (dashed lines).

5.3.3. Gold nanorod mixtures in PVA films on glass

The shape of the nanorods used approximated a hemispherically-capped right-cylinder with very few of the 'nano-peanut', 'dumbbell' or 'dogbone' shapes that have been reported.[196] A representative sample of rods is shown in Figure 5.15 (a). The distribution of aspect ratios was determined for the suspension with an extinction peak at 770 nm, R1, by inspection of SEM micrographs of dried portions of the suspension. From the data shown in Figure 5.15 (b), the mean length and diameter of this sample of rods was 47.1 (s=5.5) nm and 12.7 (s=1.6) nm, n=94 (standard deviation in parentheses).

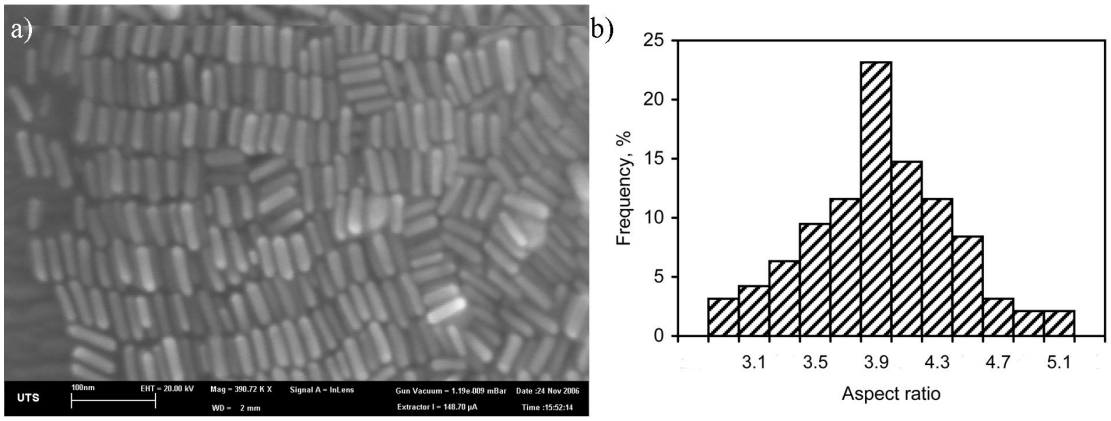

Figure 5.15: (a) Scanning electron micrograph of gold nanorods sample R1 used in the present work. (b) distribution of aspect ratios in sample R1.

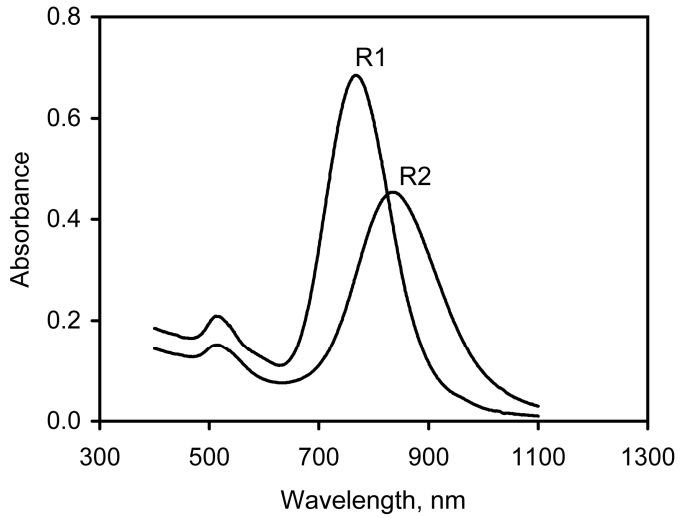

Figure 5.16: Optical absorbance spectra of two suspensions of gold nanorods, R1 (absorption maximum at 768 nm) and R2 (absorption maximum at 834 nm).

The optical transmission spectra of 'R1' and 'R2' in solution are shown in Figure 5.16. The shorter wavelength of maximum extinction for R1 indicates that these rods have, on average, shorter aspect ratios than R2. Comparison of the experimental optical data with calculated extinction spectra for rods of different aspect ratios revealed that the measured extinction bands are much broader than that expected for a monodisperse sample of rods. These two rod solutions were used as the base mixtures investigated within this experiment as they consisted of good reproducibility, peak position and quantity.

Extinction peaks at any intermediate wavelength could be obtained by mixing R1 and R2 in an appropriate ratio. Blending of R1 and R2 also has the effect of broadening the

extinction peaks further, which may be desirable in solar screening applications.[168] Selecting the desired ratio and concentration of R1 and R2 was achieved through investigation of the solution concentrations, film thickness and different ratios of R1 and R2. Also investigated was the use of dual layers of PVA rod films and examination was also conducted into the stretching of films consisting of mixtures of different aspect ratio rods.

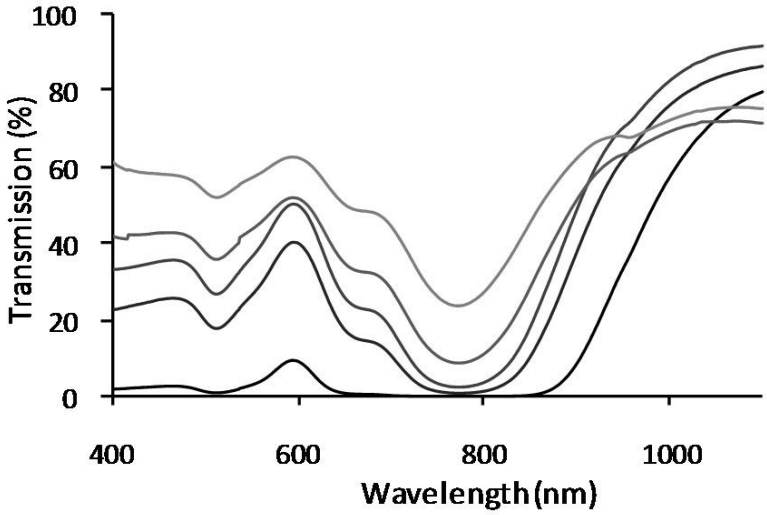

Figure 5.17: Transmission spectra of 1:1 mix of R1 and R2 gold nanorod solutions in 15 wt% PVA solution. The spectra are shown according to the concentration of rods with higher concentrations appearing darker and diluted solutions appearing lighter.

Figure 5.17 contains the transmission spectra for 1:1 mixtures of R1 and R2 gold nanorods into 15 wt% PVA solution with different concentrations of rods. Initially, both rod solutions were concentrated using centrifugation to produce the same signal from 7% of the original water volume and thus the black spectrum was obtained. Insufficient visible light was transmitted and as such the concentrated rod solutions were diluted with MilliQ water so that the solutions contained 50%, 25%, 12% and 6% of the concentrated rod solution.

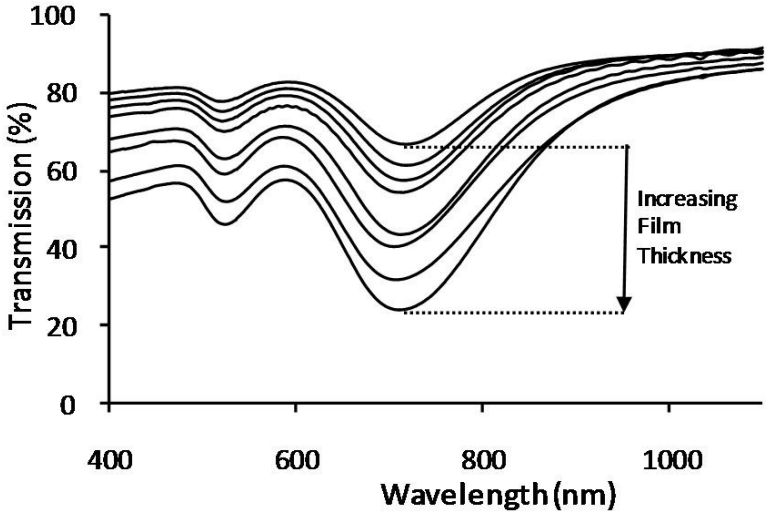

Figure 5.18: Transmission spectra of gold nanorod PVA solutions cast onto a glass slide with increasing film thickness.

It has been shown that controlling the concentration of gold rods within the solution can control the transmission spectra, particularly at the plasmon peak positions. Figure 5.18 shows that by controlling the film thickness, the transmission can also be controlled to a certain extent. No significant difference between the plasmon peak height ratios was observed when the film thickness was varied. Therefore controlling the thickness of the film can control the transmission through the film, but engineering of the desired spectra should be achieved through the control of the rod concentrations prior to final adjustment through the film thickness.

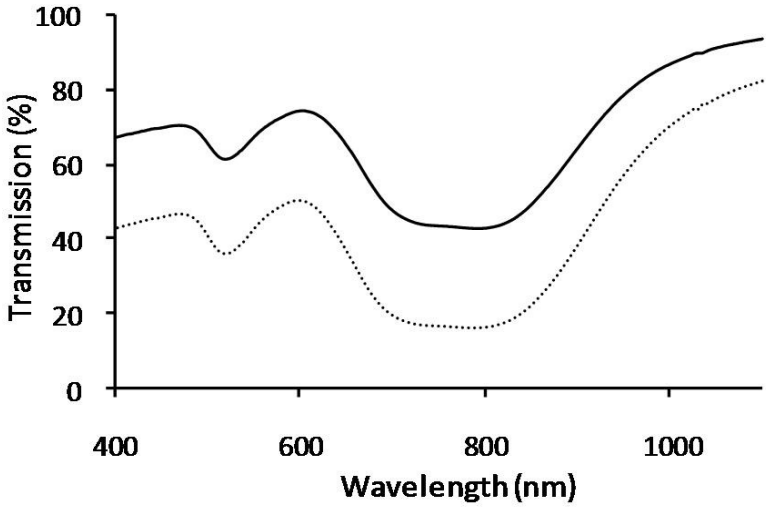

Figure 5.19: Application of two consecutive layers gold nanorod PVA films. The solid line is the first layer and the dotted layer is both layers.

The transmission spectrum for multiple layers of gold nanorod PVA solution cast onto glass is shown in Figure 5.19. The application of additional film layers achieves a similar result to increasing the film thickness, as shown in Figure 5.12. The application of an additional film layer, however, damaged the previously applied films.

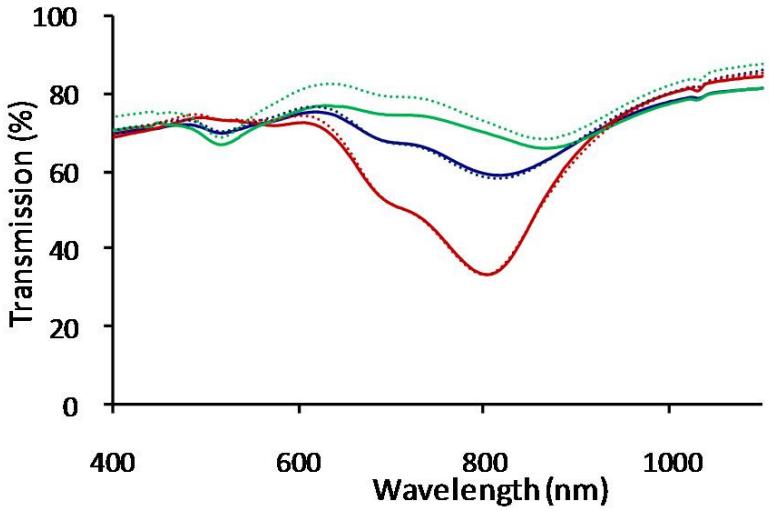

Figure 5.20: Transmission spectra of multiple gold nanorods within a PVA film on a glass substrate. The blue spectra corresponds to the measurements in unpolarised light, with red was light polarised parallel to the stretching direction and the green line consisted of light polarised perpendicular to the stretching direction. The solid lines are the initial measurements and the dotted lines are the measurements after four months.

Figure 5.20 shows that stretching a PVA film with multiple gold nanorod aspect ratios aligned all of the rods, which also occurred with the rods of a single aspect ratio (Figure 5.14). The stretching factor for this sample was 1.64. Ideally, aligned rods could be used to absorb more heat during the middle of the day than during the morning and afternoon. This could be achieved by aligning the rods perpendicular to the window such that when the sun is low in the sky, more light is passed through and when the sun is higher the light excites the plasmon resonance. Unfortunately, the ability to mass produce aligned rods in both the desired direction and quantity has yet to be achieved.

An important consideration when engineering the transmission spectra is the respective proportions of different rod aspect ratios added to the film. Figure 5.21 shows the transmission spectra of different ratios of R1 and R2 investigated. The ratio of different rods controls both the size and position of the transmission minimum. By centrifuging the samples several times in the washing process, significant quantities of remaining seed particles have been removed from the rod solution. This is shown by the

reduction in the transverse plasmon peak height relative to the longitudinal plasmon peak. By examination of the spectra in Figure 5.21 and comparison to the solar spectrum in Figure 5.1 some of the more suitable rod ratios were selected for further testing. The solar spectrum shows that highest intensity infra red radiation occurs close to the visible region of the spectrum and on average decreases further from the visible region. Therefore, one of the most important aspects to consider is to maximise absorption in the 750-1000 nm region of the solar spectrum whilst still retaining roughly 50% transmittance in the visible. The rod ratios that were chosen for further investigation are 50:50 and 33:67, R1:R2 respectively. These were selected because the broad longitudinal plasmon minima were suitable for solar screening applications,[168] and only a small portion of the upper-visible spectrum was absorbed.

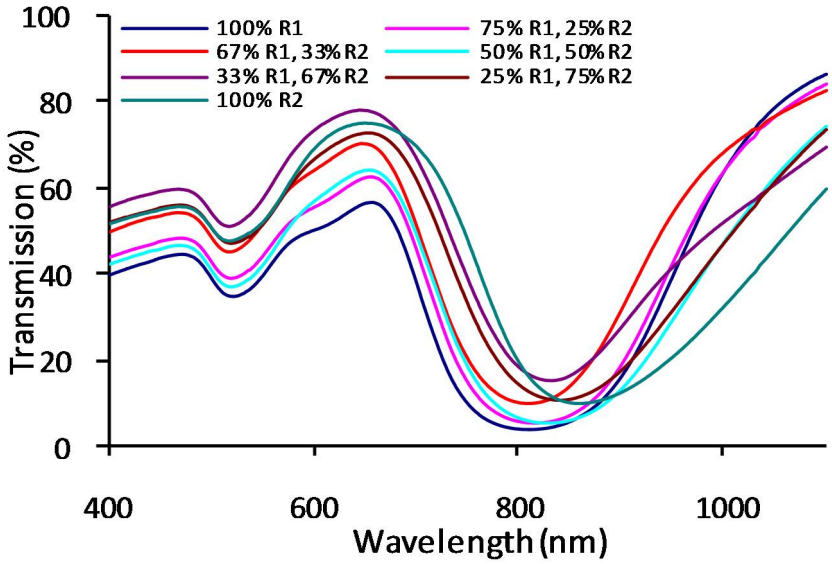

Figure 5.21: Transmission spectra of gold nanorods in PVA films with different ratios of R1 and R2.

Production of less disperse (i.e. less variation on shape and aspect ratio) gold nanorod solutions requires centrifugation to remove significant quantities of spheres. This process also allows the concentration of the rods into a smaller solvent volume which is used to control the intensity of the plasmon peaks.

5.3.4. Laboratory optical measurements of gold nanorod window coatings

The ratios chosen for the production of PVA coatings on large glass panes were (1) 50:50 and (2) 33:67, R1 and R2 respectively. These two samples are designated as

'Pane 1' and 'Pane 2' respectively. The former mixture maximized the width of the near-IR extinction trough while the latter sample allowed us to probe the effect of shifting the adsorption peak further into the infrared. The samples were examined in a scanning electron microscope, Figure 5.22. The PVA coating has a distribution of well-separated gold rods and the coating thickness of 800 μm provides a high likelihood that incident photons will encounter the gold nanoparticles.

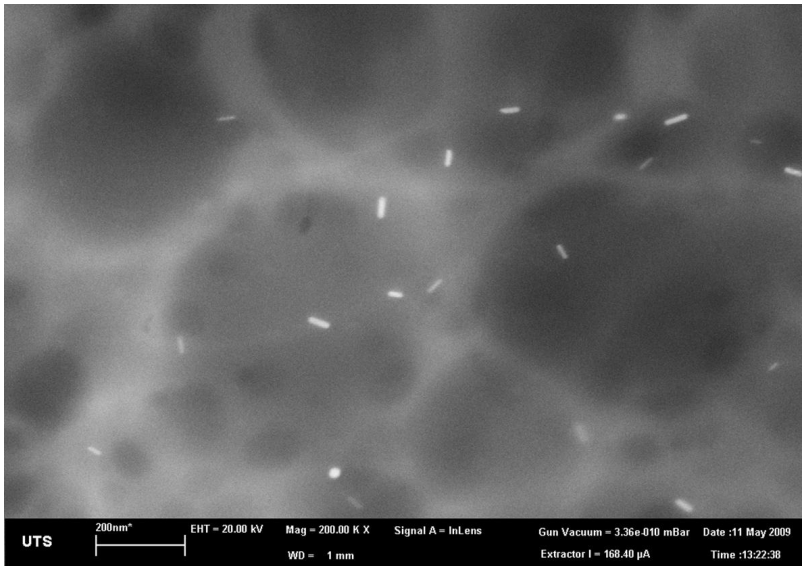

Figure 5.22: Scanning electron microscope image of the surface of the Au nanorod/PVA coating. The electron beam penetrates some tens of nanometers into the PVA and individual rods can be discerned. The cellular structure of the PVA is an artifact produced by damage induced by the electron beam.

Transmission and specular reflectance data are shown in Figure 5.23. Samples of plain glass and plain glass coated with PVA only are hereafter designated 'Glass' and 'Glass-PVA', respectively. Glass exhibits a broad band in its NIR transmittance with a minimum at 1058 nm. Relatively low reflection values (<12 %) were recorded for all of the measured samples including Pane 1 and Pane 2. This indicates that gold nanorod coatings in PVA are suitable in locations where highly reflective coatings are unsuitable. The absorption peaks between 1400 and 2500 nm for the samples Glass-PVA, Pane 1 and Pane 2 are due to the PVA and the absorption peaks from 400 through to 1400 nm in Pane 1 and Pane 2 are primarily due to the gold nanorods. The large transmission minimum at ~810 nm coincides with the expected position of the longitudinal resonance of rods dispersed in PVA. PVA has a refractive index of 1.52, which is higher than that of water and results in a red-shift of the longitudinal plasmon

resonance compared to that of rods in aqueous solution (see Figure 1.12.) The average transmission in the visible is approximately 35% for both samples. At 800 nm, Pane 1 and Pane 2 have reflection and transmission values of ~5%, implying that at this wavelength the absorbance accounts for ~90% of the incoming light. Pane 2, however, absorbs more light in the range 900 - 1400 nm and is thus more suited for use as an absorptive window coating than Pane 1.

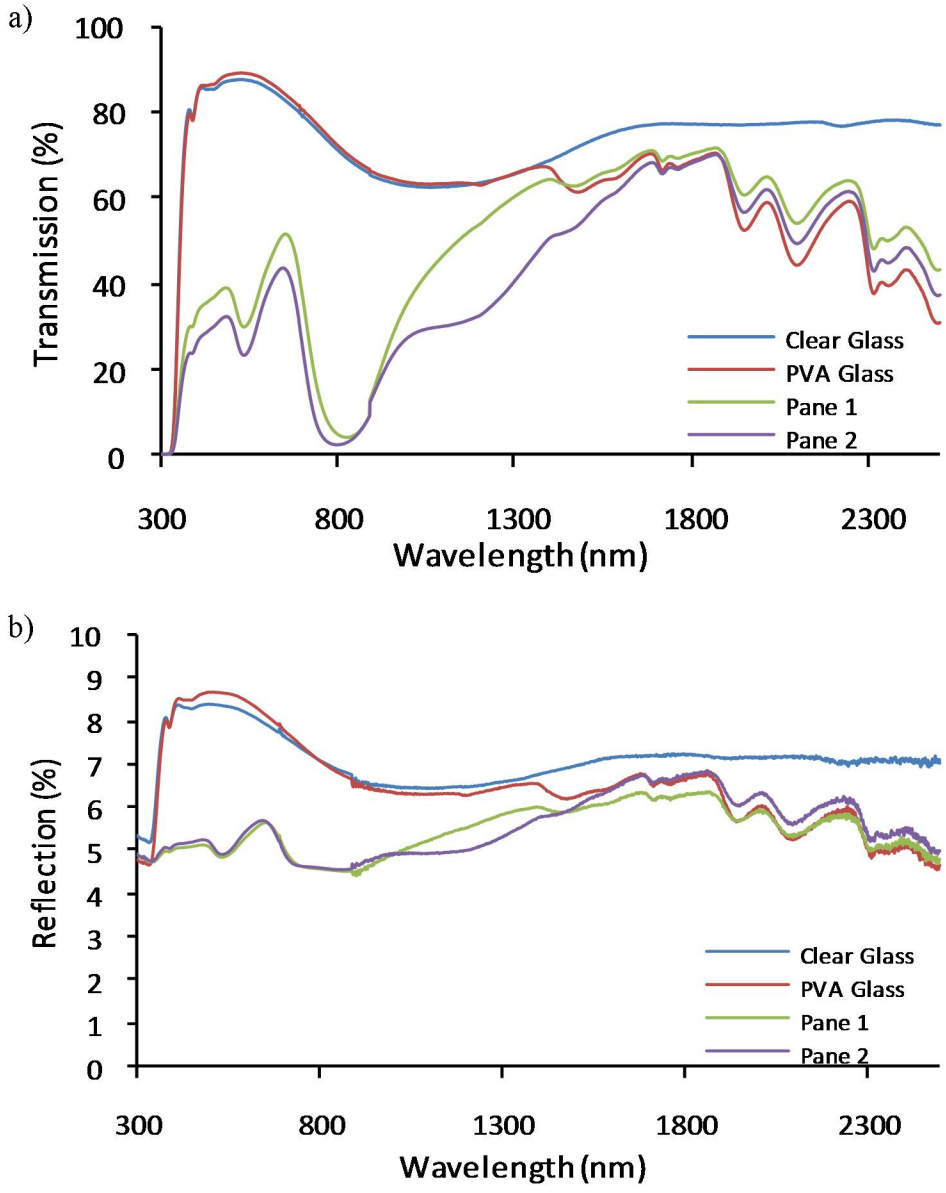

Figure 5.23: (a) Transmission and (b) reflection spectra of 4mm clear glass, PVA-glass and Pane 1 and 2.

Calculated thermal properties, from the results in Figure 5.23, are shown in Table 5-1. The very small amount of thermal re-radiation that would occur from the back face is

neglected. The optical transmission spectrum of Pane 1 indicates that it should pass only 329 W/m^2 by transmission when illuminated with sunlight at 885 W/m^2, and that 46 W/m^2 should be reflected. Therefore, the difference, 530 W/m^2, would have been absorbed and shed by convective heat transfer. If the velocity of air on both sides of the pane was identical then, because the temperature gradient across the glass is small, approximately equal amounts of this thermal energy would be shed on the 'inner' and 'outer' surfaces of the window by convection, allowing for an estimate of F_{solar}, designated here as $F_{sol\text{-}1}$ to differentiate it from $F_{sol\text{-}2}$, the estimate obtained under outdoors conditions (see Section 5.3.5. Outdoor optical measurements of gold nanorod window coatings).

Table 5-1: Calculated optical properties for plain glass, plain glass coated with PVA, and the glass panes coated with Au nanorods, with reference to the ASTM G173 standard solar spectrum.

Sample	Transmitted %	Reflected %	Absorbed % (by difference)	$F_{sol\text{-}1}$ % (for equal airspeeds on both sides of pane)
Glass	75.3	7.4	17.3	84.0
Glass-PVA	74.0	7.4	18.7	83.4
Pane 1	37.2	5.2	57.6	66.0
Pane 2	29.2	5.2	65.6	62.0

5.3.5. Outdoor optical measurements of gold nanorod window coatings

The large area gold nanorod PVA films cast onto 4 mm glass were investigated under 'natural' conditions, using the sun as the light source. The accuracy of the window efficiency under natural conditions is strongly influenced by which empirical correlation is used for the Nusselt number, which in turn is also influenced by the wind speed assumed at the time of measurement. The transmission through the sheet of commercial quality glass used as a reference sample was ~691 W/m^2 on the day, which is ~77 % of the 897 W/m^2 of solar radiation being received at that time. Therefore 23 % of the solar irradiance on this sample must have been absorbed or reflected. The temperature of the clear glass was measured to be 21.2°C and the outside temperature was 15.0°C, giving an increase of 6.2°C. Using the measured temperature, the heat convected off each face of the clear glass is calculated to be between 52 W/m^2 and 87

W/m^2 for wind speeds of between 0.5 and 1 km/hr respectively. Since there are two sides to the glass, it is evident that between 11 and 19% of the incoming radiation was absorbed and shed as heat. This fits with the figure obtained above by consideration of the measured optical property data for clear glass and the standard solar spectrum. Table 5-2 shows the performance of coated Panes 1 and 2 compared to the clear glass sample using the same methodology.

Table 5-2: Performance of Au/PVA samples compared to clear glass. Samples were measured outside under normally incident illumination from the sun. The wind speed ranges recorded are given in parenthesis.

	Incident flux (W/m^2)	ΔT (ºC)		Transmittance (%)	Convected energy (%)		Reflected (%)	F_{sol-2} (%)
		Front	Back		Front	Back		
Glass	897±5	6.2	6.2	77.1	5.8 - 9.7 (0.5-1.0 km/h)	5.8 - 9.7 (0.5-1.0 km/h)	7.4	82.9 - 86.8
PVA-Glass	909±5	6.3	6.1	75.0	5.9 - 9.7 (0.5 - 1 .0 km/h)	5.7 - 9.4 (0.5 - 1.0 km/h)	7.4	80.7 - 84.4
Pane 1	885±5	9.5	6.2	34.9	35 - 47 (2-3 km/h)	22.8 – 30.7 (2-3 km/h)	5.2	57.7 - 65.6
Pane 2	885±5	10.9	8.2	31.2	40.1 - 54 (2-3 km/h)	30 – 40.6 (2-3 km/h)	5.2	61.2 - 71.8

Panes 1 and 2 have 40% and 37%, respectively, of the incoming energy being either transmitted or reflected, leaving 60% and 63% to be absorbed and then convected. Of this, the slightly larger proportion was convected from the surface facing the sun due to it having a higher temperature. Therefore, somewhat less will be convected from the rear surface. In fact, since indoor air velocity is generally much lower than outside, the F_{solar} values of such coatings would in general be better than those shown here.

Whereas the SHGC for a coating provides a direct indication of the attenuation of solar radiation, it does not fully describe the efficacy of a coating system. An additional method to compare the efficiency is the measure the T_{lum}/T_{sol} ratio, which is a measure of the overall ability of the window to selectively transmit light visible to the eye whilst blocking infrared radiation.[193,212,215] T_{lum}, the transmitted visible proportion of the spectrum weighted by the photo-optic response of the human eye, can be found from

$$T_{lum} = \frac{\int_{380}^{760} T_\lambda V_\lambda \cdot E_\lambda \cdot d\lambda}{\int_{380}^{760} V_\lambda \cdot E_\lambda \cdot d\lambda} \qquad \textbf{(5-8)}$$

where λ is the wavelength, T_λ is the total spectral transmissivity of glass as a function of λ, V_λ is the photo-optic luminous efficiency function of the human eye as a function of λ and E_λ is the spectral irradiance of the light source as a function of λ. The limits of the integration are the wavelength in nm. T_{sol}, the proportion of the solar irradiance transmitted can be found from

$$T_{sol} = \frac{\int_{0}^{\infty} T_\lambda E_\lambda \cdot d\lambda}{\int_{0}^{\infty} E_\lambda \cdot d\lambda} \qquad \textbf{(5-9)}$$

The maximum possible ratio of T_{lum}/T_{sol} is 2.08 for a perfect window glaze allowing maximum T_{lum} and minimum T_{sol}. More realistic representative values include 0.99 for a dye based coating, 1.04 for a metalized coating and 1.7 for a state-of-the-art optimum spectrally selective coating.[212] The parameters obtained for the present samples are summarized in Table 5-3. Also shown are the CIE *L*a* b** color parameters for the glass, as perceived in transmission using ASTM D65 white light as the illuminant and the corresponding simulated colours are shown in Figure 5.24. The figure-of-merit for both panes was about unity, indicating that they do not selectively attenuate the thermal part of the spectrum relative to the visible. This is a situation that is comparable to the products available at the cheaper end of the solar glazing market.

Table 5-3: Figures-of-merit determined for samples. T_{sol-1} is calculated from the measured transmission spectrum. T_{sol-2} was measured under outdoors conditions and is equivalent to the 'transmittance' in Table 5-2.

Sample	T_{lum}	T_{sol-1}	T_{sol-2}	T_{lum}/T_{sol-1}	CIE L^*	CIE a^*	CIE b^*	Color
glass	0.87	0.76	0.78	1.15	94.6	-1.7	0.6	blue tinge
PVA on glass	0.87	0.74	-	1.19	95.1	-1.8	0.9	blue tinge
Pane 1	0.37	0.37	0.35	1.00	67.1	11.1	-0.3	purple
Pane 2	0.30	0.29	0.31	1.03	61.7	12.4	0.3	purple

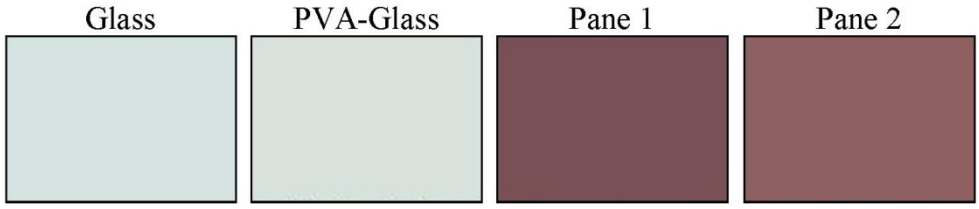

Figure 5.24: Simulated colours of the investigated solar screening films in Table 5-3.

To obtain an understanding of the effectiveness of the coatings produced, the transmission spectra of Pane 2 has been overlaid on a G. James transmission graph showing the spectra of several different absorptive coatings currently commercially available and is shown in Figure 5.25. Pane 2, the thick blue line, is more efficient near the edge of the visible spectrum, between 700 and 900 nm. However, beyond the gold nanorod longitudinal plasmon resonances, above 900 nm, the 6 mm Evergreen and green products are superior. There is also a slight reduction in the visible transmission of Pane 2 compared to the bronze and grey samples. This reduction in visible transmission is much larger for the green and evergreen samples. By adding higher aspect ratio rods the transmission between 900 nm and 1200 nm could be further reduced.

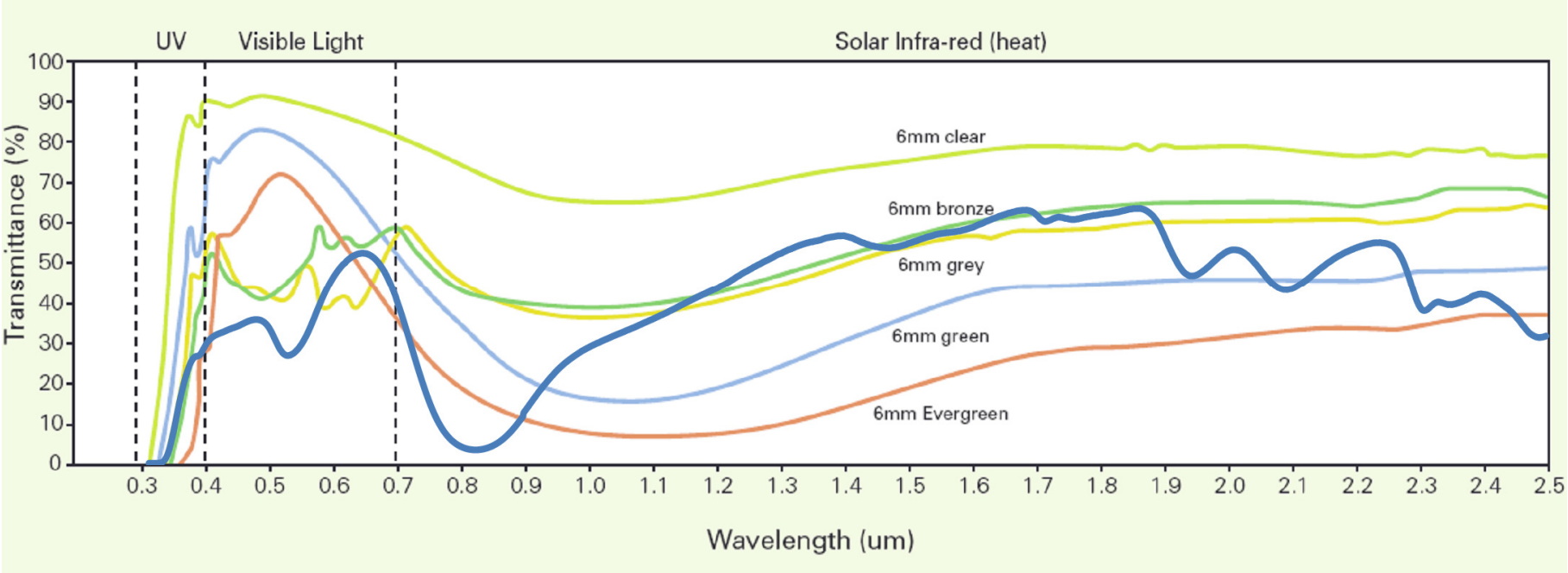

Figure 5.25: Transmittance spectra of range of 6 mm commercial absorptive glasses produced by G. James Australia.[216] Overlaid on this is the thick blue line corresponding to the transmission spectrum of Pane 2, 4 mm PVA gold nanorod coated glass with 33:66 R1:R2.

5.4. Conclusions

Methods were investigated to bind gold nanorods in colloidal suspension to glass substrates. Improvements discovered include the addition of MPTS binding layer between the rods and the substrate, and optimization of the methods used to dry the coatings. It was, however, concluded that the use of MPTS as a binding layer was not suitable for solar screening applications due to insufficient numbers of gold nanorods binding.

Gold nanorods have a well-defined optical extinction peak, the position of which is readily tuned by adjustment of the aspect ratio.

Mixtures of gold nanorod suspensions of different aspect ratios have been produced, with the longitudinal peak a combination of the initial solutions. This method allowed the peak position and intensity to be controlled to some extent. Rods stabilised in a PVA solution were found to be more stable than rods suspended in a water solution, and rods within a PVA film were stable for at least three years.

Control of the optical properties of gold nanorod/PVA films was achieved by controlling the gold nanorod concentration, the film thickness and PVA concentration. Control over the gold nanorod concentration is the method of first choice because it allowed control over the position and intensity of the transverse and longitudinal peaks.

Gold nanorod alignment was achieved by stretching PVA films with gold nanorods immersed within. Many different aspect ratio rods can be aligned at the same time along the stretching plane. Increasing the stretching factor increases the rod alignment.

Nanorods of different aspect ratios can be blended to produce a spectrally selective coating suitable for solar glazing applications. The samples transmitted between 30 and 37% of the luminance of sunlight while having a Solar Heat Gain Coefficient of between 58 and 72% of total incoming heat flux. The difference between these two sets of values is characteristic of absorptive coatings, which must necessarily shed heat by convection. Up to half of this heat load must be transferred off the inner face of the coated glass which decreases the thermal efficacy of absorptive systems. This may be offset in some applications by the fact that these systems do not reflect heat load onto adjacent buildings, and may be cheaper to produce.

The incorporation of gold nanorods of even greater aspect ratios than used here would increase their effectiveness as a window coating further. However, while a blend

of rods with aspect ratios of between 3 and 10 would be needed to achieve optimum solar screening,[199] in the present instance only rods with aspect ratios of up to 5 were available in quantity. This is because the yields of the currently known rod-making techniques drop off steeply for rods with aspect ratios greater than 4. The present coated window panes therefore represent a proof-of-principle for the use of gold nanorods rather than a commercially viable finished product.

Having determined that gold nanorods may be used as a solar screening application and that aligned rods may greatly increase the absorption under certain conditions, the next challenge was utilizing an electric field to align rods. This topic is addressed in Chapter 6.

Chapter 6:

Electric Field Interactions with Gold Nanorods

Chapter 6: Electric Field Interactions with Gold Nanorods

6.1. Introduction

The optical functionality of gold nanorods has been discussed in previous chapters but the question of how to control the orientation of wet-chemically produced rods was only briefly touched on in Chapter 5. The present chapter investigates the interaction of electric fields with gold nanorods with the aim to control their alignment, position, movement and thereby influence the position and intensity of their longitudinal plasmon peak.

The interaction of an electric field with a gold nanorod is of great interest because of its potentially easy use and scaling in industrial applications. Electric fields have been reported to align many different types of nanorods or nanowires including gold,[217-219] cadmium selenide,[220] cadmium sulphide,[221,222] zinc oxide[223] and palladium.[224] The application of electric fields to a suspension of nanowires or nanorods can align, accelerate in a direction parallel or perpendicular to its orientation, and concentrate onto designated areas or to disperse on a microscopic scale. These effects are due to the interaction between the polarised charges on the nanostructures in suspension and the applied electric fields.[219] The basic method involves an electric field applied between two or more electrodes and the nanoparticles aligning between the electrodes.

Smith *et al.* investigated the influence of an electric field on gold nanowires produced using electrodeposition in nanoporous alumina membranes. They reportedly utilised non-uniform AC electric fields to precisely align a colloidal suspension of gold nanowires between two metal pads.[217] Fan *et al.* have also investigated the manipulation of gold nanowires produced from the template method. They suggest that the large aspect ratio of nanowires amplifies the polarisation due to the AC electric field to almost 400 times more than for spherical particles.[219] The gold nanowires polarise readily in the alternating electric field due to charge separation at the surface of the nanowire. This is due to the nanowires being more polarisable than the suspension medium, so they experience a dielectrophoretic force that produces net movement in the direction of increasing field strength.[217,219,225] Fan *et al.* report that the large aspect

ratios and the low conductivity of the deionised water used as the suspension medium enhance the dielectrophoretic forces. It was concluded that the nanowires align with the electric field but accelerate along the field gradient direction.[219]

Alternatively, Van der Zande *et al.* investigated the alignment of gold nanorods of different aspect ratios in solution under the influence of an electric field. Complete alignment of rods or particles by the stretched film methods, mentioned previously in Section 5.3.2., was achieved because of the absence of Brownian motion. In aqueous solutions complete alignment is only obtained with very strong electric fields.[218] The average orientation of the rods with respect to the applied electric field is a result of the competition between the energy of orientation and Brownian energy of the rods. Therefore the magnitude of the applied field can affect the alignment of the rods and ultimately the optical properties of the solution. The applied electric field induces dipoles in the rods, which give rise to long-range interactions and forms bands of rods placed end-end due to energy minimisation.[218] It was concluded that, even in a saturated solution, a small shoulder remains of the transverse peak, indicating that complete alignment in aqueous systems is difficult to achieve.[218]

Gupta *et al.* investigated ligand-functionalised cadmium selenide (CdSe) nanorods in a polymer matrix under an applied electric field. The permanent dipole moment in CdSe nanorods and the anisotropy of the nanorods in solution leads to an alignment of nanorods along the field lines of the applied electric field[220] in a very similar process to that described for gold nanorods and nanowires. During solvent evaporation, volume contraction is sufficiently large such that when the field is removed the orientation of the nanorods is diminished. This indicates that not only is the applied field necessary to align the rods in solution but an additional force, acting in the plane of the film, is required to force a dense packing and retain the desired alignment. A strong, unfavourable polymer – ligand interactions is necessary to attain a sufficient packing density of the orientated nanorods such that alignment is not lost when the field is removed.[220]

Ryan *et al.* used a DC electric field to align cadmium sulphide (CdS) nanorods.[180] Similarly to the methods mentioned previously, the CdS nanorods were aligned by a constant electric field during a solvent evaporative process. CdS nanorods deposited under an electric field and with slow evaporation demonstrated alignment in three

dimensions where each additional nanorod layer sits in the interstitial spacings of the underlying layer.[180]

Zinc oxide nanorods were aligned using AC electric fields by Harnack *et al.*[223] The process, whereby the electric field induces charge separation and the resulting polarisation generates a dipole moment, aligns the structure to an energetically favourable orientation. The alignment force is frequency dependent because the polarisability of the nanostructure and surrounding solvent changes with frequency.[223]

Cheng *et al.* investigated the formation and alignment of palladium (Pd) nanowires under the influence of an electric field. It was discovered that formation and alignment is strongly frequency dependent. At low frequency the Pd is deposited irregularly at the edges of the electrodes or forms dendritic structures between them. As the frequency increased, the formed structures began increasing in likeness to wires. Uniform self-assembly of Pd nanowires only occurred at relatively high frequencies.[224]

These examples all suggest that to align rod shaped nanoparticles, a high frequency electric field between two or more electrodes induce a dipole moment in the nanoparticle which aligns the nanoparticle in the direction of the electric field lines.

6.2. Experimental

Gold nanorod solutions described in this chapter were produced using an identical method to that reported in Section 5.2.2.

6.2.1. Effect of electric field on gold nanorod solutions

Electric field interactions with the gold nanorod solution were investigated by placing a nanorod solution into a two-electrode cell. Figure 6.1 shows a schematic of the experimental set-up. Two transparent ITO coated glass slides were used as the electrodes and were offset so that they could be attached to a power supply. Two 150 μm thick glass pieces were used as spacers and were situated along the edges of the slides. An optional 150 μm thick glass insulating layer was used to prevent current flow and was situated on top of one of the electrodes. The edges of the cell were sealed together and then gold nanorod solution was forced into the remaining gap by capillary action. The cell was then placed into a Shimadzu UVmini 1240 UV-Vis spectrophotometer and the effect of varying the electric field on the cell optical properties was investigated. MilliQ water was used as the baseline spectrum for this experiment. If alignment of the rods occurs, then the longitudinal plasmon resonance band will disappear.

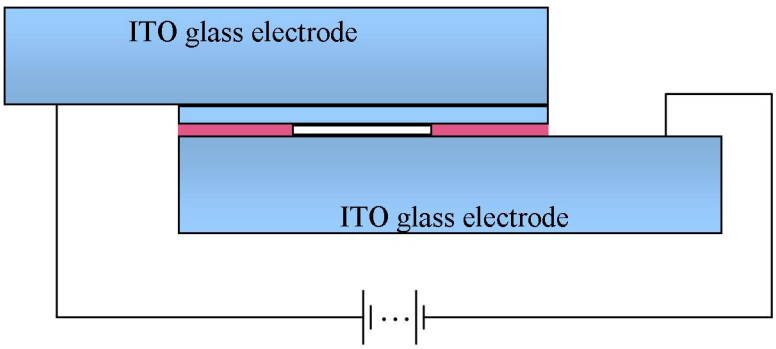

Figure 6.1: Schematic of the two electrode cell system. The two ITO glass slides act as two plate electrodes and a potential difference is applied between the electrodes. The white rectangle in the centre of the design corresponds to a 150 μm thick glass spacer. The gold nanorod solution (purple rectangle) was inserted via capillary action between the two electrodes. The light blue rectangle corresponds to an optional 150 μm thick glass insulating layer preventing charge transfer. Light is applied through the electrodes.

The electric field parameters investigated included the magnitude of AC and DC fields, and the effect of an insulating layer. The AC electric field was generated using a BWD 604 MiniLab where the attached function generator was coupled to the amplifier allowing for the creation of 18 V AC potentials with a sinusoidal wave pattern. The sinusoidal wave pattern was measured using a Phillips PM3365A cathode ray oscilloscope (CRO) throughout all the AC experiments. The DC field was generated by a regulated power supply attached to the MiniLab, allowing a total of 30 V difference between the electrodes. A Bertan Associates 210-50R high voltage power supply allowed for generated voltages up to 50 kV and was used for further experimentation with insulated DC samples. All voltages were measured during the experiments using a multimeter.

The addition of a 0.01 M NaOH solution to a gold nanorod solution was investigated to determine if the pH affected the optical properties of the gold rods in a similar way to the application of the electric fields. Optical properties and physical dimensions were measured and compared to a gold nanorod solution diluted in water such that there was identical concentration of gold in each solution.

6.2.2. Effect of electric fields on drying gold nanorod solutions

Two methods were investigated. One involved the application of a drop of gold nanorod solution onto a conducting substrate, ITO coated glass and an electric field was applied across the substrate as the drop dried. An alternative method involved creating a substrate that electrically isolated the two electrodes. This was achieved by using a glass slide as the substrate and depositing a layer of gold along two sides of the slide. The gold nanorod solution was applied such that the solution reached both electrodes and an electric field was applied from the MiniLab as the solution was dried. The samples were then investigated in the SEM. Both AC and DC electric fields were investigated.

6.3. Results and Discussion

The investigations into electric field interactions of gold nanorods were conducted in two directions. One focused on the behaviour of rods in solution whilst the other investigated rod positions when drying a solution under the influence of an electric field.

6.3.1. Electric field interactions with gold nanorod solutions

The applied electric fields investigated included both AC and DC fields both with and without an insulating glass layer. The insulating glass layer (if used) stops any electron transfer between the two electrodes.

An applied AC field of 18.3V was applied across 150 μm of gold nanorod solution and 150 μm of glass and corresponds to field strength of 61 Vmm^{-1}. The optical spectra of the rod solution before during and after the electric field was applied is shown in Figure 6.2. The field was applied for up to an hour and then the sample was allowed to rest for up to an hour with measurements taken every 5 minutes. No overall trends or changes are observed across all the measurements and the small variations in peak height are within instrument uncertainty. There is a very small decrease in peak heights between the initial and final measurements which took place over several hours.

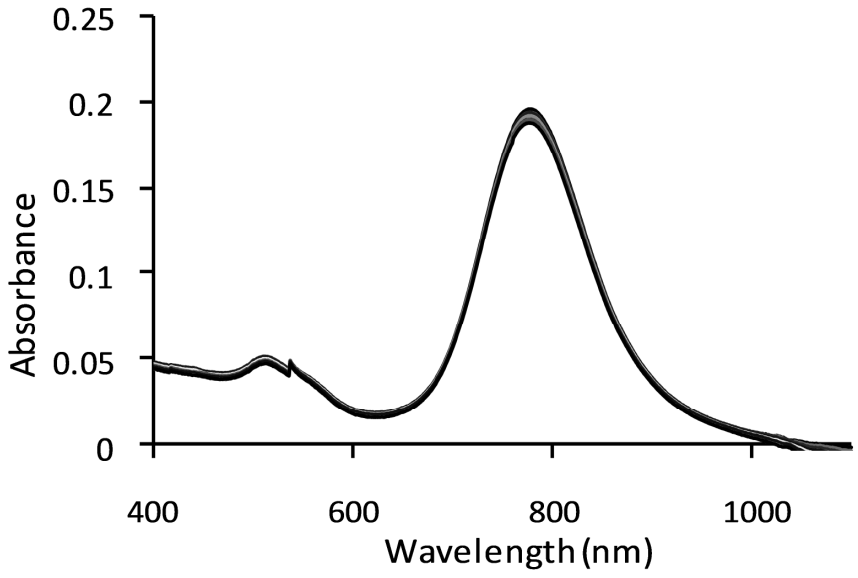

Figure 6.2: Optical spectra of gold nanorod solution in an AC insulating cell.

For all AC electric field experiments a signal generator was attached to an amplifier and connected to a cathode ray oscilloscope (CRO) so that the sinusoidal waveform could be confirmed. The generated sinusoidal wave was found to degrade at peak maxima and minima when the amplifier was set to maximum. Figure 6.3 shows the optical spectra of a gold nanorod solution with an applied AC field increasing from 0 to 127 Vmm^{-1}. The final two measurements were taken 5 minutes apart and consist of the non-sinusoidal generated wave. The light blue line corresponds to the measurement immediately following a breakdown of the sinusoidal wave, causing a net DC field, resulting in the longitudinal peak decreasing in intensity and blue-shifting. This process had almost concluded after 5 minutes with only a small peak remaining. It is thought that the breakdown of the sinusoidal wave produces a net DC field that strips the protective CTAB coating from the gold nanorods, allowing the nanorods to aggregate and precipitate from the solution.

Switching the AC field on and off causes spikes in the applied electric field, such that there is a net DC current, which with sufficient transfer of charge causes an irreversible aggregation of the rods. To avoid this aggregation, the applied AC field must be slowly increased and decreased, removing spikes in the electric field and producing negligible net DC charge transfer. Figure 6.4 shows an example of an applied AC electric field which does not cause irreversible changes to the gold nanorod solution. Several times an electric field was applied to the nanorod solution and the longitudinal peak shift that was observed to be unrelated to the applied electric field. The longitudinal peak position was measured to be 776 ± 1.2 nm and intensity of 0.192 ± 0.003 over the course of two hours. This indicates that an applied sinusoidal electric field of up to 123 Vmm^{-1} has no significant effect on the movement of the gold nanorods within the solution.

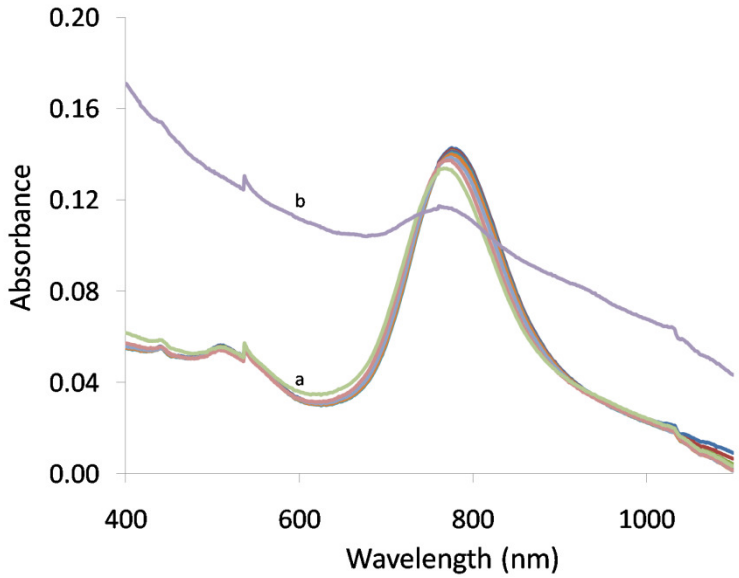

Figure 6.3: Optical spectra of gold nanorod solution under the influence of a non-insulating AC electric field. (a) and (b) correspond to consecutive measurements where the applied field is not sinusoidal.

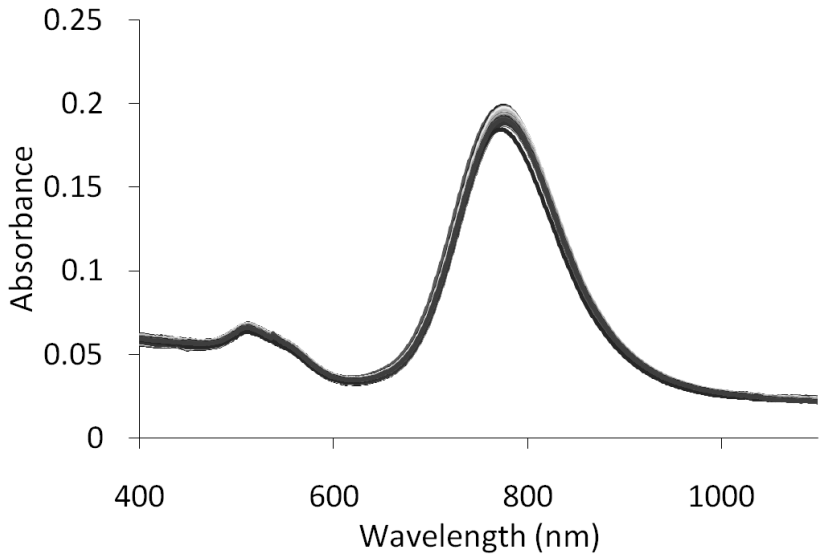

Figure 6.4: Optical spectra of a non-insulating applied AC field interacting with a gold nanorod solution.

These results differ from those obtained by van de Zande *et al.* which showed an increase in absorbance across the entire spectral range when the electric field was applied in increasing intensities. Also observed was a decreasing peak size corresponding to the increasing electric field.[218] The main difference in the experimental conditions used here compared to those used by van de Zande *et al.* was that the gold nanorods were produced using wet chemistry whilst van de Zande *et al.* used the

template method. As such, van de Zande *et al.* were able to relatively easily select a different stabilising agent than CTAB which, it seems, significantly reduces the polarisability of the nanorods.

Also investigated was the influence of DC electric fields on gold nanorods in solution. Figure 6.5 shows the optical spectra of an insulated gold nanorod solution. No significant variations in peak heights or positions were observed when using a maximum voltage of 31 V across the cell, which corresponds to 103 Vmm^{-1}. Higher electric fields were required before a change in the optical properties could be observed.

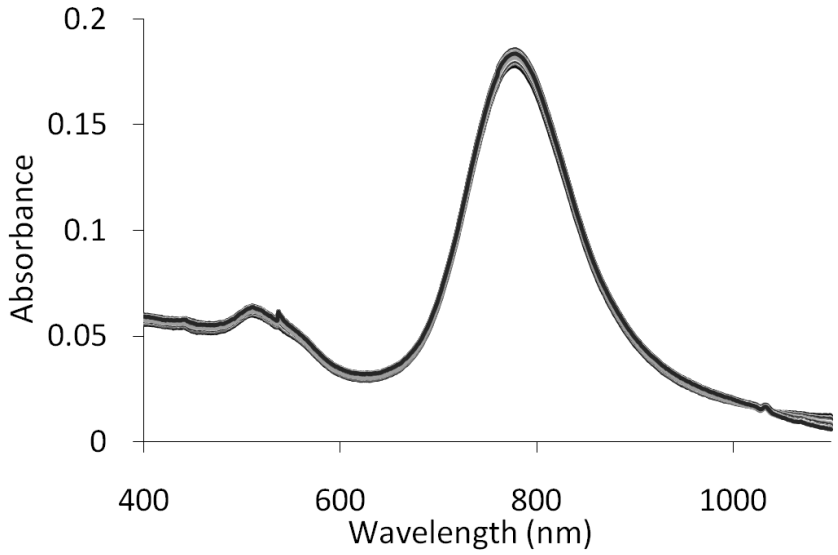

Figure 6.5: Optical spectra of an insulated gold nanorod solution under the influence of a DC electric field.

Figure 6.6 shows an investigation into the influence of larger DC electric fields on the optical properties of gold nanorod solutions. This experiment consisted of investigating 50 V, 100 V, -100 V, 500 V and 800 V across an electrically isolated cell with electrodes spaced 300 μm apart. Electric field strengths of up to 2666 Vmm^{-1} were investigated. Whilst field strengths of up to ±333 Vmm^{-1} had no significant effect on the optical properties, when the applied field was increased to 1666 Vmm^{-1} there was an immediate and irreversible decline in both the longitudinal and transverse plasmon resonance peaks. This indicates that the gold nanorods were being removed from the test area. It is possible that this occurred due to the large electric field stripping the ionic surfactant from the nanorods, thus allowing flocculation to occur. After this, flocculates

of sufficient size overcome Brownian forces and precipitate and some precipitates were observed during this experiment.

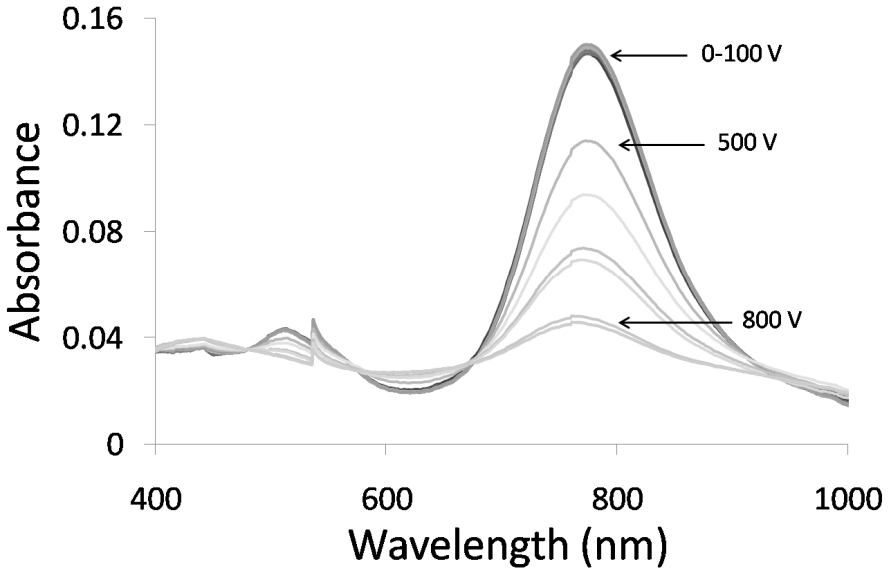

Figure 6.6: Normalised optical properties of gold nanorod solution under the influence of up to 800V or 2666 Vmm-1 of a DC electric field.

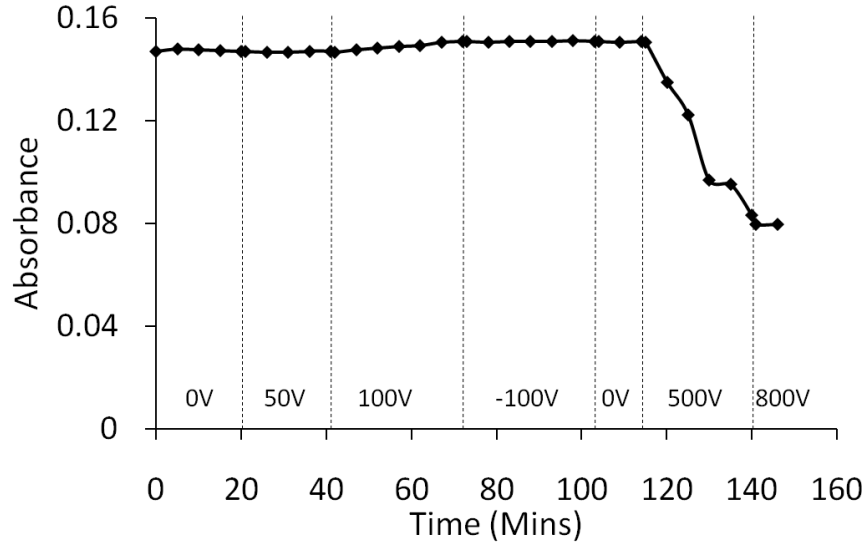

Figure 6.7: Absorbance maxima for the longitudinal resonance peaks over time with the applied electric field shown. This corresponds to the optical properties shown in Figure 6.6.

Figure 6.7 shows the longitudinal peak intensities over time, with applied voltages also indicated. Figure 6.7 consists of the peak data from Figure 6.6 and shows that there was no significant change to the longitudinal peak and therefore no possible alignment

until an applied voltage of 500 V was used, corresponding to a field strength of 1666 Vmm^{-1}. After the application of 500 V for 30 minutes the majority of gold nanorods had precipitated from solution. Further investigations revealed that significant change in optical properties occurred at electric fields over 1000 Vmm^{-1} or 300 V across the cell. Measurements at large voltages and measurements over long periods of time also caused heating of the cell. Presumably, some current was passing at these high voltages even though attempts had been made to insulate the cell. When the electric field was applied for too long, the wax that sealed the cell re-melted and the rod solution leaked out. To avoid this problem, measurements could be taken at faster rates or a period of measurements without an applied field could be utilised allowing the cell time to cool down.

Figure 6.8 shows the influence of a DC electric field on the optical properties of an *un-insulated* gold nanorod solution. The application of a 6.6 Vmm^{-1} field caused the longitudinal peak to slightly blue-shift and decrease in intensity in an irreversible fashion. This effect is more concisely shown in Figure 6.9. When the electric field is switched off there is no further change to the optical properties. As the electric field is increased the longitudinal peak decreases in intensity and blue-shifted. With an applied field of 13.3 Vmm^{-1}, or 2 V across the cell, there was a significant decrease in both the peak intensity and position. If the applied field was switched off immediately after a short period at 13.3 Vmm^{-1} the degradation of the longitudinal peak continues. Reversing the applied bias did not recover the original spectrum. It should be noted that at potentials greater than 1.23 V water is decomposed, i.e. $H_2O \rightarrow H_2 + ½O_2$.

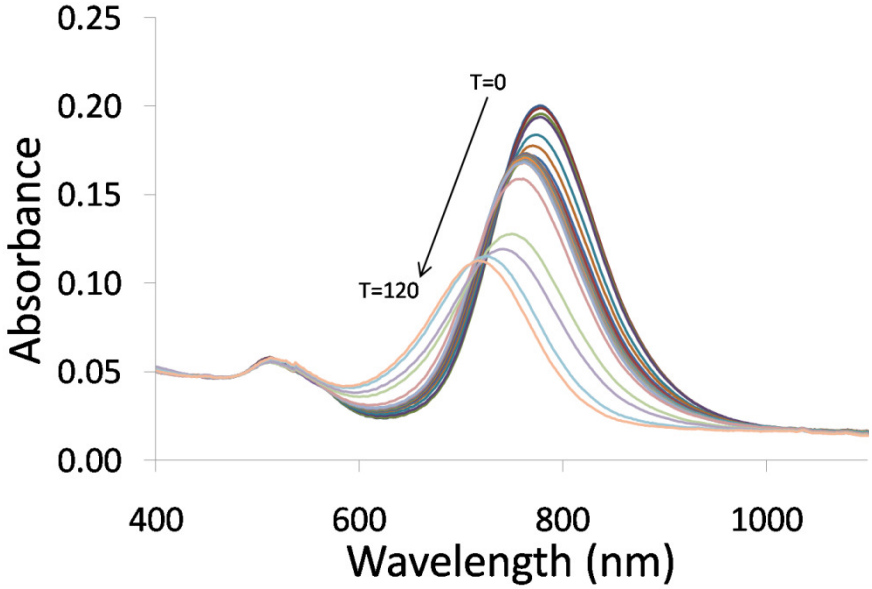

Figure 6.8: Normalised optical properties of DC electric field strengths from 0 to 13.3 Vmm^{-1} interacting with a gold nanorod solution.

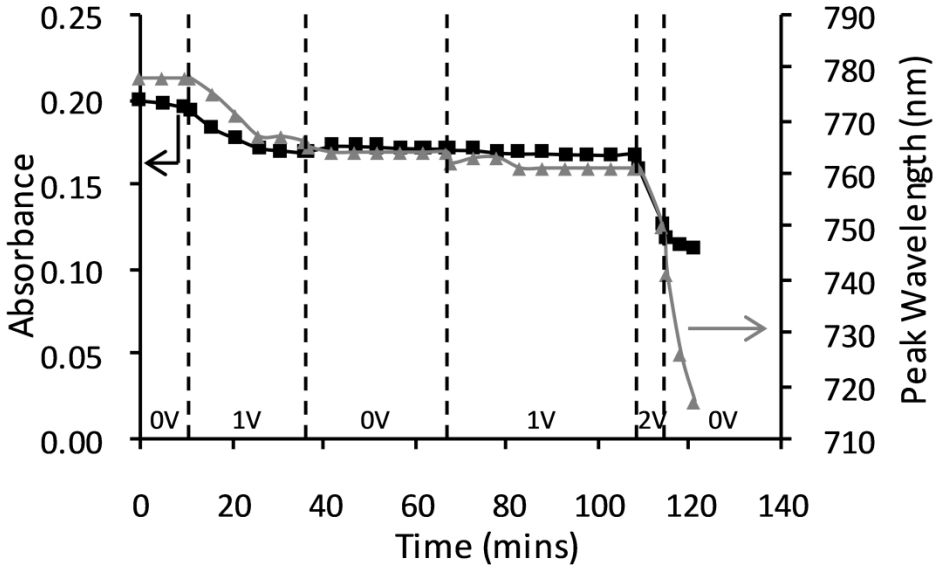

Figure 6.9: Longitudinal peak movement of both absorbance and wavelength when the DC electric field shown is applied.

When the applied DC electric field was at or above 13.3 Vmm^{-1}, the CTAB was stripped off the gold nanorods and the gold coated an electrode. This process was also observed when a non-insulating AC field was applied and there was a breakdown of the sinusoidal wave. Figure 6.10 shows the optical effect and physical structure of the samples where the gold coated the electrode. The physical structure of the gold coating is very porous, and the optical properties show no relation to the original rod spectra.

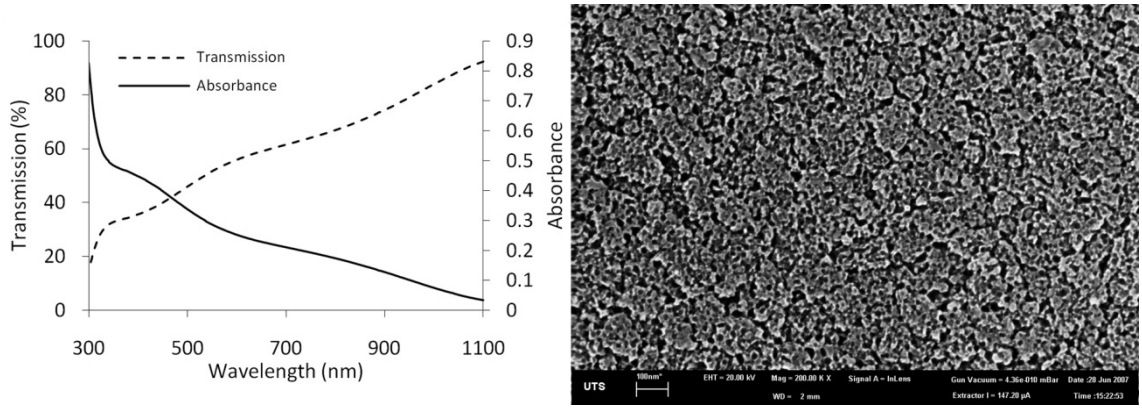

Figure 6.10: The optical properties and physical structure of a gold coated electrode.

In nearly all the methods investigated, there was no significant change in the observed optical properties until sufficient field strength was applied to cause irreversible changes to the rod solution. In other cases no significant changes were observed at all, presumably because insufficient field strength was applied. These results are very different to those observed by van der Zande *et al.* who found a gradual reversible change in both the transverse and longitudinal peaks, on the short aspect ratio rod investigated as alignment occurred.[218] The only significant change between van der Zande's experimental set-up and the one used here was the use of the wet chemically produced rods rather than use of the rods made by the template method. The main difference between the rods used is the stabiliser, with poly(vinylpyrrolidone) used as the stabiliser by van der Zande's group compared to CTAB used here. It has been shown here that the CTAB stabilised gold nanorods do not align under the influence of an electric field and, when excess field strength is applied, the CTAB is stripped off the gold nanorods causing either flocculation of the rods or electrodeposition of gold nanorods onto the electrode. During the process that causes flocculation or electrodeposition, there is a longitudinal peak blue-shift, a decrease in peak absorbance intensity and peak broadening occurring. These results are irreversible, suggesting that the optical properties of the gold nanorods must be changing, and therefore there is a reduction in the nanorod aspect ratios.

It was thought that the irreversible changes to the optical properties of the rod solution was at least partly due to the creation of OH^- ions under the influence of an electric field which cause blue-shifting the longitudinal plasmon peak.[226] This was tested through the addition of NaOH to a gold nanorod solution which altered the solution colour from red to purple. The changes in optical properties are shown in

Figure 6.11. The optical properties consist of spectra showing the gold nanorod solution in water (the relatively narrow high intensity peak) and the broad, low intensity peaks consisting of the same gold concentration with the addition of a 0.01M NaOH solution over time. Figure 6.11 (a) and (b) show the physical dimensions of the nanorods (a) with and (b) without the addition of NaOH. The average aspect ratios were measured by SEM to be approximately 3.6 for the alkaline solution compared to 4.1 for the normal solution. Also, the appearance of the alkaline nanorods is different to the normal rods with the rods appearing to be stuck into groups with multiple layers frequently occurring in even small groupings, which differs to the relatively spread out normal rods. Although the application of the OH^- ions caused the gold nanorod longitudinal plasmon peak to blue-shift, it was not identical to the results obtained for the interaction of electric fields on gold nanorods. These results are also different to those reported for the application of KOH to gold nanorod solutions. In that case, the change in longitudinal peak intensity was not as large as that induced here using NaOH.[226]

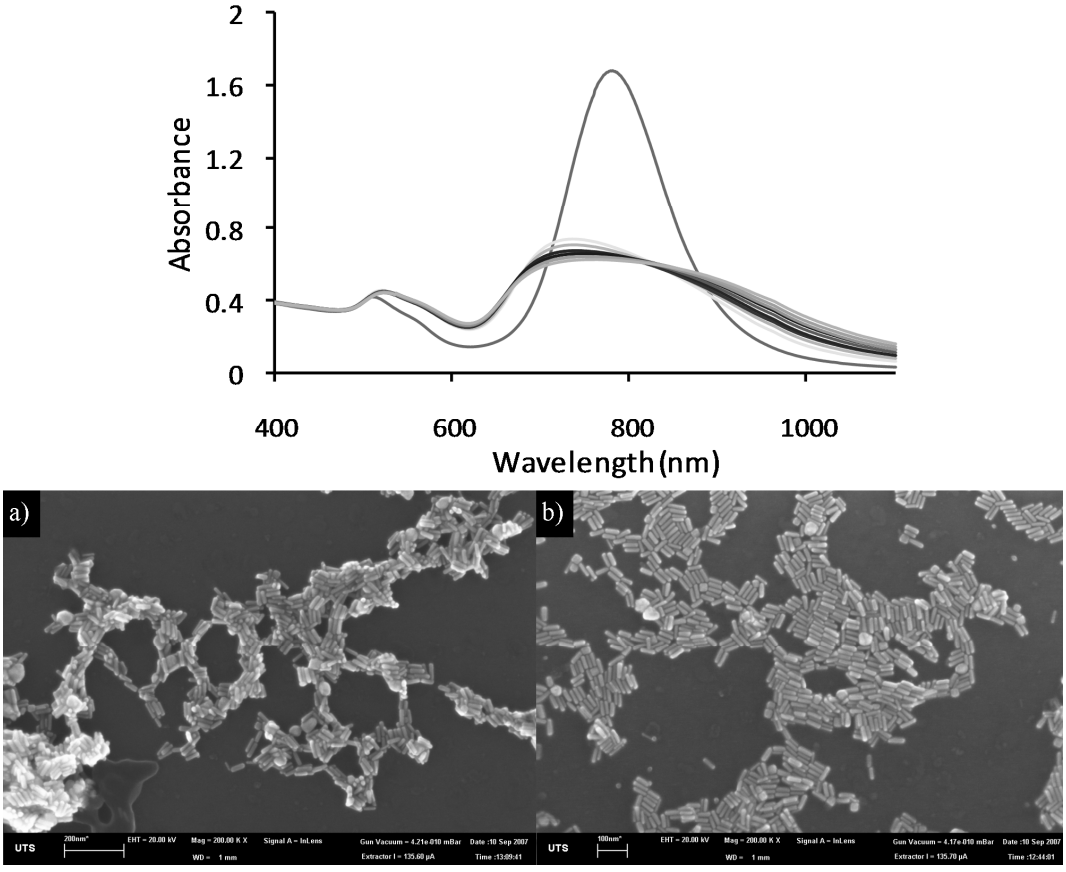

Figure 6.11: Optical absorbance spectra and SEM images showing gold nanorod solution (a) with and (b) without NaOH at the same magnification.

6.3.2. Electric field interactions of evaporated gold nanorod solutions

The ability of electric fields to affect the position or orientation of gold nanorods during the drying process was investigated. The two methods investigated involved passing a DC or AC current through (i) an ITO substrate with a drop of gold nanorod solution drying between the electrodes and the direction of the applied electric field would be along the face of the ITO glass. (ii) gold coated glass substrate, with the electrodes electrically isolated from each other, and the gold nanorod solution drying as the link between electrodes.

Figure 6.12 shows the effect of a gold nanorod solution applied to an ITO substrate drying under the influence of an electric field. Figure 6.12 (a) and (b) show the gold nanorods without the application of an electric field, whereas (c) and (d) had a 30 V DC electric field applied and (e) and (f) dried under the influence of an 18 V 10 kHz AC electric field. There were a lot more single or smaller groupings of rods when no electric field was applied, and the groupings observed consisted of no large areas of common orientation. The application of the DC field produced large groupings of commonly aligned nanorods, of which significant quantities were aligned vertically to the substrate. It was also observed that the applied AC field produced large areas of commonly aligned nanorods. The large groupings near the drop edge had common alignment parallel to the edge of the drop. AC fields were also found to produce large areas of aligned rods bound within the CTAB near the centre of the drop. Overall it was found that significantly more rods were aligned with neighbouring rods when under the influence of an applied electric field. The application of the electric field also appeared to produce larger groupings of rods, particularly in areas where the stabiliser has been removed.

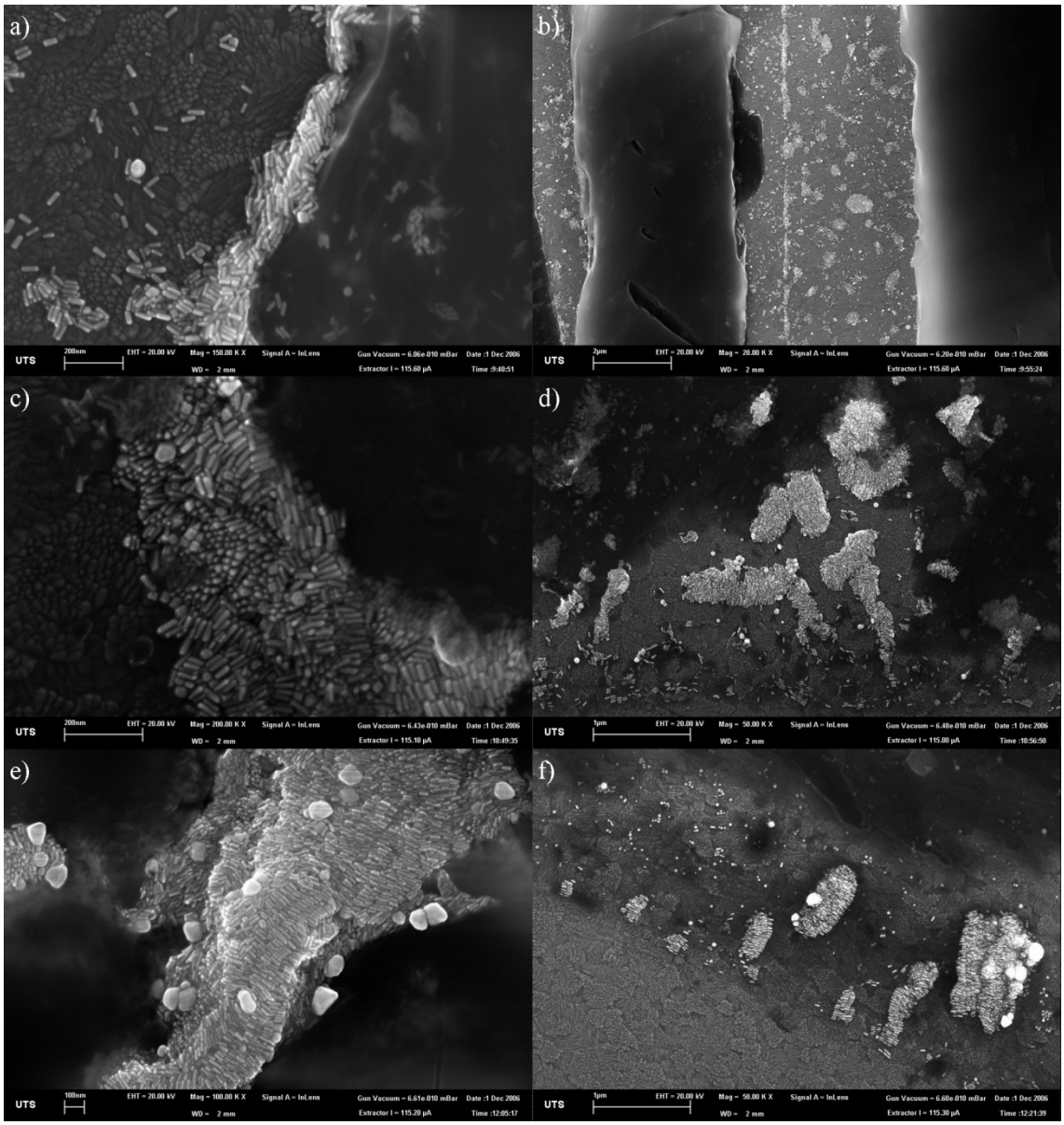

Figure 6.12: SEM images of dried gold nanorod solution under (a-b) no, (c-d) DC and (e-f) AC electric fields. The images are taken from the centre (column 1) and the edge (column 2) of the applied drop. It should be noted that the applied electric fields are along the face of the substrate, not perpendicular as with the previous experiment.

A gold nanorod solution was applied between and touching two electrically isolated gold coated electrodes on a glass substrate. An AC field of 18 V and 10 kHz was applied during the drying process followed by imaging in an SEM, shown Figure 6.13. Significantly more gold nanorods were found at the edge of the drop, and there was no noticeable difference between the quantity and alignment of rods at either electrode. As with the AC field across a drop of gold nanorod solution on ITO, gold nanorods aligned

along the edge of the dried drop. However, away from the edges of the drop many groupings of rods were aligned parallel to near neighbour orientations.

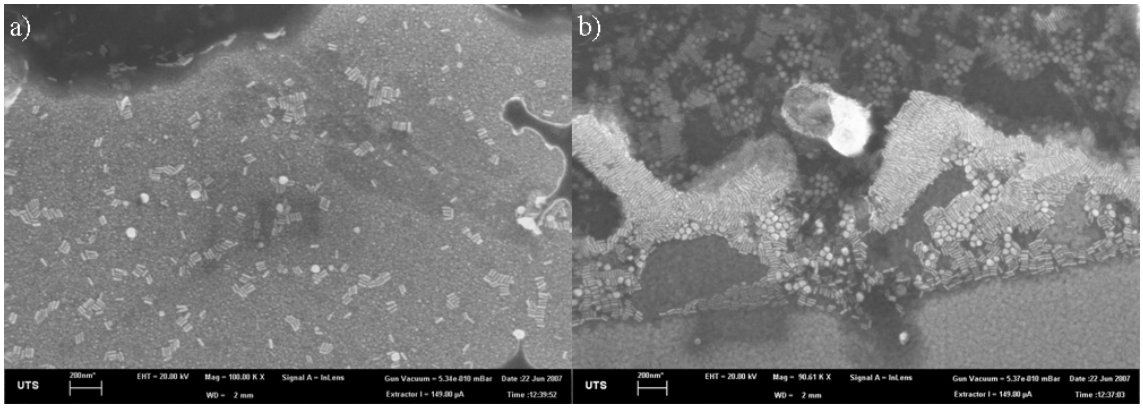

Figure 6.13: SEM images of gold nanorods deposited in an AC field at the (a) centre and (b) edge of the dried solution.

The application of a 31 V DC electric field between the two electrodes as the nanorod solution was drying resulted in the majority of gold nanorods attracted to the negative electrode. Large amounts of CTAB were observed on the positive electrode, however no gold nanorods were found. This is shown in Figure 6.14 with (a) the positive electrode and (b) the negative electrode. The attraction to the negative electrode is believed to be due to the charge of the CTAB-coated rods, which have a positive zeta potential.[227,228] No overall order in rod alignment was observed on the negative electrode, but the results are similar to those from applying a DC field on an ITO electrode as a gold nanorod solution was dried. Specifically, large groupings of rods were found with common alignment. However, although vertically aligned groupings were observed, they were not as prevalent as the DC field on ITO experiment and there were larger quantities of rod groupings with other orientations. Away from the edges of the drop, the gold nanorods behaved similarly to when an AC field was applied, with rods grouping together in the same orientation.

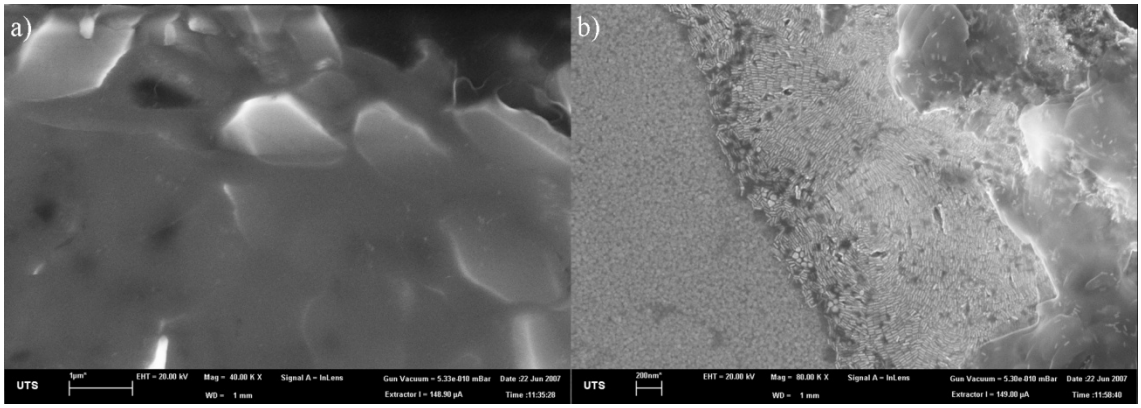

Figure 6.14: SEM images of gold nanorods dried in a DC field at the (a) positive and (b) negative electrode.

In general, the application of both AC and DC electric fields seemed to allow more gold nanorods to attach to the substrate than samples without an applied field. Gold nanorods neighbouring the drop edge, in particular under the influence of an AC field, stick parallel to the drop edge. Under the application of a DC electric field and on a substrate with two electrically isolated electrodes, the gold nanorods are attracted to the negative electrode.

6.4. Conclusions

The interactions of electric fields with gold nanorods in solution were found to produce no significant change in either the alignment or optical properties until sufficient field strength was applied to cause irreversible changes to the rod solution. As gold nanorods have reportedly been aligned using AC electric fields[218] it is possible that the CTAB stabilising agent used in the present work reduces the intensity of the induced rod dipole moment, and with the short rods investigated (AR < 5), the small induced dipole is insufficient to overcome Brownian motion in the liquid. Increasing the magnitude of the electric field is believed to eventually strip some ionic surfactant from the rods, thereby causing flocculation of the rods. The flocculation was associated with an apparent decrease in aspect ratio (as evidenced by the blue-shift of the longitudinal peak) and a reduction in peak intensity.

The application of an alkaline solution to the rods was found to cause a blue-shift, broadening, and intensity loss of the longitudinal plasmon peak. It was determined that the creation of hydroxide ions in the water could, at most, only form a very small part in the optical property changes due to the interaction of the applied electric fields.

The application of AC or DC electric fields to drying rod solutions was found to facilitate the attachment of gold nanorods to the substrate, in contrast to samples produced without an applied electric field where a washing process removed large quantities of rods. Gold nanorods neighbouring the dried solution edge, in particular under the influence of an AC field, aligned parallel to the solution edge. The application of a DC electric field across two electrically isolated electrodes resulted in the gold nanorods being attracted to the negative electrode.

From these experiments it appears that electrically-controlled realignment of gold nanorod window coatings is not feasible using gold nanorods produced using the more cost-effective wet-chemical methods. However, it would be interesting to revisit the issue in the event that gold nanorods of greater aspect ratio could be made move economically using wet-chemical methods.

Chapter 7:

General Conclusions

Chapter 7: General Conclusions

7.1. General Discussion and Conclusions

Windows are responsible for significant amounts of energy transferred into or out of buildings. Recently, coatings have been added to windows to decrease energy transfer. These coatings have a huge market; the majority of new commercial buildings, and many residential windows, include some sort of energy-saving coating. There are many different types of energy-saving coatings that have different performance characteristics that have been designed for various climates. Due to their controllable optical properties, gold nanorods have great potential for use as an energy-saving window coating.

This thesis has explored the optical properties of gold nanostructures with various shapes and dimensions. To provide a theoretical basis for the work it started using computational modelling with the discrete dipole approximation. The calculated properties of simple gold rod structures were consistent with previously reported experimental and computational data. In the present work, it was shown for the first time how modelling can be used to design an ensemble mixture of rods of different aspect ratios, with the purpose of tuning absorption characteristics to some selected range of wavelengths. Increasing the numbers of rod aspect ratios used resulted in more accurate calculations of the optical properties.

Nanoscale, crossed-rod structures made of gold provide an interesting motif to construct spectral and polarization-dependent filters. Calculations on X-shaped structures showed that variation of the angle between the rods (i.e. the arms of the structures) as well as the aspect ratio of the arms affects the plasmon resonant frequency. The individual resonances of each rod are hybridized in the crossed-rod structure and blue-shifted as a result. The numerical DDSCAT method uses multiple dipole domains to calculate optical properties. In the case of crossed-rod structures, it was found that a mesh size with a spacing of <1 nm is required for accurate results. The electric field distributions in the vicinity of the gold structures are quite complex and

have a high intensity and spatially extended nature. This type of structure may be especially useful as a nano-antenna for the generation of two-photon fluorescence in a suitable surrounding medium. Crossed-rod structures with V-shapes have similar potential for the generation of two photon fluorescence. The use of different dimensions of the V structures allows control over the optical properties and also control over the placement and size of the generated external electric field. Acute V angled structures in particular create high intensity spatially extended electric field between the arms of the structure, suitable for the generation of two photon fluorescence.

The computational data predicted interesting optical properties and so methods to prepare actual gold nanostructures were investigated. These investigations led to a number of scientifically interesting and practical findings.

EBL was found to be a useful technique (possibly the *only* technique) to generate arrays of nanostructures of sufficient size to investigate their optical properties. Current technology, however, limits the areas that may be fabricated with commercial-scale applications unfeasible. Some of the more critical factors of EBL are discussed below.

Plasma cleaning was important when used in combination with EBL but requires stringent control. Plasma cleaning of the substrate before the deposition of PMMA resists ensures a clean surface. Short plasma cleaning times (30 s or less), at low energy and after resist development, removed PMMA remnants from the holes in the structure to improve subsequent binding of the metal to the substrate. Longer plasma cleaning times removed significant quantities of PMMA and distorted the exposed structure.

When depositing a metal layer into a resist, the thickness of the metal layer should be much less than the thickness of the resist otherwise the deposited metal will be pulled off the substrate during the lift-off stage. A 20 to 30 nm thickness of deposited metal with a 100 nm thick PMMA resist was found to be effective. Gold was bound more strongly to the substrate when a thin chromium film was first deposited onto the substrate. This also yielded quite uniform gold structures. When a binding layer was not used the deposited gold structure was affected by the substrate structure: on ITO-coated glass substrates individual particles of gold resulted rather than the desired shapes. The application of a gold nanorod growth solution to these individual gold particles failed to yield the desired structures.

During the exposure process, different accelerating voltages can be used to fine tune or alter exposures. The use of higher accelerating voltages created a small exposure

area, good for high resolution structures but resulted in a more difficult lift-off process. Lower accelerating voltages provided a reduction in structure resolution but provided a more effective lift-off process. Variable pressure (VP) electron beam lithography was used to produce structures on non-conductive substrates. However, VP EBL exposes slowly compared to high vacuum (HV) due to dispersion of the primary electron beam interacting with the gas within the chamber. The structure resolution was also lower with VP compared to HV exposures because of beam dispersion and lower beam resolution. For structures requiring a transparent substrate, conducting glass substrates were more suitable than standard glass for higher resolution structures and faster exposure times. Substrate dependence was observed for the dose requirements for all structures. Higher atomic number substrates required lower dose than lower atomic number substrates. In general, the dose requirements for 100 nm thick PMMA resists were approximately 0.78 nC/cm for ITO-coated glass, 0.6 nC/cm for silicon and 0.3 nC/cm for gold. These also varied according to resist thickness and exposure pattern dimensions. Excess dose produced larger structures, and often deformed the corners of the pattern. Insufficient dose reduced the exposed PMMA quantity, and often left some areas of the pattern with only partial PMMA removal.

The optical properties of structures prepared by EBL were measured using a microscope equipped with a UV-visible-NIR spectrophotometer in transmission and reflection mode. Surface plasmon resonances were observed for all of the complete fabricated gold nanostructured arrays. Interference fringes were observed in spectra where ITO-coated glass was used as a substrate. However, these could be deconvoluted from the gold plasmon resonances using a modelling procedure. Transverse and longitudinal plasmon peaks were observed with the gold nanorod arrays. The X structure arrays displayed a single main plasmon resonance peak, which corresponded to the resonance of the long aspect of the X structure. The strong transmission minimum in the NIR region shows that the X structures have potential as window coatings. However, the intensity of the plasmon resonance transmission minima was insufficient to create efficient window coatings and multiple layers of gold structures would be required to obtain significant plasmon resonance absorption. Using several different rod aspect ratios should improve the spectral coverage.

A comparison of the measured and calculated optical extinction properties showed that the position of the surface plasmon resonance peaks of the fabricated structures

differ slightly to that of the modelled structures. This was due to differences in the structure shape and the surrounding medium and was also influenced by the spectrophotometer used.

Techniques other than EBL were also investigated, with a particular focus on methods that could be scaled industrially. An MPTS molecule was applied to a glass substrate and was found to increase the amount of gold nanorods binding to the substrate compared to gold nanorods on plain glass. It was, however, determined that MPTS bound an insufficient quantity of rods for solar screening applications.

Gold nanorods suspended in a water soluble polymer (PVA) allowed the formation of films that could be applied to glass. Mixtures of gold nanorod solutions of different aspect ratios were produced, and thereby allowed control of the peak position and intensity. Rods in a PVA solution were more stable than rods suspended in a water solution, and rods within a PVA film were stable over at least three years. The optical properties of PVA films containing gold nanorods were controlled by the gold nanorod concentration, the film thickness and polymer concentration. Gold nanorod alignment was attained by stretching PVA films immersed with gold nanorods. Many different rod aspect ratios could be aligned at the same time along the stretching plane. Increasing the stretching factor increased the rod alignment.

Nanorods of different aspect ratios were blended to produce a spectrally selective coating suitable for solar glazing applications. Window samples transmitted between 30 and 37% of the luminance of sunlight while having a SHGC of between 58 and 72% of total incoming heat flux. The absorptive nature of this coating system may be offset in some applications by the fact that it does not reflect a heat load onto adjacent buildings, and will be cheaper to produce compared to vacuum-deposited window coatings. The incorporation of gold nanorods with aspect ratios greater than five would increase the effectiveness of the window coating further. However, while a blend of rods with aspect ratios of between 3 and 10 would be needed to achieve optimum solar screening,[199] in the present instance only rods with aspect ratios of up to 5 were available in quantity. This is because the yield of the currently known rod-making techniques drops off steeply for rods with aspect ratios greater than 4. The present coated window panes therefore represent a proof-of-principle for the use of gold nanorods rather than a commercially viable finished product.

The possibilities of aligning gold nanorods under the influence of an electric field were also investigated. The interaction of electric fields with gold nanorods in solution were found to produce no significant change in either the alignment or optical properties until field strength was increased to a point where irreversible changes to the rod solution occurred. This increased electric field strength strips the CTAB from the rods, increasing rod flocculation resulting in a decrease in rod aspect ratio and causing the longitudinal plasmon peak to blue-shift and attenuate. The formation of electrically controlled gold nanorod window coatings is apparently not feasible using the relatively small gold nanorods produced using the more cost-effective wet-chemical methods.

7.2. Future Directions

Several of the areas explored in this thesis would be worthwhile pursuing in future research. For example, fabrication of large areas of different types and shapes of nanostructures can be undertaken using the lithographic processes presented within this thesis. Specific future work might consist of fabricating large arrays of V structures and X structures for the investigation into two-photon fluorescence, or into other possible uses of spatially extended electric fields. Further work could also investigate the optical properties of the large arrays of gold V structures and comparison with the modelled V structures.

The introduction of significant quantities of gold nanorods of longer aspect ratios to the PVA films would provide them with the capability to absorb significantly more of the longer wavelengths of light. Aspect ratios of between 5 and 8 should be preferentially investigated as their availability would permit coverage of the spectral region between 900 and 1300 nm. Further work is required to protect the PVA coating from the environment, especially from moisture, or to investigate the efficacy of other more hardy polymers as a means of producing coatings.

Appendix

Appendix: DDSCAT Simulations

NB: All the Appendix movies are separate files on the CD attached.

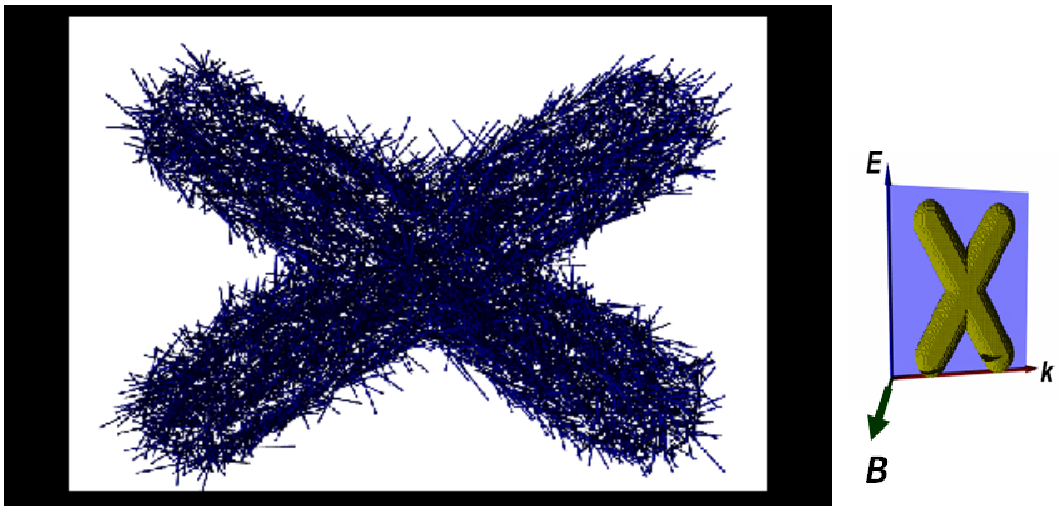

Figure A.1: A movie showing the dipole moments of a central slice of an X35 structure at resonance wavelength of 770 nm, with applied electromagnetic wave oscillating in the direction shown.

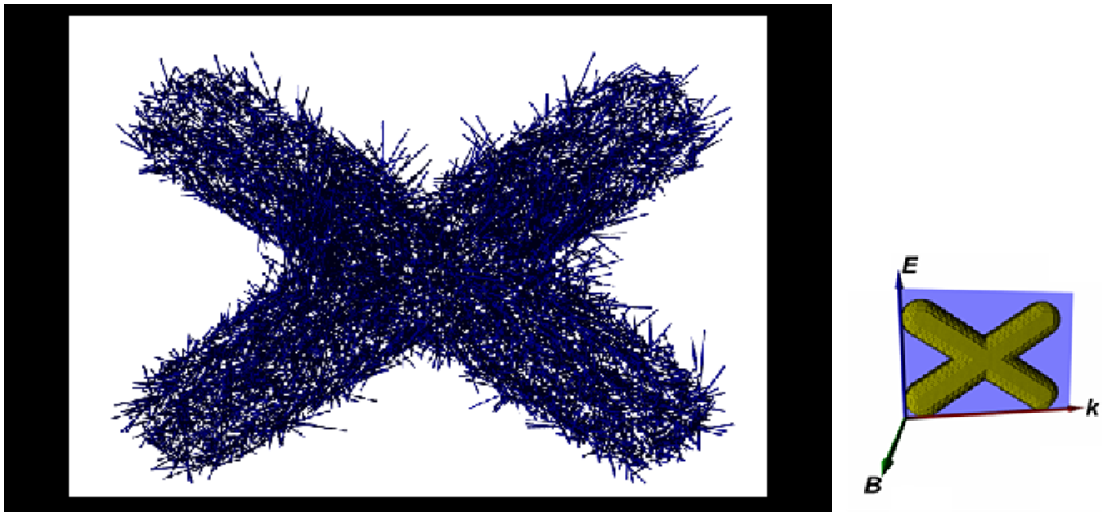

Figure A.2: A movie showing the dipole moments of a central slice of an X35 structure at resonance wavelength of 735 nm, with applied electromagnetic wave oscillating in the direction shown.

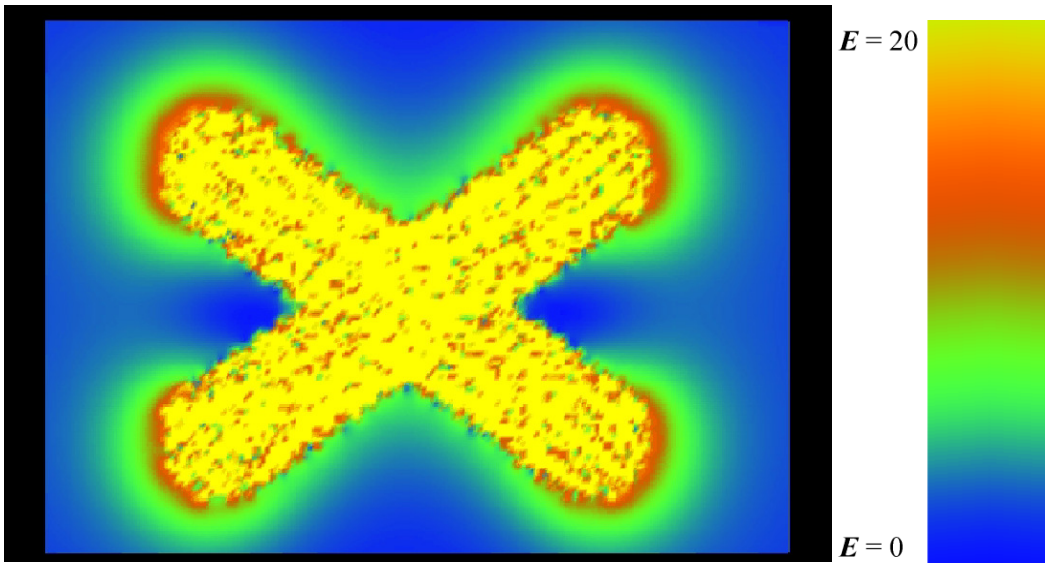

Figure A.3: A movie showing the external electric field of the X35 structure at the resonance wavelength of 770 nm, with the magnitude of the external field shown as a factor of the incident electric field.

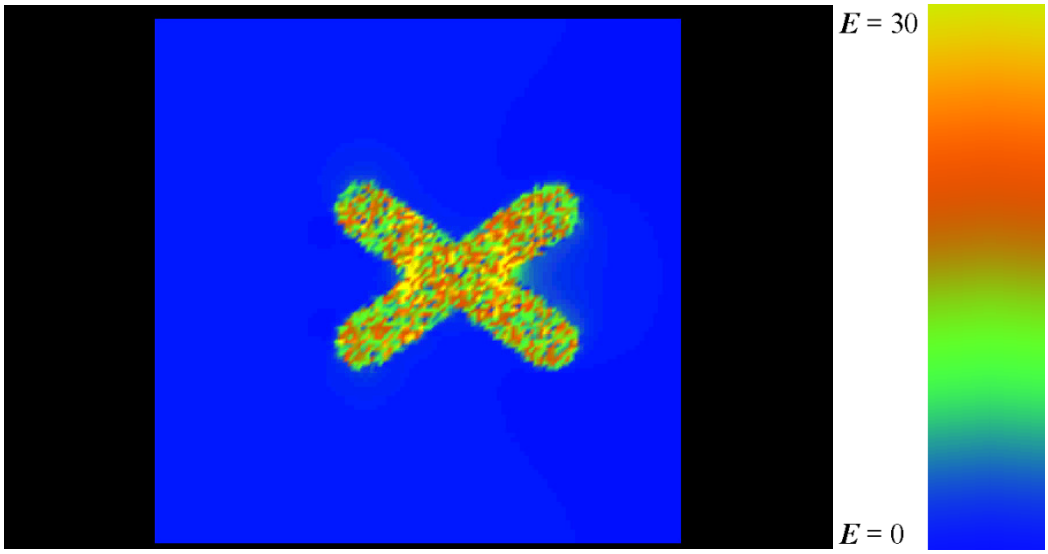

Figure A.4: A movie showing the external electric field of the X35 structure at the resonance wavelength of 735 nm, with the magnitude of the external field shown as a factor of the incident electric field.

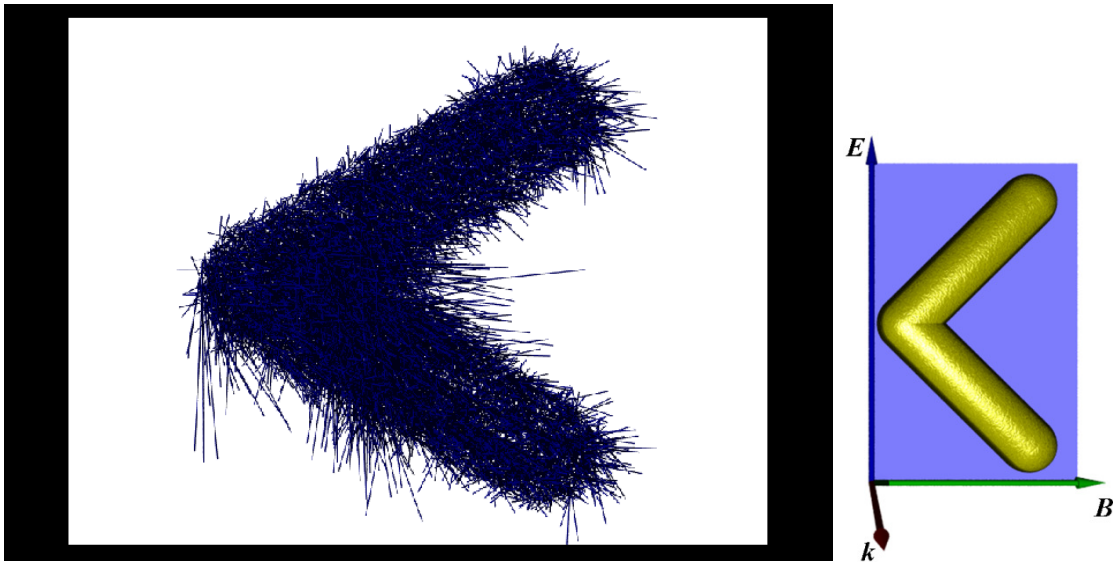

Figure A.5: A movie showing the dipole moments of a central slice of a V60 structure at resonance wavelength of 900 nm, with applied electromagnetic wave oscillating in the direction shown.

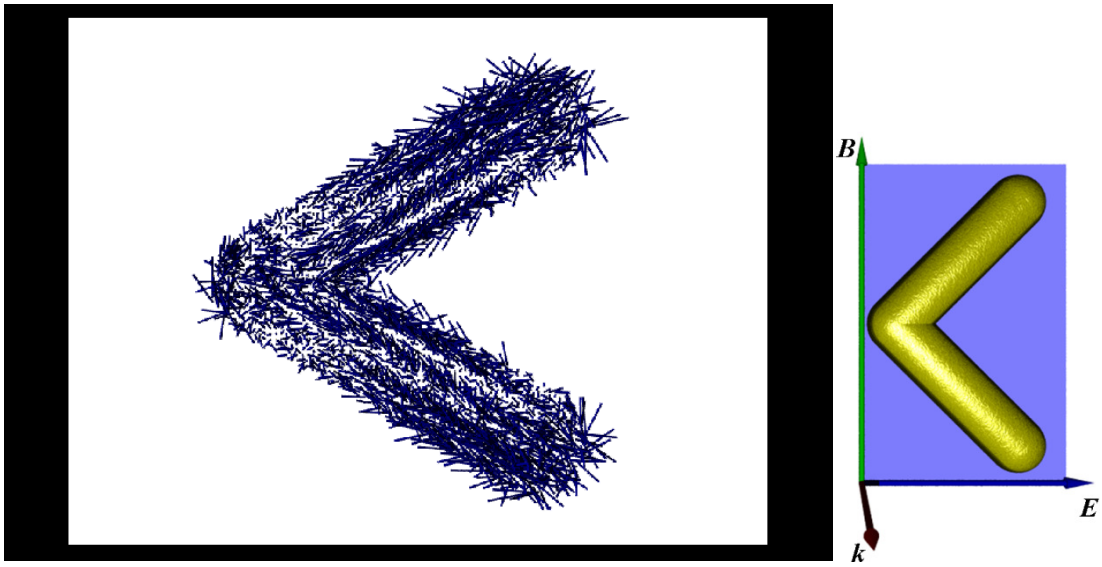

Figure A.6: A movie showing the dipole moments of a central slice of a V60 structure at resonance wavelength of 630 nm, with applied electromagnetic wave oscillating in the direction shown.

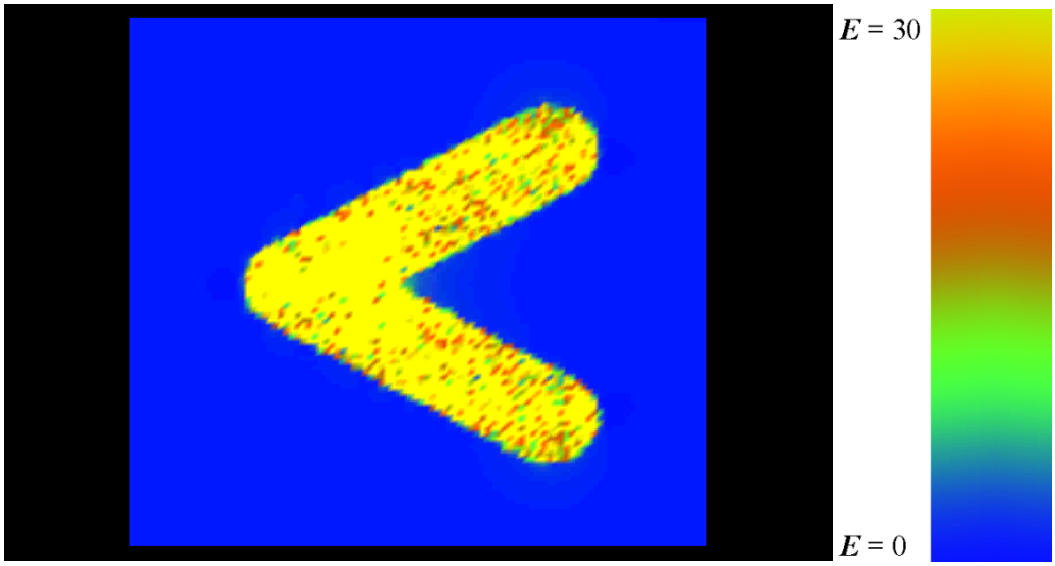

Figure A.7: A movie showing the external electric field of the V60 structure at the resonance wavelength of 900 nm, with the magnitude of the external field shown as a factor of the incident electric field.

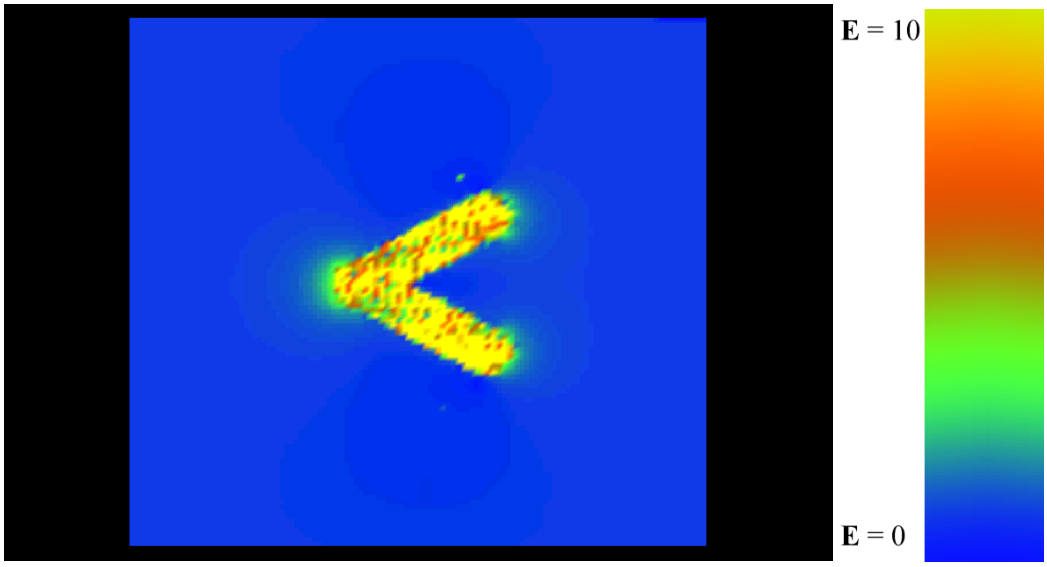

Figure A.8: A movie showing the external electric field of the V60 structure at the resonance wavelength of 630 nm, with the magnitude of the external field shown as a factor of the incident electric field.

References

References

[1] Haacke, G. 1977, 'Transparent conducting coatings', *Annu. Rev. Mater. Sci.*, **7**, 73.

[2] Pucci, A. 2005, 'IR spectroscopy of adsorbates on ultrathin metal films', *Phys. Status Solidi B*, **242**, (13), 2704.

[3] Valliappan, S., Swiatkiewicz, J. & Puszynski, J. 2005, 'Reactivity of nanosize aluminum with metal oxides and water vapor', *Powder Technol.*, **156**, 164

[4] Rai, A., Park, K., Zhou, L. & Zachariah, M. 2006, 'Understanding the mechanism of aluminium nanoparticle oxidation', *Combust. Theor. Model.*, **10**, (5), 843.

[5] Cortie, M. 2004, 'The weird world of nanoscale gold', *Gold Bull.*, **37**, (1-2), 12.

[6] Loebich, O. 1972, 'The optical properties of gold', *Gold Bull.*, **5**, (1), 2.

[7] Perez-Juste, J., Pastoriza-Santos, I., Liz-Marzan, L. & Mulvaney, P. 2005, 'Gold nanorods: synthesis, characterization and applications', *Coord. Chem. Rev.*, **249**, 1870.

[8] Anonymous 2007, *Flat Glass Industry - Summary*, Pilkington, viewed 28/05/07 <http://www.pilkington.com/about+pilkington/flat+glass+industry/default.htm>.

[9] Anonymous 2008, *International energy outlook*, in U.S.D.o. Energy (ed.)Energy Information Administration, <www.eia.doe.gov/oiaf/ieo/index.html>.

[10] Bell, J. & Matthews, J. 1998, 'Glazing materials', *Mater. Forum*, **22**, 1.

[11] Bell, J., 'Glazing selection', *Glass Processing Days*, viewed 30-01-09 <http://www.glassfiles.com/library/16/article255.htm>.

[12] Anonymous, 'Zero energy window prototype', *US Department of Energy Fact Sheet*, viewed 3/02/09 <http://windows.lbl.gov/adv_Sys/hi_R_insert/ZeroEnergyWindowDOE-FactSheet.pdf>.

[13] Boeker, E. & Grondelle, R. 1999, *Environmental physics* Second edn, John Wiley & Sons, Ltd.

[14] Anonymous 2008, *G.James*, GJames Australia, viewed 08/05/09 <http://www.gjames.com.au/>.

[15] Karlsson, J., Karlsson, B. & Roos, A. 2001, 'Performance of antireflection glazings in windows', *Glass Processing Days*, 646.

[16] Anonymous 2008, *Standard conditions of development consent*, vol. 165, Department of Planning, Sydney, p. 72.

[17] Anonymous 1997, *Energy-efficient window glazing systems*, Pacific Gas and Electric Company, viewed 11/02/09 <http://www.pge.com/includes/docs/pdfs/about/edusafety/training/pec/inforesource/energy-efficient_window_glazing_systems.pdf>.

[18] Anonymous 2008, *Efficient window collaborative*, Center for Sustainable Building Research, College of Design, University of Minnesota, viewed 4/03/09 <http://www.efficientwindows.org/>.

[19] McCluney, R. & Jindra, P. 2001, 'Industry guide to selecting the best residential window options for the florida climate', p. 20, viewed 20/05/2009 <http://www.fsec.ucf.edu/>.

[20] Rajala, M., Pimenoff, J., Hovinen, A. & Vainio, T. 2007, 'Rapid growth nanoparticle low-e coating', *Glass Performance Days*, 477.

[21] Lampert, C. 1998, 'Smart switchable glazing for solar energy and daylight control', *Sol. Energy Mater. Sol. Cells*, **52**, 207.

[22] Benson, D.K. & Branz, H.M. 1995, 'Design goals and challenges for a photovoltaic-powered electrochromic window covering', *Sol. Energy Mater. Sol. Cells*, **39**, (2-4), 203.

[23] Anonymous 2008, *Window and Door*, National Glass Association, viewed 16/04/09 <http://www.windowanddoor.com/>.

[24] Seeboth, A., Schneider, J. & Patzak, A. 2000, 'Materials for an intelligent sun protecting glazing', *Sol. Energy Mater. Sol. Cells*, **60**, 263.

[25] Beck, A., Korner, W., Scheller, H., Fricke, J., Platzer, W. & Wittwer, W. 1995, 'Control of solar insolation via thermochromic light-switching gels', *Sol. Energy Mater. Sol. Cells*, **36**, 339.

[26] Anonymous 2009, *ASTM International*, American Society for Testing and Materials, viewed 3/03/09 <http://www.astm.org/>.

[27] Anonymous 2009, *International Standards for Business, Government and Society*, International Organization for Standardization, viewed 4/03/09 <http://www.iso.org/>.

[28] Çengel, Y. 1998, *Heat transfer: a practial approach*, McGraw-Hill.

[29] Kittel, C. 1996, *Introduction to solid state physics*, 7th edn, John Wiely & Sons, Inc.

[30] Kelly, K., Coronando, E., Zhao, L. & Schatz, G. 2003, 'The optical properties of metal nanoparticles: the influence of size, shape, and dielectric environment', *J. Phys. Chem. B*, **107**, 668.

[31] Kreibig, U. & Vollmer, M. 1995, *Optical properties of metal clusters*, Springer, Berlin.

[32] Liz-Marzan, L.M. 2006, 'Tailoring surface plasmons through the morphology and assembly of metal nanoparticles', *Langmuir*, **22**, (1), 32.

[33] Noguez, C. 2007, 'Surface Plasmons on Metal Nanoparticles: The Influence of Shape and Physical Environment', *Journal of Physical Chemistry C*, **111**, 3806.

[34] Sonnichsen, C., Franzl, T., Wilk, T., von Plessen, G., Feldmann, J., Wilson, O. & Mulvaney, P. 2002, 'Drastic reduction of plasmon damping in gold nanorods', *Phys. Rev. Lett.*, **88**, (7), 0774021.

[35] Link, S. & El-Sayed, M. 1999, 'Spectral properties and relaxation dynamics of surface plasmon electronic oscillations in gold and silver nanodots and nanorods', *J. Phys. Chem. B*, **103**, 8410.

[36] Jain, P.K., Eustis, S. & El-Sayed, M.A. 2006, 'Plasmon coupling in nanorod assemblies: optical absorption, discrete dipole approximation simulation, and exciton-coupling model', *J. Phys. Chem. B*, **110**, (37), 18243.

[37] Hutter, E. & Fendler, J. 2004, 'Exploitation of localised surface plasmon resonance', *Adv. Mater.*, **16**, (19), 1685.

[38] Homola, J., Yee, S.S. & Gauglitz, G. 1999, 'Surface plasmon resonance sensors: review', *Sens. Actuators, B*, **B54**, (1-2), 3.

[39] Mulvaney, P. 1996, 'Surface plasmon spectroscopy of nanosized metal particles', *Langmuir*, **12**, (3), 788.

[40] Underwood, S.M., P. 1994, 'Effect of the solution refractive index on the color of gold colloids', *Langmuir*, **10**, (10), 3427.

[41] Krennn, J., Salerno, M., Felidj, N., Lamprecht, B., Schider, G., Leitner, A., Aussenegg, F., Weeber, J., Dereux, A. & Goudonnet, J. 2001, 'Light field propagation by metal micro- and nanostructures', *Journal of Microscopy*, **202**, 122.

[42] Specht, M., Pedarnig, J., Heckl, W. & Hansch, T. 1992, 'Scanning plasmon near field microscope', *Phys. Rev. Lett.*, **68**, (4), 476.

[43] Campion, A. & Kambhampati, P. 1998, 'Surface-enhanced Raman scattering', *Chem. Soc. Rev.*, **27**, (4), 241.

[44] Tian, Z., Ren, B. & Wu, D. 2002, 'Surface-enhanced Raman scattering: from noble to transition metals and from rough surfaces to ordered nanostructures', *J. Phys. Chem. B*, **106**, (37), 9463.

[45] Lombardi, J., Birke, R., Lu, T. & Xu, J. 1986, 'Charge-transfer theory of surface enhanced Raman spectroscopy: Herzberg-Teller contributions', *J. Chem. Phys.*, **84**, (8), 4174.

[46] Watanabe, S., Sonobe, M., Arai, M., Tazume, Y., Matsuo, T., Nakamura, T. & Yoshida, K. 2002, 'Enhanced optical sensing of anions with amide-functionalized gold nanoparticles', *Chem. Commun.*, (23), 2866.

[47] Sun, Y. & Xia, Y. 2002, 'Increased sensitivity of surface plasmon resonance of gold nanoshells compared to that of gold solid colloids in response to environmental changes', *Anal. Chem.*, **74**, (20), 5297.

[48] Raschke, G., Kowarik, S., Franzl, T., Soennichsen, C., Klar, T.A., Feldmann, J., Nichtl, A. & Kuerzinger, K. 2003, 'Biomolecular recognition based on single gold nanoparticle light scattering', *Nano Lett.*, **3**, (7), 935.

[49] Briglin, S.M., Gao, T. & Lewis, N.S. 2004, 'Detection of organic mercaptan vapors using thin films of alkylamine-passivated gold nanocrystals', *Langmuir*, **20**, (2), 299.

[50] Meriaudeau, F., Downey, T., Wig, A., Passian, A., Buncick, M. & Ferrell, T.L. 1999, 'Fiber optic sensor based on gold island plasmon resonance', *Sens. Actuators, B*, **B54**, (1-2), 106.

[51] Meriaudeau, F., Wig, A., Passian, A., Downey, T., Buncick, M. & Ferrell, T.L. 2000, 'Gold island fiber optic sensor for refractive index sensing', *Sens. Actuators, B*, **B69**, (1-2), 51.

[52] Reynolds, R., Mirkin, C. & Letsinger, R. 2000, 'Homogeneous, nanoparticle-based quantitative colorimetric detection of oligonucleotides', *J. Am. Chem. Soc.*, **122**, (15), 3795.

[53] Storhoff, J., Elghanian, R., Mucic, R., Mirkin, C. & Letsinger, R. 1998, 'One-pot colorimetric differentiation of polynucleotides with single base imperfections using gold nanoparticle probes', *J. Am. Chem. Soc.*, **120**, (9), 1959.

[54] Mirkin, C., Letsinger, R., Mucic, R. & Storhoff, J. 1996, 'A DNA-based method for rationally assembling nanoparticles into macroscopic materials', *Nature*, **382**, 607.

[55] Kohler, J.M., Csaki, A., Reichert, J., Moller, R., Straube, W. & Fritzsche, W. 2001, 'Selective labeling of oligonucleotide monolayers by metallic nanobeads for fast optical readout of DNA-chips', *Sens. Actuators, B*, **B76**, (1-3), 166.

[56] Oldenburg, S.J., Genick, C.C., Clark, K.A. & Schultz, D.A. 2002, 'Base pair mismatch recognition using plasmon resonant particle labels', *Anal. Biochem.*, **309**, (1), 109.

[57] Taton, T.A., Mirkin, C.A. & Letsinger, R.L. 2000, 'Scanometric DNA array detection with nanoparticle probes', *Science*, **289**, (5485), 1757.

[58] Yguerabide, J. & Yguerabide, E.E. 2001, 'Resonance light scattering particles as ultrasensitive labels for detection of analytes in a wide range of applications', *J. Cell. Biochem.*, (Suppl. 37), 71.

[59] Ueno, K., Juodkazis, S., Mizeikis, V., Sasaki, K. & Misawa, H. 2006, 'Spectrally-resolved atomic-scale length variations of gold nanorods', *J. Am. Chem. Soc.*, (in press).

[60] Ueno, K., Mizeikis, V., Juodkazis, S., Sasaki, K. & Misawa, H. 2005, 'Optical properties of nanoengineered gold blocks', *Opt. Lett.*, **30**, (16), 2158.

[61] Spector, S., Astolfi, D., Doran, S., Lyszczarz, T. & Raynolds, J. 2001, 'Infrared frequency selective surfaces fabricated using optical lithography and phase-shift masks', *J. Vac. Sci. Technol., B*, **19**, (6), 2757.

[62] Romanato, F., Businaro, L., Vaccaria, L., Cabrinia, S., Candeloroa, P., De Vittorio, M., Passaseo, A., Todaro, M., Cingolani, R., Cattaruzza, E., Galli, M., Andreani, C. & Di Fabrizio, E. 2003, 'Fabrication of 3D metallic photonic crystals by X-ray lithography', *Microelectron. Eng.*, **67-68**, 479.

[63] Li, M., Wang, J., Zhuang, L. & Chou, S. 2000, 'Fabrication of circular optical structures with a 20 nm minimum feature size using nanoimprint lithography', *Appl. Phys. Lett.*, **76**, (6), 673.

[64] Zhang, H., Chung, S. & Mirkin, C.A. 2003, 'Fabrication of sub-50-nm solid-state nanostructures on the basis of dip-pen nanolithography', *Nano Lett.*, **3**, (1), 43.

[65] Mützel, M., Tandler, S., Haubrich, D., Meschede, D., Peithmann, K., Flaspöhler, M. & Buse, K. 2002, 'Atom lithography with a holographic light mask', *Phys. Rev. Lett.*, **88**, (8), 083601.

[66] Jefimovs, K., Vallius, T., Kettunen, V., Kuittinen, M., Turunen, J. & Vahumaa, P. 2004, 'Inductive grid filters for rejection of infrared radiation', *J. Mod. Optic.*, **51**, (11), 1651.

[67] Green, M. & Yi, F. 2004, 'Light transmission through perforated metal thin films made by island lithography', *Thin Solid Films*, **467**, 308.

[68] Johannsmann, D. & Lemke, D. 1986, 'IR resonant filters for the wavelength region 30-200 microns', *Infrared Phys.*, **26**, (4), 215.

[69] Hanarp, P., Kall, M. & Sutherland, D. 2003, 'Optical properties of short range ordered arrays of nanometer gold disks prepared by colloidal lithography', *J. Phys. Chem. B*, **107**, 5768.

[70] Fukushima, M., Yanagi, H., Hayashi, S., Suganuma, N. & Taniguchic, Y. 2003, 'Fabrication of gold nanoparticles and their influence on optical properties of dye-doped sol-gel films', *Thin Solid Films*, **438-439**, 39.

[71] Perentes, A., Utke, I., Dwir, B., Leutenegger, M., Lasser, T., Hoffmann, P., Baida, F., Bernal, M.-P., Russey, M., Salvi, J. & van Labeke, D. 2005, 'Fabrication of arrays of sub-wavelength nano-apertures in an optically thick gold layer on glass slides for optical studies', *Nanotechnology*, **16**, 273.

[72] Stokes, N., McDonagh, A. & Cortie, M. 2007, 'Preparation of nanoscale gold structures by nanolithography', *Gold Bull.*, **40**, (4), 310.

[73] Ngo, X. & Rosilio, C. 1997, 'Lithography for semiconductor technology', *Nucl. Instrum. Meth. Phys. Res. B*, **131**, 22.

[74] Ferry, D., Khoury, M., Pivin Jr, D., Connolly, K., Whidden, T., Kozicki, M. & Allee, D. 1996, 'Nanolithography', *Semicond. Sci. Technol.*, **11**, 1552.

[75] Chen, Y. & Pepin, A. 2001, 'Nanofabrication: conventional and nonconventional methods', *Electrophoresis*, **22**, 187.

[76] Wei, J. & Wong, K. 2005, 'Physical and chemical nanolithography techniques: challenges and prospects', *Int. J. Nanosci.*, **4**, (4), 575.

[77] Fan, V., Harman, D., Jewett, J., Leet, B. & Speranza, D. 2008, 'Evaluation process for semiconductor fabrication materials that are better for the environment', *Intel Technology Journal*, **12**, (1), 69.

[78] Zhang, H., Lee, K., Li, Z. & Mirkin, C. 2003, 'Biofunctionalized nanoarrays of inorganic structures prepared by dip-pen nanolithography', *Nanotechnology*, **14**, 1113.

[79] Maier, S., Brongersma, M., Kik, P., Meltzer, S., Requicha, A. & Atwater, H. 2001, 'Plasmonics - a route to nanoscale optical devices', *Adv. Mater.*, **13**, (19), 1501.

[80] Gotschy, W., Vonmetz, K., Leitner, A. & Assenegg, F.R. 1996, 'Thin films by regular patterns of metal nanoparticles. Tailoring the optical properties by nanodesign', *Appl. Phys. B*, **63**, (4), 381.

[81] Lamprecht, B., Schider, G., Lechner, R., Ditlbacher, H., Krenn, J., Leitner, A. & Aussenegg, F. 2000, 'Metal nanoparticle gratings: influence of dipolar particle interaction on the plasmon resonance', *Phys. Rev. Lett.*, **84**, (20), 4721.

[82] Klein, M., Enkrich, C., Wegener, M. & Linden, S. 2006, 'Second-harmonic generation from magnetic metamaterials', *Science*, **313**, 502.

[83] Enkrich, C., Wegener, M., Linden, S., Burger, S., Zschiedrich, L., Schmidt, F., Zhou, J., Koschny, T. & Soukoulis, C. 2005, 'Magnetic metamaterials at telecommunication and visible frequencies', *Phys. Rev. Lett.*, **95**, (20), 203901.

[84] Linden, S., Enkrich, C., Wegener, M., Zhou, J., Koschny, T. & Soukoulis, C. 2004, 'Magnetic response of metamaterials at 100 terahertz', *Science*, **306**, (5700), 1351.

[85] Pendry, J. & Smith, D. 2004, 'Reversing light with negative refraction', *Physics Today*, **57**, (6), 37.

[86] Smith, D., Pendry, J. & Wiltshire, M. 2004, 'Metamaterials and negative refractive index', *Science*, **305**, (5685), 788.

[87] Grigorenko, A., Geim, A., Gleeson, H., Zhang, Y., Firsov, A., Khrushchev, I. & Petrovic, J. 2005, 'Nanofabricated media with negative permeability at visible frequencies', *Nature*, **438**, 335.

[88] Garwe, F., Rockstuhl, C., Etrich, C., Hubner, U., Bauerschafer, U., Setzpfandt, F., Augustin, M., Pertsch, T., Tunnermann, A. & Lederer, F. 2006, 'Evaluation of gold nanowire pairs as a potential negative index material', *Appl. Phys. B*, **84**, 139.

[89] Griffith, S., Mondol, M., Kong, D. & Jacobson, J. 2002, 'Nanostructure fabrication by direct electron-beam writing of nanoparticles', *J. Vac. Sci. Technol., B*, **20**, (6), 2768.

[90] Watt, F., Bettiol, A., van Kan, J., Teo, E. & Breese, M. 2004, 'Ion beam lithography and nanofabrication: a review', *Int. J. Nanosci.*, **4**, (3), 269.

[91] Reyntjens, S. & Puers, R. 2001, 'A review of focused ion beam applications in microsystem technology', *J. Micromech. Microeng.*, **11**, (4), 287.

[92] Matsui, S., Kaito, T., Fujita, J.-i., Komuro, M., Kanda, K. & Haruyama, Y. 2000, 'Three-dimensional nanostructure fabrication by focused-ion-beam chemical vapor deposition', *J. Vac. Sci. Technol., B*, **18**, (6), 3181.

[93] Morita, T., Watanabe, K., Kometani, R., Kanda, K., Haruyama, Y., Kaito, T., Fujita, J.-i., Ishida, M., Ochiai, Y., Tajima, T. & Matsui, S. 2003, 'Three-dimensional nanoimprint mold fabrication by focused-ion-beam chemical vapor deposition', *Jpn. J. Appl. Phys., Part 1*, **42**, (6B), 3874.

[94] Fujita, J., Ishida, M., Ichihashi, T., Ochiai, Y., Kaito, T. & Matsui, S. 2003, 'Growth of three-dimensional nano-structures using FIB-CVD and its mechanical properties', *Nucl. Instrum. Meth. Phys. Res. B*, **206**, 472.

[95] Young, R.J., Cleaver, J.R.A. & Ahmed, H. 1993, 'Characteristics of gas-assisted focused ion beam etching', *J. Vac. Sci. Technol., B*, **11**, (2), 234.

[96] Chyr, I. & Steckl, A.J. 2001, 'GaN focused ion beam micromachining with gas-assisted etching', *J. Vac. Sci. Technol., B*, **19**, (6), 2547.

[97] Liu, Y., Longo, D.M. & Hull, R. 2003, 'Ultrarapid nanostructuring of poly(methyl methacrylate) films using Ga+ focused ion beams', *Appl. Phys. Lett.*, **82**, (3), 346.

[98] van Kan, J.A., Bettiol, A.A. & Watt, F. 2003, 'Three-dimensional nanolithography using proton beam writing', *Appl. Phys. Lett.*, **83**, (8), 1629.

[99] Lison, F., Adams, H., Haubrich, D., Kreis, M., Nowak, S. & Meschede, D. 1997, 'Nanoscale atomic lithography with a cesium atomic beam', *Appl. Phys. B*, **65**, 419.

[100] Seisyan, R. 2004, 'Extreme ultraviolet nanolithography for ULSI: a review', *Tech. Phys.*, **50**, (5), 535.

[101] Fay, B. 2002, 'Advanced optical lithography development, from UV to EUV', *Microelectron. Eng.*, **61-62**, 11.

[102] Rothschild, M. 2005, 'Projection optical lithography', *Mater. Today*, **8**, (2), 18.

[103] Alkaisi, M., Blaikie, R. & McNab, S. 2001, 'Nanolithography in the evanescent near field', *Adv. Mater.*, **13**, (12-13), 877.

[104] Brunner, T. 2003, 'Why optical lithography will live forever', *J. Vac. Sci. Technol., B*, **21**, (6), 2632.

[105] Guo, H., Nau, D., Radke, A., Zhang, X., Stodolka, J., Yang, X., Tikhodeev, S., Gippius, N. & Giessen, H. 2005, 'Large-area metallic photonic crystal fabrication with interference lithography and dry etching', *Appl. Phys. B*, **81**, 271.

[106] Nakata, Y., Okada, T. & Maeda, M. 2004, 'Lithographical laser ablation using femtosecond laser', *Appl. Phys. A*, **79**, 1481.

[107] Solak, H. 2006, 'Nanolithography with coherent extreme ultraviolet light', *J. Phys. D: Appl. Phys.*, **39**, R171.

[108] Gronheid, R., Solak, H., Ekinci, Y., Jouve, A. & Van Roey, F. 2006, 'Characterisation of extreme ultraviolet resists with interference lithography', *Microelectron. Eng.*, **83**, 1103.

[109] Sun, S., Mendes, P., Critchley, K., Diegoli, S., Hanwell, M., Evans, S., Leggett, G., Preece, J. & Richardson, T. 2006, 'Fabrication of gold micro- and nanostructures by photolithographic exposure of thiol-stabilized gold nanoparticles', *Nano Lett.*, **6**, (3), 345.

[110] Chao, D., Patel, A., Barwicz, T., Smith, H. & Menon, R. 2005, 'Immersion zone-plate-array lithography', *J. Vac. Sci. Technol., B*, **23**, (6), 2657.
[111] Jung, W., Castaño, F., Ross, C., Menon, R., Patel, A., Moon, E. & Smith, H. 2004, 'Elliptical-ring magnetic arrays fabricated using zone-plate-array lithography', *J. Vac. Sci. Technol., B*, **22**, (6), 3335.
[112] Smith, H., Menon, R., Patel, A., Chao, D., Walsh, M. & Barbastathis, G. 2006, 'Zone-plate-array lithography: a low-cost complement or competitor to scaning-electron-beam lithography', *Microelectron. Eng.*, **83**, 956.
[113] Melville, D., Blaikie, R. & Alkaisi, M. 2006, 'A comparison of near-field lithography and planar lens lithography', *Curr. Appl. Phys.*, **6**, 415.
[114] Blaikie, R., Melville, D. & Alkaisi, M. 2006, 'Super-resolution near-field lithography using planar silver lenses: a review of recent developments', *Microelectron. Eng.*, **83**, 723.
[115] Melville, D., Blaikie, R. & Wolf, C. 2004, 'Submicron imaging with a planar silver lens', *Appl. Phys. Lett.*, **84**, (22), 4403.
[116] Smith, H., Schattenburg, M., Hector, S., Ferrera, J., Moon, E., Yang, I. & Burkhardt, M. 1996, 'X-ray nanolithography: extension to the limits of the lithographic process', *Microelectron. Eng.*, **32**, 143.
[117] Cerrina, F. 2000, 'X-ray imaging: applications to patterning and lithography', *J. Phys. D: Appl. Phys.*, **33**, R103.
[118] Smith, H. 1995, '100 years of X rays: impact on micro- and nanofabrication', *J. Vac. Sci. Technol., B*, **13**, (6), 2323.
[119] Li, X., Paraschiv, V., Huskens, J. & Reinhoudt, D. 2003, 'Sulfonic acid-functionalized gold nanoparticles: a colloid-bound catalyst for soft lithographic application on self-assembled monolayers', *J. Am. Chem. Soc.*, **125**, 4279.
[120] Yu, Z., Deshpande, P., Wu, W., Wang, J. & Chou, S. 2000, 'Reflective polarizer based on a stacked double-layer subwavelength metal grating structure fabricated using nanoimprint lithography', *Appl. Phys. Lett.*, **77**, (7), 927.
[121] Wilder, K., Soh, H., Atalar, A. & Quate, C. 1997, 'Hybrid atomic force/scanning tunneling lithography', *J. Vac. Sci. Technol., B*, **15**, (5), 1811.
[122] Garcia, R., Martinez, R. & Martinez, J. 2006, 'Nano-chemistry and scanning probe nanolithographies', *Chem. Soc. Rev.*, **35**, 29.
[123] Wilder, K., Quate, C., Singh, B. & Kyser, D. 1998, 'Electron beam and scanning probe lithography: A comparison', *J. Vac. Sci. Technol., B*, **16**, (6), 3864.
[124] Sung, I. & Kim, D. 2005, 'Nano-scale patterning by mechano-chemical scanning probe lithography', *Appl. Surf. Sci.*, **239**, 209.
[125] Tang, Q., Shi, A. & Zhou, L. 2004, 'Nanofabrication with atomic force microscopy', *J. Nanosci. Nanotechno.*, **4**, (8), 948.
[126] Hsieh, S., Meltzer, S., Wang, C., Requicha, A., Thompson, M. & Koel, B. 2002, 'Imaging and manipulation of gold nanorods with an atomic force microscope', *J. Phys. Chem. B*, **106**, (2), 231.
[127] Zhang, H., Li, Z. & Mirkin, C.A. 2002, 'Dip-pen nanolithography-based methodology for preparing arrays of nanostructures functionalized with oligonucleotides', *Adv. Mater.*, **14**, (20), 1472.
[128] Piner, R., Zhu, J., Xu, F., Hong, S. & Mirkin, C. 1999, '"Dip-pen" nanolithography', *Science*, **283**, (5402), 661.

[129] Green, M. & Tsuchiya, S. 1999, 'Mesoscopic hemisphere arrays for use as resist in solid state structure fabrication', *J. Vac. Sci. Technol., B*, **17**, (5), 2074.
[130] Bukasov, R. & Shumaker-Parry Jennifer, S. 2007, 'Highly tunable infrared extinction properties of gold nanocrescents', *Nano Lett.*, **7**, (5), 1113.
[131] Rindzevicius, T., Alaverdyan, Y., Sepulveda, B., Pakizeh, T., Kaell, M., Hillenbrand, R., Aizpurua, J. & Garcia de Abajo, F.J. 2007, 'Nanohole plasmons in optically thin gold films', *J. Phys. Chem. C*, **111**, (3), 1207.
[132] Zhang, G., Wang, D. & Moehwald, H. 2007, 'Ordered binary arrays of Au nanoparticles derived from colloidal lithography', *Nano Lett.*, **7**, (1), 127.
[133] Sau, T.K. & Murphy, C.J. 2004, 'Room temperature, high-yield synthesis of multiple shapes of gold nanoparticles in aqueous solution', *J. Am. Chem. Soc.*, **126**, (28), 8648.
[134] Murphy, C.J., Sau, T.K., Gole, A.M., Orendorff, C.J., Gao, J., Gou, L., Hunyadi, S.E. & Li, T. 2005, 'Anisotropic metal nanoparticles: synthesis, assembly, and optical applications', *J. Phys. Chem. B*, **109**, (29), 13857.
[135] van der Zande, B.M.I., Boehmer, M.R., Fokkink, L.G.J. & Schoenenberger, C. 2000, 'Colloidal dispersions of gold rods: synthesis and optical properties', *Langmuir*, **16**, 451.
[136] Chang, S.-S., Shih, C.-W., Chen, C.-D., Lai, W.-C. & Wang, C.R.C. 1999, 'The shape transition of gold nanorods', *Langmuir*, **15**, (3), 701.
[137] Toernblom, M. & Henriksson, U. 1997, 'Effect of solubilization of aliphatic hydrocarbons on size and shape of rodlike C_{16}TABr micelles studied by ^{2}H NMR relaxation', *J. Phys. Chem. B*, **101**, (31), 6028.
[138] Yu, Y., Chang, S., Lee, C. & Wang, C. 1997, 'Gold nanorods: electrochemical synthesis and optical properties', *J. Phys. Chem. B*, **101**, (34), 6661.
[139] Gole, A. & Murphy, C.J. 2004, 'Seed-mediated synthesis of gold nanorods: role of the size and nature of the seed', *Chem. Mater.*, **16**, (19), 3633.
[140] Murphy, C., Sau, T., Gole, A., Orendorff, C., Gao, J., Guo, L., Hunyadi, S. & Li, T. 2005, 'Anisotropic metal nanoparticles: synthesis, assembly and optical applications', *J. Phys. Chem. B*, **109**, 13857.
[141] Nikoobakht, B. & El-Sayed, M. 2001, 'Evidence for the bilayer assembly of cationic surfactants on the surface of gold nanorods ', *Langmuir*, **17**, (20), 6368
[142] Gai, P. & Harmer, M. 2002, 'Surface atomic defect structures and growth of gold nanorods', *Nano Lett.*, **2**, (7), 771.
[143] Wang, Z., Gao, R., Nikoobakht, B. & El-Sayed, M. 2000, 'Surface reconstruction of the unstable {110} surface in gold nanorods', *J. Phys. Chem. B*, **104**, 5417.
[144] Gole, A. & Murphy, C.J. 2005, 'Polyelectrolyte-coated gold nanorods: synthesis, characterization and immobilization', *Chem. Mater.*, **17**, (6), 1325.
[145] Dujardin, E., Hsin, L., Wang, C. & Mann, S. 2001, 'DNA-driven self-assembly of gold nanorods', *Chem. Commun.*, 1264.
[146] Mbindyo, J., Reiss, B., Martin, B., Keating, C., Natan, M. & Mallouk, T. 2001, 'DNA-directed assembly of gold nanowires on complementary surfaces', *Adv. Mater.*, **13**, (4), 249.
[147] Thomas, K.G., Barazzouk, S., Ipe, B.I., Joseph, S.T.S. & Kamat, P.V. 2004, 'Uniaxial plasmon coupling through longitudinal self-assembly of gold nanorods', *J. Phys. Chem. B*, **108**, (35), 13066.

[148] Chang, J.-Y., Wu, H., Chen, H., Ling, Y.-C. & Tan, W. 2005, 'Oriented assembly of Au nanorods using biorecognition system', *Chem. Commun.*, (8), 1092.

[149] Caswell, K., Wilson, J., Bunz, U. & Murphy, C. 2003, 'Preferential end-to-end assembly of gold nanorods by biotin-streptavidin connectors', *J. Am. Chem. Soc.*, **125**, (46), 13914.

[150] Gole, A. & Murphy, C. 2005, 'Biotin-streptavidin-induced aggregation of gold nanorods: tuning rod-rod orientation', *Langmuir*, **21**, 10756.

[151] Connolly, S., Cobbe, S. & Fitzmaurice, D. 2001, 'Effects of ligand−receptor geometry and stoichiometry on protein-induced aggregation of biotin-modified colloidal gold', *J. Phys. Chem. B*, **105**, (11), 2222.

[152] Hu, X., Cheng, W., Wang, T., Wang, Y., Wang, E. & Dong, S. 2005, 'Fabrication, characterization, and application in SERS of self-assembled polyelectrolyte-gold nanorod multilayered films', *J. Phys. Chem. B*, **109**, (41), 19385.

[153] Berry, V., Gole, A., Kundu, S., Murphy, C.J. & Saraf, R.F. 2005, 'Deposition of CTAB-terminated nanorods on bacteria to form highly conducting hybrid systems', *J. Am. Chem. Soc.*, **127**, (50), 17600.

[154] Draine, B.T. & Flatau, P.J. 1994, 'Discrete-dipole approximation for scattering calculations', *J. Opt. Soc. Am. A*, **11**, (4), 1491.

[155] Draine, B. & Flatau, P. 2009, 'User guide for the discrete dipole approximation code DDSCAT 7.0', <http://arxiv.org/abs/0809.0337v5>.

[156] Harris, N., Ford, M., Mulvaney, P. & Cortie, M. 2008, 'Tunable infrared absorption by metal nanoparticles: the case for gold rods and shells', *Gold Bull.*, **41**, (1), 5.

[157] Draine, B.T. & Flatau, P.J. 2004, 'User guide for the discrete dipole approximation code DDSCAT 6.1', <http://arxiv.org/abs/astro-ph/0409262>.

[158] Yurkin, M.A. & Hoekstra, A.G. 2007, 'The discrete dipole approximation: An overview and recent developments', *J. Quant. Spectroscopy. & Radiative Transfer*, **106**, 558.

[159] Myroshnychenko, V., Rodríguez-Fernández, J., Pastoriza-Santos, I., Funston, A.M., Novo, C., Mulvaney, P., Liz-Marzán, L.M. & Abajo, F.J.G.d. 2008, 'Modelling the optical response of gold nanoparticles', *Chem. Soc. Rev.*, **37**, 1792

[160] Nebeker, B.M., Peña, J.L.d.l. & Hirleman, D. 2001, 'Comparisons of the discrete-dipole approximation and modified double interaction model methods to predict light scattering from small features on surfaces', *J. Quant. Spectroscopy. & Radiative Transfer*, **70**, 749.

[161] Brioude, A., Jiang, X.C. & Pileni, M.P. 2005, 'Optical properties of gold nanorods: DDA simulations supported by experiments', *J. Phys. Chem. B*, **109**, 13138.

[162] Kelly, K.L., Coronado, E., Zhao, L.L. & Schatz, G.C. 2003, 'The optical properties of metal nanoparticles: the influence of size, shape, and dielectric environment', *J. Phys. Chem. B*, **107**, 668.

[163] Stockman, M.I., Faleev, S.V. & Bergman, D.J. 2002, 'Coherent Control of Femtosecond Energy Localization in Nanosystems', *Phys. Rev. Lett.*, **88**, (6), 067402.

[164] Bergman, D.J. & Stockman, M.I. 2003, 'Surface Plasmon Amplification by Stimulated Emission of Radiation: Quantum Generation of Coherent Surface Plasmons in Nanosystems', *Phys. Rev. Lett.*, **90**, (2), 027402.

[165] Liu, J., Cankurtaran, B., Wieczorek, L., Ford, M.J. & Cortie, M.B. 2006, 'Anisotropic optical properties of semi-transparent coatings of gold nano-caps', *Adv. Func. Mater.*, **16**, (11), 1457.

[166] Kim, F., Song, J. & Yang, P. 2002, 'Photochemical synthesis of gold nanorods', *J. Am. Chem. Soc.*, **124**, 14316.

[167] van der Zande, B.M.I., Boehmer, M.R., Fokkink, L.G.J. & Schoenenberger, C. 1997, 'Aqueous gold sols and rod-shaped particles', *J. Phys. Chem. B*, **101**, (6), 852.

[168] Xu, X., Gibbons, T. & Cortie, M. 2006, 'Spectrally-selective gold nanorod coatings for window glass', *Gold Bull.*, **39**, (4), 156.

[169] Tovmachenko, O.G., Graf, C., van den Heuvel, D.J., van Blaaderen, A. & Gerritsen, H.C. 2006, 'Fluorescence enhancement by metal-core/silica-shell nanoparticles', *Adv. Mater.*, **18**, (1), 91.

[170] Myers, B. & Dravid, V. 2006, 'Variable pressure electron beam lithography (VP-*e*BL): a new tool for direct patterning of nanometre-scale features on substrates with low electrical conductivity', *Nano Lett.*, **6**, (5), 963.

[171] Anonymous 2008, *Stanford Nanofabrication Facility*, Stanford University, viewed 16/03/09 <http://snf.stanford.edu/>.

[172] Ocola, L. & Stein, A. 2006, 'Effect of cold development on improvement in electron-beam patterning resolution and line roughness', *J. Vac. Sci. Technol., B*, **24**, (6), 3061.

[173] Rossnagel, S. 2003, 'Thin film deposition with physical vapor deposition and related technologies', *J. Vac. Sci. Technol., A*, **21**, (5), S74.

[174] Anonymous 2009, *PMMA resist datasheet*, Micro Chem Coorperation, viewed 5/03/09 <www.microchem.com/>.

[175] Anonymous 2005, *E-beam lithography procedure*, Nanotech User Facility, University of Washington, viewed 5/03/09 <https://depts.washington.edu/ntuf/>.

[176] RaithElphyPlus 2007, *Universal SEM/FIB nanolithography system*, 4.0 edn, Raith GmbH.

[177] Piaszenski, G. 2009, *Raith electron beam lithography users meeting*, *Nanolithography – strategies for a small world*, Raith GmbH.

[178] Drouin, D., Couture, A., Gauvin, R., Hovington, P., Horny, P. & Demers, H. 2001, *CASINO*, 2.42 edn, Université de Sherbrooke, p. monte CArlo SImulation of electroN trajectory in sOlids.

[179] Keller, F.J.G., W.E. & Skove, M.J. 1993, *Physics classical and modern*, Second edn, McGraw Hill.

[180] Walker, J.S. 2002, *Physics*, Prentice Hall.

[181] Isabell, T. & Fischione, P. 1998, 'Applications of plasma cleaning for electron microscopy of semiconducting materials', *Mater. Res. Soc. Symp. P.*, **523**, 31.

[182] Isabell, T., Fischione, P., O'Keefe, C., Guruz, M. & Dravid, V. 1999, 'Plasma cleaning and its applications for electron microscopy', *Microsc. Microanal.*, **5**, 126.

[183] Synowicki, R. 1998, 'Spectroscopic ellipsometry characterization of indium tin oxide film microstructure and optical constants', *Thin Solid Films*, **313-314**, 394.

[184] Guillen, C. & Herrero, J. 2008, 'Influence of the film thickness on the structure, optical and electrical properties of ITO coatings deposited by sputtering at room temperature on glass and plastic substrates', *Semicond. Sci. Technol.*, **23**, (7), 075002/1.

[185] Granqvist, C. 2003, 'Solar energy materials', *Adv. Mater.*, **15**, (21), 1789.

[186] Hamberg, I. & Granqvist, C. 1986, 'Evaporated Sn-doped In_2O_3 films: basic optical properties and applications to energy-efficient windows', *J. Appl. Phys.*, **60**, (11), R123.

[187] Laux, S., Kaiser, N., Zoller, A., Gotzelmann, R., Lauth, H. & Bernitzki, H. 1998, 'Room-temperature deposition of indium tin oxide thin films with plasma ion-assisted evaporation', *Thin Solid Films*, **335**, (1,2), 1.

[188] G173-03 2003, *Standard Tables for Reference Solar Spectral Irradiances: Direct Normal and Hemispherical on 37° Tilted Surface*, American Society for Testing and Materials (ASTM).

[189] Johnson, T. 1991, *Low-e glazing design guide*, Butterworth Architecture, Boston.

[190] Bell, J.M. & Matthews, J.P. 1998, 'Glazing materials', *Materials Forum*, **22**, 1.

[191] Granqvist, C.G. 2003, 'Solar energy materials', *Adv. Mater.*, **15**, (21), 1789.

[192] Schelm, S. & Smith, G.B. 2003, 'Dilute LaB_6 nanoparticles in polymer as optimized clear solar control glazing', *Appl. Phys. Lett.*, **82**, (24), 4346.

[193] Chowdhury, H., Xu, X., Huynh, P. & Cortie, M. 2005, 'Radiative heat transfer across glass coated with gold nano-particles', *J. Sol. Energ.-T. ASME*, **127**, 70

[194] Jain, P.K., Lee, K.S., El-Sayed, I.H. & El-Sayed, M.A. 2006, 'Calculated absorption and scattering properties of gold nanoparticles of different size, shape, and composition: applications in biological imaging and biomedicine', *J. Phys. Chem. B.*, **110**, 7238.

[195] Cole, J.R. & Halas, N.J. 2006, 'Optimized plasmonic nanoparticle distributions for solar spectrum harvesting', *Appl. Phys. Lett.*, **89**, 153120.

[196] Xu, X. & Cortie, M.B. 2006, 'Shape change and color gamut in gold nanorods, dumbbells and dog-bones', *Adv. Func. Mater.*, **16**, (16), 2170.

[197] Xu, X., Cortie, M.B. & Stevens, M. 2005, 'Effect of glass pre-treatment on the nucleation of semi-transparent gold coatings', *Mater. Chem. Phys.*, **94**, (2-3), 266.

[198] Xu, X., Stevens, M. & Cortie, M.B. 2004, 'In situ precipitation of gold nanoparticles onto glass for potential architectural applications', *Chem. Mater.*, **16**, (1), 2259.

[199] Xu, X., Gibbons, T. & Cortie, M.B. 2006, 'Spectrally-selective gold nanorod coatings for window glass', *Gold Bull.*, **39**, (4), 156.

[200] Niidome, Y., Takahashi, H., Urakawa, S. & al, e. 2004, 'Immobilization of gold nanorods on the glass substrate by electrostatic interactions', *Chem. Lett.*, **33**, (4), 454.

[201] Gole, A., Orendorff, C.J. & Murphy, C.J. 2004, 'Immobilization of gold nanorods onto acid-terminated self-assembled monolayers via electrostatic interactions', *Langmuir*, **20**, (17), 7117.

[202] Wei, Z. & Zamborini, F.P. 2004, 'Directly monitoring the growth of gold nanoparticle seeds into gold nanorods', *Langmuir*, **20**, (26), 11301.

[203] Wei, Z., Mieszawska, A.J. & Zamborini, F.P. 2004, 'Synthesis and manipulation of high aspect ratio gold nanorods grown directly on surfaces', *Langmuir*, **20**, (11), 4322.

[204] Perez-Juste, J., Rodriguez-Gonzalez, B., Mulvaney, P. & Liz-Marzan, L. 2005, 'Optical control and patterening of gold-nanorod-poly(vinyl alcohol) nanocomposite films', *Adv. Funct. Mater.*, **15**, 1065.

[205] Zhang, J., Kambayashi, M. & Oyama, M. 2005, 'Seed mediated growth of gold nanoparticles on indium tin oxide electrodes: electrochemical characterization and evaluation', *Electroanalysis*, **17**, (5-6), 408.

[206] Zhang, J., Kambayashi, M. & Oyama, M. 2004, 'A novel electrode surface fabricated by directly attaching gold nanospheres and nanorods onto indium tin oxide substrate with a seed mediated growth process', *Electrochem. Commun.*, **6**, (7), 683.

[207] Taub, N., Krichevski, O. & Markovich, G. 2003, 'Growth of gold nanorods on surfaces', *J. Phys. Chem. B*, **107**, (42), 11579.

[208] Doron-Mor, I., Barkay, Z., Filip-Granit, N., Vaskevich, A. & Rubinstein, I. 2004, 'Ultrathin gold island films on silanized glass. Morphology and optical properties', *Chem. Mater.*, **16**, 3476.

[209] Breitinger, D.K. & Herrmann, W.A. 1999, *Synthetic methods of organometllic and inorganic chemistry*, George Thieme Verlag.

[210] Jana, N.R., Gearheart, L. & Murphy, C.J. 2001, 'Wet chemical synthesis of high aspect ratio cylindrical gold nanorods', *J. Phys. Chem. B*, **105**, (19), 4065.

[211] Holman, J.P. 1990, *Heat Transfer. Seventh Edition.*, McGraw-Hill, London.

[212] Dai, Y. 2001, 'Solar control film retrofitted energy efficient windows for tropical climate', *Glass Processing Days*, Tamglass Ltd Oy, Tampere, Finland, pp. 156.

[213] Sau, T. & Murphy, C. 2005, 'Self-assembly patterns formed upon solvent evaporation of aqueous cetyltrimethylammonium bromide-coated gold nanoparticles of various shapes', *Langmuir*, **21**, 2923.

[214] van der Zande, B.M.I., Pages, L., Hikmet, R. & van Blaaderen, A. 1999, 'Optical properties of aligned rod-shaped gold particles dispersed in poly(vinyl alcohol) films', *J. Phys. Chem. B*, **103**, 5761.

[215] Smith, G., Niklasson, G., Svensson, J. & Granqvist, C. 1986, 'Nobel-metal-based transparent infrared reflectors: experiments and theoretical analyses for very thin gold films', *J. Appl. Phys.*, **59**, (2), 571.

[216] Anonymous 2000, 'G. James is glass', viewed 6/03/09 <http://www.gjames.com.au/>.

[217] Smith, P.A., Nordquist, C.D., Jackson, T.N., Mayer, T.S., Martin, B.R., Mbindyo, J. & Mallouk, T.E. 2000, 'Electric-field assisted assembly and alignment of metallic nanowires', *Appl. Phys. Lett.*, **77**, (9), 1399.

[218] Van der Zande, B.M.I., Koper, G.J.M. & Lekkerkerker, H.N.W. 1999, 'Alignment of rod-shaped gold particles by electric fields', *J. Phys. Chem. B*, **103**, (28), 5754.

[219] Fan, D., Zhu, F., Cammarata, R. & Chein, C. 2004, 'Manipulation of nanowires in suspension by AC electric fields', *Appl. Phys. Lett.*, **85**, (18), 4175.

[220] Gupta, S., Zhang, Q., Emrick, T. & Russell, T. 2006, '"Self-coralling" nanorods under an applied electric field', *Nano Lett.*, **6**, (9), 2066.

[221] Ryan, K., Mastroianni, A., Stancil, K., Liu, H. & Alivisatos, A. 2006, 'Electric-field-assisted assembly of perpendicularly orientated nanorod superlattices', *Nano Lett.*, **6**, (7), 1479.

[222] Carbone, L., Nobile, C., De Giorgi, M., Sala, F.D., Morello, G., Pompa, P., Hytch, M., Snoeck, E., Fiore, A., Franchini, I.R., Nadasan, M., Silvestre, A.F., Chiodo, L., Kudera, S., Cingolani, R., Krahne, R. & Manna, L. 2007, 'Synthesis and micrometer-scale assembly of colloidal CdSe/CdS nanorods prepared by a seeded growth approach', *Nano Lett.*, **7**, (10), 2942.

[223] Harnack, O., Pacholski, C., Weller, H., Yasuda, A. & Wessels, J. 2003, 'Rectifying behavior of electrically aligned ZnO nanorods', *Nano Lett.*, **3**, (8), 1097.

[224] Cheng, C., Gonela, R., Gu, Q. & Haynie, D. 2004, 'Self-assembly of metallic nanowires from aqueous solution', *Nano Lett.*, **5**, (1), 175.

[225] Pohl, H. 1951, 'The motion and precipitation of suspensoids in divergent electric fields', *J. Appl. Phys.*, **22**, (7), 869.

[226] Tiwari, N., Kalele, S. & Kulkarni, S.K. 2007, 'Modulation of optical properties of gold nanorods on addition of KOH', *Plasmonics*, **2**, 231.

[227] Takahashi, H., Niidome, Y., Niidome, T., Kaneko, K., Kawasaki, H. & Yamada, S. 2006, 'Modification of gold nanorods using phosphatidylcholine to reduce cytotoxicity', *Langmuir*, **22**, 2.

[228] Niidome, T., Yamagata, M., Okamoto, Y., Akiyama, Y., Takahashi, H., Kawano, T., Katayama, Y. & Niidome, Y. 2006, 'PEG-modified gold nanorods with a stealth character for in vivo applications', *J. Controlled Release*, **114**, 343.